In Vivo Confocal Microscopy In Turbid Media

Daniel S. Gareau
B.S., Electrical Engineering, University of Vermont, Burlington, Vermont (1999)
M.S., Electrical Engineering, Oregon Graduate Institute of Science & Technology,
Beaverton, Oregon (2001)

A thesis presented jointly to faculty of the
OGI School of Science & Engineering
at Oregon Health & Science University
in partial fulfillment of the
requirements for the degree

Doctor of Philosophy
in
Biomedical Engineering.

December 2006

The dissertation “Confocal Microscopy in Turbid Media and mice” by Daniel Gareau has been examined and approved by the following Examination Committee:

Steven L. Jacques
Professor
Thesis Research Advisor

Scott A. Prahl
Assistant Professor

Sean J. Kirkpatrick
Associate Professor

Molly Kulesz-Martin
Professor

Acknowledgments

Sometimes, when I see how awesomely beautiful and insanely robust nature is I just want to give up. Who are we humans (victims of seeing only what we want to see) to even attempt to understand the natural world and ourselves? Then I remember that it's already inside us and quite literally composes every fiber of our being. The time for "otherization" is over. The outward quest for the universe is only matched by the inward quest for the essence of our being. This quest requires tools like microscopes. Observation of the intense microscopic complexity of living tissue with optical microscopes requires building blocks such as knowing how light acts and interacts. This bottom-up approach, which starts with known properties of the building blocks and works toward microscope synthesis, is complemented by the top-down approach of biology which starts with the organism and work toward the properties of the building blocks.

Engineering has traditionally taken a bottom-up approach. For example, combining the functional properties of the wheel and combustion engine one can synthesize a car, or filling a resonating cavity with a population-inverted optical gain medium, one can synthesize a LASER (Light Amplification by the Stimulated Emission of Radiation). The bottom-up approach is limited though. The problem (as pointed out to me by Dr. Anna Devor) with bottom-up methodology is that in biology, every time one thinks one knows the properties of a building block, the rug tends to get pulled out with the discovery that the building block is actually composed of smaller blocks which themselves are composed of yet smaller blocks, et. cetera. Although we all know that the truth is out there, getting to that truth is a long race and (I hope) the work here is just a few strides in that direction.

The rigorous analysis probably lies in the use of fractal geometry, but for those of us who aren't there yet (because fractal geometry is challenging), the solution is to pick a

domain on nature's infinite tree and solve both the forward and reverse problems simultaneously. This is biomedical engineering since biomedical engineers must be good top-down thinkers in order to analyze and good bottom-up thinkers in order to synthesize.

This thesis involves the development of a tool for microscopic imaging capable of elucidating the structure and function of living cells, the building blocks of our bodies. It represents a small step on an immense journey. Live-tissue imaging is essential to understand life because it reveals the form of building blocks in the context of their function. Unlike noninvasive imaging techniques like x-ray or MRI technologies, light microscopy in the visible spectrum provides contrast that we can all relate to and understand. In a way, this is the most profound domain because it's all around us and intimately connected with our perception and lives.

I'd like to thank my family for putting me up to the plate, my advisor for helping me hit the ball, and my committee for playing the field. I'd like to thank my friends/colleagues in academia: Kirstin Engelking, Ted Moffitt, Yin-Chu Chen, Jessica Remella-Roman, Paulo Bargo and John Adams. I'd like to give a special thanks to Steve Jacques, and Scott Prahl who are two of the greatest teachers/people on the planet and taught me how thinking harder is cool.

Table of Contents

Part II: Mouse Studies

List of Tables

List of Figures

In Vivo Confocal Microscopy In Turbid Media

By Daniel S. Gareau

Thesis Advisor: Steven L. Jacques

Abstract

In this dissertation, a combined fluorescence/reflectance confocal microscope was built and used to detect cancer in mice by quantification of reflectance from the skin. A method for experimentally specifying the optical scattering properties μ_s and g was developed. A novel pinhole/ring detector improved resolution when imaging deeper within tissue.

Single pinholes in confocal microscopes reject diffuse light. However, when focused too deeply in tissue, diffuse light enters the pinhole and resolution and contrast are lost. A novel detection configuration is demonstrated, consisting of a pinhole and a surrounding ring of fibers. The difference between the pinhole and ring signals yields a signal associated with the focal volume after subtraction of diffuse light, thereby further suppressing its effect. Comparing the axial resolution (minimum separation between distinct objects) of pinhole/ring detection to pinhole detection alone when imaging 6-micron-diameter fluorescent microspheres within scattering gel tested this hypothesis. The axial resolution for this sample was 8 μm versus 10.5 μm with the conventional pinhole, an improvement of 31%.

A calibration technique developed for the reflectance-mode confocal microscope (RCM) enabled images to be expressed as the fraction of light reflected from tissue compared with that expected from a mirror in the focal plane so that the reflectivity of various tissues could be compared. Water/glass and oil/glass interfaces, which had calculated reflectances of 4.44×10^{-3} and 4.05×10^{-4}, respectively, were measured and used to calibrate tissue reflectance (brain, skin, muscle, liver), which was 3×10^{-5} to 5×10^{-3}.

The subsurface confocal signal behaved as a simple exponential function of depth (z_{focus}), $\rho \exp(-\mu z_{focus})$, specifying two parameters, ρ and μ. In this work, ρ and μ were mapped into optical scattering coefficient μ_s (100-1000cm^{-1}) and the scattering anisotropy g (0.5-0.95). The technique could differentiate all tissue types ($p<0.05$) except between skin and brain.

The RCM imaged the onset and development of malignant melanoma *in vivo*. A low magnification polarized imaging system guided confocal microscopy by revealing superficial melanin in suspicious lesions. Confocal microscopy revealed the hallmarks of malignant tumors such as pagetoid melanocytes (within epidermis), tumor nests and a disrupted dermal/epidermal junction.

Chapter 1: Introduction

1.A Confocal Scanning Laser Microscopy

Optical microscopes achieve resolution (smallest detail discernible) on the order of a wavelength of light ($400nm \leq \lambda_{light} \leq 800nm$) and are therefore useful to observe nuclei, cells and organelles. These structures are often too small to be resolved with the eye, which has resolution of about 10 microns. Conventional wide-field optical microscopes project an image onto the detection plane such as the retina from a thin slice of tissue (~5μm), typically fixed on a glass slide for imaging. Thin physical sectioning is necessary because multiple scattering in thicker samples degrades contrast and resolution.

1.A.1 The Confocal Principal

Confocal microscopy implements optical sectioning instead of physical sectioning, which enables the imaging of thin sections within thick samples by blocking multiply scattered light from detection. Confocal microscopy thus enables subsurface imaging in scattering biological tissue because it is preferentially sensitive to detection of light singly backscattered from the focus.

In 1957, Marvin Minsky invented the confocal microscope[1], which used a non-coherent light source focused into a slab of tissue. On the other side of the tissue, Minsky placed an objective lens focused in the same plane as the non-coherent light. The two lenses with **con**jugate **focal** planes formed the confocal microscope.

Figure 1.1 shows the basic diagram of a confocal system. The single lenses (L_1 and L_2) shown are simplified representations of multi-lens systems in practice (see Figure 2.6). The result of this configuration is a highly selective measurement of light scattering from the point of geometrical focus within the tissue. The underlying physical principal is that scattering at the focal point affects all of the optical energy since all light rays pass through the focus. The measurement is therefore sensitive to light scattered at the focus and not sensitive to light scattering from out-of-focus particles.

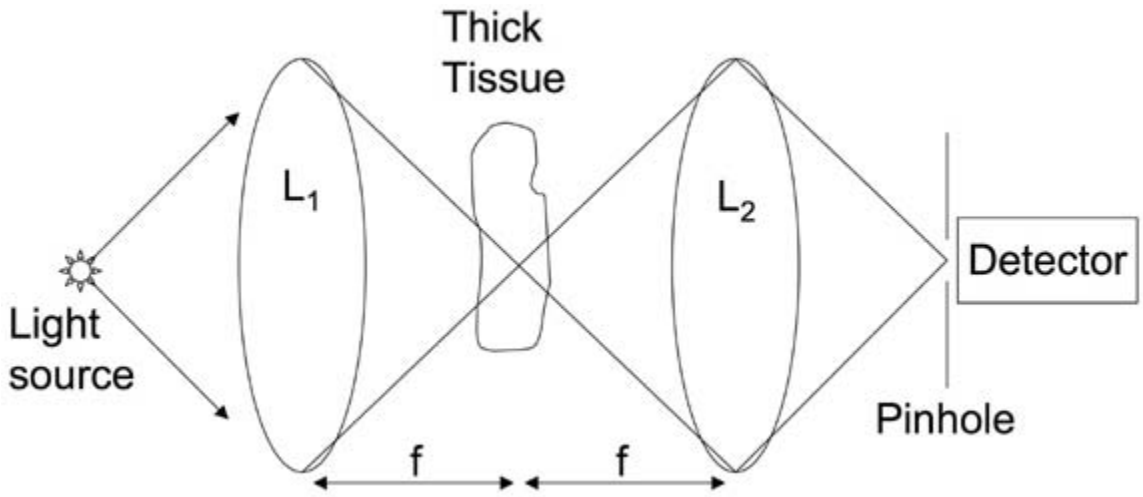

Figure 1.1 Illustration of the basic confocal microscope. A lens L_1 focuses light into a thick tissue sample. A second lens L_2 is positioned such that its focal point is at the same locus as the focal point of L_1. L_2 images the focal point within the sample onto a pinhole, which masks light coming from all other locations. θ is the half angle of focus into the tissue. The numerical aperture of the lens $NA = \sin(\theta)*n$ where and n is the sample refractive index.

By translating the sample in a plane perpendicular to the optical axis, Minsky was able to create a cross-sectional image or "optical section" of a thin plane within the thick sample. Minsky's motivation for this invention was to image in thick slices of brain to understand how "...the great machines that we call brains managed to feel and learn and think.[1]" The problem with imaging in biological tissue is that it is tightly packed with refractive index-mismatched components, which scatter light, obstructing the subsurface

view. The adverse effect of light scattering on the performance of imaging systems became Minsky's obsession[1], and was solved by his invention of optical sectioning for samples as thick as tens to hundreds of microns (depending on optical properties).

Since Minsky's invention, the framework for confocal scanning microscopy has been laid out in detail, a good overview is provided by Wilson and Sheppard[2]. Confocal microscopy has been adapted for fluorescence contrast as well as scattering-based contrast with consideration of the properties of the microscope at the excitation and emission wavelength. Some of the pitfalls of applying confocal to fluorescence imaging such as alignment, diffraction and photo-bleaching have been outlined.[3] Confocal microscopy has proven useful in biological fields besides neurology such as dermatology[4, 5, 6, 7, 8, 9, 10, 11] and ophthalmology[12, 13, 14, 15] and in non-biological applications such as silicon technology for examining microcomputer chips. Three major improvements from Minsky's initial design were: 1) the use of the laser as a light source, 2) better detectors such as photomultiplier tubes (PMT) and avalanche diodes (which have better quantum efficiency than the PMT but are slower to re-zero after a measurement), and 3) optical beam scanning as opposed to sample translation. Minsky first imaged by translating the sample with respect to the focal point to scan an image. This method is nice because it has a potentially infinite field of view, but is very slow. Today, five methods have been developed for rapid optical beam scanning: 1) scanning mirrors[16] and the spinning polygon[8], 2) Multi-focal scanning (described below), 3) acousto-optic deflectors, 4) optical switching in digital micro-mirror devices[17, 18], and 5) a vibrating fiber[19, 11].

The current standard confocal scanning laser microscope (CSLM) uses two mirrors (x,y) and a system of lenses (described in Chapter 2) to move the focus in a square raster pattern within the tissue, which becomes the field of view of the microscope. At each point in the scan, a pinhole/photo-detector measurement becomes a pixel in an image of the tissue in the focal plane of the objective lens. In this manner a two-dimensional image is produced. To produce three-dimensional images, the objective lens and its focal plane are translated in space with respect to the sample and a series of

images forms a stack of optical sections, which extends into the sample from the surface, where sections have high contrast, to deeper tissue where the optical scattering and absorption above the focal plane decreases image contrast. The goal of this work is to improve subsurface imaging. Chapter three characterizes the imaging system by experiments involving optically thin samples and Chapters four and six address the depth capabilities of CSLM for fluorescent microspheres and reflective tissue structures respectively.

1.A.2 Fluorescence

The development of optical filters with sharp spectral cut-offs has enabled chromatic separation of fluorescent emission from the sample, which is weaker at the detector than the reflected excitation light (under achromatic conditions) and hence worth isolating for measurement if an acceptable signal-to-noise ratio is to be achieved. Chromatic filters with sharp long-pass cutoff frequencies just red-shifted of the excitation laser wavelength enable fluorescent detection over the maximum chromatic range of fluorescent emission. Efficient fluorescence collection permits the use of less excitation power, which enables minimal photo-damage in the specimen. In this work, less than ten milliwatts of excitation light are focused into the sample. Commonly available photomultiplier tubes, which are more sensitive than avalanche diodes (and are hence chosen in this work), provide sufficient gains to detect fluorescent light. A back of the envelope type simulation shows that exciting with ten milliwatts yields reflectance signals on the order of a microwatt and fluorescence on the order of nanowatts (see simulation “ConfocalFluor.m” in Appendix).

Fluorescent CLSM (fCSLM) in the presence of biological fluorophores such as green fluorescent protein (GFP) has benefited many fields of science. A nice overview is provided by Billinton *et al.*[20]. Practical issues have been addressed such as autofluorescence rejection (Gareau *et al.* [21] for skin, Doyle and Snider[22] for brain and Staughton *et al.* [23] for arterial tissue) and de-convolution of a point spread function (PSF) from an image. A point spread function is the image produced by a real device of a point

source. Deconvolution of a PSF from an image can restore the contrast lost to errors caused by physical limitations in instrumentation. The shortfall of deconvolution techniques in microscopy, as pointed out by Boutet de Monvel *et al.* [24] is that the PSF is not always known and is non-uniform in heterogeneous media. The device presented in Chapter 4 of this thesis implements the subtraction of a background signal, which is an error measurement sensitive to the tissue optics for each focal position in the sample.

1.A.3 Multifocal Scanning

Multifocal confocal imaging is an interesting contrast to the single point scanning systems described thus far. Multiple, simultaneous measurements offer faster overall image acquisition with greater dwell times, which must be longer than the fluorescent lifetime (see Appendix Multifocal.doc).

The Nipkow disk[4, 25] uses a pinwheel of holes, which allows data to be simultaneously acquired. In this manner, multiple focal points are scanned through the sample simultaneously and back-projected onto multiple detection pinholes. Multifocal scanning which can also be achieved with a lenslet array[26] offers better throughput of laser light to the sample. Spinning, multifocal scanning is fast, but physically challenging to engineer. The focus of this (proof of principal) work will therefore be on a single-point scanning system with a slight modification for more robust confocal detection.

The line-scanning system[14, 16] uses a linear array detector that is optically conjugate to an illuminated line within the sample (instead of a pinhole optically conjugate to an illuminated point). This technique suffers non-confocality in the direction of the illuminated line (as pointed out by Dwyer *et al*[5]). Since adjacent spots are illuminated simultaneously along a line of focus within the sample, cross-talk between these spots can become a problem.

1.B Confocal Microscopy in Turbid, Living Tissue

Among the potential caveats of in vivo CSLM are photo-damage to sensitive living targets, image artifacts due to sample movement and image loss due to tissue optical turbidity. In order for thermal damage to occur, the dwell time during the scan must exceed 500 μs (see Appendix ThermDam.m). The dwell time in the experimental device is only 40 μs (Chapter 2.C) so living tissue at the focus isn't harmed. Mice are anesthetized with a ketamine/xylazine cocktail. Motion artifacts such as heartbeat and breathing are avoided with appropriate fixture and imaging location chosen with low proximity to the chest. The rest of this section addresses the impact of light scattering on the performance of the CSLM since tissue optics are indeed part of the microscope.

1.B.1 The Point Spread Function (PSF)

An ideal image is one that perfectly describes the sample and is impossible. All real point scanning microscopes use an optical probe that isn't an infinitely small point but a small volume of high energy density, the confocal volume, which can be approximated by[27]:

$$V_f = 10^{-15}(\pi/12)(\Delta z^3 \tan(\theta)^2 + 6\Delta x \Delta z^2 \tan(\theta) + 12\Delta x^2 * \Delta z) \quad \text{[Liters]} \qquad (1.1)$$

$$\Delta x = 0.46\lambda/NA \qquad \Delta z = 1.4\lambda/NA^2$$

where λ is expressed in [μm].

In Equation 1.1, V is the effective volume of the confocal probe centered at the point of geometrical focus. λ is the wavelength of light. Δz is the axial section thickness. Δx is the lateral resolution element. θ is the half angle of collection for the objective lens (defined by the numerical aperture NA). The pattern of focused light in non-scattering media is not an ideal point, subsequently, the image of a true point source in a non-

scattering medium will not be a true point but a 3-dimensional function which reveals the non-ideal aspects of the microscope, the Point Spread Function (PSF). There are other factors that influence the PSF under practical imaging conditions besides the inability to perfectly focus light. Wavefront aberrations and scattering from out of focus regions for example alter the pattern of focused light thereby changing the PSF for the imaging system.

In 1999, Webb[28] reviewed the theoretical basics of confocal microscopy. He considered the PSF to be the probability that an excitation photon would reach some point in the sample. Here, a similar approach is taken but the effects of light incidence and light emission from the sample are separated. In this thesis, the forward point spread function is referred to as T_{in} [unitless] and it is a function of the tissue optical properties and the depth of focus (z_f). There is a reverse PSF (T_{out} [unitless]) associated with the escape of a fluorescent or reflected photon originating from the focal volume from the tissue to successfully enter the microscope objective and pass through the pinhole detector. T_{out} is also a function of the tissue optical properties, z_f and the pinhole diameter. The total PSF for signal from the confocal volume is $T_{in}T_{out}$ assuming the point source and detector are matched. For reflectance, T_{out} equals T_{in}. For fluorescence, T_{out} will usually differ somewhat from T_{in} because the fluorescence is at a longer wavelength than the excitation and tissue optical properties are wavelength dependent. A third PSF is associated with the detection of background signal originating outside the confocal volume. Let the transport of excitation light to a point in the sample but outside the focal volume be called $T_{in.bkgd}$, and let the transport of optical signal coming from that point, escaping the tissue and propagating through the pinhole for detection be called $T_{out.bkgd}$. The total PSF for background signal from a background point is $T_{in.bkgd}T_{out.bkgd}$, and this must be integrated over the entire tissue volume to yield the total background signal. A confocal measurement meant to sample some point within the tissue will be equal to both the desired signal from the confocal volume and an unwanted background signal from outside the confocal volume:

$$signal(z_f) = T_{in}\ \ C(z_f)L_f\ \ f + \int_0^{\infty} R(r')\, f_{\Omega}(z_f, r')2\pi r'\, dr' \qquad (1.2)$$

In the first term of equation 1.2, the value L_f is the effective value of V_f/A_f where V_f is given in Equation 1.1 and A_f is the cross-sectional area of the airy spot. f is the fraction of unscattered light originating at the focus that gets collected by the objective lens (see Equation 6.3 for reflected light). The integral in the second term indicates the volume integral of background signal. R(r') is the escaping flux of multiply scattered light, and $f_{\Omega}(z_f,r')$ describes the fraction of escaping flux that is within the solid angle of collection of the confocal lens/pinhole system. The value $f_{\Omega}(z_f,r')$ decreases as z_f becomes deeper in the tissue, and drops to zero as r' increases beyond the collection zone of the lens. For reflectance, $C(z_f) = \mu_s A_f f$, where μ_s [cm^{-1}] is the scattering coefficient, A_f is the cross-sectional area of the confocal volume such that V_f/A_f equals the axial length of the confocal volume, and *f* [dimensionless] is the fraction of scattered light that is backscattered into the solid angle of collection of the lens aperture. This *f* is a strong function of the anisotropy of scattering, g [dimensionless] which is the mean cosine of polar scattering angle. The reflected or epifluorescent confocal measurement is heavily influenced by the factor f, this relationship will be discussed in Chapter 6.

The total PSF $T_{in}T_{out}$ is more spatially selective than either T_{in} or T_{out} alone. Minsky said in his memoir[1]: "Reflectance mode ... brings an extra premium because the diffraction pattern of both pinhole apertures are multiplied coherently: The central peak is sharpened and the resolution increased". We will see how a new confocal detector can enhance this "central peak" even further by allowing a correction for the contribution from the background signal in Equation 1.2.

Fluorescence confocal scanning laser microscopy (fCSLM) can be modeled as the convolution of the 3D fluorophore concentration in the object and the PSF for the system. This approach assumes that the PSF is uniform over the sample. In biological confocal microscopy of heterogeneous tissue, the point-spread function is unfortunately non-uniform which means that the microscope's response varies for subsurface regions

depending on the optical properties of the overlying regions. Optical penetration to the focus in tissues can change depending on the focal position in heterogeneous tissue.

Highly anisotropic scattering can broaden focal patterns from their diffraction-limited counterparts. This effect can vary spatially within the sample. The forward PSF in thick tissue is composed of both non-scattered and scattered light and the power distribution between the two different types of light is non-uniform over the sample. For thick samples such as living tissue, optical penetration must be considered as a function of confocal probe position within the sample since the sample is heterogeneous. This heterogeneous responsivity will be discussed in Chapter 7.

1.B.2 Reflectance Mode Confocal Scanning Laser Microscopy

Common commercially available microscopes are only able to image relatively thin (up to 50 μm) samples depending on the sample optical properties. Wang *et al.* [29] found that the effect of focused light only can penetrate to a mean-free path (MFP = average distance a photon propagates before it is scattered or absorbed), yet theoretical work by Schmitt *et al.* [30] in 1994 concluded that the maximum depth of the reflectance confocal probe in media such as dermis is 400 μm for skin under practical conditions, which is 1.6 times the MFP on the optical properties of skin[31]. Their work used a large pinhole with radius equal to 8-17 times the radial position of the first zero of the Airy function (see Figure 2.5) in the pinhole plane (v_p = 8 to 17). Kempe *et al.* [32] found that a perfectly reflective grating could be detected with v_p = 1.3 through 6 MFPs. Smithpeter *et al.* [33] found that with a pinhole radius of v_p = 3 (in media whose scattering coefficient was 100 cm^{-1}) the maximum imaging depth for a refractive mismatch boundary of 0.05 was only 200 μm (= 2 MFPs).

In skin, microscopic variations of refractive index lead to reflectance on the order of 10^{-4} times the incident laser power (see Chapter 6). Although the reflectance of tissue is far less than the highly reflective grating used by Kempe *et al.* [31], reflectance contrast can be used to image tissue structure beneath the skin surface[6, 7, 8, 9]. In 1993, Corcuff *et*

al. adapted the confocal microscope to image human skin in vivo, using a white light source and a spinning disk of pinholes[4]. In 1995 Rajadhyaksha *et al.*[8] developed a reflectance-mode confocal microscope designed to image human skin and in 1999 reported on advances made on their first design that included better resolution, contrast, depth of imaging and field of view[9]. Depths of up to 350 μm were imaged in human skin using the optical contrast of melanin, agreeing with Schmitt *et al.*[30]. These developments led to a commercially available model called the VivaScope 1500 (Lucid Technologies), which can image up to 350 μm deep with 2-μm lateral resolution (5 μm axial resolution, λ=830 nm). Busam *et al.*[10] explored the use of this microscope for detection of amelanotic malignant melanoma.

1.B.3 Comparable Imaging Techniques

Other noninvasive imaging modalities include optical coherence tomography (OCT) [34, 35, 36], high frequency ultrasound[37], and magnetic resonance imaging[38]. OCT involves delivery and collection of light by a single-mode optical fiber that essentially is a pinhole of detection and interferes the tissue-reflected signal with that reflected from a reference beam, which samples a mirror. OCT began to offer a competitive axial resolution with rCSLM in the mid-nineties[39] as new light sources became available, approaching the resolution < 10 μm axial[40]. OCT provides optical sectioning similar to that of histology but lacks adequate lateral resolution because it typically uses a low numerical aperture lens to allow for extended axial scanning. Ultrasound and MRI provide resolution that is typically 10-1000 μm that is useful for observing morphology and function at the organ level. Confocal microscopy offers both high lateral resolution (0.1-1 μm) and optical sectioning (1-3 μm) that is comparable to histology, which allows visualization of cellular detail.

1.B.4 *In Vivo* Fluorescence Confocal Microscopy

For fluorescence-mode confocal microscopy, the most common contrast agent for living biological samples is green fluorescent protein (GFP) and its variants[41]. Adapted

from the jellyfish *Aequorea victoria*, GFP has an absorption peak at 489 nm and an emission peak at 510 nm, and can be genetically encoded in living tissues, making it a useful fluorescent contrast agent for *in vivo* fluorescent confocal microscopy. In animal skin, GFP offers a contrast agent that is not as invasive as injecting fluorescent dye[11].

GFP is useful as a contrast agent for quantitative assessment of gene expression. Genetic modifications are used to tag proteins in certain phenotypes such as cartilage[21, 42]. Cells expressing GFP yield imaging contrast through detection of fluorescent emission. Recent advances in biochemistry have led to the development of an enhanced GFP (EGFP). EGFP is highly resistant to photo-bleaching and 35 times brighter than wild type GFP[41]. With such a bright biological fluorophore the power of fluorescent emission escaping the tissue surface is enough to detect with a commonly available spectrometer[21]. However, imaging cells through thick sections of skin requires the use of scattered photons, which produce images with poor contrast. Chapter 4 illustrates this problem and offers a means to recover the contrast loss due to optical turbidity in thick samples.

Although preliminary work[21] on young mice with EGFP-expressing chondrocytes showed that subdermal green fluorescent emission could be confocally detected through full thickness skin by implementing confocal spectroscopy, in subsequent imaging with fCSLM it was found that although the EGFP yielded contrast to the macroscopic ossification front, the microscopic contrast was too poor to resolve individual cells. The conclusion from this preliminary work is that scattered fluorescent emission contaminates the signal penetration through the confocal aperture.

The hypothesis of this work is that two signals can be combined to produce a confocal measurement with improved contrast in the presence multiple scattering. Chapter two documents the physical design of the experimental apparatus. Chapter three investigates its use in the non-scattering regime. Chapter four provides a conceptual introduction to the new technique proposed and illustrated its use in the scattering regime.

Gan *et al.*[43] addressed the use of scattered photons in image formation. For high NA objective lenses without scattering, the diffraction-limited resolution is on the order of a micron. Forming an image using all photons that have scattered twice, whether scattered from the confocal volume or not, the resolution limit is worse than 14 μm where resolution limit is defined by the minimum separable distance between objects resolvable as individual by the Rayleigh criteria. High resolution implies a smaller resolution limit. In sub surface imaging, smaller pinholes produce higher resolution because they transmit less scattered light. The trade-off between resolution and signal strength is apparent because smaller pinholes yield higher resolution but also yield smaller signals.

Both larger NA lenses and bigger pinholes accept more scattered photons for detection, and hence produce images with lower resolution. Lower NA lenses offer higher resolution when imaging in semi-diffuse situations because the smaller cone of collection accepts less multiply-scattered photons. When the limiting aperture is chosen as a small pinhole (rather than low objective NA), the scattered light filtration lost by using a large NA lens is regained. Choosing a high NA brings the additional benefit of a tighter focal spot, which improves the optical sectioning. This suggests the use of high NA objective lenses, which accept more scattered photons. Such a lens (NA = 0.9) is used with a new detector in Chapter four.

The pinhole size determines the number and type of photons collected. Larger pinholes collect more multiply-scattered photons. Reducing the pinhole size for higher resolution fails as signal strength weakens. The pinhole and focused laser spot in the sample form a conjugate pair, which means they are spatially congruent in the two conjugate planes of the microscope. Traditional confocal gating (appropriate pinhole size) is achieved by matching the radius of the pinhole to the radius of the central disc of the Airy pattern of a focused laser beam (see Figure 2.5) that back-projects from the sample focal plane into the conjugate pinhole plane, capturing about 80% of the total power[27]. This “diffraction limited” resolution model is only useful for singly scattered light, and hence limits its application to optically thin samples. As pointed out by Stelzer *et al.*[44], diffraction limited resolution can never be achieved by real devices. Sandison *et*

al.[45] illustrated the use of scattered light by showing low contrast images in a turbid media where no pinhole was used at all. Then he showed images acquired using a pinhole 0.9 and 6-fold as big as the Airy pattern which were both much crisper than the no-pinhole image.

Using the convention of diffraction limit to characterize resolution is only useful in the non-scattering regime where thin samples are imaged and the vast majority of collected photons are singly backscattered from the focus (or in fluorescence mode, fluorescent photons emitted from the focus which propagate un-scattered to the pinhole detector). In the non-scattering regime, the term "resolution limit" means the minimum separation distance between point sources that can be resolved as separate in the image by the Rayleigh criteria. In the scattering regime, optically thick specimens demand the use of multiply scattered photons. In this regime, the term "contrast" means the ratio of signal collected from the object at focus to the background signal composed of diffuse light.

The work of Gan *et al.*[43] suggested that the confocal signal could be treated as a conglomerate of photon populations where the image created solely by one population will have a resolution dependant upon the number of scattering events that population has experienced. For instance, an image created with only photons singly backscattered from the focus (type 1) will have a higher resolution than one created with only doubly scattered photons (type 2). These populations convey different information but are left un-separated with the conventional pinhole, which can either collect type 1 if it is small or the sum of both types if it is large. The goal of this work is to develop a confocal probe capable of measuring type 1 and type 2 photons separately. In addition to the conventional pinhole measurement, a ring of collection surrounding the pinhole will measure the signal composed of scattered light. A new collection probe configuration is developed in Chapter four to enable dual collection of photons (both singly and multiply-scattered) in order to increase contrast and resolution in the scattering regime, enabling deeper noninvasive imaging, and will hopefully be a significant advance for confocal microscopy. Of chief importance for live cell imaging is the ability to resolve subsurface

targets. Resolution is characterized by the minimum proximity at which two objects are distinguishable by the Rayleigh criteria and will be tested in fluorescence mode to document the advantage of dual mode collection.

1.B.5 Chapter Outline

Part one of this thesis is devoted to basic science studies and consists of chapters one through five. Chapter two outlines the development of a confocal microscope used as a platform for development of the novel technique outlined in chapter four for imaging in scattering media. Chapter three addresses device performance in non-scattering media. Calibration images of standard samples are shown to illustrate device performance. A Monte Carlo model of confocal imaging presented in chapter five provides deeper insight into the effect of turbid tissue on image contrast and resolution, and provides context for interpretation of experimental results presented in chapters six and four for reflectance and fluorescence imaging respectively.

Part two of this thesis deals with imaging in living mice and consists of chapters six through eleven. Chapter seven shows how reflectance mode confocal microscopy can be applied to study the onset and progression of malignant melanoma. Chapter eight involves the combination of confocal microscopy with polarized light microscopy to provide a low-to-high magnification approach, which is useful in surveying large areas of skin with subsequent honing in on malignant epidermal tumors. In chapter nine, the optical scattering properties (scattering coefficient and scattering anisotropy) of mouse skin at the 488 nm wavelength are investigated. In chapter ten, confocal fluorescence spectroscopy is applied to detect sub-dermal cartilage with green fluorescent protein. Finally, chapter eleven shows the Monte Carlo simulation of the forward focusing of li[illegible] into scattering medium.

Chapter 2: Instrumentation

In this dissertation, a confocal scanning laser microscope (CSLM) was built to allow technical development of a novel confocal detector for experimental imaging in cultured cells, animals, and Agarose gels with polystyrene microspheres, The microscope allows *in vivo* non-invasive imaging of tissue in both fluorescence and reflectance modes. Design criteria were that the CSLM be able to image living mice (Chapters 7,8) and image with two confocal apertures (Chapter 4) at two wavelengths. This chapter details the CSLM's technical development. Part B details the optical aspects of the experimental design and part C, the electronics. Part A provides an overview of system's composition.

2.A.1 System Layout

Figure 2.1 shows the confocal microscope and control electronics. Optical elements from various manufacturers were used to yield a device that is comparable to commercially available systems in terms of performance and has versatile interchangeable parts in order to develop a new confocal detection technique. The components of the entire system cost about $21,000. A laptop computer running Labview™ software served as the controller for the scanning hardware as well as the data acquisition.

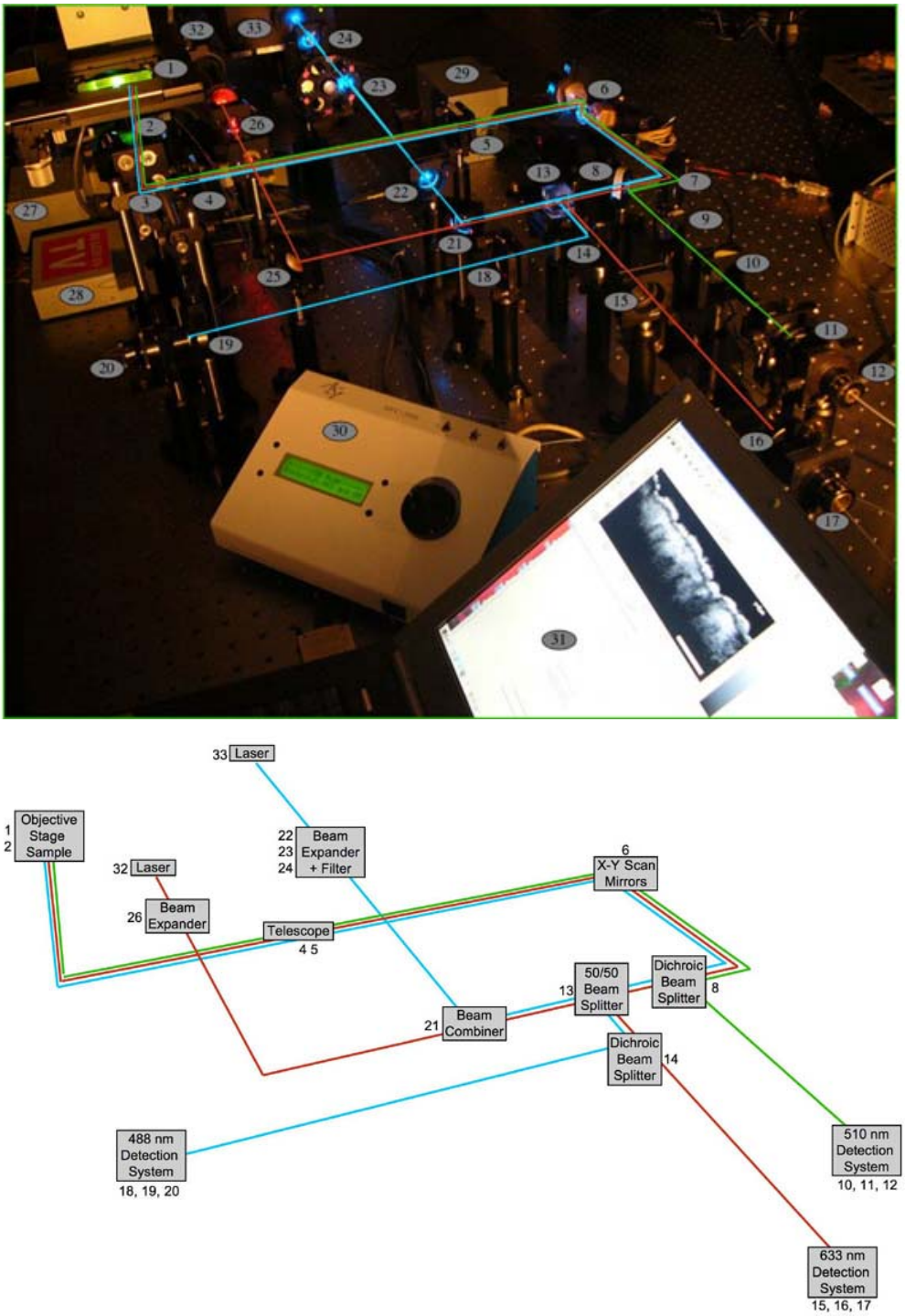

Figure 2.1 The Confocal Microscope. False beams are drawn to illustrate the optical path. A block diagram below illustrates the subsystems of the microscope's composition with the component numbers indicated. Optical components can be identified with the element numbers in table in the component list below.

Figure 2.1 shows the layout of the CSLM. The lower illustration is a block diagram of the upper illustration. Laser beams emitting from two lasers (elements 32 and 33) are expanded to 1 cm diameter, each beam by a set of lenses separated by the sum of their focal lengths such that the light is focused and re-collimated at a wider beam width since the longer focal length lens of the pair is situated downstream of the laser source. The 488 nm beam expander contains an attenuation filter wheel (23) so that the power of the argon ion laser (33) can be decreased from 100 mW to 5~10 mW, a power similar to that of the 633 nm laser (5 mW). Optical losses in the system are primarily due to the 50/50 beam-splitter. Optical transmission from the laser into the sample was measured to be 0.63 (+/- 0.03, n = 4 different days) excluding loss at the 50/50 beam-splitter. Half of the 633 nm and 488 nm incident laser light is lost as well as half of the reflected light.

The beam-splitter was non-polarizing but had a ¼-wave plate been placed between elements 3 and 2, directly before the objective lens, a polarizing beam splitter could have been used, which would have transmitted the linearly polarized laser efficiently from the laser to the sample. Upon incidence of the ¼ wave plate, the laser would change to circularly polarized. Upon reflecting from the focus the signal would have changed circular-polarization handedness and been converted back to linear polarization when returning back through the ¼-wave plate. The axis of polarization of the returning signal would be orthogonal to the incident light's linear polarization axis and be diverted to the detectors by the polarizing beam splitter. This polarization-sensitive technique was not used and therefore the system was sensitive to reflections from the lenses (4, 5), necessitating the use of antireflective lens coating. Although the ¼-wave plate is useful in reflectance imaging, it is not useful for fluorescence imaging because fluorescent emission has semi-random phase and is not fully polarized. Since fluorescence imaging more light starved, the ¼-wave plate isn't used to minimize attenuation of detectable fluorescence.

The telescope (4, 5) is a pair of lenses separated by sum of their focal lengths and positioned to create two pupil planes, one at the X-Y scan mirrors (6) and one at the back aperture of the objective lens called the shoulder plane where the screw threads meet the

body of the objective. This design for raster scanning was adapted from Rajadhyaksha *et al.*[8].

In figure 2.1, the sample consists of concentrated fluorescein dye sandwiched by a cover slip onto a microscope slide to provide a thin planar layer of fluorescence (<5 μm thick). This sample was chosen to yield bright fluorescence for the purpose of illustration and was used to align the fluorescent pinhole. This slide is replaced with an imaging plate (Chapters 7,8) and an animal rests directly on the plate for in vivo reflectance imaging. In this epi-fluorescent or inverted system, light focuses upward into the sample. Signal is detected when light back-propagates from the focus to one of three detection systems, each containing a focusing lens, pinhole (in the focal plane) and fiber to collect the signal that passes thorough the pinhole.

Component List:

1) Sample, water immersion stage
2) 60X objective, air, focal length = 3 mm, NA = 0.85 (Newport)
   60X objective, water, focal length = 4 mm, NA = 0.90 (Olympus LUMPlanFl)
3) Inverting mirror
4) Raster Lens (L2 in schematic), antireflective coating, focal length = 175mm
5) Raster Lens (L1 in schematic), antireflective coating, focal length = 150mm
6) Orthogonal raster-scanning galvanometric mirror pair (Nutfield Technologies)
7) Mirror
8) Fluorescence separation filter (Chroma Z488/633) see spectrum (fig 2.3)
9) Raman Filter (Omega XR300), OD 6 at 488 nm
10) Lens, focal length = 150 mm
11) Pinhole, diameter = 25 μm
12) Optical Fiber, diameter = 200 μm
13) 50/50 non-polarizing beam splitter
14) Dichroic, passes 633 nm, reflects 488 nm
15) Lens, focal length = 250 mm
16) Pinhole, diameter = 50 [μm]

17) Optical Fiber, diameter = 200 [μm]

18) Lens, focal length = 250 [mm]

19) Pinhole, diameter = 50 [μm]

20) Optical Fiber, diameter = 200 [μm]

21) Dichroic, passes 633 [nm], reflects 488 [nm]

22) Re-collimating lens

23) Attenuation filter wheel, OD = [0.1 0.3 0.5 1 2 3]
where transmitted power = (10^{-OD}) incident power

24) Beam-expanding Lens

25) Mirror

26) Beam expanding lens pair (analogous to 22 & 24)

27) Photomultiplier tubes (Hamamatsu H5773-01)

28) National Instruments SCB-68 I/O box, 6062E DAQ card

29) Driver hardware for galvanometric scan mirrors

30) Z-axis translation stage (Applied Scientific LS-50A, MFC-2000)

31) Laptop computer (Gateway, Windows 2000) with Matlab and Labview software

32) Helium-Neon LASER, λ = 633 nm, P = 5.6 mW (Melles-Griot 05-LHP-201)

33) Argon ion LASER, λ = 488 nm, P = 200 mW (Melles Griot 35LAL-415-220R)

The microscope is shown with a lens/pinhole/fiber at the fluorescent probe arm (10, 11, 12). The use of a modified confocal aperture to replace this pinhole for confocal light detection will be discussed in Chapter 4. Lens pairs (22, 24) and (26) expand the laser beams from a diameter of roughly 1 [mm] to 1 [cm] in order to overfill the objective lens, which is 7.5 mm. The beam expanding power is chosen such that the radius of the back aperture of the objective lens is approximately equal to the beam $1/e^2$ radius, which is the radius on the Gaussian beam profile at which the power has fallen to $1/e^2$ of its central peak value. The optical pupil of the objective lens transmits the truncated Gaussian. Since a beam profiling charged coupled device was not available, the $1/e^2$ radius was judged by eye. The eye is capable of detecting light extending to a radius of 1.5 times the $1/e^2$ radius.

A schematic diagram specifying the actual physical layout and distances for the optics is presented in Figure 2.2. The magnification of the reflectance channels (r and b) is the product of the ratio of the focusing lens (10, 15 and 18) to the objective lens (2) and the magnification of the telescope (4, 5). The system magnification is 97 for the reflectance channels, making an Airy disc in the sample plane (diameter ≈ 0.5 μm) back-project to a 50-μm pinhole in the conjugate plane achieving confocal gating. For the fluorescence channel, the system magnification is 58 and the pinhole is overfilled.

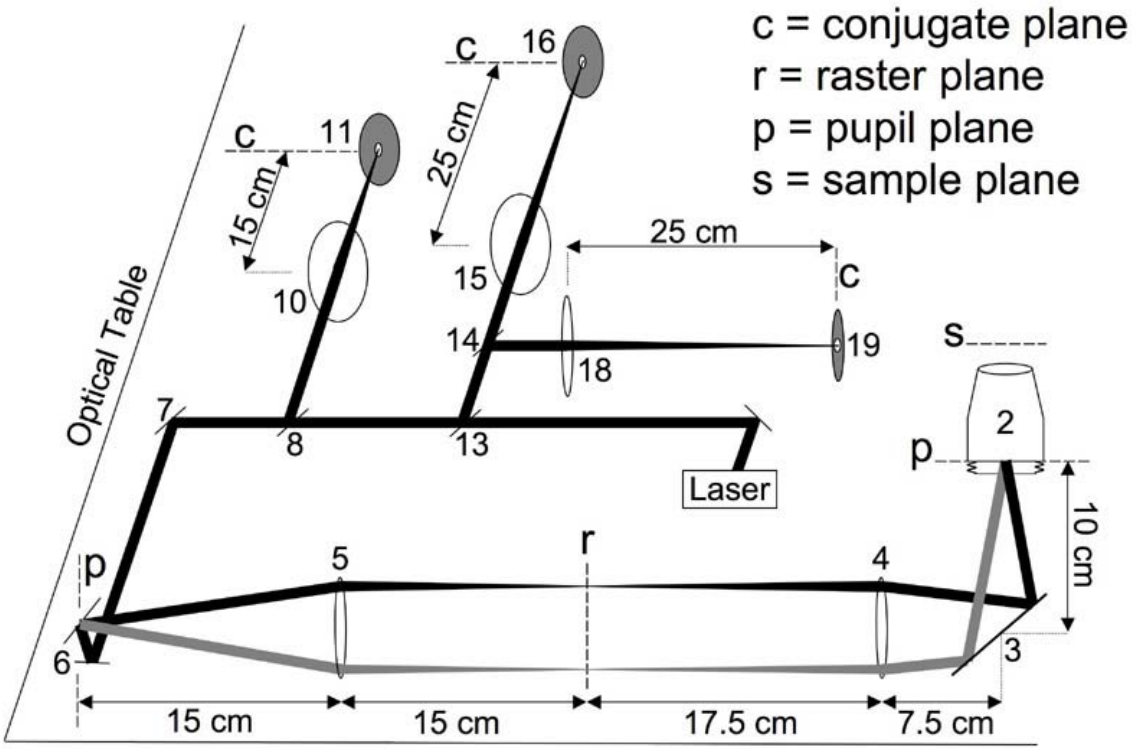

Figure 2.2 A schematic diagram showing the focusing optics and their relative positions. All components are in the plane of the optical table except the objective lens (2) whose axis is perpendicular to the table in the inverted configuration. Lenses (4, 5, 10, 15 and 18) are thin biconcave lenses of 1-inch diameter with antireflective coating from Newport Corporation.

Three lens/pinhole pairs [(18, 19) (15, 16) and (10, 11)] form three confocal probe arms. The pinholes lie in three planes that are each optically conjugate to the sample

plane. A telescoping lens pair (4, 5) controls the beam propagation between two pupil planes located at the x-y scan mirrors and at the shoulder of the objective. The beam scan is illustrated with black and gray lines.

2.A.2 Three Channels

Laser light from blue (33) and red (32) lasers (Melles Griot 35LAL-415-220R, 488 nm 200 mW and 05-LHP-201, 633 nm 5 mW, respectively) were combined in the optical path using a dichroic mirror (21), which reflected the blue and transmitted the red wavelength. The combined beam was focused into tissue using an inverted water-dipping lens (2, Olympus LUMPlanFl 60X/0.90W). Water immersion is chosen for its refractive index 1.33, which is sufficiently close to that of tissue (n ~ 1.37) to minimize unwanted refractive effects when photons cross the boundary of refractive index mismatch from the immersion medium into tissue. Reflected blue light, reflected red light and green fluorescent light were separated with dichroic mirrors on the return detection path and focused into three pinhole/fiber collection assemblies.

Two photomultiplier tube circuits (27, circuit shown in Figure 2.9) were connected to separate input acquisition channels on the national instruments acquisition board (28). To collect co-registered pictures of either fluorescence and reflectance at the 488 nm wavelength or reflectance at 488 nm and reflectance at 633 nm the two photomultiplier tubes were sequentially selected by Labview™ software. Registration of images was accomplished by sequentially acquiring 3D images starting from a field of view at the same depth (z position on the optical axis) as measured with one-micron repeatability by the translation stage (30). The mechanical stage resolution (200 nm) was better than the axial optical resolution (700 um from Equation 1.1). For acquiring co-registered image stacks, the stage was re-zeroed for *exvivo* samples. Due to motion in living mice, the repeatability was poorer ranging from 1 μm to greater than 10 μm.

2.B Optics

The argon ion laser (488 nm) was chosen because it is optimal for excitation of green fluorescent protein, provided strong scattering from melanosomes in the mouse melanoma model studied, and it achieves sufficient penetration to study the upper 50 μm of the mouse model (see Chapters 7 and 8), while achieving high lateral and axial resolution due to the short wavelength (see Figure 3.1). Reflectance-mode confocal scanning laser microscopy (rCSLM) avoids chromatic aberration because of its monochromaticity, while fluorescence microscopy offers minimal chromatic aberration because the wavelengths of excitation and emission for GFP are similar (488 nm and 510 nm, respectively).

2.B.1 Filters

Reflected or fluorescent light emanating from the focus back-propagated to a band-rejection filter (8) (Chroma Z488/633) that diverted GFP emission to a lens/pinhole/fiber assembly (10, 11 and 12). The fluorescent pinhole detector was aligned by placing a sample consisting of the thin layer of fluorescein (Fluka 46960) solution sandwiched between class cover slips in the focal plane of an air immersion lens and adjusting the pinhole aperture for maximum throughput. This calibration was chosen instead of one using the normal water-dipping lens because pressing fluorescent dye between glass yields a thin plane source of fluorescence. The water dipping lens is not suited for imaging through a cover slip but both objective lenses have infinity-corrected optics. The two configurations objective lens configurations are therefore optically equivalent since they both focus collimated light to a point in the focal plane.

An optical filter (9, Omega XR3000) whose optical density is 6 (transmits 10^{-6}) at the 488 nm wavelength but transmits GFP fluorescence with 92% efficiency prevented any reflected blue light from penetrating the sensitive GFP detection assembly. The transmission spectra of filters (8, 9) are shown below.

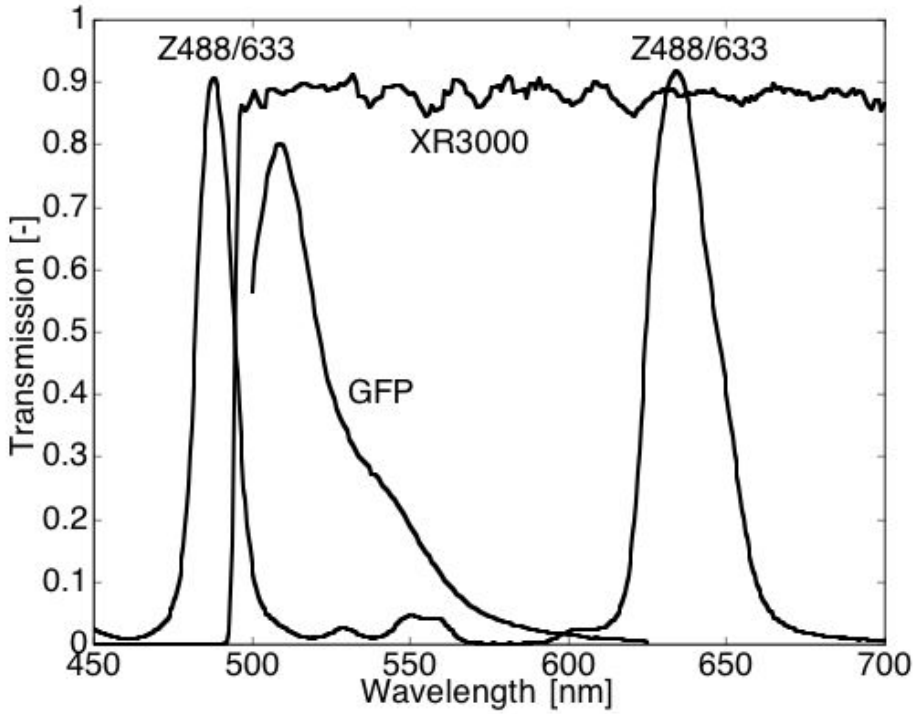

Figure 2.3 The transmission spectra of the filters used for GFP detection are shown (provided by the manufacturer) with the emission spectrum of GFP (measured in Chapter 10, arbitrary units). Z488/633 (8) separates GFP emission from the optical path by reflecting it and diverting it toward the detector. XR3000 (9) transmits the returning green fluorescent light to the fluorescence detection channel but blocks any reflected 488 nm light from detection.

Blue and red reflected light is transmitted through Z488/633 (8) and is diverted by the 50/50 beam splitter (13) toward two reflectance detection channels. The dichroic mirror (14) splits the blue and red reflectance signals for incidence on two lens/pinhole/fiber assemblies (15, 16 and 17) and (18, 19 and 20). In this manner, the separation of three signals is achieved: 488 nm reflectance, 633 nm reflectance and green fluorescence. Simultaneous acquisition of all three signals would require an additional filter before the GFP collection pinhole to reject 633 nm light with high optical density (OD = 6 or better) and was not implemented.

2.B.2 Scanning

The scanning optics (adapted from Rajadhyaksha *et al.* 1995[8]) implement a raster scan to move the focus laterally within the sample.

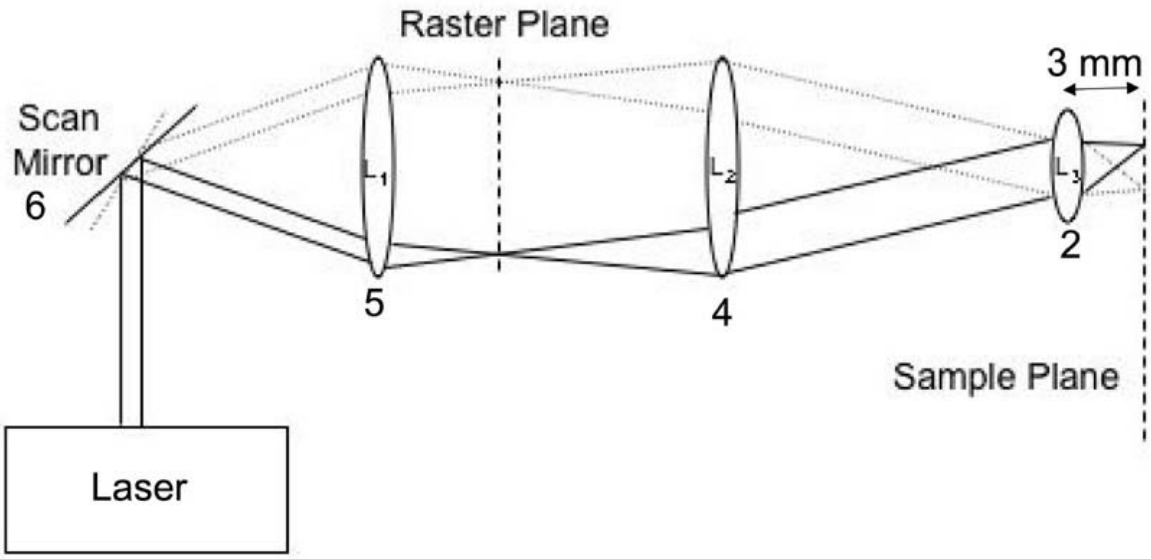

Figure 2.4 Illustration of raster scanning. Lenses L_1 and L_2 form a raster scanning pair. Varying the angle of the scan mirror varies the angle of incidence of the collimated beam on the objective lens (L_3) and scans the lateral focal position in the sample. The objective lens has a 4 mm focal length and a working distance of 3 mm, which means the principal plane (shown as the lens position in the figure) is 1 mm inset from the front glass surface in the objective lens.

There is a linear relationship (Equation 3.4) between the angle of incidence of the collimated beam on the objective lens and lateral displacement of the focus within the sample. While Figure 2.4 shows only a one-dimensional scan for simplicity, the microscope uses an orthogonal pair of mirrors (6, Nutfield Technologies RS15) to scan in two dimensions. The microscope acquires 25,000 samples per second. The 512-pixel square image acquisition takes about ten seconds.

Photons that reflect or fluoresce from the sample and escape within the cone of collection for the objective lens are collected, get de-scanned by the galvanometric mirrors (6) and back-propagate through the optical system until they are steered by the filters (8 and 14) toward the appropriate lens/pinhole assembly consisting of a lens that focuses the beam through a pinhole. Photons penetrating the pinhole are collected by a 600-μm fiber which is much larger than the 50-μm pinhole and less than 1 mm behind it, and delivered to a photomultiplier tube (PMT). Since the returning light is de-scanned, only the central 7.5 mm of the focusing lenses (10, 15 and 18) is used. Since the focal lengths of these lenses are (15 cm, 25 cm, and 25 cm) respectively, then the numerical apertures of focus are (0.033, 0.020 and 0.020) respectively which is smaller then the numerical aperture of the collection fiber (NA = 0.15), and consequently all the light is collected by the fiber.

2.B.3 Magnification

The condition of "confocally matched gating" is typically achieved by choosing a pinhole size that accepts eighty percent of the light reflecting off a mirror in the focal plane. This is achieved by setting the pinhole radius R_{ph} to be equal to the product of the magnification of the system and the lateral resolution element $\Delta x = c\lambda/NA$ where λ is the wavelength, NA is the numerical aperture of the objective lens and c is 0.61 for incoherent light, 0.82 for uniform coherent light and 0.46 for a laser beam with Gaussian radial profile. The lateral resolution element is chosen to capture eighty percent of the power in the focused spot. A point source of light such as a laser is focused through an objective lens as a truncated Gaussian. The beam has been expanded to overfill the objective lens aperture in the shoulder plane of the objective (P_2, Figure 2.2) the resulting pattern in the focal plane is approximated by the Airy function [27]:

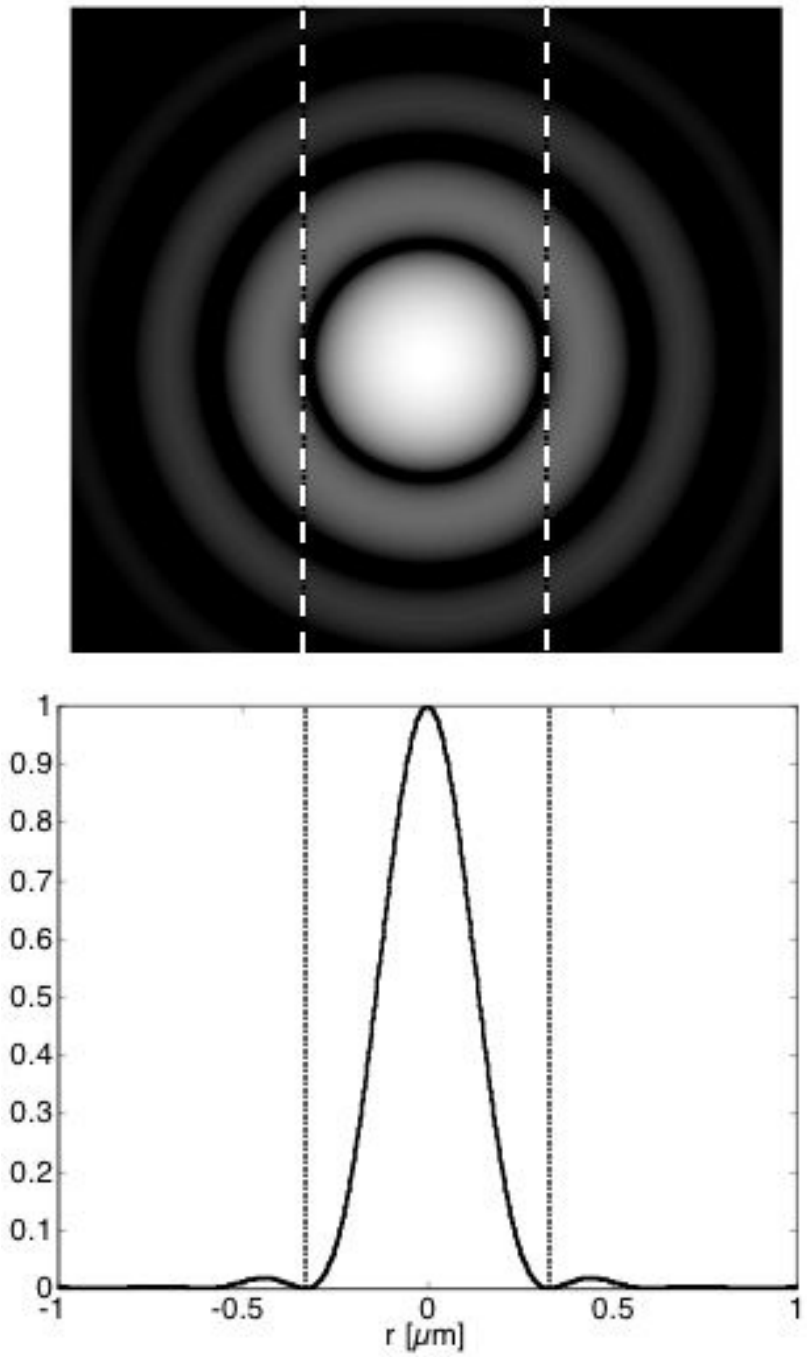

Figure 2.5 The Airy Function. The picture shows the spatial profile of a focused laser beam at the plane of focus. Of prime interest is the central disc because it contains the majority of the optical power. The diameter of the disc is given by $D_3 = 0.92\lambda/NA$ where λ is the vacuum wavelength of light and NA is the numerical aperture of the lens used to focus the beam.

Confocal microscopy gets the prefix “con” because it creates a **con**jugate plane to the **focal** plane within the sample in the pinhole plane. Relay lenses are used whose focal length determine the magnification of the system.

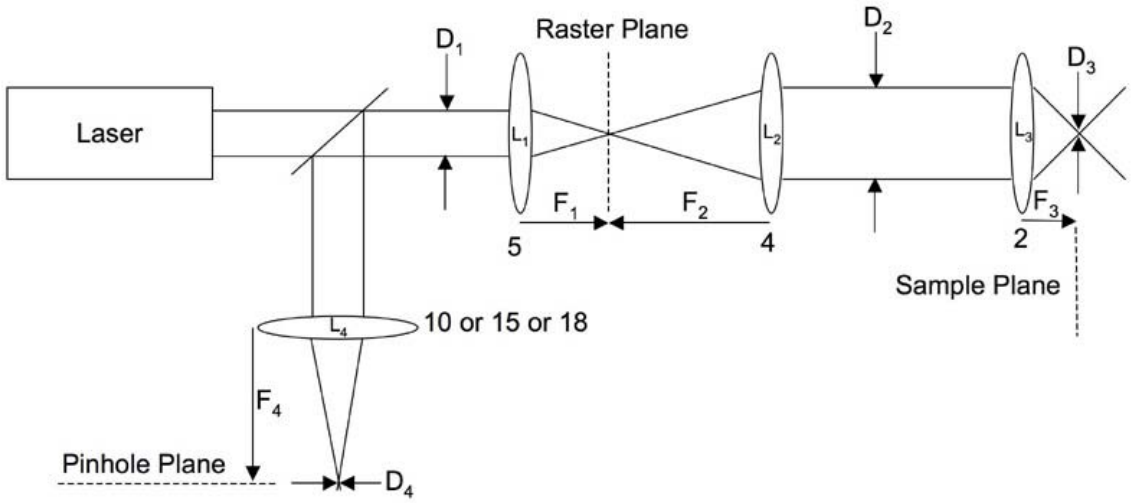

Figure 2.6 An illustration of the magnification in a confocal microscope. D_1 and D_2 are the $1/e^2$ beam diameters emanating from the laser/beam-expander combination and entering the objective lens respectively. D_3 and D_4 are the Airy disc diameters in the sample focal plane and the conjugate pinhole plane respectively.

If there were a mirror in the sample plane, the Airy pattern would reflect and back-propagate to the pinhole plane. The central disc in the pinhole plane would have a diameter determined by the magnification of the system, which is a function of the focal lengths of the lenses used (Equation 2.1). Lenses L_1 and L_2 were chosen to expand the beam to overfill the objective lens (L_3). The beam was expanded until the $1/e^2$ diameter is equal in size to the back aperture of the objective lens. In this system the beam is expanded before the raster scanning lenses so little beam expansion is required. Therefore, the raster scanning lenses were chosen to have approximately equal focal lengths and the magnification is small ($D_2/D_1 = 1.17$). L_4 is chosen for a specific system magnification such that D_4 is equal to the diameter of a particular pinhole to be used. A

confocally matched pinhole gate was achieved. The relationships between the $1/e^2$ laser beam diameters (D_1 and D_2) and Airy discs (D_3 and D_4) in Figure 2.6, which specify the magnification as a function of the focal lengths of the lenses used, are given:

$$D_2 = (F_2/F_1)D_1$$
$$D_3 = 0.92\lambda/NA$$
$$D_4 = (F_2/F_1)(F_4/F_3)D_3 \qquad (2.1)$$

Table 2.1 Optical magnification specifications for experimental device. The system optical magnification M is the ratio of the focal lengths of the lenses used $(F_2/F_1)(F_4/F_3)$.

	Reflectance 488nm	Reflectance 633nm	Fluorescence 510nm
F_1	150 mm	150 mm	150 mm
F_2	175 mm	175 mm	175 mm
F_3	4 mm	4 mm	4 mm
F_4	250 mm	250 mm	150 mm
$M=(F_2/F_1)(F_4/F_3)$	73	73	43
D_3	500 nm	647 nm	
D_4	36 μm	47 μm	

Table 2.1 shows the magnification specifications and the result of Equation 2.1 for the experimental apparatus. A 50 μm pinhole was used which was slightly larger the diameter of the focal spot (D_4) in the sample focal plane. The configuration was slightly less than confocally matched but chosen to accept more light with the dilated confocal pinhole.

2.B.4 Pinhole/Ring Detector

In the fluorescence channel, the tip of a bifurcated fiber bundle was used as the confocal detector. On the collection end of the fiber bundle that replaced the pinhole, a ring of fibers surrounded a central fiber. The fiber bundle face was placed in the pinhole plane of the fluorescence channel on the microscope. Figure 2.7 depicts the fiber bundle face.

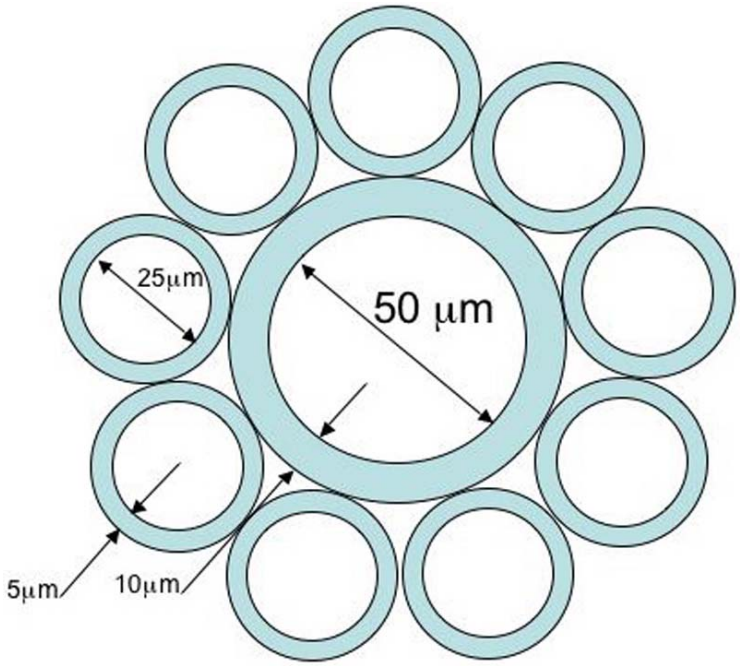

Figure 2.7 The face of a 9-around-one fiber probe (FSI Fiberoptic Systems, 50-2223). This bifurcated fiber bundle terminated with the large central fiber to one SMA connector and the nine smaller surrounding fibers to another. Dark regions represent jacket and cladding material. The probe was glued together with epoxy. The numerical aperture is 0.55.

On the detector side of the bundle, the bundle bifurcated into two terminations, one for the central fiber and a second for the sum of the 9 surrounding fibers. These two terminations were each coupled into an SMA connector for connection to the PMT.

The fiber bundle face was aligned in the conjugate pinhole plane so that the central 50 μm-core-diameter fiber directly replaced the 50 μm-pinhole. Neglecting the ring fibers, the pinhole fiber formed a confocal aperture comparable to a conventional metal pinhole in the fluorescence probe arm. A total of 4 fiber probes could be swapped into the two PMTs: 488 nm reflectance, 633 nm reflectance, 510 nm fluorescence from the central fiber and 510 nm fluorescence from the sum of the ring fibers.

2.C Electronics

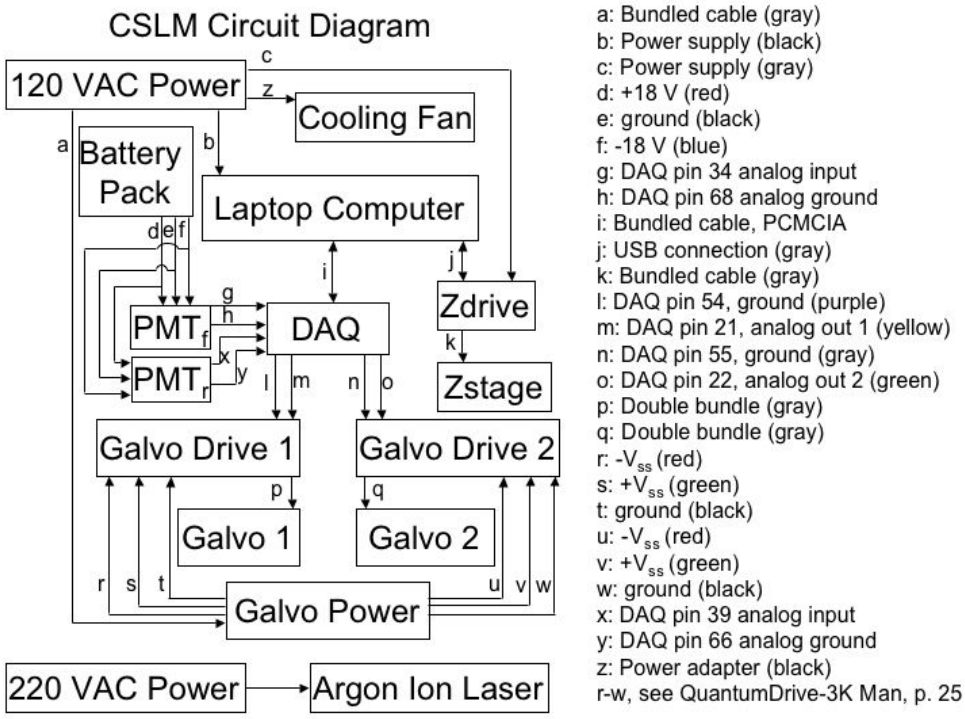

Figure 2.8 The circuit diagram for the confocal microscope.

Figure 2.8 shows the top level circuit diagram for the confocal microscope with wiring connections. The battery pack and PMT sub-circuit is shown in Figure 2.9. The Sub-circuit labeled DAQ is composed of a PCMCIA type card (National Instruments 6062E), which connects the signal I/O box (National Instruments SCB-68) to the laptop computer.

2.C.1 Scanning

The electro-mechanical components of the system included a motorized axial translation stage to scan in the z direction (Applied Scientific LS-50A, MFC-2000), which had a resolution of 200 nm and a repeatability of 1 μm and galvanometric scan mirrors to implement the x-y raster scanning (Nutfield Technologies). The fast scan axis (x) mirror was driven at 195 Hz, well within specification limits. Differential voltage outputs from the data acquisition card (DAQ) (model 6062E, SCB 68, National Instruments) controlled the x-y scanner and the z-axis translation stage. Two input channels of the DAQ measured the voltage output from the photomultiplier gain circuits with twelve bit A/D conversion.

2.C.2 Detection

Detection of light penetrating the confocal apertures was achieved with photomultiplier tubes from Hamamatsu Corporation (H5773-01). The PMT produced minute currents from detected light, which drove a current-to-voltage operational gain amplifier. The PMT output voltage V_{out} was measured using an analog input channel of the data acquisition card.

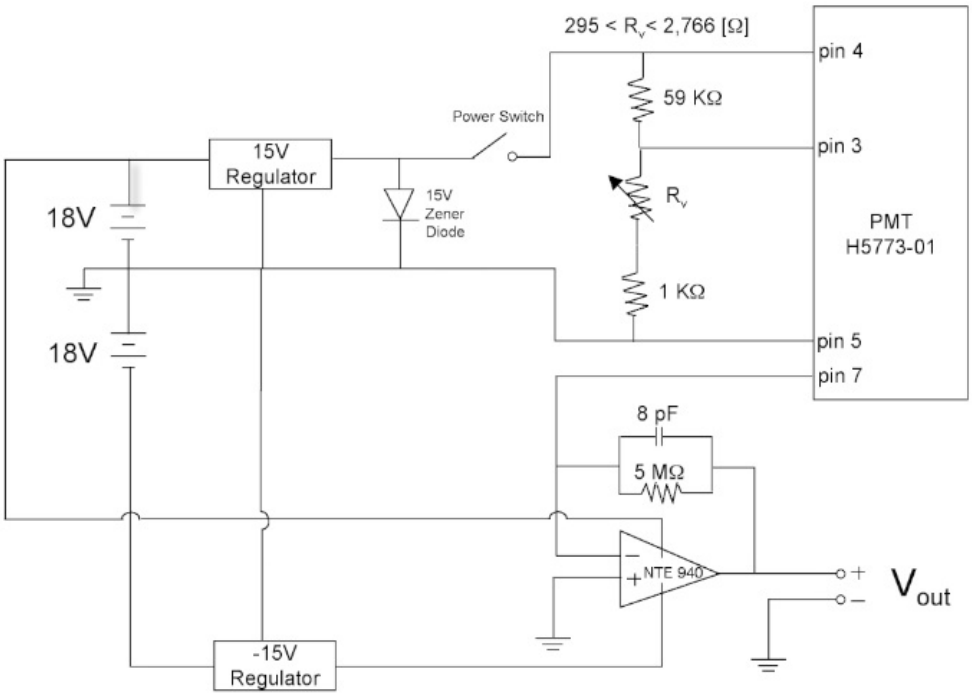

Figure 2.9 Circuit diagram for the photomultiplier tube. Four 9-Volt batteries were used as an isolated low noise power source for the PMT (Hamamatsu, 5773-01) and the FET type input operational amplifier (NTE, 940).

Figure 2.9 shows the circuit designed for light detection in the confocal microscope. The variable resistor R_v served as the gain control for the PMT. The value of resistance (ten equally spaced resistances from 295 to 2,766 Ω) determined the voltage divider that sets the gain voltage input at pin 3 on the PMT (ten equally spaced voltages from 0.250 to 0.900 Volts). Pin 7 of the PMT injects current to the gain amplifier. The total gain of the entire PMT circuit is determined by the resistance values of R_v and the load resistor on the current-to-voltage amplifier. The 5-MΩ value was chosen for the load resistor such that the total gain dynamic range (including R_v) suits both reflectance imaging (gain settings 1-3) and fluorescence imaging (gain settings 8-10) which yields a light signal four to five orders of magnitude weaker than the reflectance signal.

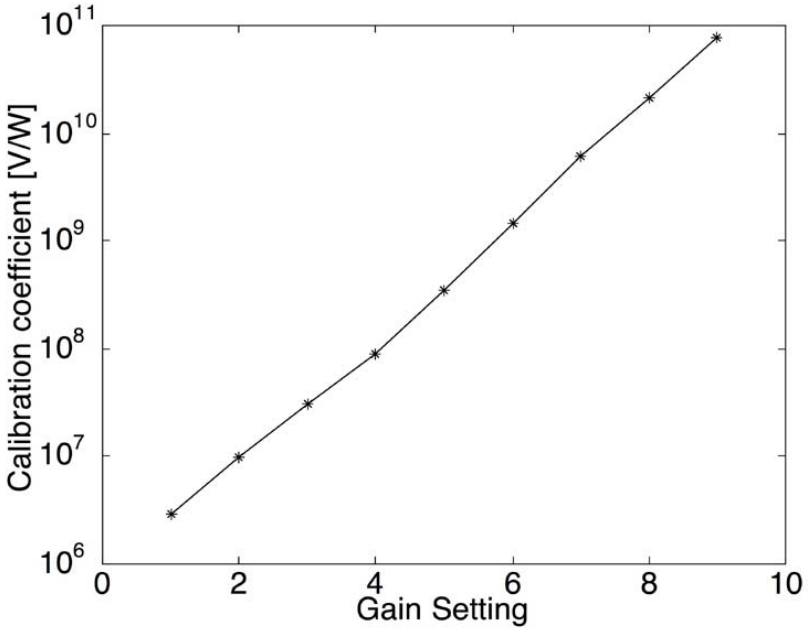

Figure 2.10 The PMT gain setting calibration coefficients.

A total of 4 PMT's were used over the course of the 5 years of work represented by this thesis. Although the final PMT left on the system was left un-calibrated in terms of volts output to Watts input and instead a calibration measurement was developed (see Equation 3.3), a calibration of the initial PMT circuit showed the relative sensitivity of the gain settings. Figure 2.10 shows the calibration coefficients of the various gain settings for the initial PMT in the microscope. Subsequent PMTs, which were also controlled with 9 linearly increasing gain-setting voltages, were calibrated in volts per unit reflectance of the sample (see Chapter 6).

2.C.3 Data Acquisition and Processing

The PMT circuit output voltage (V_{out} in Figure 2.9) was connected to a DAQ card (National Instruments 6062E, SCB 68), which digitized the signal for input to a laptop computer (Gateway Computer, Microsoft Windows XP operating system). A virtual environment (VI) written in Labview Software serves as a graphic user interface for the confocal microscope and acquires stacks of images as well as simply scanning repeatedly

at the same z position for sample orientation. The first VI developed, Scan.vi implemented a repeating raster scan and displayed the image.

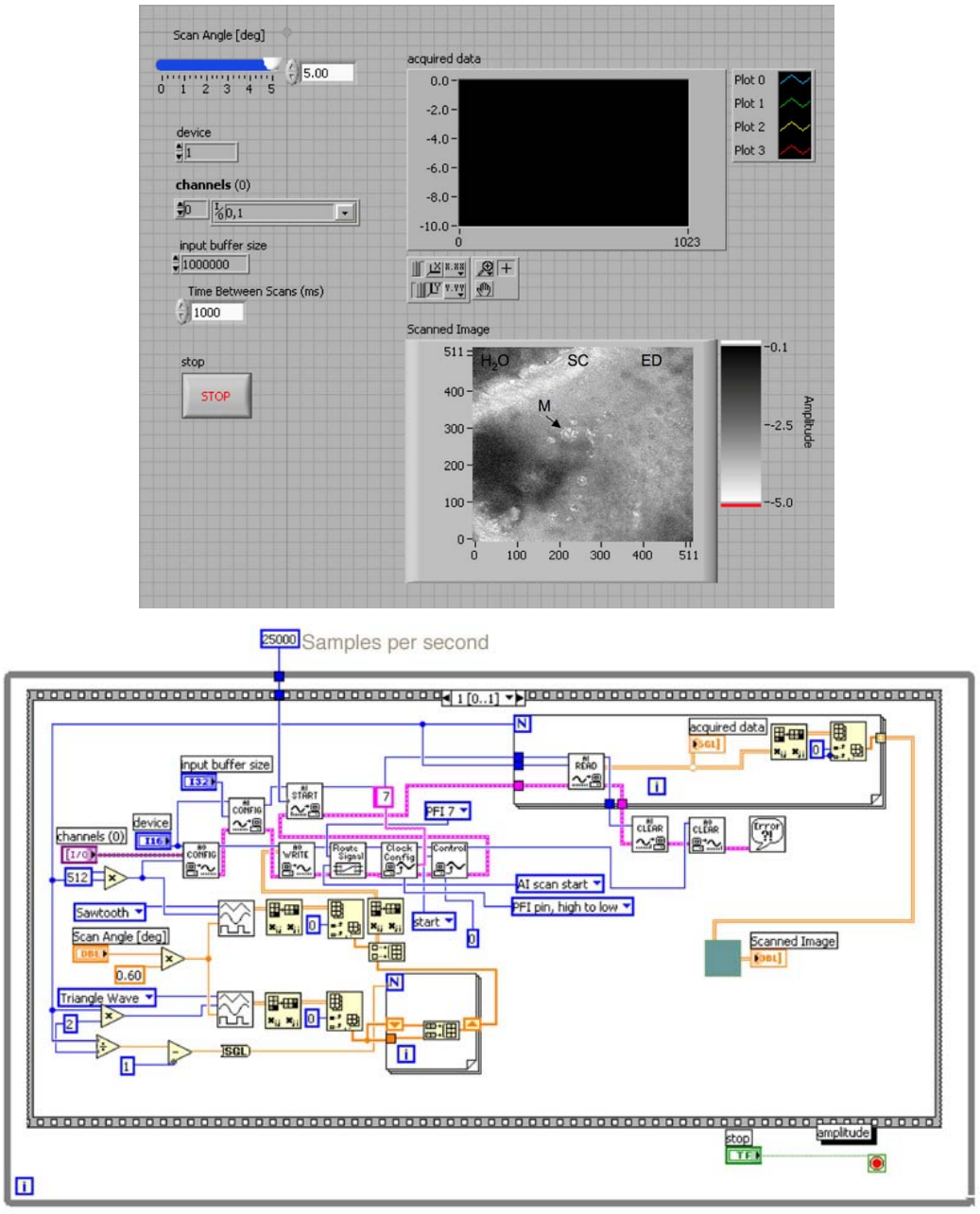

Figure 2.11 Scan.vi acquires the raw data during imaging scanning. The scanned image, (pasted in for illustration), shows a typical view of melanoma in mouse skin with the melanoma (M), stratum corneum (SC) and epidermis measured as well as the immersion medium (H2O).

Figure 2.11 shows the program Scan.vi that drives the scanning and displays the scanned image. The top image shows the user interface panel. The user input “Scan Angle” is the functional zoom and specifies the field of view (see Figure 3.9). The bottom image illustrates the block diagram logic of the program. The top box labeled “Scan Rate” is used to control the acquisition speed: the input (25000) specifies the scan rate in samples per second.

The blue-green box labeled “Flipper” is a sub-program Flipper.vi. Flipper was executed after an image was acquired and before it was displayed and implemented data preprocessing which was necessary for the following reason. The x-scan mirror was driven with a triangle waveform and data was constantly acquired at a rate of 25,000 per second as the y-scan mirror was driven with a staircase waveform, which ramped from the bottom to the top of the image.

The data collection in Scan.vi was sequential with a reset of x-position for each step in the y-scan staircase waveform, so images were produced with every other sequentially sampled constant y line inverted about the mean x value, essentially registered backwards. At the maximum excursion of the x scan mirror, the software recorded the beginning of the next line before the mirror had time to overcome it’s inertia so each other line was not only recorded backwards but offset as well. The sub-program flipper corrected both the backwards registration and shifting due to inertial mirror recovery in a data-preprocessing step each time a 2-dimensional image was recorded.

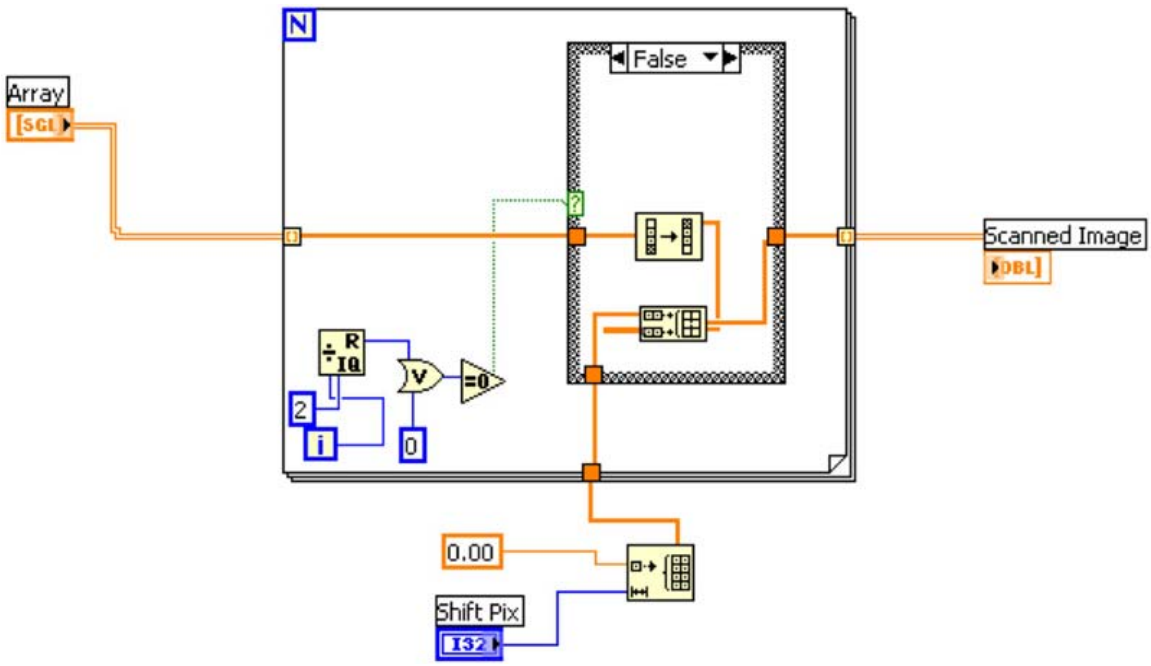

Figure 2.12 Flipper.vi implements data preprocessing. Each image was broken up into data arrays consisting of a horizontal line of pixels (constant y-position). Every other line array was flipped and shifted 14 pixels for correct registration with the image.

Scan.vi was used in combination with the manual control of the z-stage to locate the sample surface. After the surface was located and the sample was backed off a few microns such that there was an initial picture of darkness, the sample was imaged in 3 dimensions by another program called Stack.vi. The conventional x-y-z sample coordinate system throughout this thesis will have an origin on the tissue surface, and a positive z-axis pointing into the tissue, just as the data is acquired.

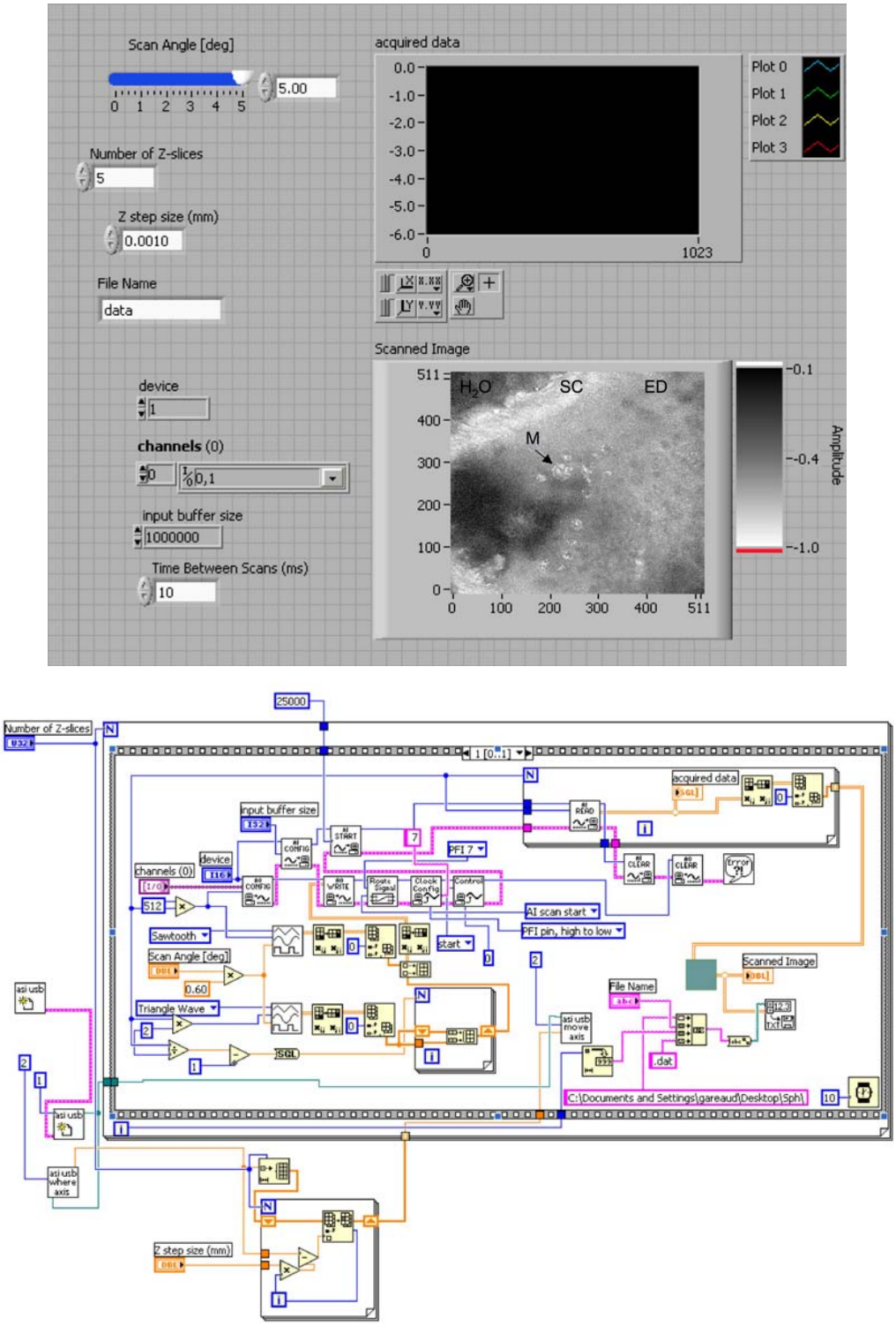

Figure 2.13 Stack.vi collects 3-dimensional images. The user input "Number of Z-slices" specified the number of sequentially acquired optical sections. The user input "Z step size (mm)" specified the step size for sequential sections.

After each complete two-dimensional X-Y scan was accomplished with the scan mirrors (512 x 512 pixels in about ten seconds), the z-stage stepped the sample along the optical axis, and a stack of images is acquired in this manner. For tissue imaging, step sizes of one to five μm were typically used. The program saved the output files to Stack.vi's parent folder with the name input to the field "File Name" of the graphic user interface to be "data." A set of sequential optical sections would be called [data1.dat data2.dat data3.dat …..].

The assumption that the focal plane is fixed in space with respect to the objective lens was checked when the focal plane is scanned into a medium whose bulk refractive index *n1* differs from that of the immersion medium *n2*. Refraction elongates the focus beneath the sample surface. Figure 2.14 illustrates a simple model of focusing into a semi-infinite sample.

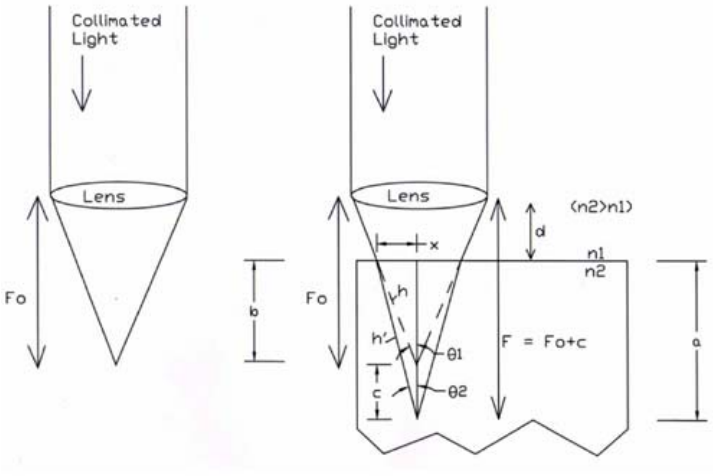

$$x = b\tan(\Theta_1) = a\tan(\Theta_2)$$

$$c = a - b$$

$$c = \frac{x}{\tan(\Theta_2)} - (F_0 - d)$$

$$c = \frac{b\tan(\Theta_1)}{\tan(\Theta_2)} - (F_0 - d)$$

$$c = (F_0 - d)\left[\frac{\tan(\Theta_1)}{\tan(\Theta_2)} - 1\right]$$

$$c = (F_0 - d)\left[\frac{\tan(\sin^{-1}(na))}{\tan(\sin^{-1}\left(\frac{n_1}{n_2}na\right))} - 1\right]$$

Figure 2.14 A calculation of focal elongation due to a high refractive index sample. Collimated light is focused in uniform refractive index *n1* (left) and in the presence of a semi-infinite sample of refractive index *n2*. The working distance of *Fo* increases to *F = Fo + c* as the cone of focus elongates within the sample.

Figure 2.14 illustrates a simple model of a biological specimen that has a higher refractive index than the immersion medium. The bulk refractive indices of epidermis and dermis are 1.39[46] and 1.34[9] respectively were close to that of the immersion medium (water or saline *n1* = 1.33) so the correction factor c was small for acquiring data within the epidermis and moderate in the dermis. A sample calculation of the correction factor for focusing through b = 100 μm dermis yielded a c = 22 μm such that the true focal depth in the sample was a = 122 μm.

Post processing of data acquired in a series of optical slices, saved to .dat files was implemented to generate a 3D data cube saved as a .mat file and then load it to create movies using MATLAB™ Software. Movies were produced of a plane, which moves through the image both axially (top view) and laterally (side view). The Matlab image processing code can be found in the Appendix.

The preliminary version of a data acquisition code that simultaneously acquired multiple signals was created but never completed. The dedication of a photomultiplier tube to each of the pinhole/fiber collection assemblies and adaptation of the Labview™ software to allow parallel acquisition of the three separate channels could allow the three images to be acquired simultaneously during a single scan. This parallel operation was not implemented in this dissertation, but the system was designed to allow this next step of improved performance.

2.C.4 Operating Instructions

Connections: the DAQ PCMCIA card must be plugged into the computer. The Z drive must be connected to the laptop via the USB connection.

1) Turn on laser, power supply, Z drive.
2) Create new folder with software inside
3) Change path for saving files in “stack.vi” to folder name
4) Open and run ‘scan.vi” and turn on PMT

5) Bring sample into focus and locate surface using “scan.vi”
6) Close “scan.vi” and open “stack.vi”
7) Choose Z step size, angle and number of slices to acquire
8) Run “stack.vi”
9) Put acquired files into a subfolder
10) Put “code.m” into subfolder, choose appropriate n, angle and dz
11) Run “master.m” with the appropriate subfolder name
12) Open “top.avi” or “side.avi” in the subfolder and view your data

* Note: the fluorescent PMT has noise until you zero it as follows. Leave the PMT on for 1 minute. Disconnect the ground wire from the optical table and re-connect. This will zero out the noise, watch this happen on “scan.vi.”

** The National Instruments software allows trouble shooting and enables one to set the positions of the scan mirrors and monitor the PMT output. To open this software, double click “Measurement & Automation” on the desktop. Click the “+” symbol to the left of “Devices and Interfaces.” Right click the DAQ card. Choose “open test panel.” The output window lets you update the voltage output to the mirrors, set both channels (0 and 1) to zero to align the beam up the middle of the objective lens. NEVER UPDATE THE MIRROR VOLTAGE TO MORE THAN THREE VOLTS (or less than -3V)!!!!!! The input window lets you monitor the PMT output voltage. This can be useful for finding the surface of the sample.

Chapter 3: Imaging in Non-Scattering Media

The confocal microscope described in chapter two was tested in reflectance mode (λ = 488 nm) by imaging a water/glass interface. The test aimed to verify that the microscope yielded resolution near the diffraction limit by measuring the axial PSF. A second goal was to characterize the microscope's response from standard targets such as a planar boundary of known refractive index mismatch. This result is useful, in reflectance mode, to calibrate the images of tissue relative to the reflectance of a standard water/glass interface of reflectivity R = 0.0044 [unitless] (see equation 3.1), where R = 1 would be a perfect mirror.

In fluorescence mode, standard fluorescent polystyrene microspheres (Molecular Probes , λ_{ex} = 488 nm, $\lambda_{em} \approx$ 515 nm) were imaged in non-scattering gel. The images showed the response from the pinhole and the ring detectors (Chapter 2.B.4), which will be used in Chapter 4 for scattering media.

3.A Reflectance-Mode Calibration

Calibration in reflectance mode is conveniently monochromatic, both incident light and reflected light share the argon laser wavelength (λ = 488 nm). Various calibrations were performed to characterize the microscope's response. Section 3.A.1 demonstrates resolution near the diffraction limit. In section 3.A.2, the reflectance off a standard water/glass interface of differential refractive index is measured and used to

normalize tissue measurements. The field of view is determined from images of a reticule standard in section 3.A.3. This section presents results and analysis of standard reflective targets, which were used to characterize the performance of the rCSLM.

3.A.1 Axial Point-Spread Function for rCSLM

A glass cover slip was placed on the microscope stage so that a three dimensional image of the interface of refractive index mismatch could be acquired and analyzed. Acquisition of 28 optical sections took about 5 minutes. At the water/glass interface, the reflectance is a function of the refractive index of the immersion medium (n_1) and the refractive index of glass ($n_2 = 1.52$). In this work n_1 was either that of a sucrose gel ($1.34 < n_2 < 1.43$, Figure 3.4) or water ($n_2 = 1.33$).

$$R = ((n_1 - n_2)/(n_1 + n_2))^2 = 0.0044 \text{ [unitless]} \quad (3.1)$$

In Equation 3.1, the reflectance of the water/glass interface was calculated. This value was be assigned to the experimental image intensity (V_{out}, Figure 2.9) when the rCSLM focused on the interface. The image was sampled by choosing random x-y positions, which selected a depth profile (vary z) indicative of the axial point spread function of the confocal microscope in reflectance mode. The reflectance profile is shown in Figure 3.1.

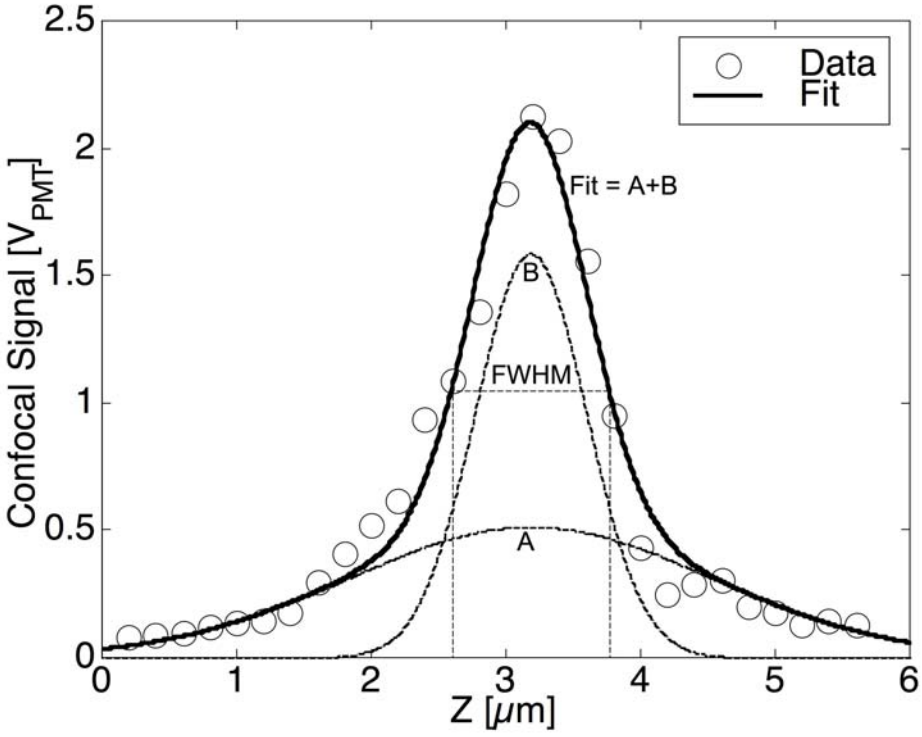

Figure 3.1 The axial profile of a water/glass interface. Experimental data are black circles. The 2-Gaussian fit (solid line) was used to designate the full width half maximum (FWHM = 1.17 μm). The fitting curves A and B are Gaussian g = C*exp(-(z/(2w)).^2) where C and w are 1.6 V and 0.3 μm respectively for curve A and 0.5 V and 1.0 μm respectively for curve B.

Figure 3.1 shows the axial point spread function of the reflectance mode confocal microscope. The raw data (black circles) is fit by the black line, which is the sum of two Gaussian curves. The full width at half maximum (FWHM) of the point-spread function is 1.17 μm. The 1.17-micron FWHM measured in reflectance mode by the confocal microscope is slightly larger than that predicted by theory in the diffraction limited case for a plane source which is given by:

$$FWHM = 0.95\lambda n/NA^2 = 0.76\ \mu m \qquad (3.2)$$

Another interpretation of the PSF is the implied Rayleigh resolution limit of the system, which is the minimum separation distance between resolvable points. The fit curve (solid line in Figure 3.1) was processed by the program GetResol.m (see Appendix) to yield the axial resolution limit of the system, which was 1.25 μm. This technique is further addressed in Chapter 4.C for fluorescence.

3.A.2 Reflectance Normalization

For calibration in reflectance mode such that the results can be expressed in units of reflectance, images must be normalized by what would be expected from a mirror in the focal plane. The normalization assumed the mirror to have a reflectivity of R = 1, and calculated the tissue reflectance by comparing the PMT voltage signal produced by the tissue to the signal produced at the water/glass interface where R = 0.0044. The signal levels from cells and tissue were two to three orders of magnitude smaller than the signal level at the water/glass interface.

B-16 melanoma cells were cultured on glass cover slips in high-calcium nutrient media to use as test targets for imaging. The following protocol (adapted from [47]) was used.

Cell Culture Protocol

1) In a sterile hood, culture medium was siphoned and discarded.
2) The cell layer was rinsed with Dulbecco's phosphate buffered saline solution to remove all traces of serum that contains trypsin inhibitor.
3) 3.0 ml of 0.25% (w/v) Trypsin- 0.53 mM EDTA solution was added to flask and cells were observed under an inverted microscope until cell layer was dispersed (usually within 5 to 15 minutes). Note: In some cases, the Trypsin failed to detach many of the cells and gentle scraping with a plastic edge was necessary.
4) 6.0 to 8.0 ml of complete growth medium was added as a Trypsinizing inhibitor and cells were aspirated by gentle pipetting.

5) The cell suspension was centrifuged at 1000 revolutions per minute for five minutes.
6) The growth medium and Trypsin were siphoned off the cell pellet and the cells were immersed in fresh growth medium and suspended by gentle pipette aspitation.
7) Appropriate aliquots of the cell suspension were added to new culture vessels. a subcultivation ratio of approximately 1:10 was used to seed cells appropriately to achieve a confluent monolayer at the 2 to 3 day incubation period.
8) Cultures were incubated at 37°C for 2 to 3 days

By placing sterile microscope cover slips in the new culture vessels before the aliquots of cell suspensions were added, cells were seeded to grow on the cover slips. The cover slips were then placed on the microscope for imaging. By adjusting the sample's z-position such that the focal plane was just above the water/glass interface in the cells attached to the glass, an image was acquired which shows the cellular detail such as the pleomorphic nuclei of these cancer cells.

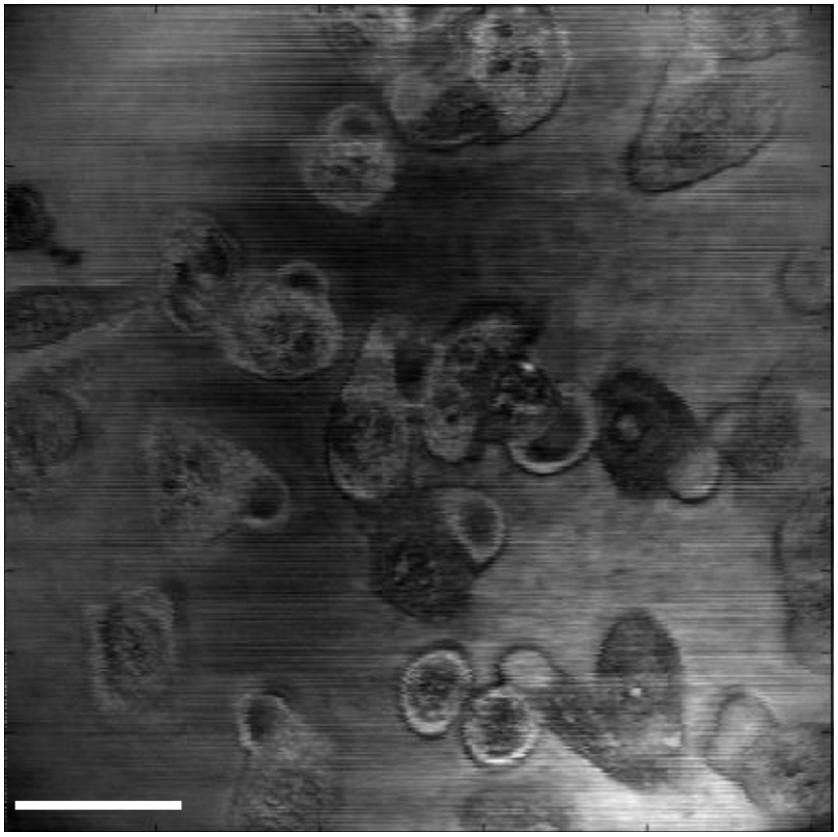

Figure 3.2 Melanoma cells on a glass cover slip. Scale bar = 50 μm.

The melanoma cells shown in Figure 3.2 of diameter 20 to 30 μm are larger than healthy keratinocytes (diameter = 5 to 10 μm, also imaged but not shown) and have distinct reflective properties because they contain melanin which is highly scattering and absorbing. The size and reflectivity of malignant cells in living animals characterize tumor tissue (see Chapter 7), but in these cell culture experiments, cultured melanoma cells provided tissue reflectance in close proximity to a standard reflective glass interface such that a comparison could be made.

The optical section shown in Figure 3.2 is a slice from an image cube. To compare the level of reflectance of the cells to the glass interface, an x-y position at the center of a cell was chosen and the z profile (perpendicular to the image shown in Figure 3.2) was isolated from the image cube. At each depth z, the mean value of a 7 by 7 pixel [3.6 by 3.6 μm] x-y window was calculated for display in Fig. 3.3 as a function of depth.

The 7 by 7 window size was chosen as the smallest window where the standard deviation across the window fell to 1/e of its value for a 3 by 3 window. In this manner, the smallest sampling window was selected while limiting pixel-to-pixel variation.

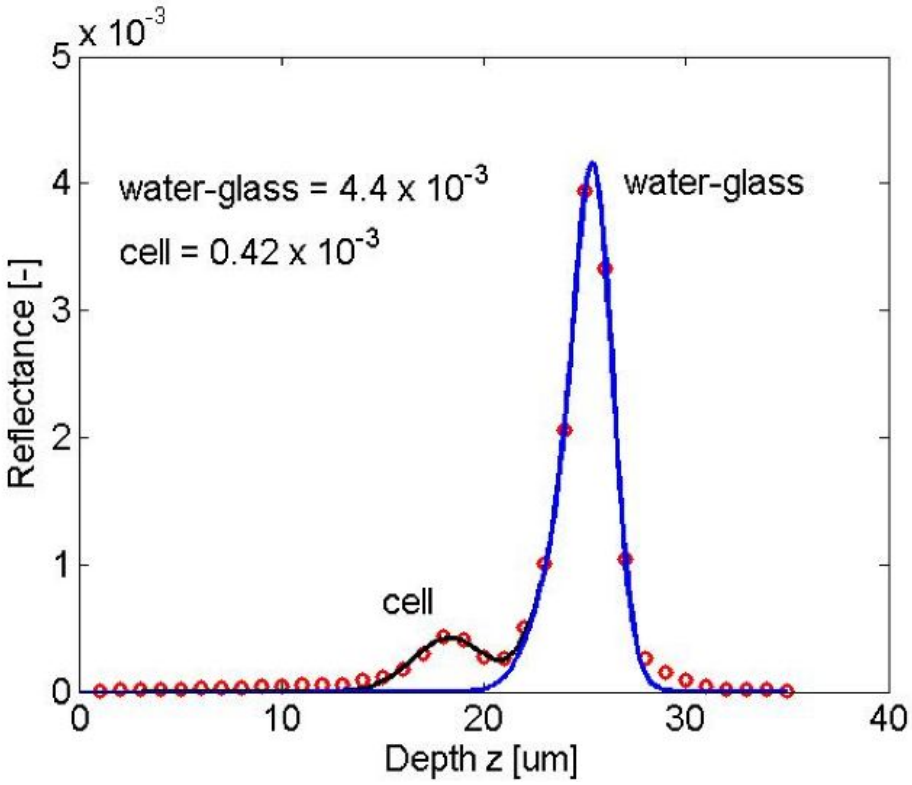

Figure 3.3 The axial profile of a melanoma cell on a glass cover slip. The scan through a cell and the underlying glass slide shown as red circles. The axial fit (black line) is the sum of a scan through water-glass slide only (blue line, fit like in Figure 3.1 from a z-profile adjacent to the cell location) and a Gaussian profile to represent the cell.

Figure 3.3 shows the axial profile of a melanoma cell on the surface of the glass interface. The glass interface at a depth of z = 25 μm yielded a PMT voltage ($V_{water\text{-}glass}$) on the photomultiplier tube within the microscope. In the normalization routine, this voltage became the signal expected by the reflectance of a water/glass interface, which is known to be 0.0044 [-] from Equation 3.1. The cell centered at a depth of z = 18 μm

yielded a voltage (V_{cell}) on the PMT which when normalized, indicates a reflectance of 0.00042 [-] which is calculated in Equation 3.3.

$$0.00042 = 0.0044\ V_{cell}/V_{water\text{-}glass} \tag{3.3}$$

The reflectance of tissue is more complex than the reflectance from the standard glass interface and is influenced by the size and shape of the scattering particles, their relative refractive index and the probe geometry. Equations 3.1 and 3.3 provide a reproducible normalization (albeit an oversimplified model) for tissue reflectance that allows characterization of tissues.

To test the normalization technique on reflective boundaries of smaller differential refractive index (closer to that in tissue), agarose gels with various sucrose concentrations were imaged. The refractive index in the gel was found to be directly proportional to sucrose concentration. After gels were set with sucrose concentrations of 5, 10, 20, 30, 50 and 80 % sucrose (weight by weight), their refractive index was measured using an Abby refractometer.

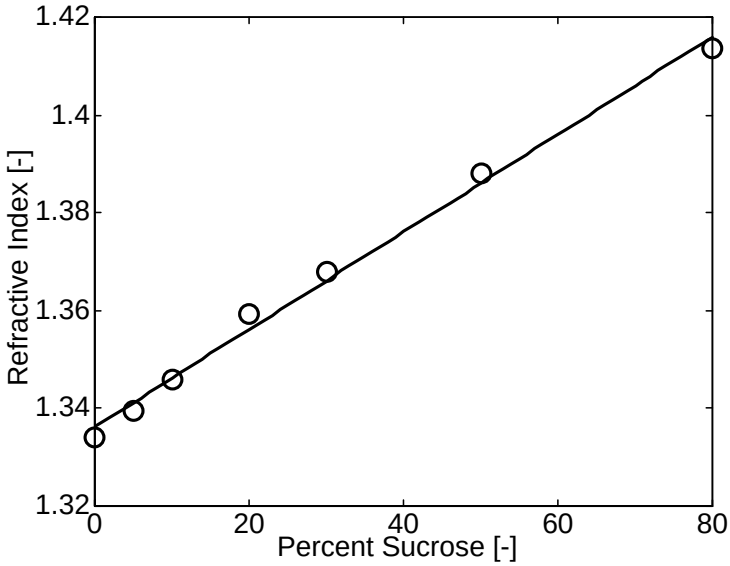

Figure 3.4 The refractive index of agarose gel as a function of sucrose concentration.

Figure 3.4 shows the linear relationship between sucrose concentration and refractive index. The linear fit to the data was given by y = mx + b where the slope m was 0.001 per percent and the intercept b is 1.336.

Gels with high sucrose concentration (c = 20, 40, 60 and 80%) were imaged in the confocal microscope. The sample was set up such that the focus was in the vicinity of the interface where the sucrose gel contacted a glass cover slip. The expected reflectance at this interface was $R = ((n_1 - n_2)/(n_1 + n_2))^2$ as in Equation 3.1 where n_1 is the refractive index of the sucrose gel and n_2 is the refractive index of glass ($n_2 = 1.52$).

The samples were imaged in three dimensions to yield an image cube of the refractive index mismatch of the gel/glass interface, then sampled at a constant x-y position 49 times to show the axial confocal response just like for the water/glass interface shown in Figure 3.1. The axial profiles were fit with Gaussian curves for three fitting parameters: center position, peak magnitude and width. The peak magnitude was taken as the reflectance signal for the sample and converted into true reflectance units by using the calibration technique in Equation 3.3.

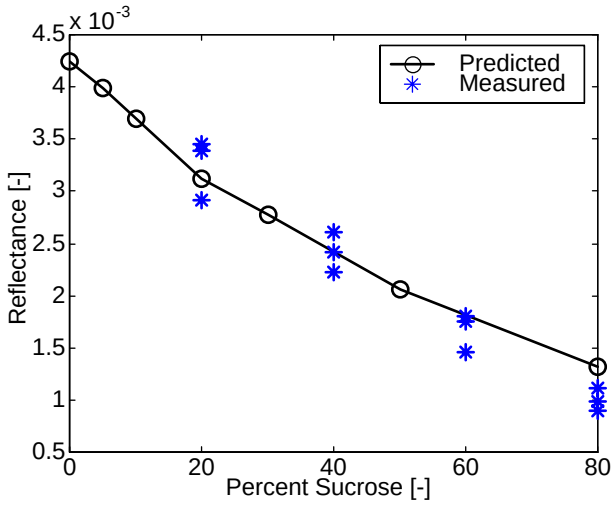

Figure 3.5 Reflectance of sucrose gel/glass interface as a function of concentration. Each measurement asterisk represents the mean of N = 49 measurements

Figure 3.5 shows the results of an imaging experiment on sucrose gels. Three different gel samples were constructed for each of the chosen four sucrose concentrations (c = 20, 40, 60 and 80%). Each measurement represents the mean of 49 measurements on each sample. The standard intra-sample variation for the 49 measurements was always less than three percent. The black circles represent the expected reflectance according to Equation 3.1. The blue asterisks represent the experimental data expressed in units of reflectance where a glass interface measurement was used for normalization as in Equation 3.3.

In chapter 6, both the surface reflectance and depth attenuation of the rCSLM signal in mouse tissue will be discussed. Early results shown here from imaging different porcine tissue types show the range of reflectance of biological tissue. In these experiments, 3-dimensional samples were imaged. The reported value of reflectance was taken from measurements within 10 microns of the surface of the sample, and not on the actual surface. Depending on the tissue type and the cut of the tissue, surface reflectance was highly variable. This technique is refined in Chapter 6. Means and standard deviations are expressed for ten measurements at different x-y positions on each sample. Fairly homogenous tissues such as brain and liver were randomly sampled for the x-y positions while tissues like muscle where sampled in chosen locations where the axial decay was well behaved since strands protruding from the surface and holes within the sample yielded non-convergent fits in other locations.

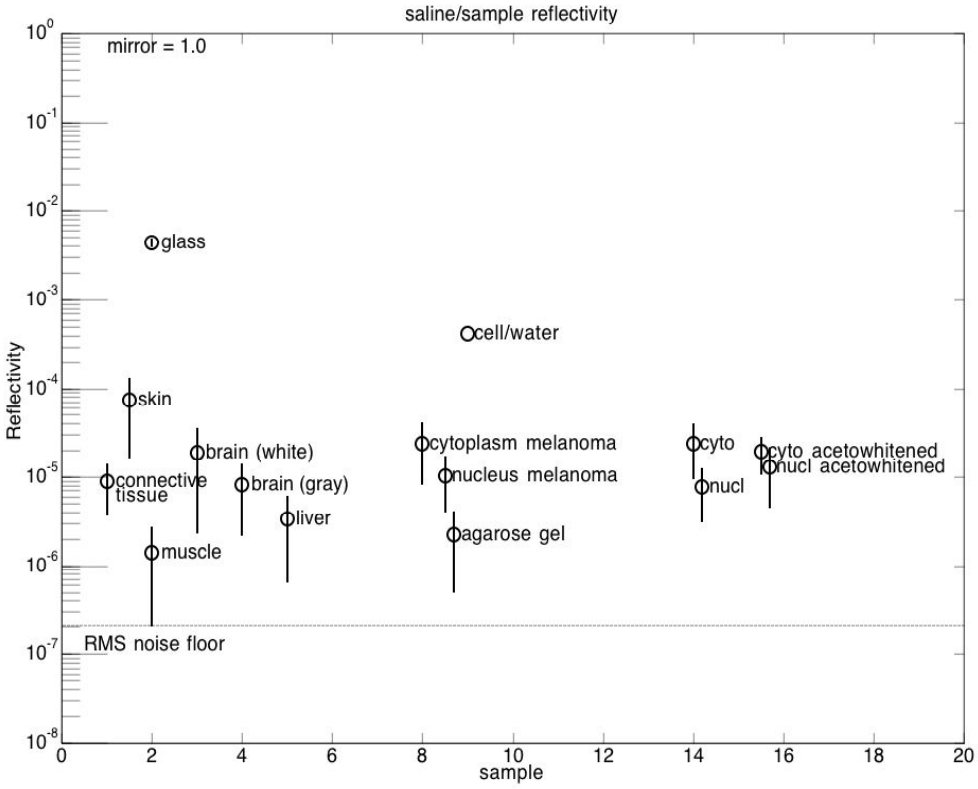

Figure 3.6 Reflectivity values for porcine tissue samples, melanoma cells in vivo in murine skin, cells embedded in agarose gel ± acetic acid to achieve aceto-whitening, cell on glass exposed to water, glass slide, all relative to the expected reflectance from a mirror.

Figure 3.6 shows that the reflectance of tissue ranges from 10^{-4} to 10^{-6} in units of absolute reflectance, which are dimensionless and represent the fractional incident power which is reflected and confocally detected.

In tissue, the angular dependence of scattered light is a function of the irregular shape, size and refractive index of the scattering particle. The method of comparing tissue reflectance to that of a mirror is oversimplified because collimated laser light reflects off a planar interface at only one angle where scattered light is multidirectional. A model is developed in Chapter 6 to integrate the angular scattered light intensity over

the solid angle of collection for the objective lens being used. Propagation through the confocal pinhole is yet another gate that decreases the detected reflectance.

A simple model of a keratin-epidermis planar boundary (developed in Chapter 7) predicts a reflectance 30-fold higher than the reflectance of skin in Figure 3.6, underscoring the failure of the simple planar model to accurately characterize microscopic reflectance from tissue. Nonetheless, comparing tissue reflectance to a reflectance provides is a useful standardization for experimental data.

3.A.3 Field of View Calibration

A reticule (Bausch & Lomb) consisting of a front surface mirror with etched lines of 10-μm spacing was imaged at different galvo-mirror scan angles. The scan angle is the total angular variation of the incident beam on the objective (see Chapter 2.B.2). Observing the standard grating in sample space determined the field of view of the microscope (via Equation 3.4), which is assigned to the image in the display software.

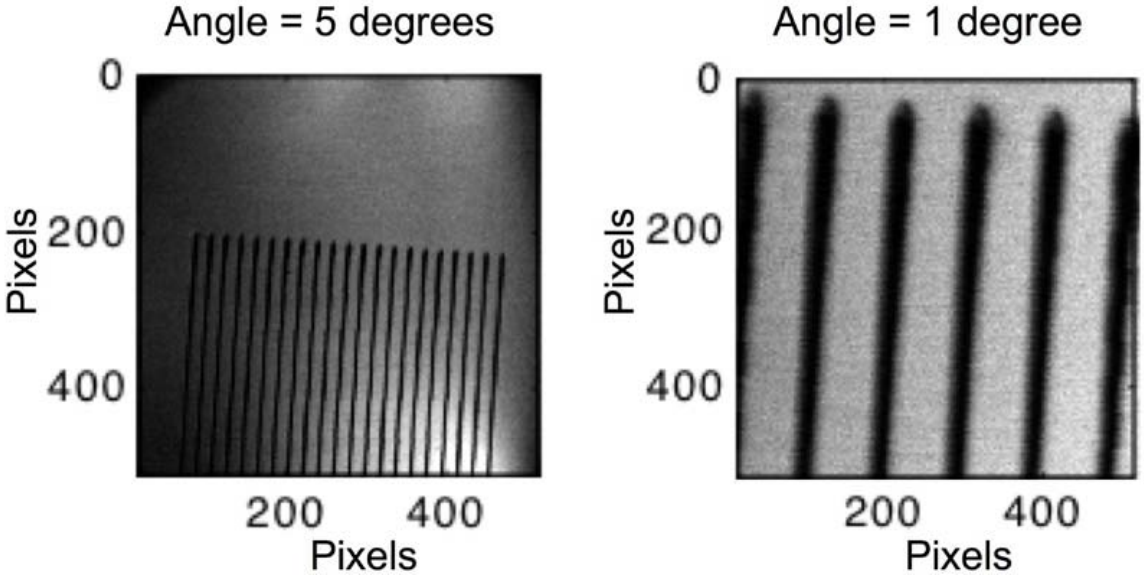

Fig. 3.7 Reticule Images taken at galvo-mirror scan angles of one and five degrees. The x and y axes are pixel number.

The angle of incidence of the laser on the objective lens' pupil plane (which is a focal length in from the shoulder where the threads meet the objective body) is directly proportional to the lateral displacement of the focused spot in the focal plane. The images in Figure 3.7 were analyzed to give the characteristic equation for the proportionality (Equation 3.4).

The scan mirrors have a maximum angular deflection that, through the telescope relay (components 4 and 5 in Chapter 2A) sets the angular scan range and the field of view of the microscope which is defined as the spatial difference between largest and smallest x position in the image.

Figure 3.7 shows images of the reticule taken with the scan mirror's maximum angular deflection set to 5° and 1°. Pixel samples were taken on a line at constant y-position and showed the period of the 10-μm etchings in pixels, and are shown in Figure 3.8. The period of the etchings in the images was used to find the total field of view for scans of various maximum angular deflections (Figure 3.9). A relationship (Equation 3.4) was then established between the maximum angular deflection of the scan mirrors and the resultant field of view of the microscope.

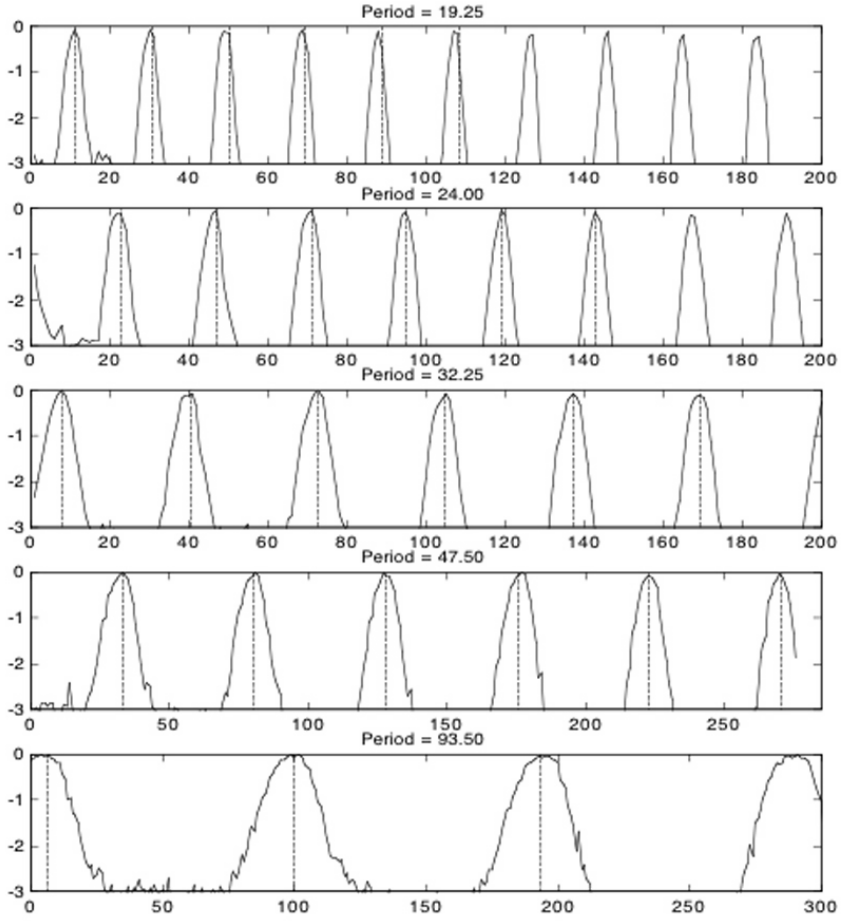

Figure 3.8 Pixel samples along constant y-line in Figure 3.5. The five functions (top to bottom) correspond to the scan angle equal to 5°, 4°, 3°, 2° and 1° respectively. The units of the y-axis are $\log_{10}$(PMT voltage) and the units of the x axis are lateral pixels in the image.

Figure 3.8 shows the period in pixels for the grating lines at each of five different maximum angular deflections. Equating this period to ten μm, which is the known spatial period of the grating, a total lateral field of view was determined for the 512-pixel images for each of the five experimental results.

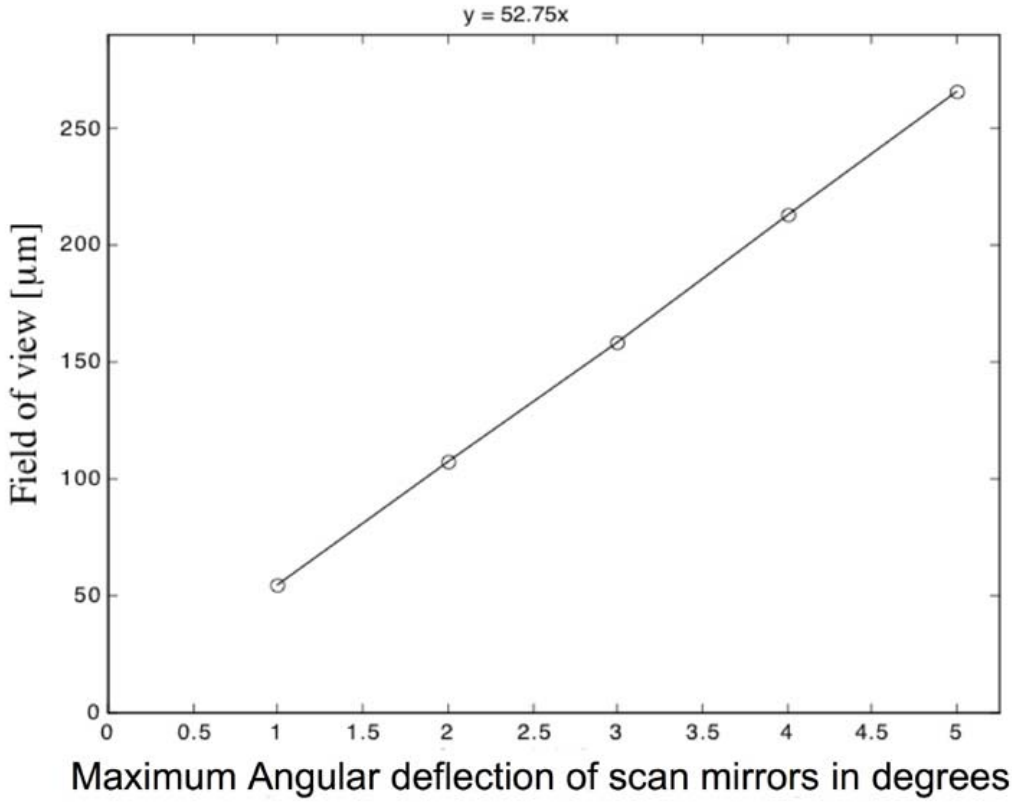

Figure 3.9 The field of view (y) as a function of the maximum angular defection of the scan mirrors (x). The linear relationship y = 52.75x will be used through out this thesis to assign physical dimensions to results based on the microscope setting during the experiment.

Figure 3.9 shows the relationship between angular position of the galvanometric scan mirrors and the lateral focal position within the sample:

$$\text{field of view} = 53(\theta)\ [\mu m] \tag{3.4}$$

where θ in degrees is the scan angle of the scanning mirrors. The calibration constant 53 [μm/degree] characterizes the dimension of the scan in terms of scan angle. This calibration enables the user to specify the zoom of the microscope, which is inversely proportional to the field of view. The field of view is directly proportional to the

maximum angular deflection, which is recorded during image acquisition. The maximum angular deflection and axial motor step size in degrees and μm respectively are inputs to the image acquisition software and enable the image processing software to assign physical coordinates to the data (see "code.m" in the image acquisition and processing software appendix). For example, the field of view divided by the number of pixels (512) yielded the inter-pixel spacing.

3.B Fluorescence Mode Calibration

The fluorescence confocal aperture was aligned using a calibration sample consisting of a drop of fluorescent fluid (fluorescein in solution) sandwiched between a microscope slide and cover slip. Without any spacer between the glass, the liquid thins to less than 5 microns as measured with a caliper. The water-dipping lens was switched out for an air immersion lens for this calibration, which is designed to focus through a glass cover slip. Both objective lenses were infinity corrected such that collimated incident laser light focuses in the focal plane of the objective lens. The two lenses are therefore equivalent for the purposes of calibration. Bringing the thin planar fluorescent sample into focus caused the fluorescent light to focus to a spot in the pinhole plane. The pinhole was mounted on an x-y micromanipulation stage and could be traced across the focus in calibration. The pinhole was placed in the focal plane of the sample arm lens (10) and translated in the focal plane (in x and y) until the detected fluorescent light from the calibration sample was maximized.

3.B.1 Microsphere Images in Non-Scattering Medium

Fluorescent microspheres (Molecular Probes A-7302, diameter = 2.5 [μm]) suspended in clear, 2% agarose gel were imaged to evaluate the microscope in fluorescence mode. The gel was coupled to the water-dipping objective lens with a drop of water.

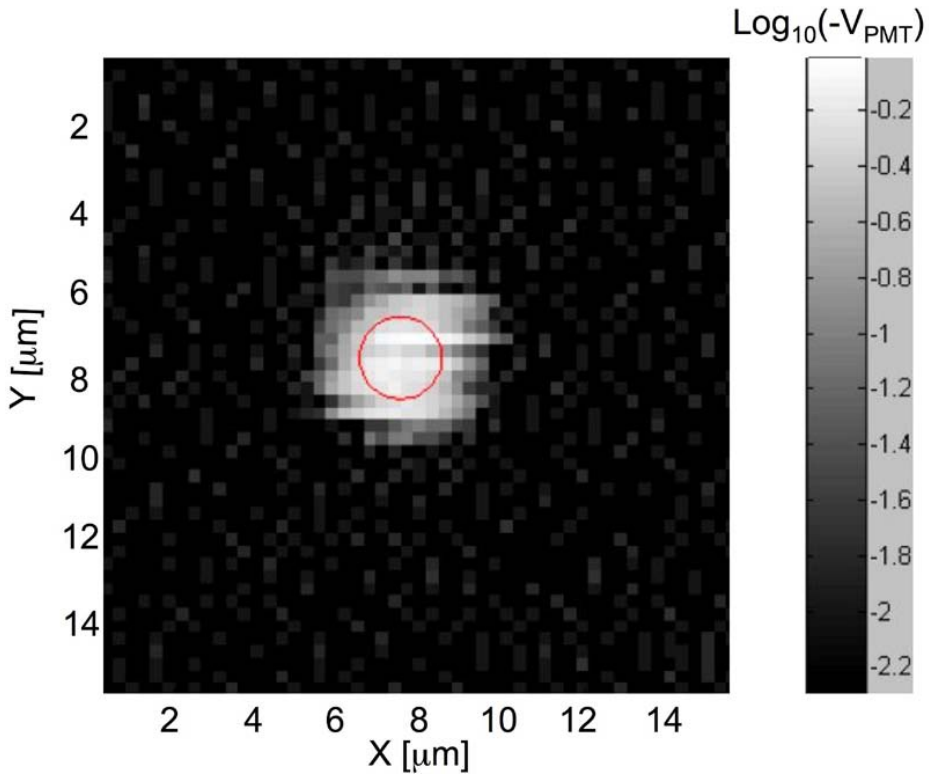

Figure 3.10 X-Y cross sectional image of a single 2.5-μm-diameter fluorescent polystyrine microsphere suspended in non-scattering gel as seen by the pinhole detector, the corresponding image for the ring detector is not shown. The red circle indicates the true size of the plastic sphere. The pixel values shown are the log of the inverted PMT voltage. The x and y units were calculated from pixel number using Equation 3.4. The total image was 150 by 150 μm but only a 16 by 16 μm window is shown.

12 axial profiles (shown in Figure 3.11) were extracted from 3-dimensional images of 2.5-μm microspheres like the one shown in Figure 3.10 (cross section). The mean FWHM for the pinhole and ring signals were 2.5 ± 0.2 μm (n=12) and 3.6 ± 0.3 μm (n=12), respectively. While Figures 3.10 and 3.11 show the log of the data for the purpose of illustration, the FWHM is taken directly from the original data.

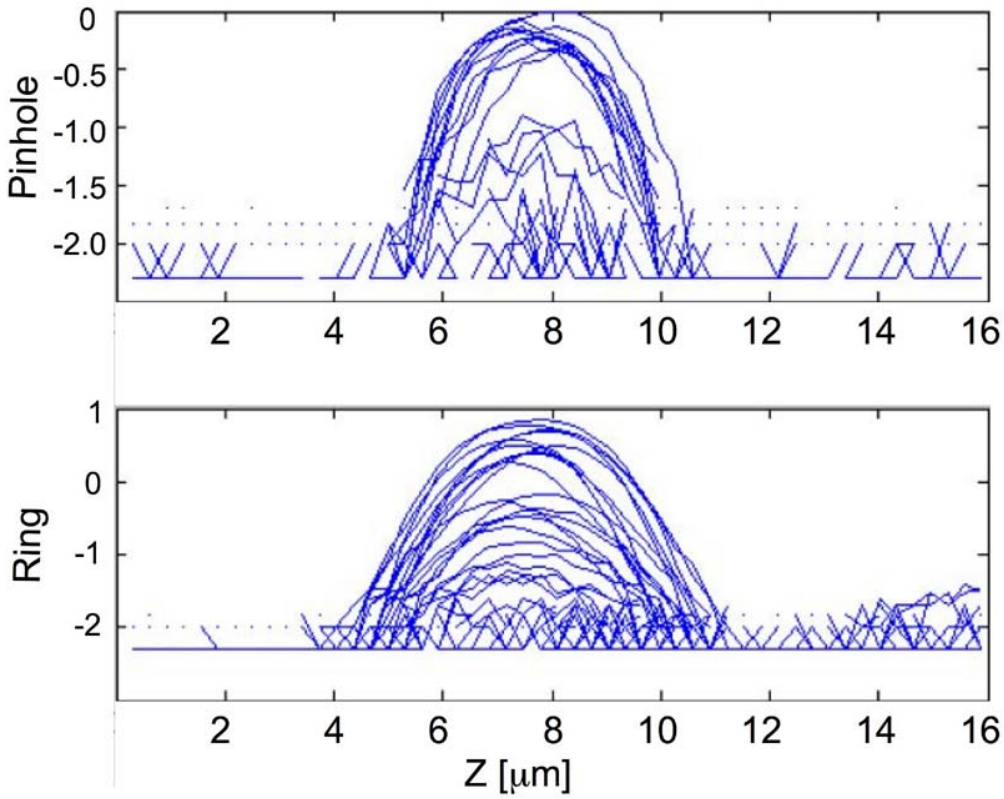

Figure 3.11 Axial profiles of microspheres are shown for the responses of both the pinhole and ring detectors (see Figure 2.7 for physical layout of the detectors) to twelve 2.5-μm-diameter fluorescent microspheres. As in Figure 3.10, the results are expressed (y-axis units) as the log of the PMT voltage.

Figure 3.11 shows the axial profile of 2.5-μm-diameter microspheres in non-scattering media. The ring detector shows a broader image since it acts somewhat like a widened pinhole and collects more out-of-focus photons. The images of the spheres were characterized by picking each y-position on an x-z plane bisecting the sphere and fitting the axial profile to a Gaussian curve.

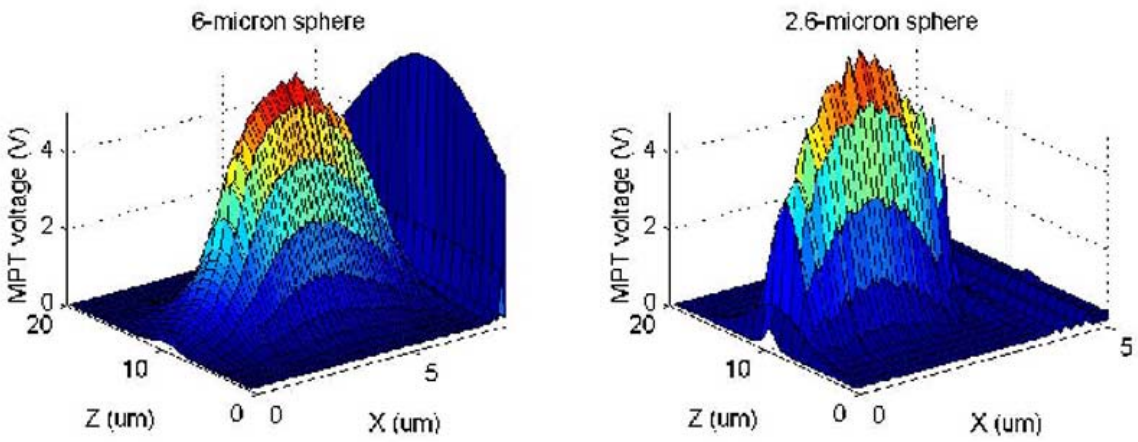

Figure 3.12 The microsphere profiles of 2.5-micron and 6-micron spheres are recreated by the fits to the axial behavior in the x-z plane bisecting the spheres. Note the scale of the x-axis is different showing the microsphere size. The z-axis is image intensity. Microsphere profiles from pinhole detection are shown in cross section orthogonal to the sample surface. These 2-D data sets consist of a set of Gaussian curves (constant x-position) located at each x position, which were fit to the actual data.

The purpose of this experimental imaging on fluorescent microspheres in a non-scattering environment was to produce images showing apparent size of the microsphere in the image to compare with the known microsphere size. The dimensions of the microspheres as seen in Figure 3.12 illustrate that in a clear medium, the central fiber pinhole of the fluorescence channel produces images as expected. This experiment served as a test of the fluorescence mode channel.

3.B.2 Imaging a Fluorescent Neuron

Fluorescence imaging was also tested on thin biological tissues. In Chapter 4, imaging within optically thick samples will be discussed. Here, samples include a thin layer of target tissue beneath a thick optically clear medium such as a slice of brain tissue mounted beneath a conventional 100-μm glass cover slip.

A ventromedial hypothalamal brain slice from a mouse was imaged. The slice was approximately 10 μm thick. The tissue was sectioned by cryostat and immediately immersed in saline solution to prevent dehydration. The genetic mutant mouse expressed enhanced green fluorescent protein (SF1-EGFP) in hippocampal neurons and was used for a separate experiment. Left-over brain slices were generously donated by Kate Elecott. The purpose of this experimental imaging was to show that the microscope had the sensitivity to detect fluorescence from GFP at concentrations typical of expression in biological tissue.

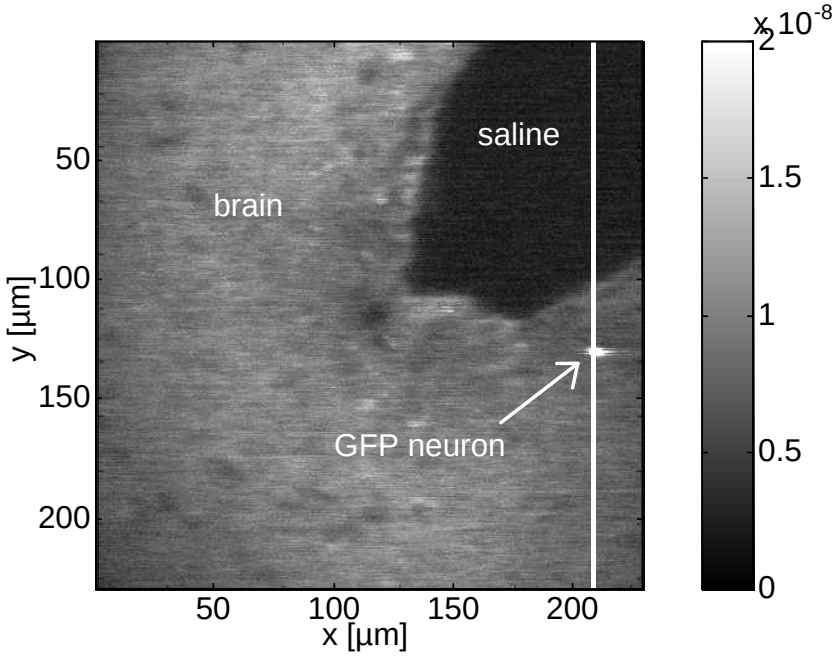

Figure 3.13 Image of a single fluorescent neuron within murine brain tissue. The overall folding of brain tissue is apparent: the dark region in the upper right is a "nook" in the nook-and-cranny appearance of folded brain tissue. Color bar (0 - $2x10^{-8}$ W) shows the actual power [W] emitted from the confocal volume. The image has been scaled to correct for the transmission optics and PMT sensitivity. The correction included division by the fractional transmission through the microscope and division by the fraction of collection of the objective lens (fluorescent emission is assumed to be isotropic). The laser power incident on the tissue was 5 mW at the 488 nm wavelength.

Figure 3.13 shows three distinct regions. The upper right dark region has no biological tissue and indicates the signal level of aqueous solution. The majority of the picture is given contrast by the bulk autofluorescence of brain tissue, primarily lipofuscin autofluorescence[22]. A single neuron expressing enhanced green fluorescent protein (EGFP) can be seen in the middle-right of the field of view. The maximum pixel value at the site of the neuron is actually 5.4×10^{-8} (as shown in the next figure) but the scale of this image was chosen to have a maximum of 2.2×10^{-8} to give contrast to the autofluorescent region. This particular brain slice was chosen because it contained only 1 green fluorescent neuron in order to emphasize the detected fluorescence levels for three regions: aqueous solution (no fluorescence), bulk gray matter fluorescence (autofluorescence) and neuronal fluorescence (EGFP). From these three levels of signal, one can immediately deduce the signal-to-noise ratio for the fluorescence channel of the microscope as well as the contrast of imaging EGFP embedded within autofluorescent brain tissue. To quantify the fluorescence levels, pixel values were sampled along the dashes white line in Figure 3.13. The values are shown in Figure 3.14.

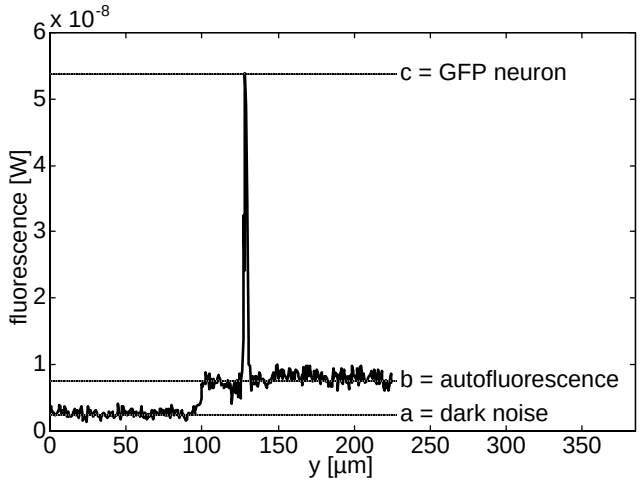

Figure 3.14 The pixel values along the dashed white line in Figure 3.13 are plotted as a function of position. (Scale = 0-5.5 x 10^{-8} W of fluorescence in response to 5 mW excitation.)

Figure 3.14 shows the signal levels for three image regions. The dashed line drawn on the image in Fig. 3.13 indicates the x-axis position of pixel values shown in the graph of Fig. 3.14. The region labeled (a) represents the signal collected for the focus in the non-fluorescent region. This 100 mV RMS (≈ 10 pW) dark noise is typical of the microscope's high gain setting in tissue with bulk fluorescence. The signal to noise ratio of the GFP fluorescence over the dark noise was (c-a)/a = 16.8. The contrast of the GFP neuron over the autofluorescence was (c-(b-a))/(b-a) = 9.7.

3.B.3 Imaging the Iris of a Living Mouse

Composite imaging of fluorescence and reflectance enables imaging of in vivo phenomena such as uptake of fluorescent dye by dendritic cells in a living mouse eye while also providing an image of the background tissue structure. As illustration of the dual mode image acquisition capabilities of the microscope, Fig. 3.15 shows an in vivo image of a mouse iris, taken by viewing through the cornea, as part of a study with Dr. James Rosenbaum, Dept. of Ophthalmology, OHSU, on immune cells in the mouse iris. Mice were anesthetized with a ketamine/xylazine cocktail (1 ml i.p.). The experiment involved injection of fluorophore-tagged antigen (green fluorophore attached to ovalbumin) into the vitreus humour of the eye, which attached to dendritic cells. The image used the fluorescent channel to acquire the green fluorescence of labeled dendritic cells and the blue reflectance channel to acquire the structure of the background tissue. Reflectance from iris tissue shows biological structure, which can reference the position and movement of fluorescent targets in vivo. Translating the x-y scans as a function of depth allows localization of the dendritic cells within the iris.

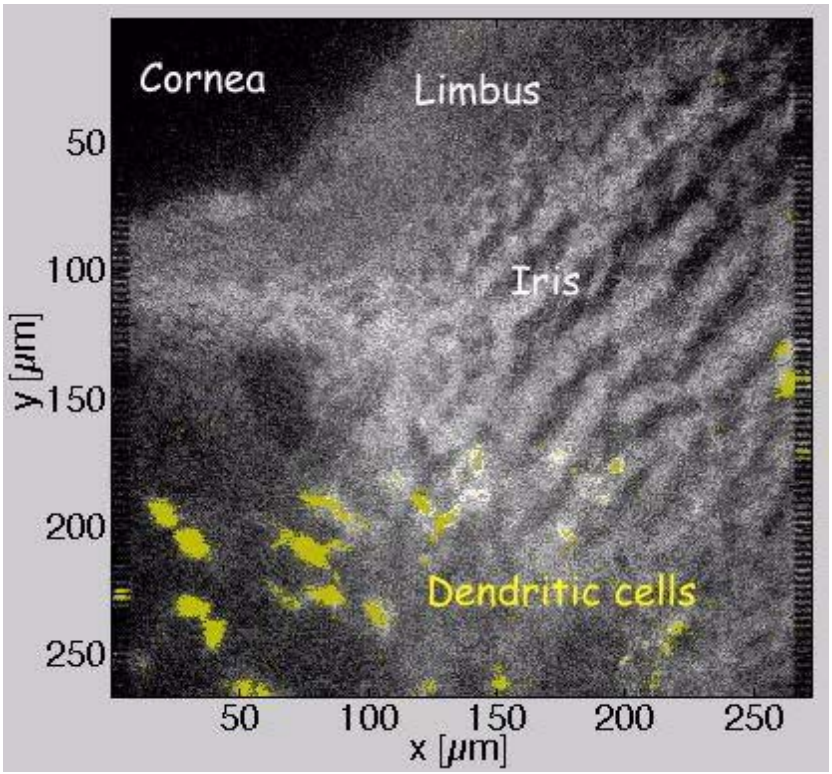

Figure 3.15 The eye of a living mouse was imaged in reflectance (grayscale, blue argon ion laser) and fluorescence mode (false color yellow, green-fluorophore-tagged dendritic cells).

In 3D imaging experiments, it is particularly useful to acquire both fluorescence and reflectance images. The reflectance image reveals the structure of the bulk sample and can give a graphic reference for fluorescently tagged cells of interest. Before euthanasia, the animal's eye was imaged as dendritic cells in the iris took up the antigen and became fluorescently labeled. In Figure 3.15, the reflectance image (grayscale) shows the ultra-structure of the iris and the limbus. The dendritic cells are revealed by superposition onto the reflectance image and are false-colored yellow.

3C Conclusions

The axial point spread function was measured to validate the microscope performance by using a water glass interface. The FWHM of the axial point spread

function was 1.12 μm, which was comparable to the 0.76 μm FWHM predicted by theory. The peak magnitude of the point spread function yielded a measurement (PMT voltage) that was designated characteristic of the reflectance 0.0044 [unitless] expected from the interface between glass and water, and was used to normalize the measured reflectance from biological tissue.

The field of view of the microscope was determined by imaging a reticule. Analysis on images of the etched lines compared their spacing (in pixels on the image) to the total number of pixels in the image to designate the field of view in microns. The field of view was proportional to the maximum angle of deflection for the scan mirror during imaging.

The fluorescence mode was tested using fluorescent polystyrine microspheres. The confocal pinhole fluorescence image showed the lateral FWHM of a 2.6 μm microsphere to be 2.5 ± 0.2 μm (n=12). The ring detector produced a FWHM which was larger as expected. This effect will be discussed in detail in the next chapter.

Fluorescence imaging in biological tissues showed that the microscope had sufficient sensitivity to detect fluorescent emission, which is weaker than reflected light. A neuron with endogenous GFP expression was seen to have sufficient contrast to be imaged above the background bulk autofluorescence of brain tissue.

Chapter 4: Novel Confocal Detection for Imaging in Scattering Media

4.A Introduction

The presence of scattered photons in confocal microscopy inevitably leads to poor contrast and resolution.[43] It is impossible to completely filter out scattered light. This is not feasible because signal shrinks with pinhole size. The confocality, which is constriction of the confocal aperture (traditionally the pinhole diameter), determines the level at which multiply-scattered light is filtered. The trade-off is contrast vs. signal. Better spatial filtering (smaller pinhole) necessarily means less signal detected. Signal loss can be prohibitive of fluorescence imaging in turbid media, which is already at high gain. Although it was not recorded with a charged-coupled device in this work, the fluence rate falling on the pinhole plane was seen with the eye to be centered on the pinhole and have a diameter of about 100 μm and 1 mm in non-scattering environments and scattering environments respectively.

In non-scattering and weakly-scattering samples, the focus within the sample (T_{in}, Equation 1.2) retains its diffraction limited spot size in the focal plane on the order of a micron (see Figure 5.1). The obvious choice of pinhole size is to match this narrow diameter, which contains most of the fluorescent optical power, to the pinhole diameter using the magnification (see Chapter 2.B.3). However in turbid media, the fluence rate distribution (Watts per square cm) falling on the confocal plane is broader and includes multiply scattered light from the focal region as well as fluorescence excited outside of the focus. In such a situation, a diffraction-limited spot-sized pinhole may not transmit

enough fluorescent light to dominate over the noise of the system. One solution is to dilate the confocal aperture until the minimum acceptable signal level is attained and suffer the poor contrast at that level of nonconfocality. Thus the trade-off between signal strength and optical sectioning is challenging when both are desired.

The pinhole/ring confocal detector geometry (Chapter 2.B.4) is proposed to allow use of more photons falling on the pinhole plane. It is proposed that photons previously omitted from detection because they fall outside the pinhole be used to correct for the diffuse fluorescence penetrating the pinhole during the confocal measurement, which decreases the contrast. Diffuse fluorescence can arise from background bulk autofluorescence of the sample[21, 22, 23], or from scattered fluorescent photons which originated from the focus. The pinhole ring detector is proposed to produce better images by subtracting a factor proportional to the diffuse fluorescence from the confocal measurement to produce a modified confocal response (MCR, Equation 4.4). For the case of background bulk autofluorescence, which is common to the pinhole and ring detector, the MCR offers common mode noise rejection.

The image produced by the ring detector is blurred because it is produced with scattered light, which forms images of less resolution[43]. For the case of fluorescence of focal origin that has been scattered, this is similar to subtracting a blurred image. In image filtering, the process of subtracting a blurred image is known as unsharp masking. $f'(x,y) = f(x,y) - f_{blurred}(x,y)$ describes the operation. An image is produced f’(x,y) which is more crisp than the original image f(x,y) by subtracting from the original image, a blurred image $f_{blurred}(x,y)$. Figure 4.1 shows the result of the unsharp mask in digital image processing[48].

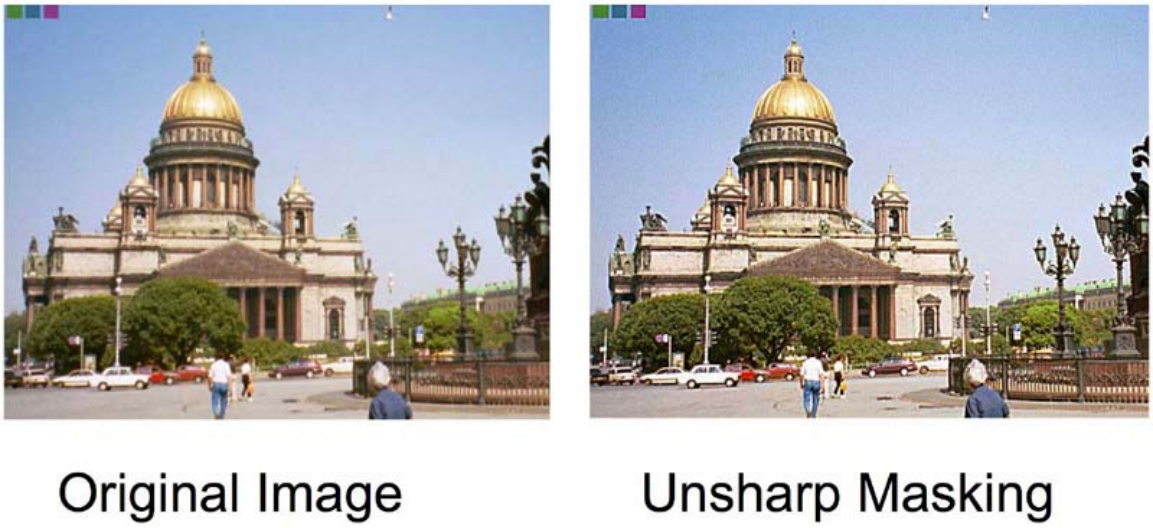

Figure 4.1 Example of unsharp masking in digital image processing reproduced with permission from [48].

In this chapter, pinhole detection and ring detection are used to produce images which serve as the original image f(x,y) and the blurred image $f_{blurred}(x,y)$. These two images yield a modified confocal image f'(x,y) which should yield resolution superior to the original pinhole image f(x,y). This hypothesis is proven by analysis of microsphere images produced with the ring and pinhole detectors. The blurred image, collected by the ring detector, contains information about the scattered light that can not be obtained from the pinhole image. This technique is therefore impossible through digital post acquisition processing of the pinhole image alone.

The extent to which subtracting the ring signal can improve resolution will be discussed in this chapter. The rational behind the pinhole/ring detector will be addressed in this context. Results form imaging experiments using standard fluorescent microspheres in scattering gels will show how resolution can be improved using the pinhole/ring detector. Images were acquired using a fiber bundle with 9 fibers surrounding a central fiber to replace the confocal pinhole (see Figure 2.7). The central fiber acted as the confocal pinhole, and the ring of fibers surrounding the central pinhole fiber collected a second signal to characterize the diffuse fluorescence. The ring signal

was subtracted from the pinhole signal to mitigate background diffuse fluorescence and boost resolution when imaging in situations where scattering or background fluorescence in layers above the focal plane otherwise caused image degradation.

Section 4.A.1 presents experimental images where scattering in overlying tissue degraded the contrast and resolution of fluorescent cells. The effect was seen to be proportional with thickness of overlying tissue. Section 4.A.2 shows the point-spread function (PSF) grows with increasing depth using a Monte Carlo Model which explains the result of Section 4.A.1. Section 4.A.3 analyzes the Monte Carlo output data to yield the resolution as a function of depth. Section 4.B further describes the concept and implementation of the pinhole/ring detector. Section 4.C provides experimental results using the pinhole/ring detector.

4.A.1 The Effect of Scattering in Transdermal Confocal Microscopy

The presence of full thickness mouse skin between the objective and its focal plane prevents resolution of cellular detail. The effect of optical scattering on image contrast was demonstrated by imaging fluorescent cartilage cells under conditions of various overlying layers of scattering skin (Fig 4.2). Col2-GFP reporter mice with enhanced green fluorescent protein (EGFP) expression in their chondrocytes[42] were used (collaborating with Dr. William Horton, Dept. of Molecular Biology and Genetics, OHSU). A mouse pup was sacrificed and imaged on the paw and on the chest within an hour of euthanization. All imaging was done on a commercially available confocal microscope (Leica) using an oil immersion objective lens. The pinhole size was adjusted to be as small as possible (best optical sectioning) while still allowing enough light through to register signal enough to contrast the xyphoid process (sternum within the chest.

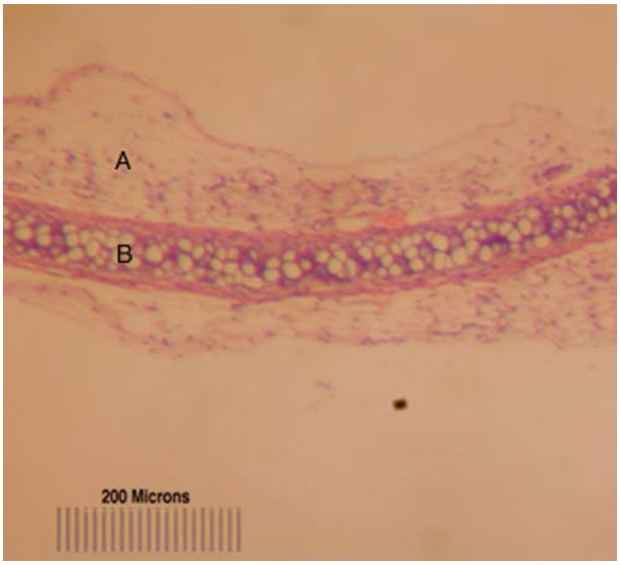

Figure 4.2 Sagittal view of the xyphoid process stained with Hematoxylin and Eosin. A: connective tissue, B: Cartilage.

In the xyphoid process, the cartilage lies beneath the 5-μm stratum corneum, 10 μm epidermis, 100-μm dermis and 85-μm connective tissue, a total depth of 200 μm. Under this condition, images were formed where sub-dermal cartilage could be discriminated from bulk tissue but the cells were blurred in the image and not resolvable. Cell resolution loss at this depth results from optical scattering within the epidermis and connective tissue.

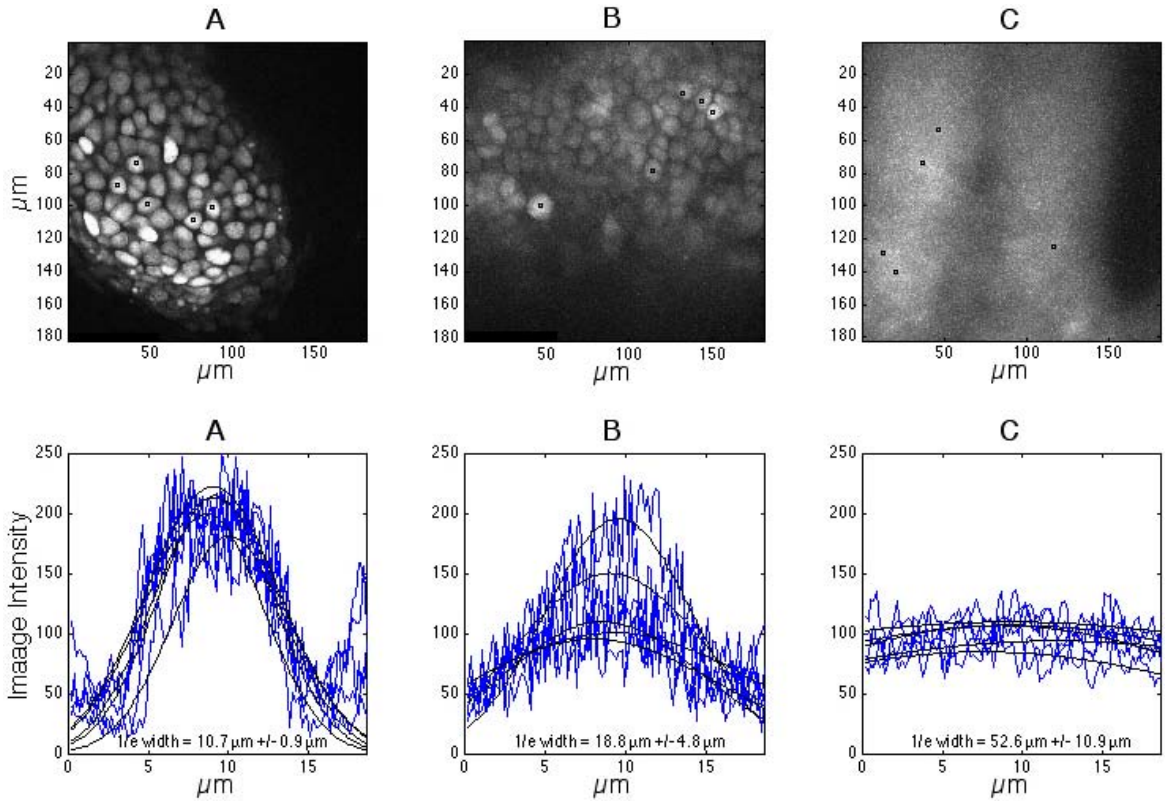

Figure 4.3 Confocal fluorescence images of EGFP-expressing Chondrocytes at anatomical sites with increasing overlying tissue on a whole mouse pup. (A) The fingernail-cuticle has no overlying tissue, and the cells are clearly distinguishable. (B) Cartilage in the knuckle of the animal shows cells underneath 100 μm of epidermis, dermis and connective tissue. (C) Cartilage of the xyphoid process (sternum) with 250 μm of overlying tissue. Visual inspection enables resolution among the cell population in A, arguable resolution in B and arguably no resolution in C. Below the images are the fits to the vertical profile of five representative cells marked on the images. Skin thickness was histologically deduced by comparison of fixed specimens to the reticule used in Chapter 3.A.3 and is approximately due to unknowns such as tissue shrinkage during fixation and the Hematoxylin and Eosin staining process.

Figure 4.3 C suggests that sufficient fluorescent light propagates to the tissue surface for detection but the semi-diffuse state of the detected light prohibits imaging with enough contrast to resolve cells as discrete which is necessary for population

assessment. The pixel samples shown illustrate the profile of the cells. The locations of analysis were chosen to represent typical cells in the image. For no overlying tissue (A) the cells can be easily distinguished; the signal strength for the cell stands out about 7-fold higher than the background signal which can be considered the noise. The signal to noise ratio is SNR = 7. For 100 μm of overlying tissue (B) the cells are still distinguishable but the contrast, defined as the difference in signal level between the cell center and the background measured between cells divided by the background, is considerably less (SNR = 3). For 250 μm of overlying tissue (C, blue) contrast is almost totally lost (SNR ≈ 1).

To further quantify the results, five cell profiles from each image were fit to a Gaussian intensity function. The three parameters in the least-squares fit included a peak magnitude at the center of the cell, the center position and a 1/e radius, which is the radial position relative to the cell center at which the image intensity has fallen to a value of 1/e times the peak magnitude. The Gaussian fitting function was chosen to specify the apparent width of the cell, which is reported as two times the 1/e radius.

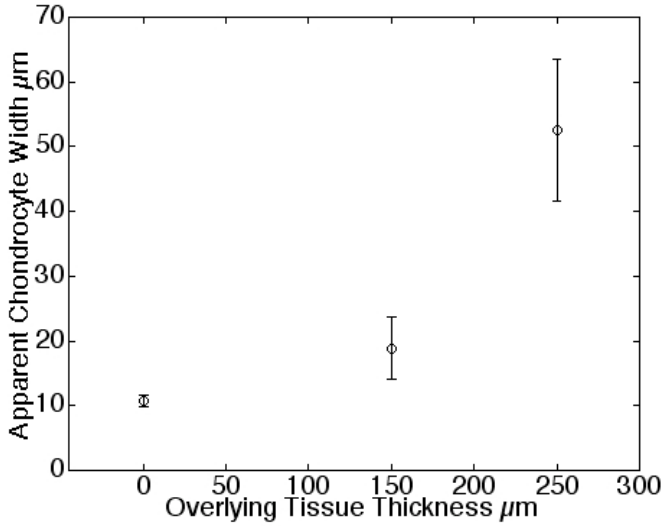

Fig. 4.4 The apparent Chondrocyte width (twice the radius from the cell center at which the Gaussian fit fell to 1/e of its central value). Mean and standard deviations are shown for five cells.

The more overlying tissue, the more scattered light contributes to the image and the less sharp the images become. In the blurred image (C), the cell profile has become so large that the cells overlap in the image and are therefore unresolvable. The broadening of fit Gaussian fit with increasing thickness of overlying tissue results from the inclusion of scattered photons in the detected confocal signal and results from dilating the confocal pinhole in order to increase the light collection at deeper depths. All three experimental images were collected with the same pinhole diameter, chosen to yield adequate signal for the thickest overlying tissue (C).

In conclusion, scattering corrupts resolution in subsurface confocal detection of cells. The ability to resolve individual cells is degraded with increasing thickness of overlying tissue. Confocal masking of scattered light from the detector is adequate for samples thinner than 100 μm. In thicker samples, scattered light comprises a greater fraction of the measurement and the contrast and resolution decrease as a result. This section analyzed cell images in the optical section. The following section will quantify the PSF for fluorescent confocal detection axially in scattering media to investigate this effect.

4.A.2 Theoretical Example Monte Carlo Point-Spread Function

The Monte Carlo simulation in the Appendix (fcmc.c) was used to generate the confocal PSF as a function of depth within a turbid phantom (μ_a = 2 cm^{-1}, μ_s = 2500 cm^{-1}, g = 0.98, lens NA = 0.90, matched surface boundary). The optical properties were chosen based on the measurements in Chapter 9. Details of the simulation will be discussed in Chapter 5. In this chapter, the results are presented and used to explain the observation of the previous section; that images become blurred under increasing thickness of overlying scattering tissue.

The PSF is the image that results from a point source in the sample. The purpose of a PSF is to characterize the point-spreading due to physical limitations of the optics

and to sample conditions such as scattering in superficial regions with respect to the focus. In this work, the axial behavior of the PSF is investigated considering the geometry of focused light and scattering in the sample.

Due to the geometry of focused light (see Figure 5.4), point-spreading is worse axially than laterally by a factor of 3NA/n (see [25] Equations 6 and 7) where n is the immersion medium refractive index and NA is the numerical aperture of the objective lens. The PSF of a focused beam is larger on axis than in the radial direction, forming a football shaped volume of high energy density at the focus. In a Monte Carlo simulation (see fcmc.c in the Appendix) whose details will be discussed in chapter 5, the axial PSF was simulated for a point source placed at four depths (Fig. 4.4). The PSF included propagation into the medium,

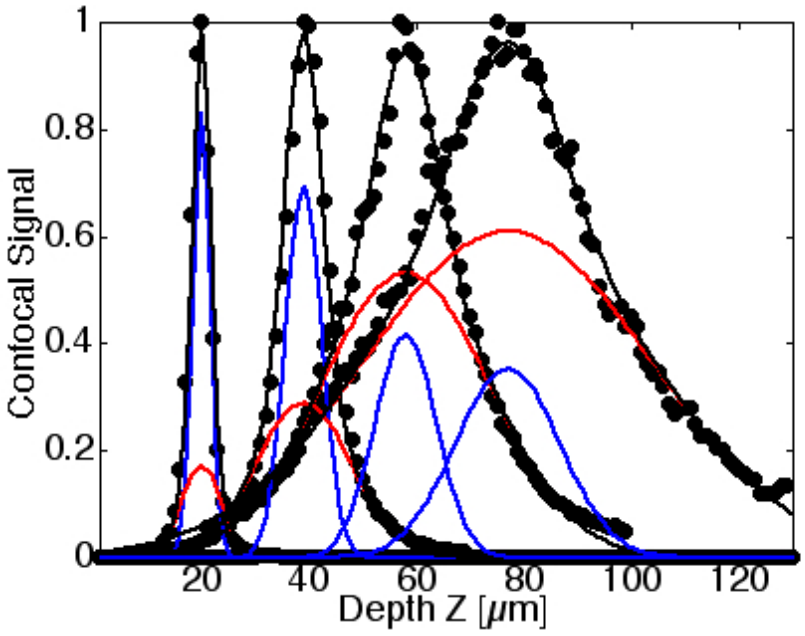

Figure 4.5 Axial point spread functions for point sources located at Z = 20, 40, 60 and 80 μm. Scattering properties of the phantom were chosen to mimic scattering in murine skin (μ_s = 2500 cm^{-1}, g = 0.98, see chapter 5 for simulation details). Each Monte Carlo output data set (black circles) was fit as the sum of two Gaussian curves. Red line + blue line = black line = data fit.

The Monte Carlo output data (black circles) shown in Figure 4.5 is the result of 4 separate simulations normalized to have a peak value of 1. The PSF broadens with depth. This has been shown experimentally by Dwyer et. al.[49] who found the axial spreading to have a 7.6 μm FWHM under 60-μm full thickness human epidermis which is larger than the 1.7 FWHM reported under no skin. By comparison, the Monte Carlo result presented here shows a 20 μm FWHM 60 μm within the scattering sample. The discrepancy results from a difference in confocal probe geometry (theta detection in the case of [49] and full pupil detection in the case of the Monte Carlo) as well as a higher level of scattering in the case of the Monte Carlo, which is modeled after mouse dermis which has more scattering than human epidermis (see Chapter 9). The Monte Carlo point spread function for each point source was fit with the sum of two Gaussians (black line) to yield analytical functions, which were used to approximate the Monte Carlo output data for use in production of the resolution in the following section. The method of fitting to the sum of 2 Gaussians will be discussed in the following chapter.

4.A.3 Analysis

Layers of overlying scattering were seen to degrade images of cells in optical sections (section 4.A.1) and broaden the PSF in the axial dimension (section 4.A.2). In this section, the Rayleigh resolution limit is determined for each of the four point sources simulated in section 4.A.2. For the purposes of determining the resolution limit the Monte Carlo output data was fit to a curve that was taken to be the PSF for a particular depth. Four PSFs were generated (see fits in Figure 5.8) and each used in the following process to yield the Rayleigh resolution limit.

1, Two identical point-spread functions were generated and separated by a distance δ.

2. The sum of the two curves was computed and normalized to have a peak value of 1 to simulate the axial confocal response form two point sources separated by a distance delta.

3. The parameter δ was increased until the dip between the maxima of the sum curve was $8/\pi^2$. The criteria that the minimum value within the dip between resolvable points be less than $8/\pi^2$, is known as the Raleigh resolution limit. The separation distance δ, between the two point-spread functions when this condition was met was the resolution limit for a particular depth (see Figure 4.9 for a graphic illustration of resolution).

The algorithm is not precisely correct because the PSF should have changed with depth, as the parameter delta (the separation distance) was increased. This effect was assumed to be negligible because the ranges for delta were small compared to the depth of the fluorescent sources. To be precise, the point-spread functions should be broadened as they get deeper and thin as they get shallower. The effect of this error is negligible since the maximum delta considered was only fourteen μm (compared to the 80-μm source depth).

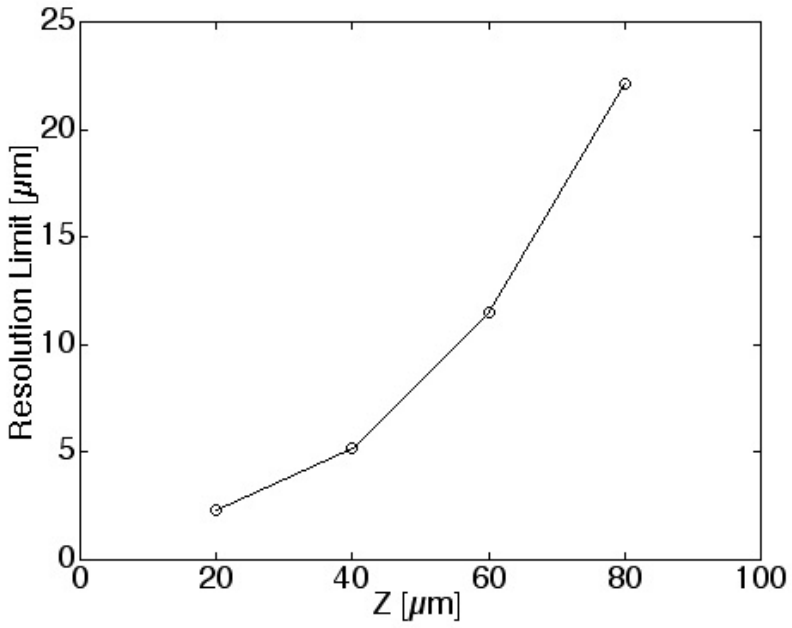

Figure 4.6 Rayleigh resolution limit for fluorescent point sources in a scattering medium located at four depths within a scattering medium based on Monte Carlo simulations.

Figure 4.6 shows the resolution limit predicted by the Monte Carlo simulation. The reduced mean free path of the tissue, which is the mean distance a photon travels before it is scattered or absorbed corrected for the anisotropy of scatter, was 190 μm so photons contributing to the point source at a depth of 80 μm had scattered on average, once. The resolution limit at a depth of 80 μm is about 22 μm. This result agrees with the conclusion of Gan *et. al.*[43] who reported that photons scattered twice construct images with resolution larger than 14 μm. This agreement between their result for transverse resolution and our result for axial resolution suggests that the contribution to the PSF from tissue scattering is about the same axially as transversely, as opposed to the contribution from the geometry of focus which is worse axially.

4.B Modified Confocal Detection

A confocal detector is proposed that produces a response based on two measurements instead of the pinhole measurement made in conventional confocal microscopes. The two measurements are 1) the traditional pinhole signal that is measured with a single central fiber and 2) a ring signal that is measured with nine fibers surrounding the pinhole (see Figure 2.7).

The role of the confocal pinhole aperture is well documented[50, 51]. To understand the role of the ring detector, a ray tracing analysis is provided. The ring detector is modeled as a large pinhole with a central obstruction.

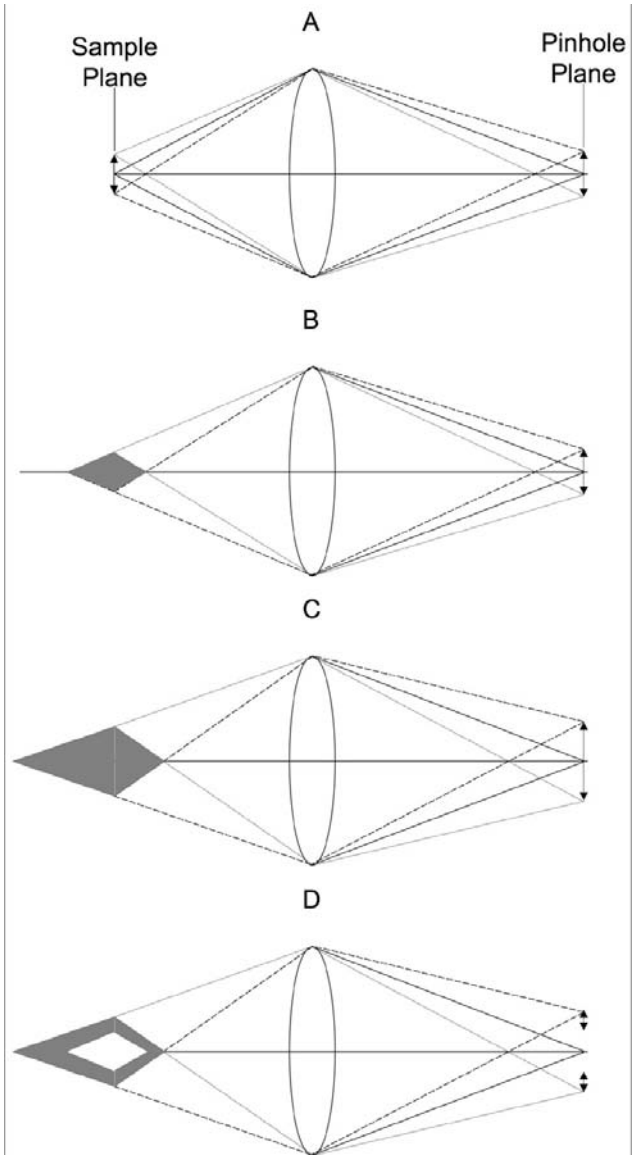

Figure 4.7 The confocal pinhole is modeled in Figure A. The vertical arrows represent the diameter of the focused spot of light on the left within the sample and the diameter of the pinhole on the left. Figure B shows the shaded area of pinhole-detection sensitivity within the sample. Since the system possesses cylindrical symmetry about the optical axis, the shaded area represents a volume of sensitivity. Figure C shows the region of sensitivity for a larger pinhole (denoted by the larger vertical arrow in the pinhole plane on the right). Figure D shows the region of sensitivity for the ring detector, which is simply Figure C minus Figure B.

Figure 4.7 shows the region of sensitivity for the pinhole (B) and ring (D) detectors. The pinhole detector is sensitive to the focal region while the ring detector is sensitive to a volume enclosing the focal region. It should be noted that the true response of the physical detectors is the convolution of the point spread function with the geometric region of sensitivity.

In studies of the effect of an annular aperture[52], it was found that a circular block placed in the back aperture of an objective lens to create a ring of detection yielded higher contrast since the effective NA was increased. Adding a circular block to the center of a dilated pinhole has the opposite effect and creates a broadened ring-spread function (RSF).

The modified confocal response (MCR) was composed of the pinhole measurement (P) minus the ring signal (R), which measures the background signal multiplied by a constant (c). The result is a PSF sharpened with respect to the original PSF since the broader RSF is subtracted.

$$MCR = P - cR \tag{4.1}$$

The value of c is chosen such that the MCR for a homogeneous scattering medium is zero, since cR = P.

The rationale for subtracting the background signal detected by the ring is two fold. First, neighboring fluorophores to the focus emit photons, which with small angle scattering can propagate through the pinhole. Subtracting the ring detection, which sensitive to the neighboring fluorophores, corrects pinhole measurement of this errant light. The second rationale, which differs in concept from unsharp masking, is to minimize bulk fluorescent emission detected from the sample. Bulk skin autofluorescence overlying EGFP chondrocytes was found to comprise about 10% of the confocal measurement (see Chapter 10). In section 4.A.1, bulk EGFP fluorescence was

detected between cells making them un-resolvable. The subtraction appropriately corrects the pinhole measurement for the diffuse light that decreases resolution and contrast.

As the focus of the objective lens penetrates deeper and deeper into a scattering medium, the detected fluorescent photon populations shift from being primarily composed of photons originating at the focus to (1) photons originating nearby the focus (type 1 photons), and (2) multiply scattered photons from far away but escaping with the right trajectory to penetrate the pinhole (type 2 photons).

Since the focal plane in the sample and the pinhole plane are optically conjugate, the pinhole ring/detector is mapped into the sample such that the pinhole is sensitive to fluorescent emission at the focus and the ring is sensitive to type (1) fluorescent emission from a ring around the focus in the focal plane. In three dimensions the ring detector is sensitive to a defocused shell surrounding the focus within the sample. Subtracting it from the pinhole signal implements a 3 dimensional optical edge detector where the negatively weighted region is a volume enclosing the geometrical focus.

The diffuse photons of type (2) escape the tissue surface and a fraction of these escaping photons, depending on the angle of escape pass through both the aperture of the objective lens and the confocal pinhole. These photons constitute optical noise since they did not originate from the focus within the sample. Fortunately, such photons strike both the ring and pinhole. Thus subtracting the ring measurement implements a common mode noise rejection of diffuse fluorescent light.

4.C Microsphere Imaging

Scattering gel samples (0.1-μm-diameter non-fluorescent polystyrene micropheres served as scatterers, $\mu_s = 97\ cm^{-1}$, $g = 0.112$) were used to characterize the response of the confocal detector to fluorescent microspheres of diameter 2.5 and 6 μm. The confocal detector is described in Chapters 2 and 3 (see Figure 2.7). Fluorescent microspheres were

imaged to demonstrate the efficacy of the confocal pinhole/ring detector. A total of fifteen spheres were imaged at various depths within the scattering gel up to 107 μm deep. A sixteenth microsphere was imaged at a depth of 155 μm but not included in the results because during analysis, the fitting algorithm failed to converge.

In the gel samples, fluorescent spheres which were scarce at a concentration of approximately 3.4×10^{-7} (cm^{-1}) or 1 sphere per cubic volume = 260μm x 260μm x 5μm as seen in images. This concentration enabled imaging of isolated fluorescent spheres at different depths within the scattering medium.

The surface of the sample was located using the CLSM in reflectance mode. The CLSM was switched to fluorescence mode for imaging fluorescent spheres. Images of 512 x 512 pixels were acquired at a field of view (FOV) of 50 μm. Images were acquired with a 0.5-μm Z-step spacing for the 2.5 μm spheres.

In the first step of the data processing, 3D images of single spheres were cropped out of images with multiple spheres for analysis, so the cubes of data (3D images) only contained one microsphere per image cube. Image cubes were acquired with 0.5 μm axial inter-voxel spacing and 0.1 μm lateral inter-voxel spacing. The data cubes were analyzed in Matlab by first locating the sphere centers, then fitting the axial and radial sphere profile with a Gaussian curve. Locating the sphere center was aided by creation of a single X-Y image and a single Y-Z image out of each 3D sphere image. The X-Y image was generated by summing over Z. The Y-Z image was generated by summing over X. The sphere's center position was determined with the ginput command in Matlab which allows the user to click on the sum picture in apparent center of the sphere and yields the coordinates.

The axial profile was extracted by keeping the x and y positions constant at the center of the sphere and extracting all z values. To minimize noise, at each z position an average pixel value was taken by averaging over a 3x3-pixel square region in the x-y plane.

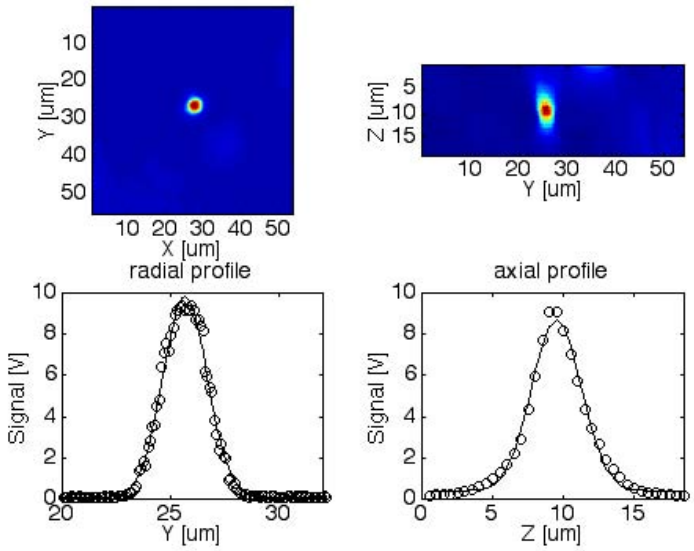

Figure 4.8 Sample fit of a microsphere profile for the ring detector. The microsphere was located at a depth of 7 microns within the scattering gel.

Figure 4.8 shows a sample fit to a microsphere image cube. The axial fit to the data consisted of a single Gaussian curve with an offset (total of 4 fitting parameters). The diameter at which the signal intensity fell to 1/2 of its peak value is reported in Figure 4.9 for the pinhole and the ring detector for each of the 15 spheres imaged at various depths.

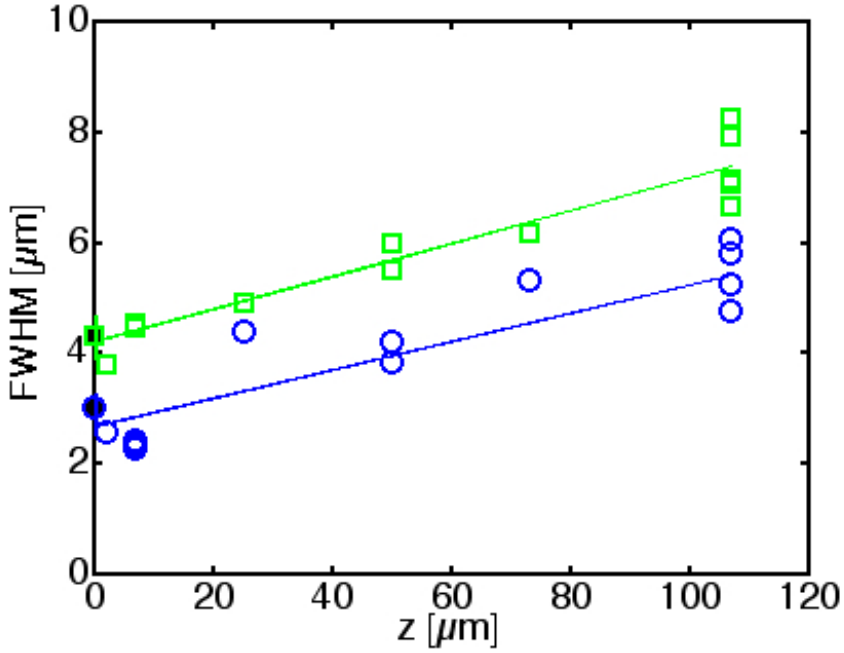

Figure 4.9 The FWHM of the axial Gaussian fitting results for the 2.5 μm fluorescent microspheres in scattering gel. The pinhole results are shown in blue and the ring results are shown in green.

Figure 4.9 shows the fitted FWHM sizes of the microspheres. The data points with solid black centers at Z = 0 represent microspheres imaged under no scattering gel (from section 3.B.1). The image widths measured by the pinhole and ring were different (paired student-T test $p < 0.01$). Linear regression of the data in Figure 4.9 yields (4.2)

$$w_{pinhole} = Z(0.0258) + 2.69\ \mu m \qquad (4.2)$$
$$w_{ring} = Z(0.0296) + 4.22\ \mu m$$

Equation 4.2 gives the axial FWHM width of the microsphere images as a function of depth in the scattering phantom for pinhole detection and ring detection ($w_{pinhole}$ and w_{ring} respectively). It should be noted that the pinhole width for Z = 0 is 2.69 μm which is about the 2.5 μm width of the sphere. In control images of spheres in clear gel (not shown), the 1/e widths remained 2.5 and 4 μm (for the pinhole and ring

respectively) for spheres ranging in depth from the sample surface to 120 μm deep. The approximate axial profiles P(z) and R(z) for the pinhole and ring detectors, respectively, can be recreated for various microsphere depths:

$$P(z) = \exp(-Z^2/w_p(Z)^2) \qquad (4.3)$$
$$R(z) = \exp(-Z^2/w_r(Z)^2)$$

Equation 4.3 recreates the axial profile as seen by the pinhole P(z) and the ring R(z) detectors for a microsphere at depth z within the scattering phantom as deep as 120 μm. Generating the profiles allows calculation of the MCR using Equation 4.1. A sample pair of profiles and calculated MCR are shown in Figure 4.10.

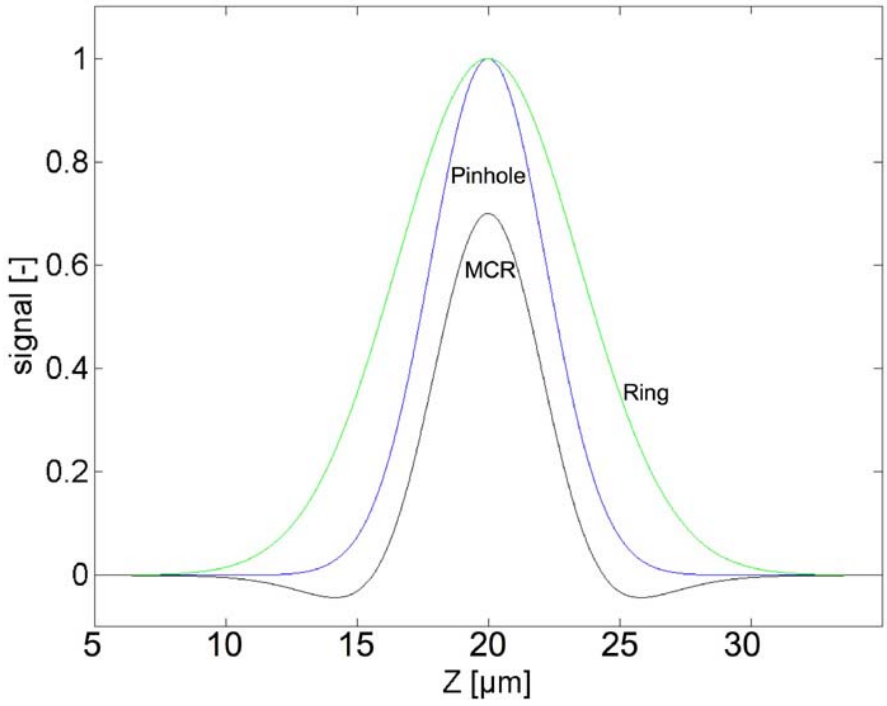

Figure 4.10 Normalized pinhole (blue), ring (green) and modified confocal response (MCR) functions. The recreated normalized profiles for the pinhole and ring detector are shown with the MCR calculated with Equation 4.1. This example shows a microsphere located at a depth of 20 μm and uses the constant of c = 0.3.

The response profile of the modified confocal detector (MCR) is generated by subtracting the ring profile weighted by a factor c from the pinhole profile as in Equation 4.1: $MCR(z) = P(z) - cR(z)$. Figure 4.9 shows a sample set of curves for a 20 μm-deep microsphere using a constant of $c = 0.3$. These values were arbitrarily chosen for the purposes of display.

The MCR is effectively an unsharp masking filter in optical conjugate space because the ring signal is blurred compared to the pinhole image. What makes the MCR different from simply taking a confocal image and applying a digital filter on the pixel-map is that the MCR makes an independent off-axis measurement of scattered light. The off-axis measurement provides information about out-of-focus fluorescence and background fluorescence that is not contained in the pinhole measurement. This information can't be recreated from a series of confocal pinhole measurements alone.

To determine the resolution limit from the MCR, two identical MCR's (for a particular depth z and constant c) were separated in z such that the normalized sum curve dipped to $8/\pi^2$ between its two peaks. A sample sum of two identical MCR's separated by the resolution limit is shown in Figure 4.11.

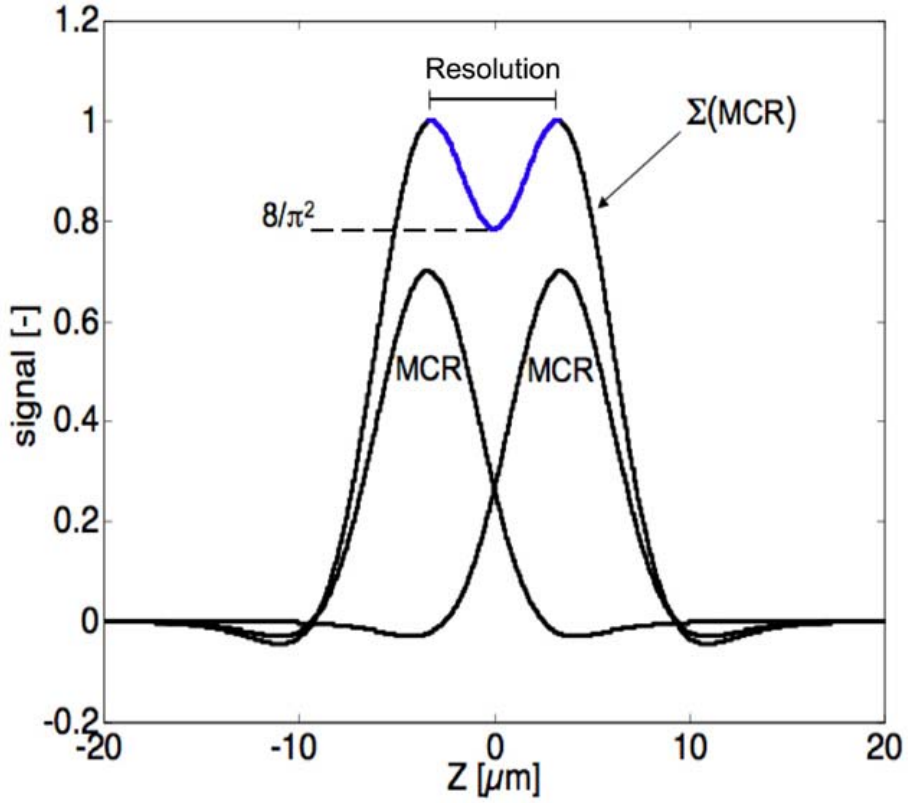

Figure 4.11 A sample pair of identical MCR's are separated by the minimum distance to be "resolvable" in the Rayleigh resolution limit. This criterion is met when the sum of the MCR pair dips to $8/\pi^2$ in the center.

Figure 4.11 shows the resolution limit of a MCR for a particular depth (z = 20 μm) and constant (c = 0.3). The separation between the two MCR's is chosen such that the sum curve has two peaks resolvable by the Rayleigh resolution criteria. This separation is the resolution and is dependant on the values chosen for z and c. These choices were varied over a range of zero to 140 μm for z and 0 to 0.7 for c to specify their impact on the resolution. The range of z was chosen to encompass the experimental data (i.e. values for z > 140 μm would not be supported by experimental data) and the range of c was chosen such that the center of the MCR remained greater than 0.3.

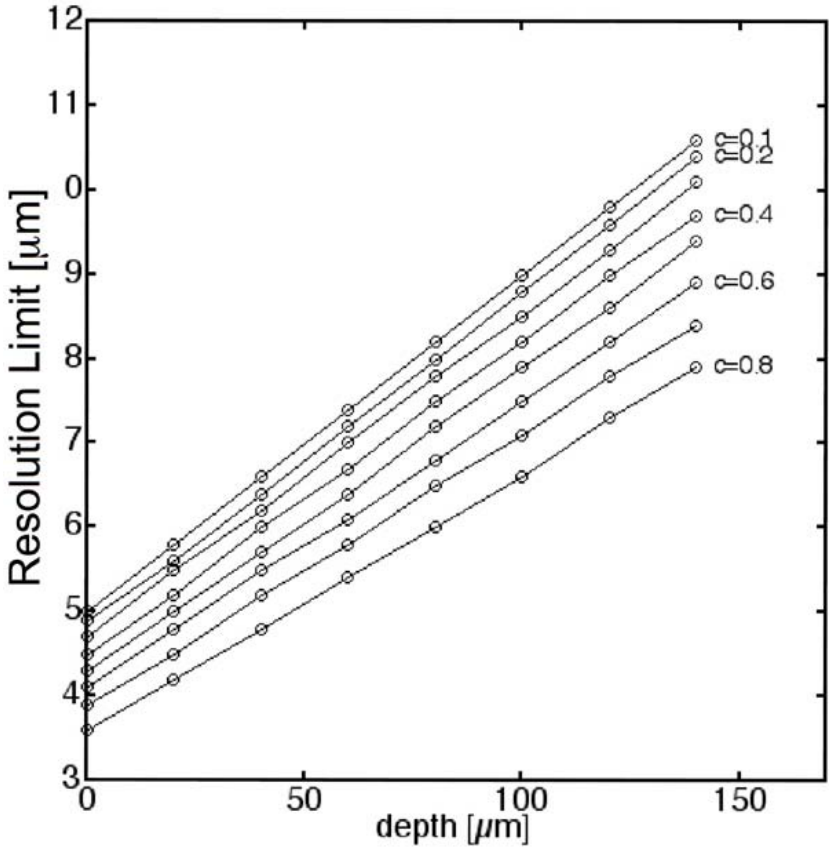

Figure 4.12 The minimum separation between resolvable sources (Resolution Limit [μm]) is shown as a function of depth and c. c is the fractional weight of the ring signal (Equation 4), and depth is beneath the surface of the semi-infinite scattering media. The c = 0 data is for the pinhole alone. Curves for c > 0.7 were omitted because as c approaches unity, the central value for the MCR approaches zero (since the pinhole and ring components are normalized: 1 – 1 = 0).

Figure 4.12 shows that the resolution limit increases with depth, the same way that resolution increased with depth in Figure 4.4 for the Monte Carlo point spread function. The slopes of linear regression fits are 0.183 and 0.039 [μm/μm] for Figures 4.4 and 4.9 respectively (the resolution degradation rate). The variation is because the scattering properties were different. In the Monte Carlo simulation, scattering properties mimicked scattering in murine dermis (Chapter 9) $\mu_s = 2500$ [cm^{-1}], g = 0.98 [-]. In the scattering gel sample, $\mu_s = 95$ [cm^{-1}], g = 0.13 [-]. Although the reduced scattering

coefficients: μ_s' = (dermis, phantom) = $\mu_s(1\text{-}g)$ = (83, 50) [cm^{-1}] were similar, the confocal signal is dominated by the true scattering coefficient μ_s which is 26 fold greater for the Monte Carlo simulation than for the microsphere phantom. There exists an unknown proportionality between the true scattering coefficient μ_s and the resolution degradation rate.

In summary, the pinhole and ring responses or axial profiles can be found as a function of depth by substituting the characteristic 1/e widths from equation 2 into equation 3. Once they are known, a MCR can be found using eq. 4.4 and picking a value for the constant c. Figure 8 shows the results when the depth and c are varied over practical ranges.

Chapter 5: Monte Carlo

5.A Introduction

Propagation of light in scattering media is a complex problem that can be modeled using statistical methods such as Monte Carlo simulations. A Monte Carlo simulation was developed (modifying C code called mc321.c from [53], and described in [54]) to mimic the focus of a Gaussian-profile laser beam in turbid tissue and subsequent confocal detection of reflected light and fluorescent emission. The simulation propagates photon packets by mapping random numbers into photon step sizes and angles of scatter. At each scattering event, a fraction of the photon packet's weight is dropped into a local voxel due to absorption. The result is a three-dimensional map of deposited weight, which can be converted into fluence rate using the absorption coefficient. Knowing the fluence rate of forward excitation and the absorption and quantum yield of the fluorophore, fluorescence can be generated and propagated from each position within the sample to confocal detection.

5.B Photon Launch

5.B.1 Gaussian Beam at the Tissue Surface

The algorithm included photon launch at the tissue surface with initial position and trajectory characteristic of the focused Gaussian beam. This algorithm was first developed by Gareau *et. al.*[55] The description here was adapted from a web tutorial[56]. The relationship between a random number (ξ_i) evenly distributed between 0 and 1 and a radius of launch (r_i) following a Gaussian probability density function with 1/e intensity radius (r_e) is determined:

$$E(r) = \frac{1}{\pi r_e^{\,2}} e^{-\left(\frac{r^2}{r_e^{\,2}}\right)} \tag{5.1}$$

$$p(r) = E(r)2\pi r = \frac{2r}{r_e^{\,2}} e^{-\left(\frac{r^2}{r_e^{\,2}}\right)} \tag{5.2}$$

Equation 5.1 characterizes a Gaussian beam. The probability density function in equation 5.2 gives the probability of a photon launch from an infinitesimal radial interval at radius r. Note $\int_0^\infty p(r)dr = 1$. The distribution function for sampling each radius of launch r_i is then:

$$F(r_i) = \int_0^{r_i} p(r)dr = 1 - e^{-\left(\frac{r_i^{\,2}}{r_e^{\,2}}\right)} \tag{5.3}$$

Noting that $F(\xi_i) = \int_0^{\xi_i} p(\xi)d\xi = \xi_i$ where ξ_i is the random number, and setting $F(\xi_i)$ equal to $F(r_i)$:

$$r_i = r_e\sqrt{-\ln(\xi_i)} \tag{5.4}$$

For photon launch at a depth (Z_f) within tissue, r_e was calculated with the numerical aperture of the objective lens used (NA).

$$r_e = Z_f \tan\left(\sin^{-1}(NA)\right) \tag{5.5}$$

5.B.2 Focusing to an Airy Distribution

At launch from the tissue surface, photons were given an initial trajectory pointed to a radial position in the focal plane such that the focal intensity distribution for the non-scattering case is the Airy function produced by the circular aperture of the objective

lens. The light intensity $J_1(v)$ in the focal plane is a first-order Bessel function of the first kind is a function of optical coordinate v (Equation 5.6) where v is an optical coordinate related to the physical radius r (Equation 5.7)[27, 53].

$$I(v) = \left[2\frac{J_1(v)}{v} \right]^2 \tag{5.6}$$

The relationship between the optical coordinate v (which is unitless) and the real physical coordinate r, which has the unit of length is given in Equation 5.7 where NA is the numerical aperture of the objective lens and λ is the wavelength of light (488 nm in this work).

$$v = \left[\frac{2\pi}{\lambda} \right] rNA \tag{5.7}$$

$$I(r) = \left[\lambda \frac{J_1\left(\frac{\pi r NA}{\lambda} \right)}{\pi r NA} \right]^2 \tag{5.8}$$

The probability density function is normalized such that $\sum p_i dr_i = 1$.

$$p(r) = \frac{I[2\pi r]}{\sum I[2\pi r\ ]dr} \tag{5.9}$$

The cumulative probability approaches 1 for large radii.

$$F(r_i) = \sum_0^{r_i} p(r)dr \tag{5.10}$$

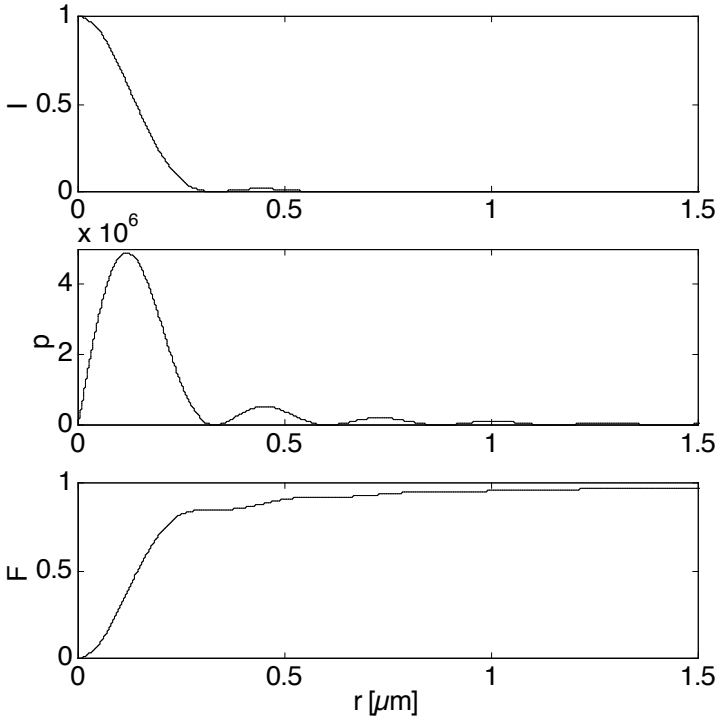

Figure 5.1 The intensity I (5.6) is shown as a function of radius r. p is the probability density function of photons in the focal plane and F is the cumulative probability.

Producing an Airy distribution requires a method for producing pseudo-random numbers that works for any cumulative probability density function (CPDF). The algorithm involves re-sampling the CPDF such that random indices can be drawn to yield appropriate radial coordinates. A large population of such coordinates will then follow the correct probability density function. The algorithm simply forms an input/output look-up table, which consists of the re-sampled CPDF. A thousand sequential input decimals equally spaced between 0 and 1 were created as the indices for the look-up table. These values correspond to the range on the y-axis of Figure 5.1 (bottom). A for-loop steped through the input decimals. For each input decimal, a nested for-loop stepped through the CPDF finding the corresponding radial coordinate. The radial coordinate was recorded as the output for the input decimal. Figure 5.1 (bottom) shows the CPDF, F(r), as a function of radius. The method described in this paragraph simply

enabled determination of the appropriate radial coordinate r = lookup[i] for an integer index i between 1 and 1000 selected by the random number generator. The output vector generated was randomly sampled as a radius such that many radii yield a distribution that follows the airy pattern of equation 5.6.

In summary, the initial position and angle of photons launched into the Monte Carlo simulation were chosen based on Equation 5.4 and a lookup table. Equation 5.4 maps a random number to a radial coordinate of launch on the tissue surface to mimic a Gaussian power distribution. The lookup table (which can be found in the Monte Carlo code rcmc.c in the Appendix) mapped a random number into a radial coordinate in the focal plane to direct the launched photon toward such that light falling in the focal plane follows the Airy distribution. By choosing this destination coordinate, the angle of launch is specified.

As a check, focused light was simulated in an absorbing-only medium. The fluence rate distribution was Gaussian at the tissue surface and followed the Airy distribution at the focal plane.

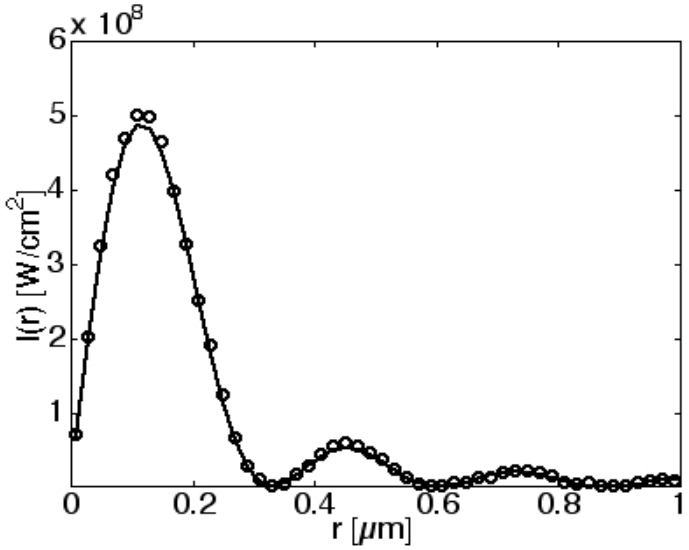

Figure 5.2 The Monte Carlo output I [W/cm^2]in the focal plane (circles) is shown to match the intended Airy power distribution p(r) in Figure 5.1 (solid line).

The axial pattern of a focused Gaussian beam is given by Rajadhyaksha *et al*[27]:

$$I(u) = \left[\frac{\sin(u/4)}{u/4} \right] \tag{5.11}$$

where u is the optical coordinate:

$$u = (8\pi/\lambda) z \sin^2(\alpha/2) \tag{5.12}$$

In Equation 5.12, α is the angle such that $\sin(\alpha)$ equals the numerical aperture of the lens used. The Monte Carlo simulation yielded the exact radial distribution in the focal plane and approximated the correct axial behavior.

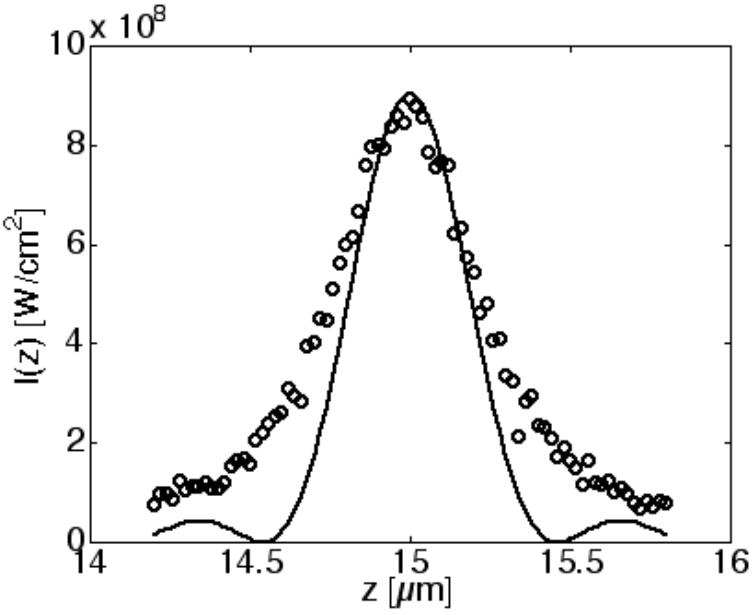

Figure 5.3 The on-axis excitation Monte Carlo result for a non-scattering medium (circles) is shown with the theoretical value from equation 5.11 (line). Note that the theoretical $\sin^2$ behavior can't be mimicked because it has zeros between the central peak and the side lobes. This illustrates a limitation of Monte Carlo, which didn't propagate

photon packets near the axis through any particular z-layer without depositing some energy.

Figure 5.4 shows a cross section of the Monte Carlo output. Since the simulation was cylindrically symmetric only half of the plane bisecting the conic focus is shown.

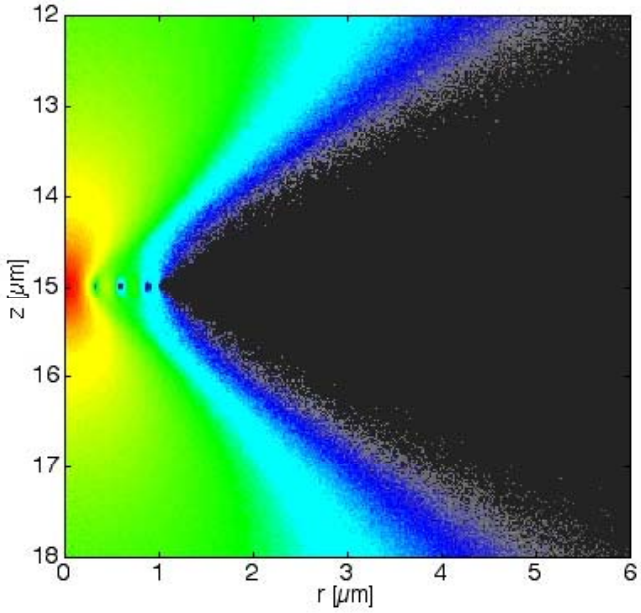

Figure 5.4 The log of the fluence rate is mapped nearby the focus. The focal spot was simulated by launching in an absorbing-only medium. The focal plane is located at z = 15 μm and the optical axis is located at r = 0 μm. This map shows the series of zeros in the radial Airy function at the focal plane .

Figure 5.4 shows the distribution of focused light for an absorbing-only Monte Carlo simulation. The light distribution on the surface of the tissue was chosen to be Gaussian. The progression from a Gaussian radial profile at the tissue surface to an Airy distribution at the focus is not strictly correct because the Fourier transform of a Gaussian is Gaussian, not the Airy function[57]. In real microscopes, the radial laser intensity profile is usually Gaussian in the pupil plane of the objective lens. Fourier optics dictates that the spatial distribution of light in the focal plane is the Fourier transform of the light

distribution of the distribution in the pupil plane. Therefore, the Gaussian distribution at the pupil plane should be Gaussian at the tissue surface and Gaussian at the focal plane. One factor to consider however is that laser beams are typically expanded in diameter to larger than the entrance aperture of the objective so the transmitted beam is a truncated Gaussian. Approximating the truncated Gaussian by a flat field in the pupil plane yields the Airy pattern in the focal plane[57].

5.C Photon Propagation

5.C.1 Propagation in Media

After being launched at the tissue surface, photons were propagated on with the "hop, drop and spin" routine[54] through the simulated phantom. In the "hop" subroutine photons propagated a distance between simulated scattering events, which was determined by using a random number to draw from a probability distribution defined by the scattering and absorption coefficients of the phantom. In the "drop" subroutine, at the location of each scattering event, a fraction of the photon weight was deposited into the local voxel C(ir,iz) due to absorption. In the "spin" subroutine, the photon's trajectory was altered due to scattering by sampling the Henyey-Greenstein scattering phase function[58] with another random number to determine the angle of scatter. The propagation routine thus dictated optical propagation by sampling probability distributions with random numbers. The output of the simulation was the matrix of accumulated weight C(ir,iz), deposited as a function of position within the phantom and had units of Watts per Watt incident.

Each photon was given initial weight of unity to represent a watt of incident light such that normalizing output data by the total number of photons N would yield units of Watts absorbed per Watt incident. Due to the cylindrical symmetry of a focused beam in a homogenous medium, results are expressed as a function of their axial and radial position (ir,iz). The fluence rate distribution I(ir,iz) [W/cm^2] was calculated from the accumulated weight concentration C(ir,iz).

$$I(ir,iz) = \frac{C(ir,iz)}{V(ir)\mu_a N} \tag{5.13}$$

where the cylindrical shell volume at radial position r(ir) is V(ir) = (ir-0.5)2πdr^{2}dz and N is the number of photons launched into the simulated phantom. μ_{af} was the absorption coefficient of the tissue phantom. The value used for the voxel size used to produce Figure 5.4 was dr = dz = 10 nm in order to mimic the airy pattern in the focal plane and validate the pseudorandom launch algorithm.

5.C.2 Fluorescence

A second Monte Carlo simulation was necessary for simulating fluorescence. In the second step, fluorescence light was launched isotropically from each voxel with weight W determined by the deposition of excitation photon weight C (ir,iz).

$$W(ir,iz) = \frac{C(ir,iz)}{\mu_a N}\mu_{af}\Phi(ir,iz) \tag{5.14}$$

where μ_a was the absorption coefficient of the background tissue, μ_{af} was the added absorption due to the presence of the fluorophore and Φ (ir,iz) was the fluorescent quantum yield.

Once fluorescent photons were launched from within the phantom, they were propagated until they became absorbed or escaped the tissue surface. Figure 5.5 shows a block diagram of the simulation. The fluorescence simulation performed the sequence outlined in the block diagram for each voxel that had a nonzero quantum yield of fluorescence Φ.

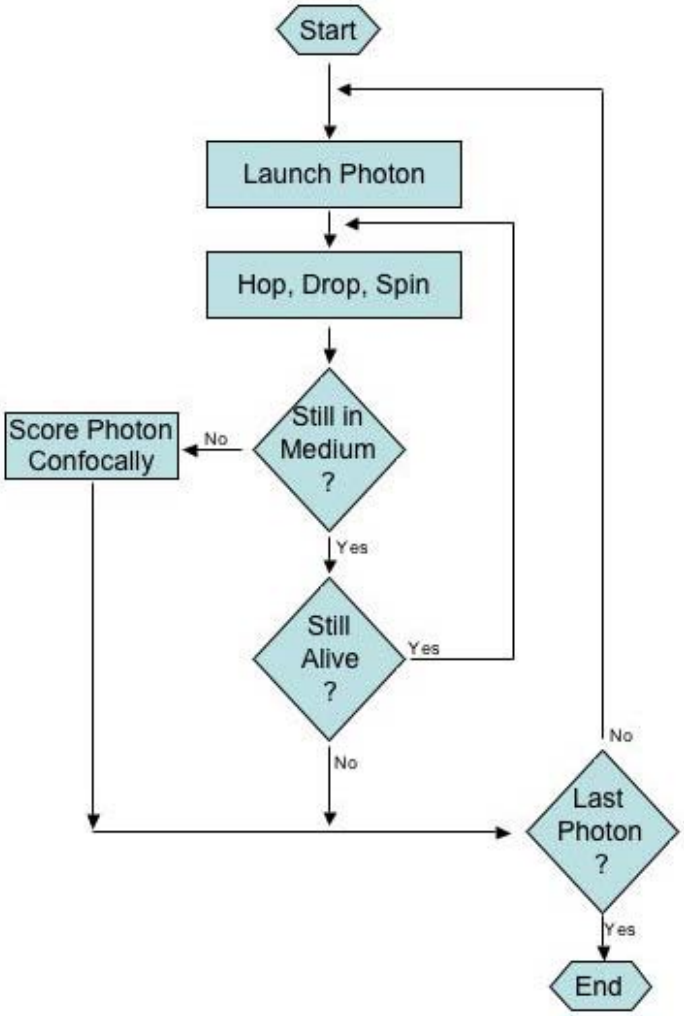

Figure 5.5 Flow chart for the Monte Carlo simulation. The launch routine and the confocal scoring of tissue-escaping photons are new. All other parts are standard of Monte Carlo programs[54].

Figure 5.5 shows the flow of the fluorescence Monte carlo simulation. When photons escaped the surface of the phantom they were scored in radial bins that specified their position in the conjugate focal plane with respect to the confocal aperture. This method is described in the following section.

5.C.3 Confocal Detection

At the beginning of each simulated confocal measurement, a radial D(ir) array was initialized to collect tissue-escaping photons that reached the detector. Tissue-escaping photons were scored in radial bins indicative of where they appeared to come from in the focal plane $p_3 = [X_3\ Y_3\ Z_3]$ where Z_3 is the depth of focus. The radial array D(ir) of such back-projected photons is equivalent to the radial distribution of escaping photons reaching the detector plane where the pinhole of the confocal system is located because the pinhole and sample focal planes are optically conjugate. For each tissue escaping event, the trajectory of escape was back-projected to the focal plane in the tissue at depth z_f as shown in Figure 5.6. After the "hop" step, if the new position $p_1 = [X_1\ Y_1\ Z_1]$ was found to be outside the tissue surface, the previous position was noted $p_2 = [X_2\ Y_2\ Z_2]$ the photon was terminated and its weight deposited in the appropriate radial array bin D(ir): D(ir) = D(ir) + W. Only photons that escaped within a radius specified by the radius of the aperture of the objective lens were back-projected for inclusion in the detector response D(r). Refraction at the tissue surface was not considered because it was assumed that the modeled tissue (epidermis n = 1.34) had the same refractive index to the immersion medium (water n = 1.33).

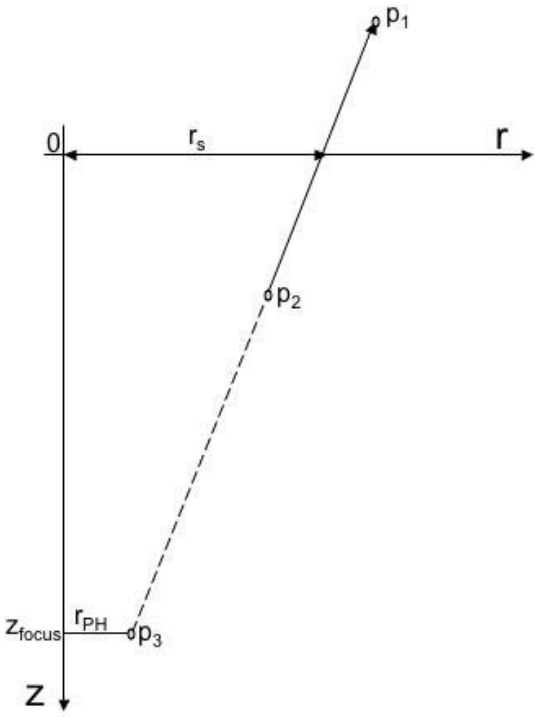

Figure 5.6 Diagram of tissue escaping photon. The tissue surface is located at z = 0. The focal plane is located at a depth z = z_{focus}.

Figure 5.6 depicts a photon escaping the surface of the sample. The last point of scatter within the tissue and the point of destination for the escaping photon (points p_2 and p_1 in Figure 5.6, respectively) are used to determine the point of apparent origin in the focal plane (p_3 in Figure 5.6). Tissue-escaping photons can only be detected confocally if they escape within the cone of acceptance defined by the numerical aperture of the objective lens. At the tissue surface, the radius of this cone is the r_e (from equation 5.5). The position on the tissue surface (X_s, Y_s, Z_s=0) where the photon escapes is calculated, and the (X_s,Y_s) converted to a radial position (r_s):

$$\begin{aligned} X_s &= X_1 - Z_1((X_1 - X_2)/(Z_1 - Z_2)) \\ Y_s &= Y_1 - Z_1((Y_1 - Y_2)/(Z_1 - Z_2)) \\ r_s &= \sqrt{X_s^{\,2} + Y_s^{\,2}} \end{aligned} \qquad (5.15)$$

The condition for photon escape within the cone of acceptance of the numerical aperture of the objective lens is then $r_s < r_e$ (r_e from equation 5.5). In the simulation, if the condition $r_s < r_e$ was true, then the interpolated position (X_3,Y_3,Z_3=z_{focus}) of apparent origin at the focal plane was calculated, and a radial position (r_{PH}) calculated:

$$\begin{aligned} X_3 &= X_1 - (Z_1 - Z_3)((X_1 - X_2)/(Z_1 - Z_2)) \\ Y_3 &= Y_1 - (Z_1 - Z_3)((Y_1 - Y_2)/(Z_1 - Z_2)) \\ r_{PH} &= \sqrt{X_3^{\,2} + Y_3^{\,2}} \end{aligned} \tag{5.16}$$

This strategy was used because confocal microscopy constructs a conjugate pinhole plane, which is an image of the focal plane with a magnification determined by the lenses in the microscope. This method is therefore equivalent to propagating photons back to the pinhole plane. The bins of acquisition $r_{PH}[ir]$ correspond to rings of collection of area $2\pi r_{PH}[ir]\Delta r$ where Δr is the width of the bins. To find the signal passing through a particular confocal pinhole size, one sums the collected photon weight in the appropriate bin $r_{PH}[ir]$.

Reflectance confocal microscopy was simulated with a simpler version of the fluorescence routine. The second Monte Carlo simulation where fluorescent photons were propagated out of the tissue was omitted. The confocal criteria (described by equation 8) was simply applied to the excitation photon packets when they escaped the tissue boundary. The reflectance mode confocal simulation simply launches photons and propagates them until they escape the phantom. Photons escaping the surface of the phantom are registered confocally reguardless of whether they were singly backscattered from the focus or multiply scattered in the sample. The simulation thereby measures the sum of these two signals. The first is the transport to the focus * fraction scattered at focus * fraction backscattered at collection lens * transport back to surface. The second is multiply scattered photons which satisfy the confocal criteria (i.e. propagate to the pinhole). The first type of optical transport can be modeled analytically but the second type requires the Monte Carlo model.

5.D Discussion

The Monte Carlo model developed in this chapter can be used to simulate a variety of light-transport scenarios. Three such scenarios include the forward focus of light into a tissue phantom (Chapter 11), the collection of the reflected confocal signal (Chapter 6) and determination of the fluorescent point-spread function (Chapter 4). The simulations that yielded the results in Chapters 6 and 4 are given in the appendix as rcmc.c and fcmc.c respectively. The simulation that yielded the focal fluence rate addressed in Chapter 11 is a simpler version of the code that only output the fluence rate map of the forward focus into tissue and is not given but can be recreated by saving the matrix Ccyl in either of the two simulations in the appendix.

Verification of the simulation included running a non-scattering phantom and reproducing the Airy pattern in the focal plane (Figure 5.2). In the axial direction, the verification failed to precisely mimic the theoretically predicted pattern of focused light (Figure 5.3). Photons that escaped the phantom were accounted for in overflow bins such that the total photon energy could be summed after the simulation. This summation verified that energy was conserved. The Monte Carlo simulation served as a useful tool to predict the focusing behavior of confocal microscopy as well as both the reflected and fluorescent confocal signal.

Chapter 6: Reflectance Mode Confocal Microscopy of Multiple Tissue Types

6.A Abstract

Reflectance mode confocal scanning laser microscopy (RCSLM) produced 3-dimensional images of 5 mouse tissue types. Analysis of the images yielded the surface reflectance (ρ [-]) and the subsurface attenuation coefficient (μ [cm^{-1}]). A pair of simple functions, $\rho(\mu_s,g,NA)$ and $\mu(\mu_s,g)$, related the experimental parameters of ρ and μ to the tissue optical properties, the scattering coefficient (μ_s [cm^{-1}]) and the anisotropy of scattering (g [dimensionless]), and to the numerical aperture (NA) of the collection lens. Experimental measurements on gels with polystyrene microspheres were used test the functions and provide calibration. A Monte Carlo simulation provided a numerical experiment to test the functions. Experimental measurements on 5 types of mouse tissues were conducted and the functions used to specify the tissue optical properties of these tissues.

6.B Introduction

Optical sectioning in reflectance confocal scanning laser microscopy (rCSLM) provides preferential sensitivity to light singly back-scattered from the focus. The optical sectioning implemented by the pinhole aperture and the forward focusing of a point source of light enables imaging of tissue at the focal plane with minimal interference from tissue at other locations.

Besides the image confounding effects of diffuse light (discussed in Chapter 4 experimentally and 5 theoretically), the depth-limiting factor for imaging is signal loss due to optical attenuation. The exponential decay versus depth of the confocal signal S(z) [W] can be measured, simulated and used to specify the scattering properties of the tissue, μ_s [cm^{-1}] and g [unitless]. As focal depth z [μm] increases within a turbid sample, the confocal signal decays according to a coefficient (μ [cm^{-1}]) from the level of reflectance at the tissue surface (ρ [-]). Equation 6.1 gives the behavior of the confocal signal s [-] as a function of depth z [μm]. The confocal signal s [-] is unitless since it is the fraction of light delivered to the tissue that reflects from the focus and gets detected.

$$S(z) = \rho e^{-\mu z} \tag{6.1}$$

Both the reflectance at the tissue surface (ρ) and the subsurface signal attenuation rate (μ) are directly influenced by optical scattering in the sample. Equation 6.1 simplifies the signal by separation of the variables into the factor ρ that depends on the scatterer and optics of collection, and the factor μ that describes the attenuation of photons during propagation due to multiple scattering. These two variables, ρ and μ, are briefly introduced in the following paragraphs, and are fully discussed in this chapter.

The factor ρ depends on the two factors: (1) the fraction of light reaching the focus that is scattered by the tissue within the focus, and (2) the fraction of scattered light that backscatters into the collection lens, ignoring any attenuation due to multiple scattering. The fraction scattered within the focus is proportional to the scattering coefficient μ_s. The fraction of this scattered light backscattered into the lens depends on the numerical aperture (NA) of the lens and the scattering function p(θ) of the tissue scatterer, where θ = 180° refers to direct backscatter. In the absence of multiple scattering, only photons backscattered within |θ| < arcsin(NA) will be collected by the lens. In this chapter, p(θ) will be approximated by the Henyey-Greenstein scattering function, for which p(θ) is a function of the anisotropy g = <cosθ>. Hence, the fraction of

light scattered within the focus which is directed toward the collection lens is a function of g. Therefore, ρ is a function of μ_s and g and the NA of the collection lens.

The factor μ depends on two factors: (1) the number of scattering events per unit pathlenght which is specified by the scattering coefficient μ_s, and (2) the ability of multiply scattered photons to still reach the focus (or to reach the pinhole when escaping) which can occur when the scattering is very forward directed. In other words, the ability to reach the focus (or pinhole) depends on $p(\theta)$ and, using the Henyey-Greenstein scattering function, depends on g. While the depth of focus is described by z, the actual photon pathlength depends on the NA of the lens that delivers photons at an angle toward the focus. Hence, μ is a function of μ_s, g and NA.

This chapter investigates the functions $\rho(\mu_s,g,NA)$ and $\mu(\mu_s,g)$. Experimental measurements on gels with polystyrene microspheres was used to test the functions. Monte Carlo simulations provided a numerical experiment to test the functions. Experimental measurements on 5 types of mouse tissues were acquired and analyzed using the functions to yield the μ_s and g of the tissues.

6.C Materials and Methods

6.C.1 Gel with Polystyrene Microspheres

For calibration, a 2% agarose gel was prepared with 0.1-μm-dia. polystyrene microspheres added at concentration of 2.5% volume fraction (f_v = 0.025) to yield a light-scattering phantom. The gel was formed between a glass coverslip and a glass slide. The objective lens was coupled to the front glass cover slip by water. The Mie calculator provided by Scott Prahl (http://omlc.ogi.edu/software/mie/index.html) was used to calculate an expected scattering coefficient of 75 cm^{-1} and anisotropy of 0.112 for this gel at 488 nm wavelength (n_{gel} = 1.35, n_{sphere} = 1.57, sphere density = $f_v/(4\pi 0.05^3/3)$ = 47.7 μm^{-3}).

6.C.2 Monte Carlo Simulation as Numerical Experiment

A numerical experiment was performed using the Monte Carlo simulation discussed in Chapter 5 and found in the appendix, rcmc.c. The simulation produced measurements of reflected signal S(z) which were analyzed to yield ρ and μ values for a range of μ_s and g. values. For each combination of various scattering coefficient (μ_s = [500:50:750] cm^{-1}) and scattering anisotropy (g = [0.70:0.05:0.95]) values, a set of confocal measurements at various focal depths (Z = [3:3:24] μm) was simulated to yield the reflected confocal signal in units of Watts collected per Watt incident, S(z).

6.C.3 Mouse Tissue Studies

Experimental measurements on murine tissues were conducted. *S(z)* was extracted from 3-dimensional images of 5 types of tissues: brain white matter, brain gray matter, skin, muscle and liver. In sample preparation for imaging, mice were sacrificed and tissue samples were immediately excised starting with the brain. Images consisted of 3-dimensional matrices of size [Nx,Ny,Nz] = [512, 512, Nz], Nz(512^2) total voxels. Image processing used MATLAB. The inter-voxel spacing was [dx,dy,dz] = [0.5μm, 0.5μm, dz]. dz was chosen to be 1 μm in brain tissues, 2 μm in skin and liver and 7 μm in muscle. Nz was determined during imaging by the maximum number of steps before the background signal due to multiple scattering began to dominate the signal. This depth was typically as small as 20 μm for brain tissue and as large as 200 μm in muscle.

The results of two mouse studies are presented. Three microscope gain settings were used to image the various tissue types, which had variable reflectivity. Each gain setting was calibrated before each experiment. The first study used three C57/B6 mice and used a water/glass calibration. The second study used 8 albino mice (Harlan Sprague Dawley, ND4) and used a glass/oil interface calibration. The water/glass interface had a

reflectance of 0.0044 (see Equation 3.1) and for the oil/glass interface, the reflectance was 0.000217 (n_{oil} = 1.46). In the water/glass interface normalization, the laser was attenuated with an optical density filter and the results corrected for the filter attenuation. This step was necessary because the high reflectivity of the water/glass interface. Since the reflectivity of tissues is closer to the oil/glass reflectance, the oil-glass standard proved to be the better standard and is now used routinely. The data for the two studies included each tissue type with the exception of brain white matter, which was not measured in mice 5-8 in the second study.

6.D Analysis Grid

A simple analytic expression was developed to approximate the behavior of the confocal signal, S(z). The expression is:

$$\begin{aligned} \rho &= \mu_s L_f(\lambda, NA) b(g, NA) \\ \mu &= \mu_s a(g) 2G(NA) \\ Signal \;\; S(z) &= Measurement / P_O = \rho e^{-\mu z} \end{aligned} \tag{6.2}$$

where the factors,P_o, μ_s, g, NA, L_f, a(g), b(g,NA) and G(NA) are explained below. The fraction $\mu_s L_f$ is the fraction of light reaching the focus that is scattered within the focus. The factor b(g,NA) is the fraction of this scattered light that is backscattered into the collection cone of the lens. The factor a(g) mitigates the attenuation by scattering and hence allows some multiply scattered photons to reach the focus (or escape to the pinhole). The factor 2 accounts for the photon path into and out of the tissue. Hence, Eq. 6.2 summarizes the simple functions $\rho(\mu_s,g,NA)$ and $\mu(\mu_s,g,NA)$ used for analysis.

P_o = total power delivered by confocal microscope [W]. The experiments also measured the reflectivity from water/glass and oil/glass interfaces to allow calibration of the measurement of reflected power (outlined in Chapter 3.A.2). The normalization of measurements by the measurement from the water/glass or oil/glass interface canceled P_o. Hence P_o is not included in the analysis

μ_s = scattering coefficient [cm^{-1}], proportional to the scattering cross-section (σ_s cm^2) presented by scatterers in the tissue times the density of scatterers (ρ_s $1/cm^3$), $\mu_s = \sigma_s\rho_s$.

g = anisotropy of scattering [unitless], which equals the mean projection of the trajectory of scattered light onto the original axis of propagtion prior to scattering, in other words g = <cosθ> where θ is the angle of deflection due to scatter.

NA = the numerical aperture of the lens, equal to the ratio of lens radius to focal length in air, such that the half-angle of collection by the lens equals arcsin(NA/n), where n is the refractive index of the medium contacting the lens (n ≈ 1.33 for water).

$L_f(\lambda/NA) = 1.4\lambda/NA^2$, axial length of the focal volume in the tissue within which scattering occurs that can be collected by the pinhole.

b(g,NA) describes the fraction of light undergoing scattering that back-scatters within the cone of collection of the lens system of the confocal microscope to yield observed reflectance. The behavior of b(g,NA) was determined by integrating the Henyey-Greenstein scattering function[58] over the solid angle of collection of the lens aperture (θ = 0-42°, where the half angle of collection is 42° for a 0.90-NA water-immersion lens). If g is close to 0, the value of b(g,NA) is maximum due to strong backscatter. As g drops and light becomes forward-directed, the value of b drops rapidly.

$$b(g,NA) = \int_0^{\theta_{NA}} I(\theta) 2\pi \sin(\theta) d\theta \tag{6.3}$$

a(g) = a factor that diminishes the effectiveness of the scattering coefficient. For isotropic scattering (g = 0), a(g) = 1. As scattering becomes forward-directed (g < 0), a(g) drops toward zero. The function a(g) was determined by Monte Carlo simulations (see chapter 11) of the transport (T) of light to the focus as a function of g and the depth of

focus (z), $T = \exp(-a(g)\mu_s z_f G)$. The factor G is explained in next paragraph.

G(NA) = the geometrical factor that describes the increased average photon path-length from the surface to the focus since the light is delivered as a focused Gaussian beam from a lens with a large NA rather than as a narrow collimated beam orthogonal to the surface. The factor G accounts for the fact that the photons do not travel in and out of the tissue normal to the surface. The value of G(NA) varies with the numerical aperture of the lens used in the experiment. In our case for NA = 0.9, the value of G was 1.37. G(NA) was found numerically as the expectation value of the round trip photon pathlength in the tissue of collected photons normalized by twice the depth of the focal volume ($2z_{focus}$) within the sample. Equation 6.4 yielded G(NA):

$$G(NA) = \frac{\sum_i \sum_j \frac{L_i + L_j}{2z_{focus}} P_{i,j} \sin\theta_i \sin\theta_j}{\sum_i \sum_j P_{i,j} \sin\theta_i \sin\theta_j} \tag{6.4}$$

Figure 6.1 shows the objective lens focusing into tissue. Refraction at the tissue surface is not considered since the immersion medium (saline, n = 1.34) is sufficiently close to tissue that the refractive effects are small.

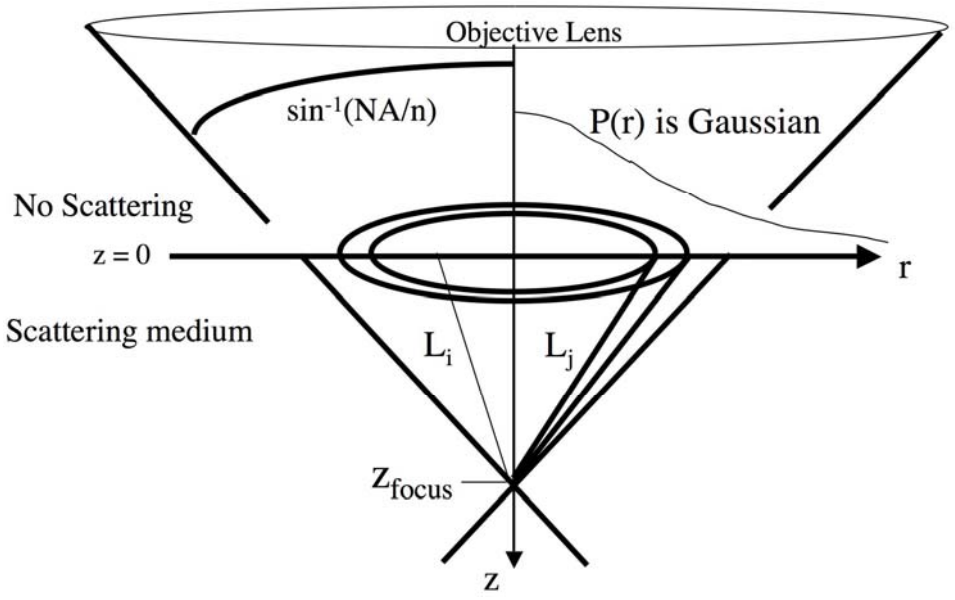

Figure 6.1 Schematic diagram of the sum in equation 6.1

Figure 6.1 illustrates the double sum in equation 6.4. Since the problem is rotationally symmetric about the z axis, elements of the calculation are shown on both sides of the axis. The path-length as photons penetrate to the focus (L_i) and the path-length as photons escape from the focus (L_j) combine to yield the total photon path-length ($L_i + L_j$). Equation 5 integrates the power P_{ij} over all i^{th} angles of incidence and all j^{th} angles of escape to yield the expectation value for $(L_i + L_j)/(2z_{focus})$.

6.E Results

6.E.1 Analysis Grid Using Eq. 6.2

The behavior the functions $\rho(\mu_s,g,NA)$ and $\mu(\mu_s,g,NA)$ are summarized as a grid of μ_s and g values, connected by iso-μ_s and iso-g contours, drawn within a graph of the experimental parameters μ versus ρ, as shown in Fig. 6.2. This plot is referred to in this chapter as the analysis grid. Fig. 6.2(left) shows the grid ignoring the factor a(g), i.e., a = 1 regardless of g. Fig. 6.2(right) shows the grid including the effect of a(g), and is the grid used to analyze data.

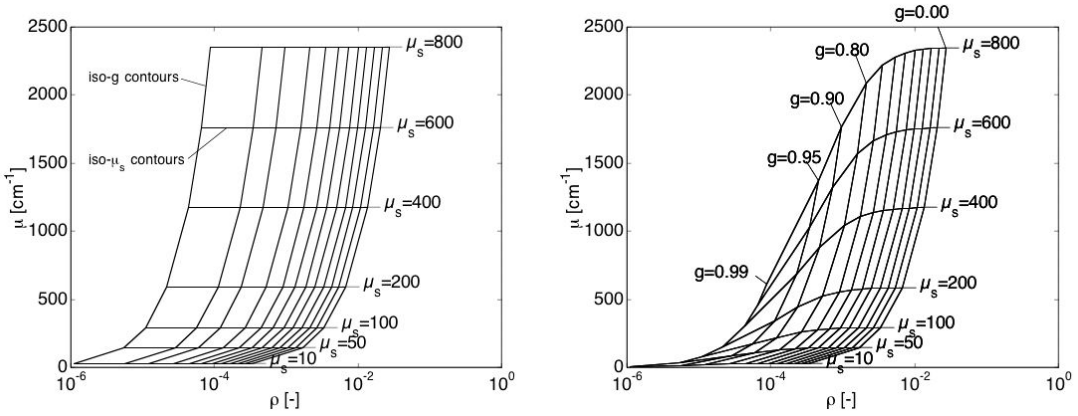

Figure 6.2 The analysis grid. (Left) Grid where a(g) is ignored, i.e., a = 1 regardless of g. (Right) The analysis grid showing the effect of a(g). This is the grid used for data analysis.

6.E.2 Analysis Grid Using Monta Carlo Simulation

Figure 6.3 shows the numerical data generated by the Monte Carlo simulation. The exponential fits using Eq. 6.1 are shown as solid line curves. Figure 6.4 compares the analysis grid generated by the Monte Carlo simulation with the analysis grid of Fig. 6.1b, specified by Eq. 6.2. The agreement is not perfect, but the general shape and trends of the Monte Carlo grid match the analysis grid. The Monte Carlo grid presented too low μ values and a little lower ρ values compared to the analysis grid of Eq 6.2. The simulation of the grid took 3 months to complete, because a very small-sized voxel grid was required and many photons needed to fill each voxel with good statistics. Given this huge computational cost, a decision was collectively made to not pursue the trouble shooting of the Monte Carlo simulation, but to focus instead on the experimental calibration of the analysis grid using polystyrene microspheres.

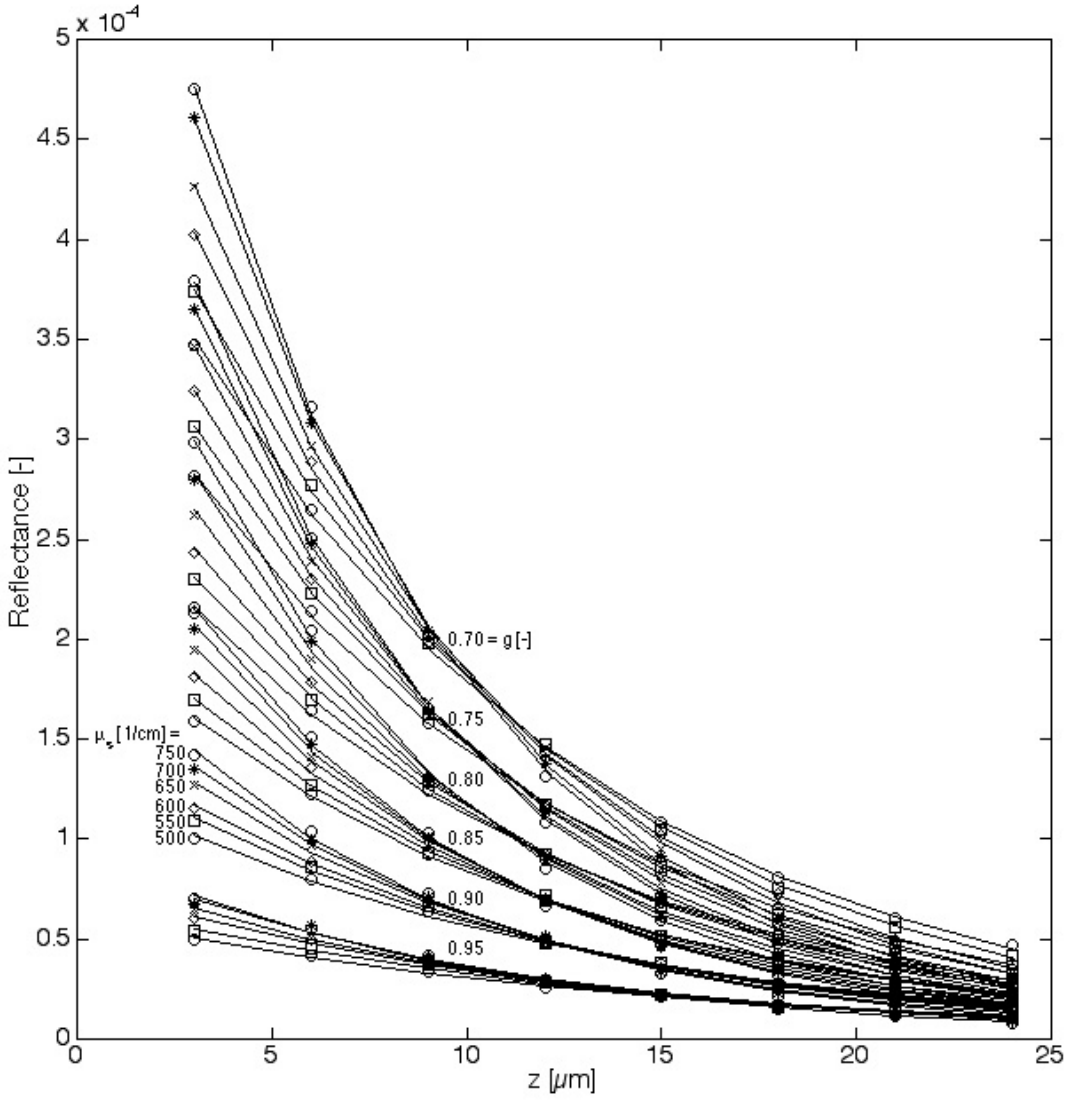

Figure 6.3 Monte Carlo data (symbols) simulating the reflectance signal S(z) as a function of the depth of focus (z). The S(z) was fit with a decaying exponential (lines) using Eq. 6.1. Various μ_s and g values were used in the simulations.

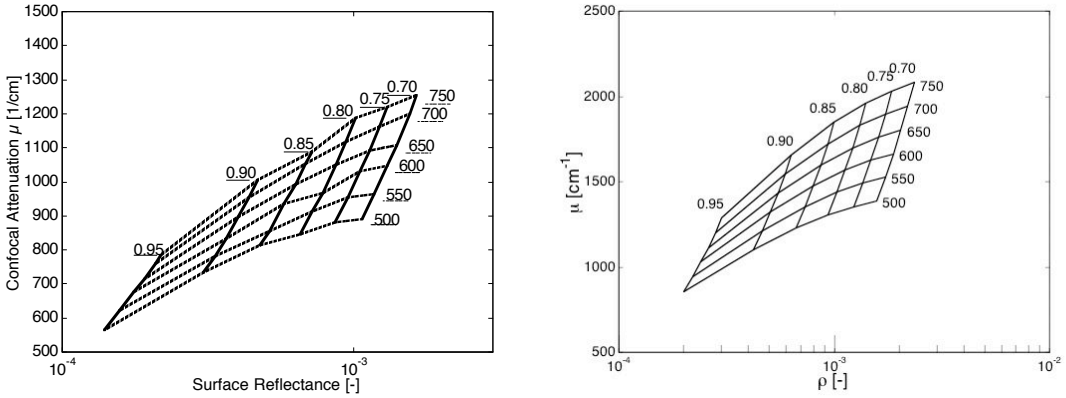

Figure 6.4: (Left) Numerical simulation of analysis grid using Monte Carlo. (Right) Analysis grid using Eqs. 6.2. The iso-g curves extend from 0.70 by 0.05 to 0.95. The iso-μ_s curves extend from 500 by 50 to 750 cm^{-1}.

6.E.3 Mouse Tissue Studies

Figure 6.5 shows typical images of the 5 tissue types studied. Because of the variability in the optical properties among tissue types, the depth extent of the images varied. Muscle for example required large axial scans of up to 200 μm with 7 μm z-steps while brain required only small axial scans of up to 40 μm with 1 μm z-steps. In brain gray matter, dendritic structures were visualized but interestingly, their contrast rapidly degraded (~10 minutes) after sacrifice. In liver, hepatocytes were visible with dark nuclei. In a separate study (not shown) the liver nuclei were seen to acetowhiten (become bright) quite dramatically after soaking in 3% acetic acid. In skin, keratinocytes in the granular and spinous layers were easily visualized with dark nuclei and collagen fibers appeared bright in the dermis. In muscle, the fibers were visible, Figure 6.5E shows a muscle fiber bundle in the center of the image after it has been severed and oriented with the cut end facing upward toward the reader. Figure 6.5F shows a typical plot of the reflectance signal S(z) and the exponential fit using Eq. 6.1.

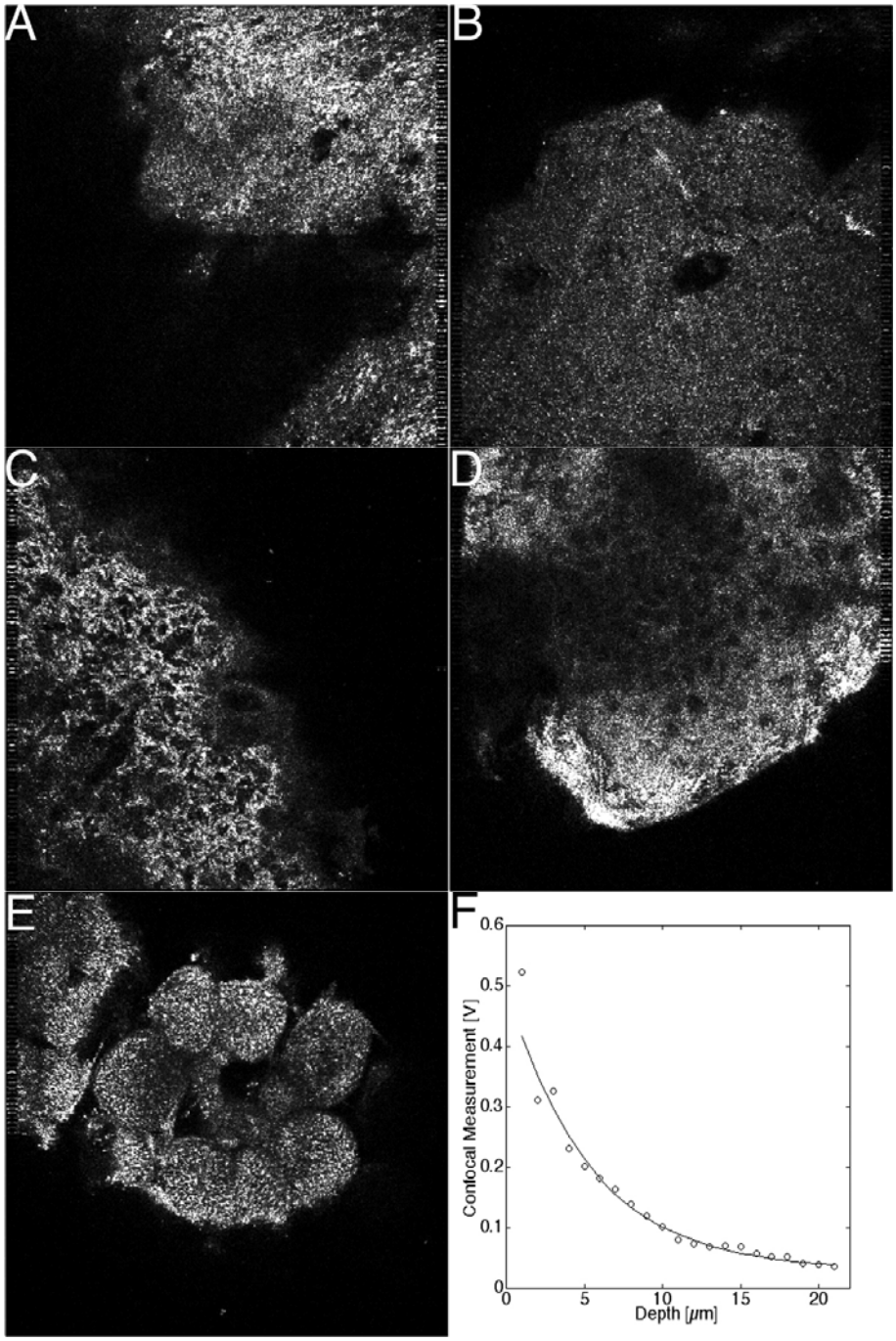

Figure 6.5 Typical horizontal images for the different tissue types. A: brain white matter. B: brain gray matter. C: liver. D: Skin. E: Muscle. A typical fit to the axial (vertical) behavior of the confocal signal is shown for brain white matter.

Images were analyzed with a fitting algorithm which fit the decaying signal (Equation 6.1) resulting in characteristic values for μ and ρ. After each image matrix was acquired, an algorithm written in Matlab sampled the matrix in 10 x,y positions that fit the following two criteria: 1) the total error in the fit was less than one and 2) the surface of the tissue was sufficiently close to the surface that the fit was valid over the majority of the depth profile. The first criteria avoided regions where the tissue was broken and or highly inhomogeneous and the second criteria avoided locations where the majority of axial information was zero reflectance from the saline immersion media. The analysis drew random x,y positions until 10 fits that met the criteria were achieved. For each x,y position, the axial signal was extracted as a function of depth (z). At each z-position, the extracted value consisted of the mean of 121 pixels in a 11-pixel (6-μm) squared x,y neighborhood. Then the mean values for each of the 10 positions on each 3-dimensional image were analyzed to yield a net mean and standard deviation (n = 10 position) that characterized the tissue.

For the first study on the C57/B6 mice, the mean values for each of the 10 positions on each 3-dimensional image were analyzed to yield a net mean and standard deviation (n = 10 position) that characterized the tissue. The results are shown in Fig. 6.6. The scattering coefficients appeared in the 400-600 cm^{-1} range, and the anisotropy values varied from 0.90 to about 0.995.

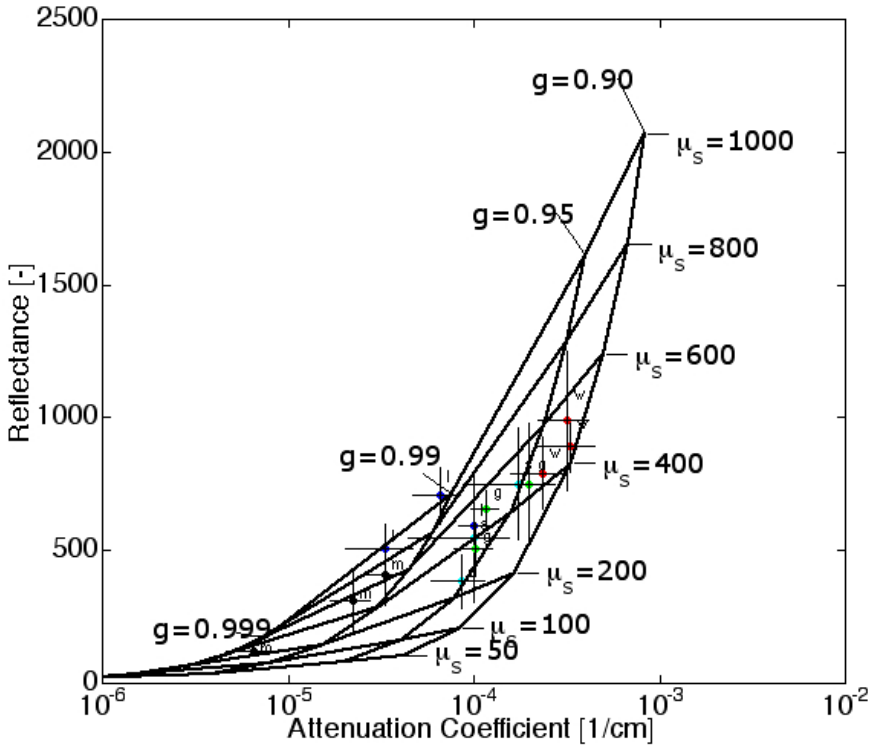

Figure 6.6 Samples of each tissue type (w = brain white matter, g = brain gray matter, s = skin, l = liver and m = muscle) were imaged form three animals. The results are mapped in terms of the measured attenuation coefficient on the y axis (μ [cm^{-1}]) and the reflectance on the x axis (ρ [-]). Equation 6.2 was used to create an analytical grid to overlay the data on. Experimental results are shown with the analytical grid.

The mean values of reflectivity (ρ) were statistically different ($p < 0.05$) between tissue types with three exceptions: 1) between liver and muscle, 2) between skin and brain gray matter, and 3) between liver and brain gray matter. This means that the measurement was sufficiently sensitive to distinguish the tissue types with those exceptions. In a correlation test, ρ was statistically the same ($p < 0.05$) between two tissue type combinations: 1) skin and brain white matter, and 2) skin and brain gray matter.

Figure 6.7 shows the experimental results of the polystyrene microsphere study and the second mouse study. In this case, the μ versus ρ data is plotted on a log-log plot. The 0.1-μm-dia. microspheres data show as the black circle (μ_s = 101 cm^{-1}, g = 0.234). The prediction of Mie theory using the analysis grid was expected at the position of the black diamond (μ_s = 75 cm^{-1}, g = 0.112). Work continues in the laboratory on the calibration using microspheres.

The mouse data is shown in colored symbols, as mean ± standard deviations (n = 10 x,y positions per tissue site), for 3 sites on each of 5 tissues on 8 mice. This experiment used the oil/glass calibration which proved to be a more reliable calibration than the water/glass calibration combined with optical density filters, used in the first mouse study. In this second study, the mouse tissue scattering coefficient varied over a broader range from about 100-1500 cm^{-1}, and the anisotropy varied from about 0.5-0.95. There are a few outlier data, since the choice of tissue sites was automated and occasional hair follicles and other epidermal heterogeneities complicated the fitting.

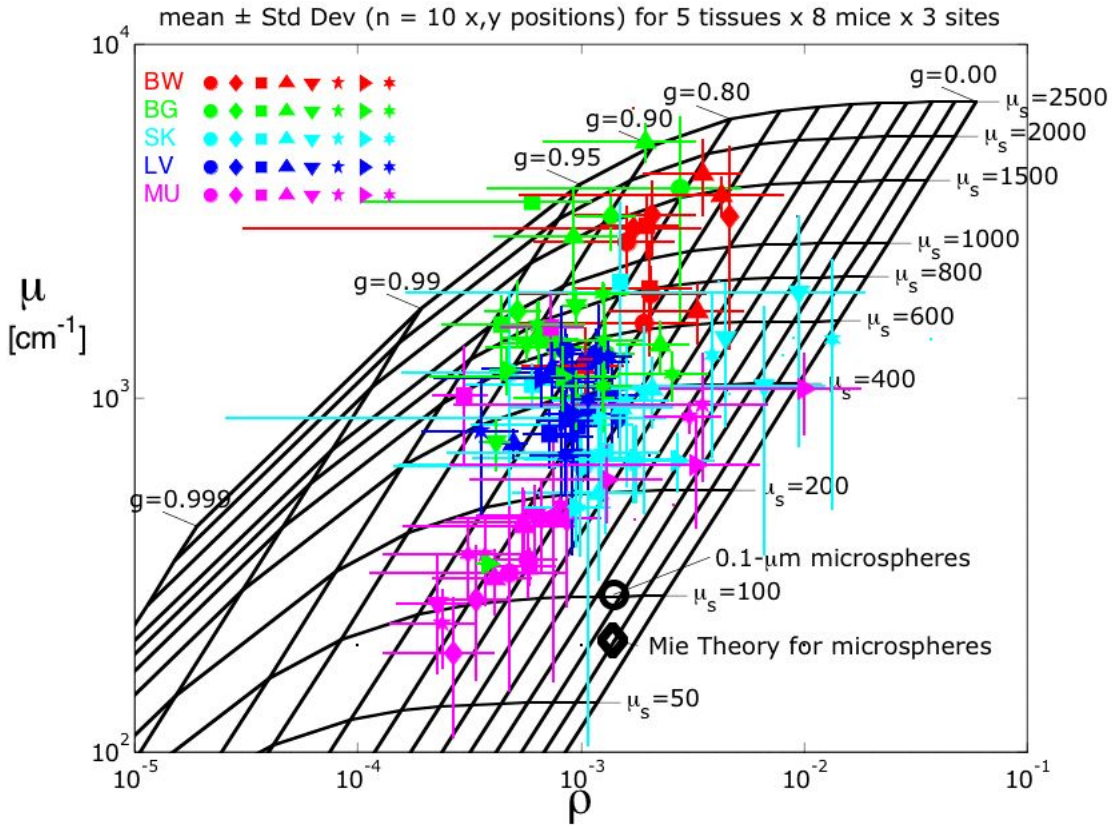

Figure 6.7 Results for the albino mouse studies. Results for 8 animals appear as 8 symbols. The tissue sites are color-coded. Each symbol and color appears three times for repetition on the same animal at the same site. The error-bars represent intra-sample variation.

Figure 6.8 summarizes the values of μ_s and g deduced from Fig. 6.7, plotting ms versus g. Table 1 summarizes the mean values of the optical properties for each tissue type, included the calculated value of $\mu_s' = \mu_s(1-g)$. The brain tissues showed the highest μ_s and g values. Muscle showed the lowest μ_s and g values. The values of μ_s' for 488 nm are comparable to literature values (see Table 9.2).

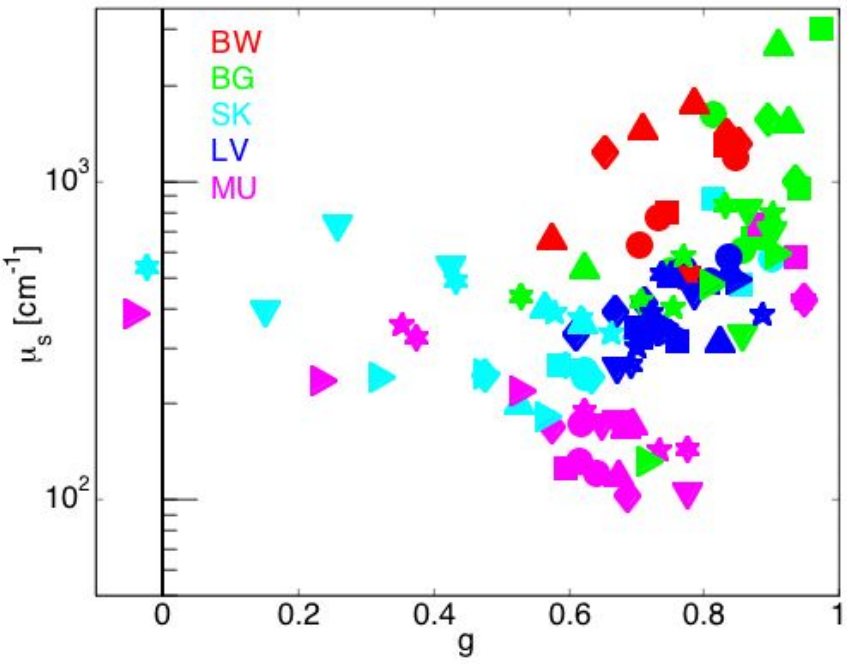

Figure 6.8 The extrapolated optical scattering properties μ_s and g for the experimental data from the second study. Data are for 3 sites on 5 tissues on 8 mice.

Table 6.1 Average scattering coefficient, μ_s, ,scattering anisotropy, g, and reduced scattering coefficient, $\mu_s' = \mu_s(1-g)$, of the 5 tissue types.

Tissue Type	μ_s [cm^{-1}]	g [-]	μ_s' [cm^{-1}]
Brain White Matter	1,081 ± 394	0.75 ± 0.08	270
Brain Gray Matter	910 ± 707	0.83 ± 0.11	155
Skin	382 ± 174	0.54 ± 0.21	176
Liver	399 ± 92	0.75 ± 0.07	100
Muscle	244 ± 162	0.63 ± 0.23	90

6.F Discussion

The RCSLM images were analyzed by fitting the depth profile of reflectance, S(z), with the Eq. 1, $S(z) = \rho\exp(-\mu z)$, to yield the experimental parameters ρ and μ. An analysis grid was used, based on Eqs. 6.2, $\rho(\mu_s,g,NA)$ and $\mu(\mu_s,g,NA)$, to map ρ and μ into the optical properties μ_s and g.

Calibration measurements using a gel with 0.1-μm-dia. polystyrene microspheres demonstrated approximate agreement between experiment ($\mu_s = 101\ cm^{-1}$, g = 0.234) and the predictions of Mie theory ($\mu_s = 75\ cm^{-1}$, g = 0.112).

Monte Carlo simulated numerical measurements were generated and used to create an analysis grid, which was compared with the analysis grid predicted by Eq. 6.2. The shapes of the two grids were similar. The Monte Carlo simulation produced significantly lower values of μ, but only slightly lower values of ρ, compared to the predictions of Eq. 6.2.

The measurements of mouse tissues yielded the values for the μ_s and g of tissues. Traditionally, the lumped parameter $\mu_s' = \mu_s(1-g)$ is measured in optical experiments recording light transport. This work demonstrates the ability to separate the values μ_s and g. The measurements are suitable for noninvasive *in vivo* measurements.

Chapter 7: Noninvasive imaging of melanoma with reflectance mode confocal scanning laser microscopy in a murine model.

7.A: Abstract

A reflectance-mode confocal scanning laser microscope (rCSLM) was developed for imaging early stage melanoma in a living mouse model without the addition of exogenous contrast agent. Lesions were first located by surveying the dorsum with a polarized light camera, then imaged with the rCSLM. The images demonstrated two hallmarks of melanoma in this animal model: (1) Melanocytes and apparent tumor nests at the superbasal layer of the epidermis in a state of pagetoid spread and (2) architectural disruption of the dermal-epidermal junction. The superbasal melanocytes and apparent tumor nests had a high melanin content, which caused their reflectivity of light to be 5-fold greater than the surrounding epidermis.

7.B Introduction

Reflectance mode confocal microscopy (rCSLM) offers a means to image mouse skin *in vivo* by exploiting scattering from microscopic variations in refractive index within the tissue. The light scattering properties of cutaneous tissues provided optical contrast for imaging the presence and spatial distribution of pigmented melanoma against the background of healthy tissue in a highly pigmented murine model, the hepatocyte growth factor/scatter factor transgenic mouse (HGF/B6)[60]. Components of skin whose refractive index are higher than the bulk refractive index of epidermis (n_{epi} = 1.34)[9], such as keratin in stratum corneum (n = 1.51)[9], hydrated collagen (n = 1.43)[3] and melanin (n = 1.7)[62], can be imaged with backscattered light. Using these refractive

indices, the Fresnel reflectance[63] predicted from a plane of melanin or keratin within epidermis is:

$$R = ((n_{epi} - n)/(n_{epi} + n))^2 \quad (7.1)$$

Setting n = 1.51 and n = 1.7 for keratin and melanin respectively, R_{ker} = 0.0024 and R_{mel} = 0.014 are the Fresnel reflectances expected from an epidermis/keratin or epidermis/melanin interface, respectively. Since melanin reflectance is R_{mel}/R_{ker} = 5.2-fold higher than that of keratin, melanoma cells (which scatter based on the melanin-epidermis refractive index mismatch) will present with bright contrast against the background epidermis, which scatters based on the keratin-epidermis refractive index mismatch. In an alternative calculation (not shown), Mie theory was used to calculate the scattering coefficient (μ_s) of very small spheres (10 nm dia.) to mimic keratin fibers and melanin granules within a background epidermis. The ratio of R_{mel}/R_{ker} was 4.4. Therefore, melanin granules are expected to scatter more strongly than keratin fibers.

Conventional wide-field microscopy on histological sections is limited to 3-10 μm-thick tissue samples depending on sample optical properties. In thicker samples, light reflected from tissue above and below the plane of focus is also collected, which causes loss of image contrast. Optical sectioning in rCSLM blocks multiply scattered light so the image of the tissue in the plane of focus remains sharp despite light scattered above and below that plane. Confocal microscopy is limited in depth to the ballistic regime where photons propagate unscattered to the focus, backscatter from the focus toward the objective lens and escape the tissue without scattering. At deeper depths, the low level of light due to multiply scattered photons becomes the optical noise floor for the image, specifying the practical depth limit for rCSLM imaging. The imaging depth range rCSLM in this work (50-100 μm) was limited primarily by the laser wavelength used (488 nm). Since mouse epidermis is thin (~15 μm, see Fig. 7.4), even enlarged epidermis (~40–μm, see Fig. 7.5) associated with tumors can be imaged fully. By comparison, imaging in human skin[9] with 830-nm laser light encounter 1.7-fold less

optical scattering and 4-fold less optical absorption[64] so the imaging depth range is increased to 250 μm, which also sufficiently images the epidermis (60-100 μm).

The long-term goal of this work is to contribute to on-going efforts to "humanize" the mouse melanoma model such that melanoma onset and progression in the mouse model better mimics human early stage melanoma. Such "humanization" involves developing melanoma models in which melanomas originate in the interfollicular epidermis and invade locally downward through the epidermal-dermal junction rather than originating in the deeper dermis as in current mouse models. In human skin, melanomas are characterized by polymorphic (multi-lobed) melanocytes while normal skin presents monomorphic melanocytes[65]. One goal of this work was to survey the features of this animal model to identify characteristic structures that occur only in melanoma and not in normal tissues.

The rCSLM images can detect the early progression of melanoma in the sub-epidermal layer and its violation of the epidermal-dermal junction by showing the distribution and overall concentration of melanin in this well-characterized animal model of ultraviolet (UV) induced melanoma[60]. Melanoma can be characterized by high reflectance off the top surface of heavy melanin concentrations and strong attenuation within tumors. Melanin granules (~10 nm diameter within melanosomes) have a refractive index of 1.7[62] compared to the surrounding cytoplasm of 1.35[66]. Therefore melanin granules scatter light, providing a strong endogenous contrast agent for rCSLM[9] of melanocytes. The two key features of melanoma imaged by rCSLM were (1) the irregular distribution of melanocytes reminiscent of melanocytic pagetoid cells in the epidermis, and (2) altered skin ultra-structure described as the disruption of the DE junction. The ability of rCSLM to image the development of these features suggests that time-course imaging may elucidate the dynamically invasive nature of melanoma lesions in this mouse model.

7.C Materials and Methods

7.C.1 Animals

The HGF/B6 murine melanoma model[60] developed at the National Cancer Institute and George Washington University was used in this study. These genetically engineered mice over-express hepatocyte growth factor/scatter factor, making them susceptible to melanoma induced by UV radiation on the back[60]. Mice used in this study have a pigmented C57BL/6 genetic background. The UV irradiated HGF/B6 mouse develops melanoma through a series of stages, starting with multiple skin lesions appearing first as a small tumor (< 1 mm diameter, Figure 7.1) followed by a progressive swelling of the dermis as shown in Figure 7.3. Mice with tumors that grew to 1 cm in diameter were immediately euthanized and imaged. All animal studies were approved by the Oregon Health & Science University Institutional Animal Care and Use Committee. Hair was removed chemically (Nair™). Tumors on the lower back were imaged to avoid motion from the heart and lungs. The underside of the mice was also imaged as a control for skin that had not developed melanoma through UV-induced radiation.

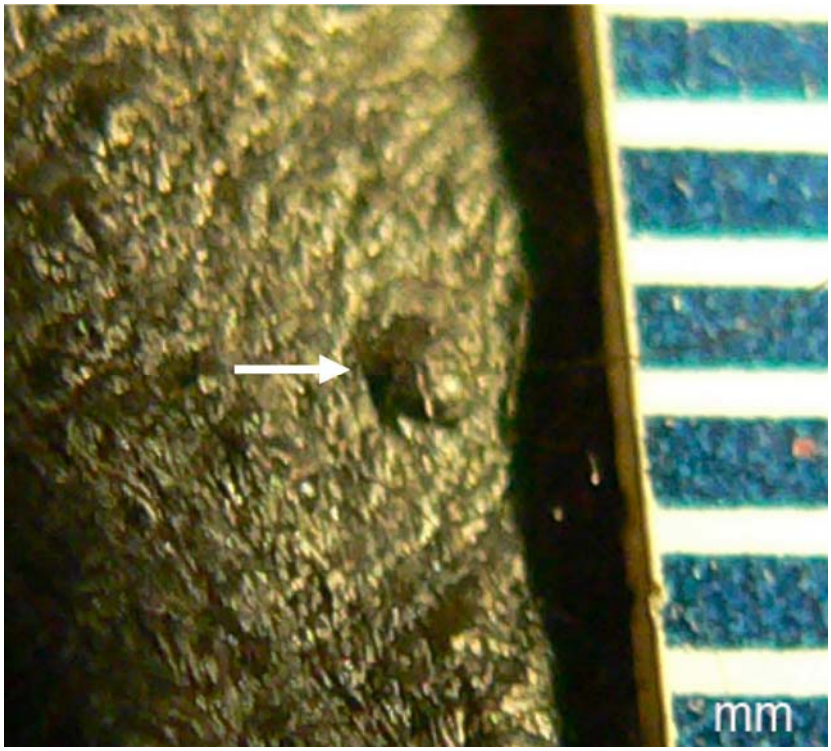

Figure 7.1 Digital photograph of dorsal melanoma tumor (center). Millimeter markings show the tumor's diameter to be about 0.7 [mm]. The animals had already developed lesions as large as 5 mm in diameter, but also had early stage lesions (less than 1 mm diameter), which were deemed early lesions and chosen for imaging.

Figure 7.1 shows an early stage lesion. Each animal presented multiple early stage lesions, which were followed through tumor development. About half of the early stage lesions became enlarged and spread laterally. The results presented in this paper constitute a subset of the laterally spreading lesions vs. normal skin.

One-year-old animals from previous collaborators' experiments were used to minimize overall animal use. Lesions were identified by eye and then imaged with a polarized wide-field microscope[**67, 68,** 69] to identify lesions that were superficial and hence likely to present epidermal melanin. Animals were placed on a metal plate the size and shape of a standard glass slide, with the tumor of interest centered over a 2-mm-diameter hole in the plate. Optical coupling between the objective lens of the rCSLM and

the skin surface was achieved with a drop of saline solution, and no glass coverslip was used. The animal was immobilized by about 10 wrappings of an elastic string (SpiderThread™, Redwing Tackle Onterio, Canada), which is commonly used for fixing bait to fishing hooks. This method immobilized the animal in a least invasive manner, avoiding pressure points, and sufficiently stabilized the skin region of interest to minimize movement artifacts due to breathing. The 3D images took about 15 minutes to acquire (field of view was x,y,z = 260, 253, 80 μm). The animal (36 g typical weight) was anesthetized by a ketamine/xylazine cocktail (0.5 ml i.p., adjusted for animal weight, age, and tumor load) during the handling and measurement procedure, sufficient for a 45 minute imaging session.

7.C.2 Reflectance Mode Confocal Scanning Laser Microscope (rCSLM):

An rCSLM incorporating reflectance and fluorescence channels was designed and assembled. The fluorescence mode capabilities were designed for other experiments and not used in this report. The rCLSM used a 488-nm (blue) argon ion laser, x- and y-axis scanning mirrors, 60x water-dipping objective lens 0.90 N.A. (Olympus LUMPlanFl), relay lens system that magnified the image to project the central lobe of the Airy function[27] to slightly overfill a 50-μm-diameter pinhole for confocally matched gating[70], a photomultiplier tube (Hamamatsu Photonics, 5773-01), a data acquisition board (National Instruments, 6062E), a z-axis motorized stage (Applied Scientific Instrumentation, LS50A) for supporting the animal, Labview software to control the system, and a Gateway laptop computer running a Microsoft Windows 2000 operating system. The scanning mirrors provided x-y scans (512 x 512 pixels, 25 kHz pixel acquisition rate, 10.5 seconds per image) at each depth z in the tissue. The axial resolution limit measured for the system was 1.25-μm. The motorized stage advanced the animal in 1-μm steps along the z-axis before each x-y scan. The extent of images was typically x,y,z = 526 x 512 x 80 pixels = 260 μm x 253 μm x 80 μm image, and was acquired in 15 minutes. Post processing of data to generate images was carried out using MATLAB™ software.

In order to express image pixel values in the units of optical reflectance, calibration was achieved by imaging the water/glass interface of water contacting a glass coverslip with a neutral density filter (optical density OD = 1.0) attenuating the laser beam, and equating this reflectivity to the Fresnel reflectance for a planar water/glass interface with a refractive index mismatch $R = ((n_1-n_2)/(n_1+n_2))^2 = 0.0044$ for water (n_1 = 1.33) and glass (n_2 = 1.52). The reflectance (R) of the mouse skin measured without the neutral density filter was calculated based on the confocal signal in Volts from the mouse (V_m) and from the water/glass interface (V_{wg}):

$$R = \frac{V_m}{V_{wg}} \frac{0.0044}{(10^{-OD})} \tag{2}$$

Typical values of R for skin of the C57/B6 mouse were 10^{-5}-10^{-4}. Pixel values in the confocal images in this report are presented as the log of the data $\log_{10}(R)$ over the range $10^{-5} < R < 10^{-3}$. This graphical display allocates the dynamic range in the image to optimally include the range of reflectance of the tissue.

7.C.3 Experimental Protocol

The back of the animal, which had been exposed to the tumor-inducing UV radiation, was examined for tumor growth. After anesthesia, each animal was digitally photographed (Panasonic DMC-FZ20), then imaged with a wide field-of-view polarized-light imaging system[67] that aided in finding early superficial lesions (Figure 7.2). Superficial lesions appeared black in both normal-light and polarized-light images, while deeper lesions appear black only in normal-light images.

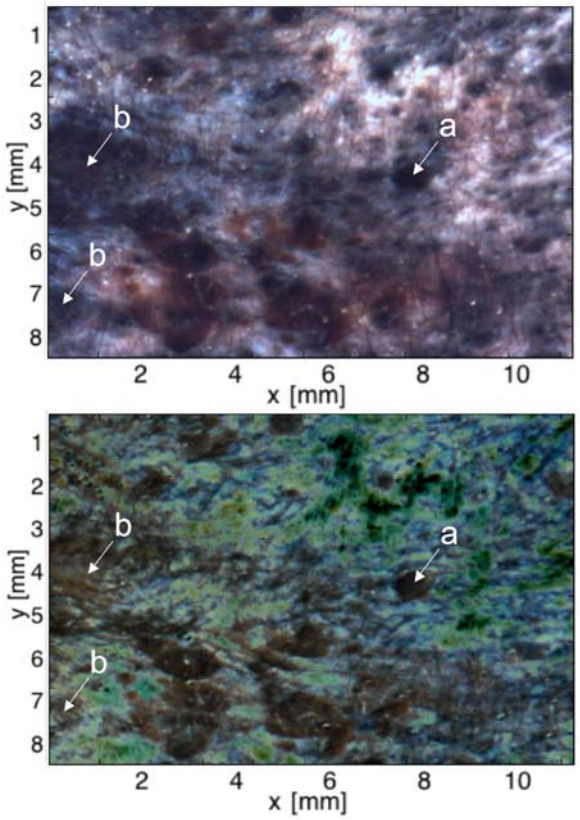

Figure 7.2 Polarized image of dorsal melanoma tumors. (upper) Normal light image. (bottom) Polarized light image, based on difference between two images, one through linear polarizer oriented parallel to the polarized illumination and the second cross-polarized perpendicular to the illumination. The epidermal lesion (a) remained dark in the polarized light image while the non-superficially pigmented lesions (b) appeared bright.

After selecting lesions using the polarized images, the animal was immobilized on the metal plate for confocal imaging. The metal plate holding the immobilized animal was placed plate down on the microscope stage and the 60X water dipping objective lens was coupled to the skin surface from below using phosphate buffered saline.

Multiple lesions on each animal were imaged 1 to 3 successive times over a one-month period. Digital photography (Figure 7.3), wide-field polarized light imaging[67] (Figure 7.2), and landmarks of biological features such as tumor shape and hair follicle location helped keep track of the lesions to assure the same lesions were imaged on

successive days. Landmarks were recorded in drawings of the tumors, specifically noting their size, shape and relative location. At the last time point of in vivo imaging, the tumors were excised for histology with the position and orientation landmarks of the tumor noted.

7.D Results

7.D.1 Histopathology

Excised samples were fixed in formalin, processed for histopathologic microscopy by standard methods, sectioned and stained using H&E. In parallel, a melanin bleach method was implemented to better reveal the sub-cellular detail in melanoma cells containing high melanin concentration and verified the atypical nuclei of the tumor cells. Samples stained with a histological counter-stain for iron pigment showed that the pigment was in fact melanin. Immunochistochemical staining with the antibody PEP8H specified the melanocyte antigen DCT and verified the presence of melanocytes. Figure 7.3 shows images of the bleached and immunohistochemically stained tumor biopsy.

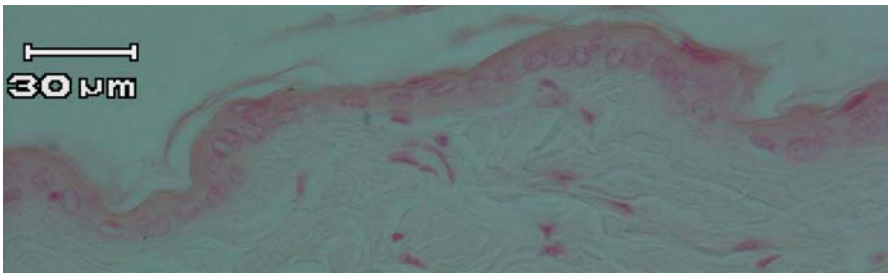

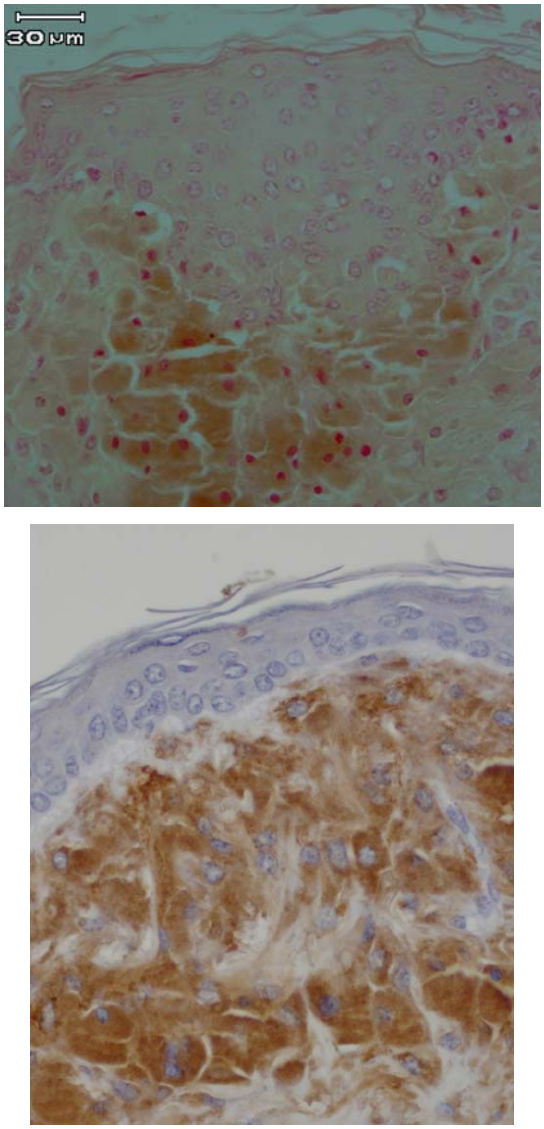

Figure 7.3: (Upper): Normal skin histology with melanin bleach. (Middle): Epidermis above tumor is thickened in the center of the tumor. (Bottom) The immunohistochemical stain for DCT verifies that the tumor is a melanoma.

7.D.2 Reflectane Mode Confocal Microscopy rCSLM

Figure 7.4 shows a typical experiment where a lesion is identified (a) and imaged over three weeks. The nodular tumor is indicated both with (b) and without (a) involvement of the surrounding dermis, which was seen to develop in approximately half of the observed tumors.

Figure 7.4: Digital photograph of (a) early stage tumor, (b) late stage tumor two weeks later.

Lesions identified with the wide-field polarized microscope showed suspicious areas of uneven reflectance in the epidermis and at the dermal/epidermal junction. Eight lesions and five normal areas on two animals were imaged with rCSLM in vivo. Roughly half of the melanoma lesions identified then showed rapid nodular growth (as in Figure 7.4).

Healthy skin (Figure 7.5) was characterized in a sagittal view (image of a plane perpendicular to the surface) by a relatively uniform reflectivity with the absence of highly reflective structures. As a measure of dermal reflectance uniformity, the maximum contrast (brightest pixel value divided by dimmest) was 1.3 +/- 0.2. The epidermis in normal mouse skin is about fifteen μm thick and one or two cell layers thick based on the histological image (Figure 7.5 upper). Collagen reflectivity in the underlying dermis is uniform and the dermal/epidermal junction is relatively flat. Melanocytes were sparse among keratinocytes, yet frequent enough to give the skin a dark tone to the eye. Melanocytes accounted for less than one percent of epidermal cells

as observed by rCSLM and histology. In contrast, melanoma lesions were well populated with pleomorphic melanocytes and polymorphic melanocyte nests.

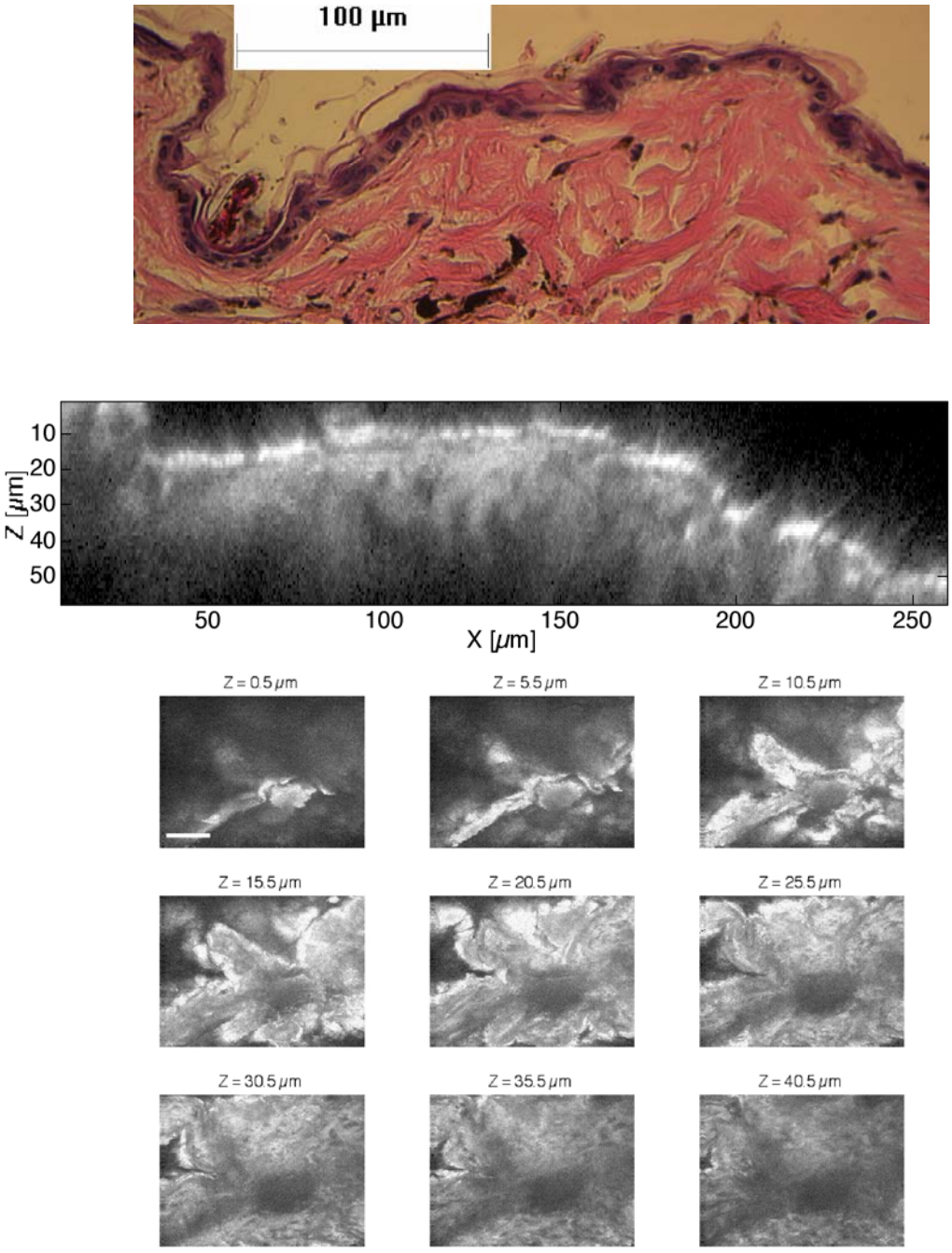

Figure 7.5: Figure of normal skin, correlating histology (upper) with confocal microscopy of normal skin in sagittal view (middle). (Bottom): A set of en face images taken at various depths on a different normal skin site.

Melanoma lesions (Figure 7.6) were found to contain high levels of melanin, and lesions could be located repeatedly by digital photography and mapping of the lesion architecture, then imaged with confocal microscopy. Malignant tumors were characterized by nodular regions of high reflectivity and thickened epidermis and were often proximal to hair follicles. Figure 7.6 (upper, middle) is a single sagittal image. Features seen in the confocal images Figure 7.6 (middle, lower) (as well as in all tumor images) included melanocytic cells migrating upward into the epidermis. Figure 7.6 (lower) shows a series of en-face images progressing from the surface of the skin through the epidermis into the dermis.

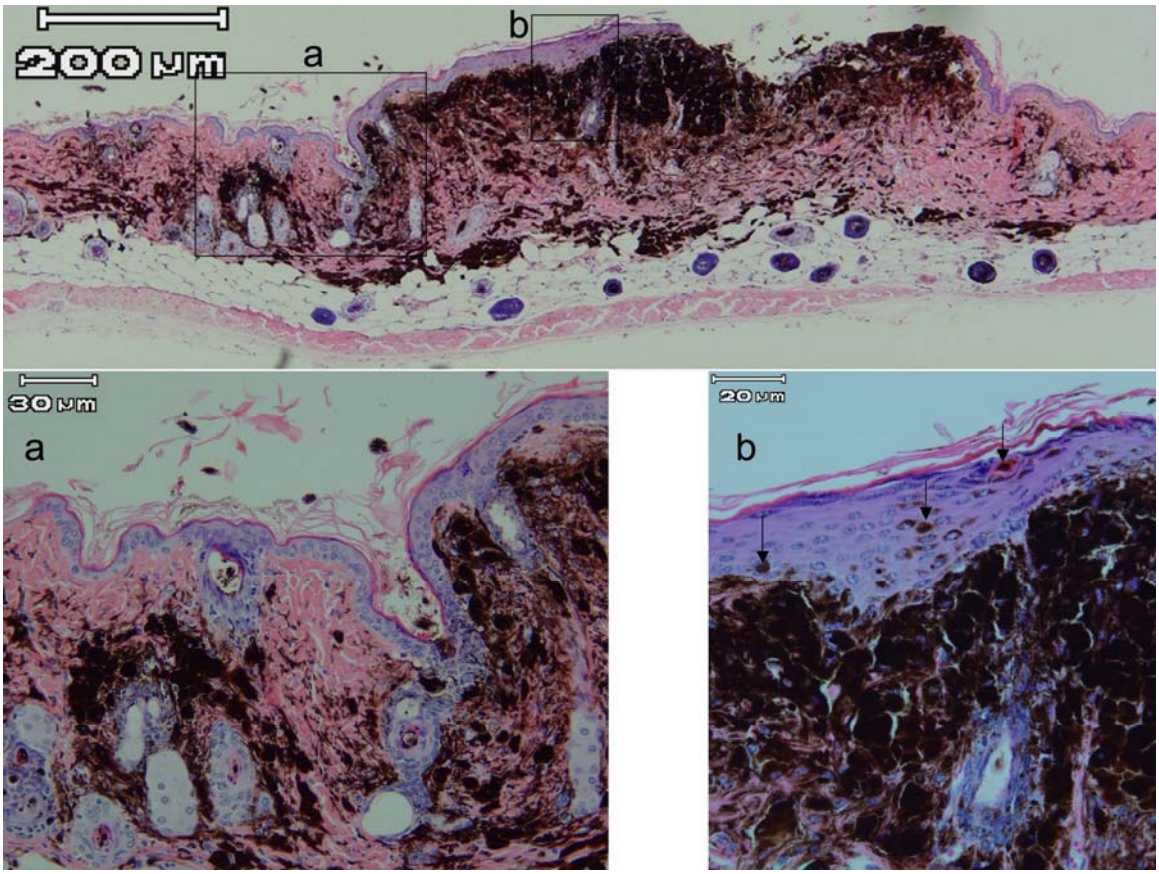

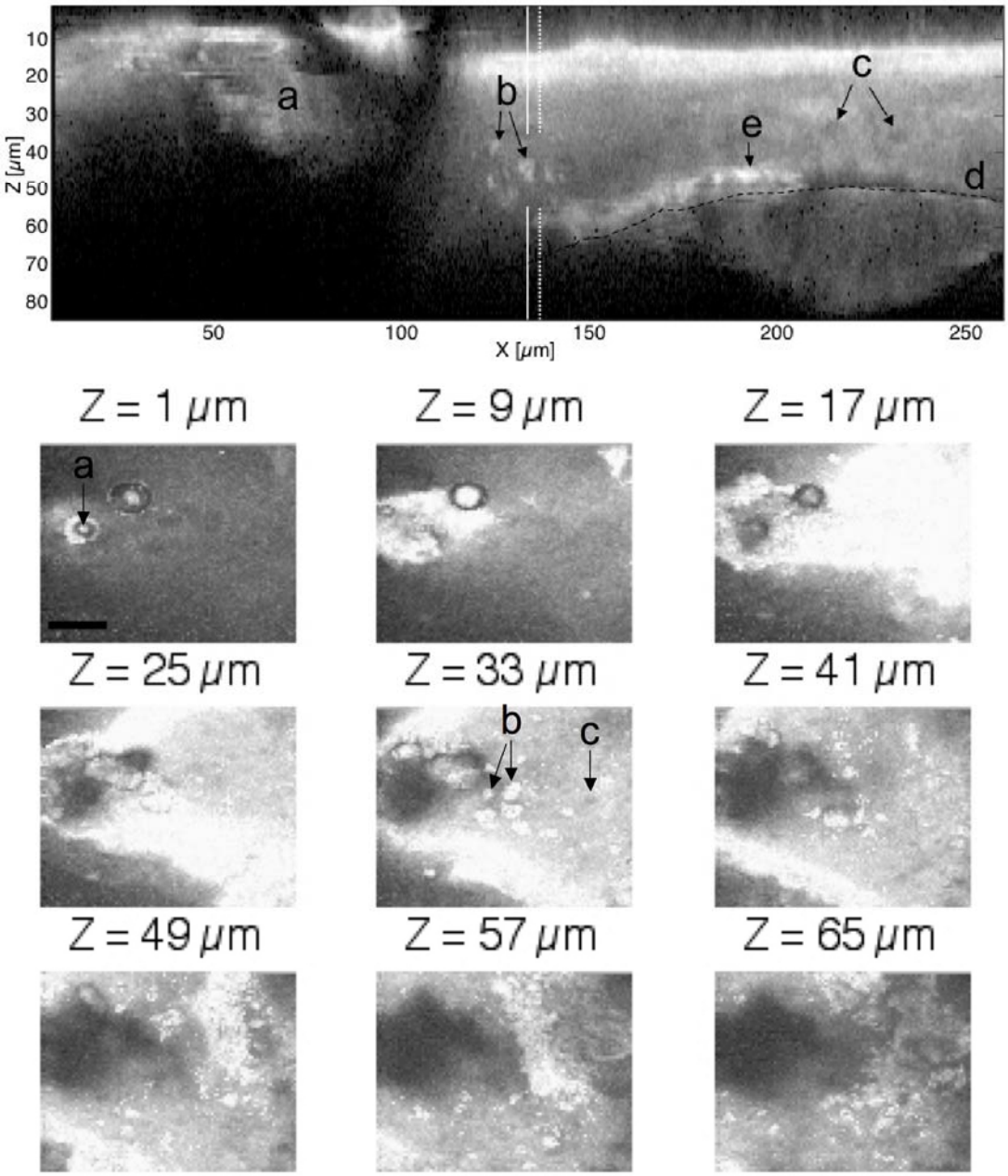

Figure 7.6: (Upper): histology with an iron counter-stain shows that the pigment is not iron. This late stage tumor has ulcerated. The insets show (a) the epidermal thickening (left to right) and (b) the epidermal melanocytes indicated with arrows. In the confocal images (middle, bottom) malignant tumor is identified by bright areas of high melanin density located in single epidermal melanoma cells and at larger structures of these cells at the dermal / epidermal junction. a) Hair follicle (hair has been Nair'd™) 50 μm in diameter. b) Epidermal melanocytes. c) Granular cells with dark nuclei beneath the

stratum corneum. Cells in the granular layer within the epidermis appear with dark nuclei, which backscatter less light than the surrounding cytoplasm / cell wall / extra-cellular matrix. d) Dermal-epidermal junction e) Irregular groups of polymorphic melanocytes at dermal-epidermal junction. The white lines at x = 132 marks an axial z-profile that will be analyzed in Figure 7.7.

To the eye, the tone of the skin on the melanoma-induced HGF/B6 mouse is similar to the tone in the melanoma lesions and the normal pigmented tissue although the histology and confocal microscopy clearly show an increased presence of melanotic features with strong backscattering of light. The putative melanoma cells were large, abundant and irregularly shaped.

In Figure 7.7, an axial profile of reflectance is plotted versus depth. The profile is from the vertical white lines in Figure 7.6(middle), one intersecting an epidermal melanocyte and the other just adjacent. The calibration of Eq. 3 was applied to the data to yield reflectance units.

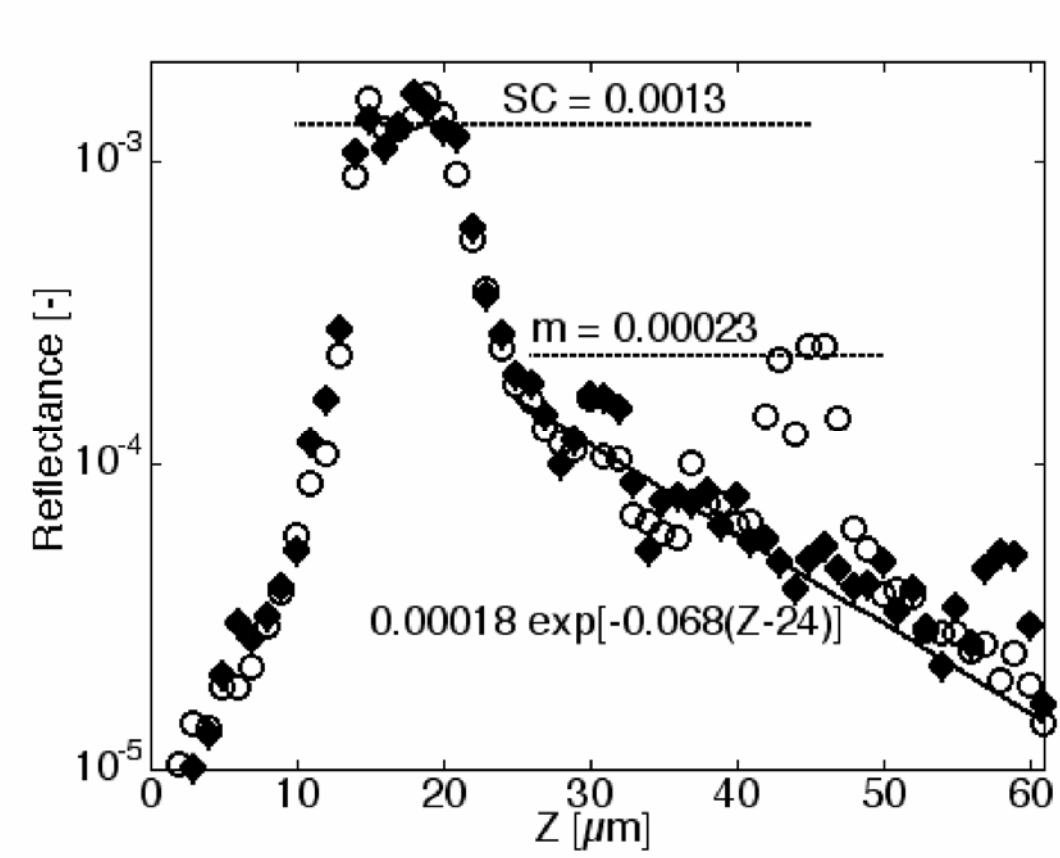

Figure 7.7 The axial reflectance profile through one melanocytic cell, relative to surrounding epidermis. Circles represent the data from the solid white line in Figure 7.6(middle), diamonds represent data from the dashed white line. Centered at Z = 16 μm, the reflectance of the stratum corneum (SC) is 1.3×10^{-3}. Beneath the SC, the bulk tissue reflectance decay is fit with an exponential. Centered at z = 45 μm, an epidermal melanocyte's measured peak reflectance is $m = 2.3 \times 10^{-4}$, which is 1.87×10^{-4} above the epidermal background at z = 45 μm (4.3×10^{-5}). The decaying exponential least square-error fit to the data, which is not sensitive to data points in the SC (Z < 24 μm) or in the melanocyte (40 > Z > 48), represents the background reflectance of the epidermis.

At the tissue surface (z = 16 μm, Figure 7.7) the reflectivity off the water/stratum corneum interface was $R_{measured} = 0.0013$. The Fresnel reflectivity (eq. 1) predicted from an interface of water ($n_{H2O} = 1.33$) and stratum corneum (n = 1.47) is $R_{theoretical} = 0.0025$.

The difference between $R_{theoretical}$ and $R_{measured}$ is likely due to roughness of the stratum corneum.

At z = 45 μm, the reflectance of the melanocytic cell (Figure 7.7) was R_{mel} = 0.00023, and the reflectance of the background was only R_{epi} = 0.000043. The melanocytic cell stands out from the background epidermis by a factor of R_{mel}/R_{epi} = 5.3. This measured result agreed with the theoretically calculated value from Equation 1 which is R_{mel}/R_{epi} = 5.2. The agreement suggests that the isotropic scattering expected for melanin granules and keratin fibers within the epidermis and consequently the confocal measurement is determined primarily by the degree of refractive mismatch. Since similar tissue attenuation occurred over the adjacent regions chosen as melanocytic cell and epidermis, the attenuative effects of the overlying tissue were presumably sufficiently similar to compare the results.

In addition to the axial decay characterization described above, an *en face* analysis was used to compare populations of tumor characteristics. Tumor cells and nests were characterized by directly comparing their reflectance to that of the laterally surrounding epidermis.

Five features, either melanocytic cells or tumor nests, were picked from Figure 7.6(lower) along with the corresponding 5 adjacent normal areas. Figure 7.8(upper) shows the same en face images as in 6(lower) re-plotted with the tumor features marked. A 3-by-3 pixel (1.5-by-1.5 μm) square region centered on the points picked as tumor and normal was averaged to yield the reflectance of tumor (R_t) and normal (R_n) tissue, respectively. In Figure 7.8(upper) the black open circles indicate normal sites and aterisks to indicate tumor sites. Figure 7.8(lower) shows the paired points, R_t vs R_n, for the tumor and normal sites of Figure 7.8(upper). The average reflectances shown for the five pairs represent the mean and standard deviation of 9 pixels in a square region. Although the reflectance variability within a particular tissue was large due to the natural texture of the tissue, the mean reflectance level was consistently larger for the tumor ($R_t \approx 5.2R_n$).

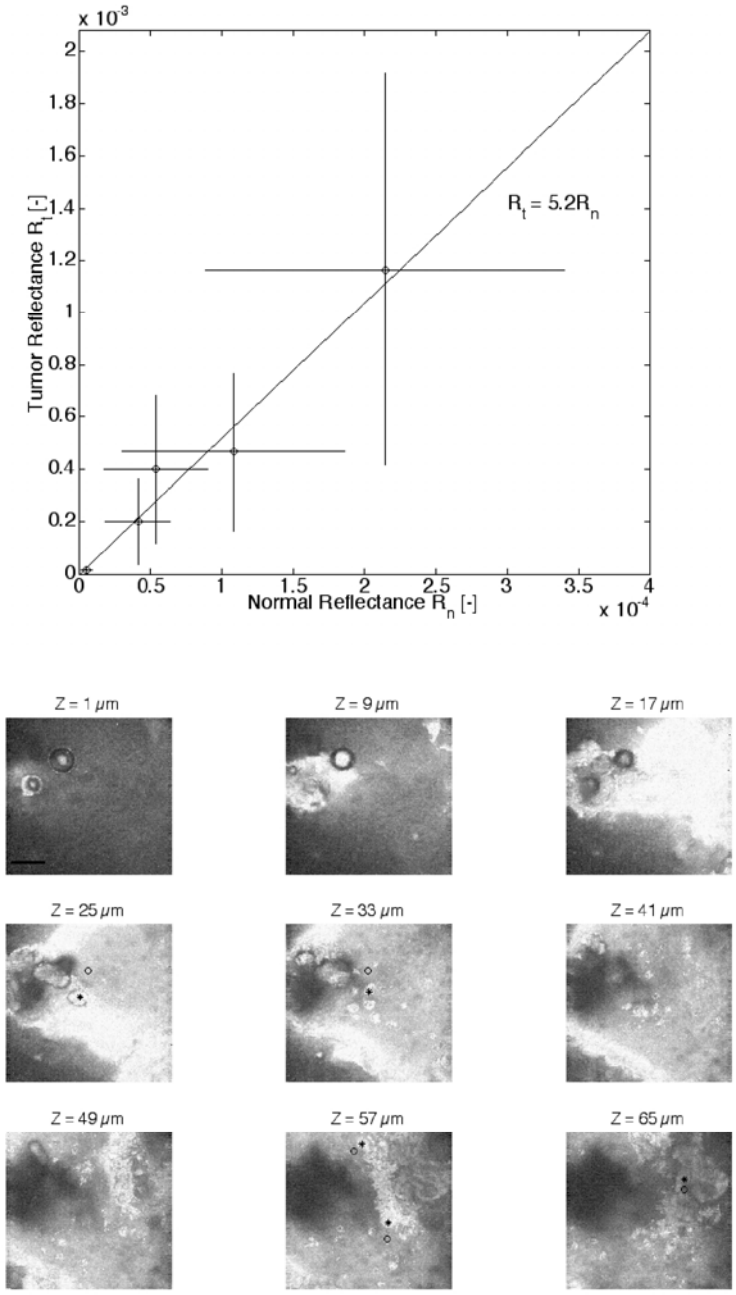

Figure 7.8: (Upper): Five paired tumor (*) and normal (o) sites were chosen at various depths. (Lower): The reflectance at the 5 tumor locations is shown as a function of their normal counterpart's reflectance.

Table 7.1 lists the mean ratio of melanocyte reflectance (R_t) to epidermal reflectance (R_n). For the 5 tumors imaged, the value of (R_t/R_n) was 5.0 +/- 1.6 which is in agreement with the simple model discussed in the Introduction, $R_t/R_n = 5.2$. Table 7.1 also includes the results from a seperate tumor on the same animal and three 3 tumors on a separate animal (images not shown).

Table 7.1 The contrast between atypical tumor features and background tissue. The reflectance of tumor features (epidermal melanocytes or tumor cell nests) R_t is divided by the reflectance of 5 normal surrounding tissue R_n. Each result, the mean and standard deviation, n = 5 features per site for each of 5 tissue sites on two animals, represents the ratio R_t/R_n. The 5 features per site were a mixture of melanocytes and tumor nests.

Tissue Site	Mean R_t/R_n	Standard Deviation R_t/R_n
1, Figure 7.5	5.0	1.6
2, Not Shown	4.7	0.7
3, Not Shown	6.7	1.8
4, Not Shown	6.3	1.0
5, Not Shown	5.3	0.7

Figure 7.9 compares en-face confocal images of tumors vs. normal tissue. In general, the characteristic tumor structures were strongly scattering. Two distinct forms of involvement were seen. 1) In the epidermis, atypical melanocytes and tumor nests were observed in the tumor where only normal granular cells presented in the normal. The melanocytic lesions in the mouse epidermis exhibited pagetoid spreading, characteristic of human intraepidermal melanoma cells that occur singly or in clusters. 2) At the basement membrane where the dermal/epidermal junction is fairly flat and continuous in healthy tissue, tumors presented irregularity where the architecture of the dermal/epidermal junction was disrupted.

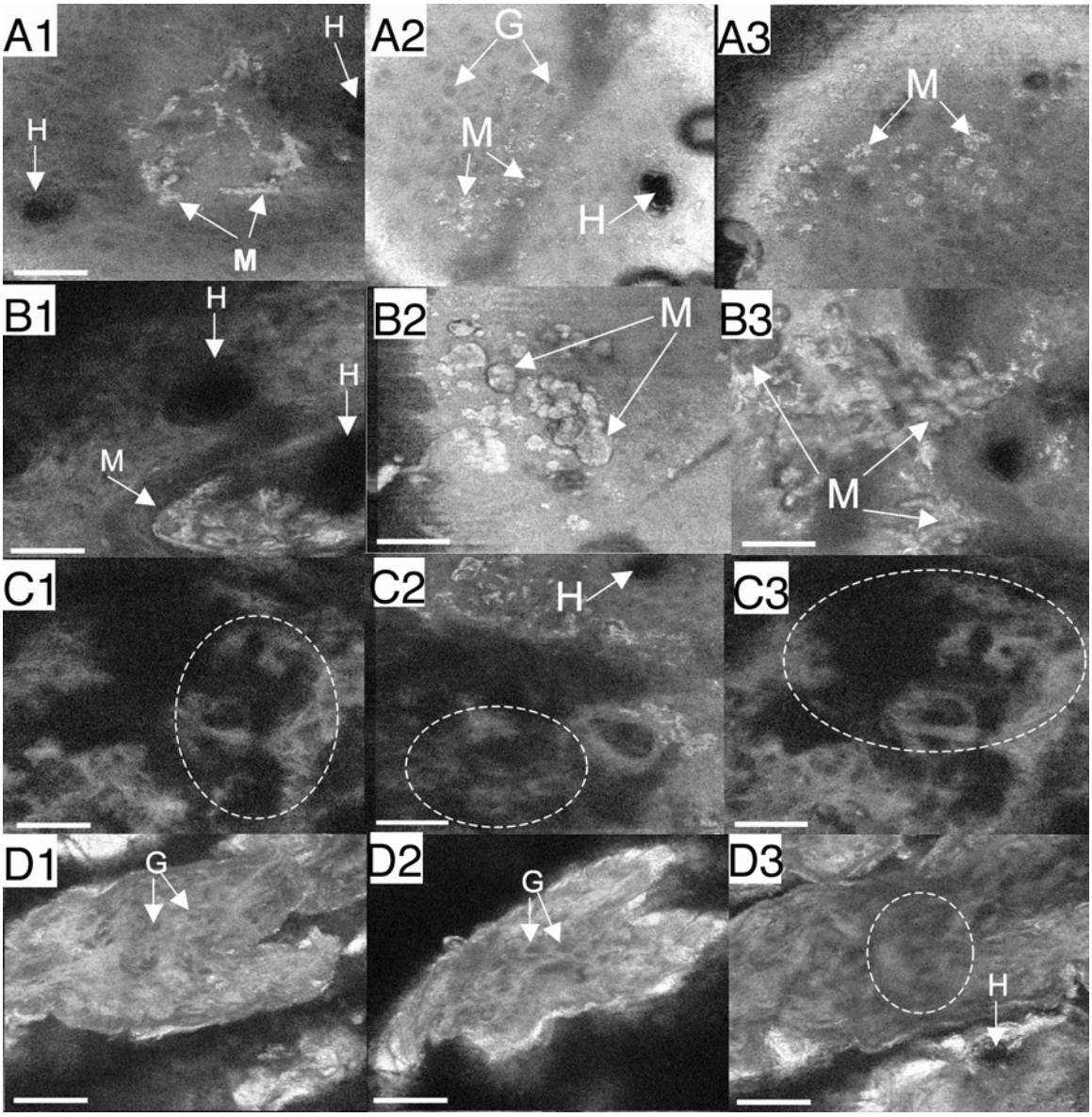

Figure 7.9 Tumor images (A-C) vs. normal images (D). A: Irregular epidermal melanocytes (M) in the epidermis and hair follicles (H). B: a melanoma tumor nest (M) and hair follicle (H). C: Disruption of the dermal/epidermal junction is characterized by its broken appearance. D1,D2 healthy epidermis presents granular cells with dark nuclei. D3: Approximately 10 μm below the healthy epidermis, the healthy dermal/epidermal junction presents as relatively uniform and intact.

7.E Discussion

This report illustrates our attempt to image melanoma and characterize malignancy in early-stage tumors. It was a challenge to follow lesions on a living animal and prepare histology of the same region with precision. The endogenous landmarks used such as hair follicles proved insufficient to reliably and consistently correlate the confocal microscopy with the histology. Exogenous markers such as tattooing should be pursued. Although the resolution limit of the eye is less than 100 μm, lesions less than 1 mm were chosen as starting points. Comprehensive cancer imaging for detection of epidermal tumors might include confocal mosaics[71] of a large square region (~2x2 cm), marked by tattoo on younger animals over time with corresponding polarized light images[67, 68, 69].

The highly pigmented HGF/B6 mouse develops a heavily melanized, flaking stratum corneum (SC) that presents in the confocal microscopy as a very bright superficial 5 μm layer. A gentle sponge cleaning prior to imaging minimized this effect. This strong reflectance occured because the bulk refractive index of stratum corneum (n = 1.47) is higher than that of epidermis (n = 1.34) and even higher when containing melanin (n = 1.7). This highly reflective layer was seen to cast shadows on the deeper epidermis and obstruct epidermal and dermal imaging for some but not all areas. The effect of shadowing in confocal images was not fully understood. In addition to the shadows cast by the melanized stratum corneum, shadowing was seen beneath some melanocytic cells but not all (images not shown).

This report has concentrated on illustrating two features of apparent melanoma: (1) the presence of melanocytic cells and tumor nests in the epidermis indicative of pagetoid spread, and (2) disruption of the dermal/epidermal junction. The epidermal melanocytes and tumor nests were both characterized by bright reflectance due to melanin. The relative reflectance of a melanoma cell vs. background epidermis (Figure 7.6) was measured to be 5.3, which agreed with the simple model of a melanin/epidermis interface, which is 5.2 (Eq. 7.1). Five tumors additionally studied (table 7.1) showed a

relative reflectance of 5.6 +/- 0.9, also agreeing with the model. In general, the images of tumors contained a high degree of heterogeneity in rCSLM images compared with their normal counterparts.

The rCSLM images were able to distinguish normal skin sites from sites with apparent melanoma. This imaging modality is expected to enable studies of the onset and progression of melanoma lesions in animal models.

Chapter 8: Imaging melanoma in a murine model using reflectance-mode confocal scanning laser microscopy and polarized light imaging. (Published, see [67])

8.A Abstract

The light scattering properties of cutaneous tissues provide optical contrast for imaging the presence and depth of pigmented melanoma in a highly pigmented murine model, the C57/B6 mouse. Early lesions are difficult to identify when viewing black lesions on a black mouse. Two methods were used to image early lesions in this model. (1) A reflectance-mode confocal scanning laser microscope (rCSLM) was built to provide horizontal images (x-y at depth z) and transverse images (x-z at position y) non-invasively in the living mouse. (2) A polarized light imaging (PLI) camera was built using a linearly polarized white light source that viewed the skin through an analyzing linear polarizer oriented either parallel or perpendicular to the illumination's polarization to yield two images, "PAR" and "PER", respectively. The difference image, PAR-PER, eliminated multiply scattered light and yielded an image of the superficial but subsurface tissues based only on photons scattered once or a few times so as to retain their polarization. rCSLM could image melanoma lesions developing below the epidermis. PLI could distinguish superficial from deeper melanoma lesions because the melanin of the superficial lesions attenuated the PAR-PER image while deeper lesions failed to attenuate the PAR-PER image.

8.B Introduction

This report summarizes a presentation at the 53rd annual Montagna Symposium on Skin Biology, Salishan Lodge, Gleneden, OR, Oct. 15-19, 2004, which described the use of two novel optical imaging techniques to monitor the onset and progression of melanoma lesions in a highly pigmented murine model, the C57/Black-6 mouse (C57/B6) (Jhappan *et al*, 2003[72]). The two techniques are (1) reflectance-mode confocal scanning laser microscopy (rCSLM) (Rajadhyaksha *et al*,1995[8]), and (2) polarized light imaging (PLI) with a CCD camera, which was introduced by (Jacques *et al*, 2000[68], 2002[69]).

The ability of the eye to detect early cancer lesions is limited. In human tissues, this task is comparable to discerning a drop of milk on a white plate. There is no contrast based on color. However, there is a difference in light scattering. Techniques such as rCSLM and PLI provide contrast based largely on photon scattering and can discern early changes that appear colorless but influence photon scattering. Imaging early lesions in a highly pigmented skin like the C57/B6 mouse offers a similar challenge, comparable to discerning a drop of black ink on a black plate. Again, the difference in light scattering offers a mechanism of contrast.

In this report, the ability of rCSLM and PLI to image early melanoma lesions in the C57/B6 mouse is demonstrated. The significance of such imaging is that early lesions can be detected for biopsy, and that lesions can be followed with noninvasive imaging in longitudinal studies to monitor the progression of cancer in this model.

The reflectance-mode confocal scanning laser microscopy (rCSLM) follows the work of Rajadhyaksha *et al*,1995, but uses the short wavelength of an argon ion laser (blue light, 488 nm) to optimize the reflectivity from very superficial epidermis and sub-epidermal layers of mouse skin. The mouse skin is very thin, eg., the epidermis varies between 10-20 μm in thickness, and imaging must be able to perform well in this superficial region.

The polarized light imaging (PLI) at first glance would appear to be similar to the current common practice of dermatoscopy, which often illuminates with linearly polarized light and views through a "parallel" polarizer to accent the surface glare or views through a "perpendicular" polarizer to reject the surface glare and accent the multiply scattered light. The latter image back-illuminates blood vessels and melanin and provides very good images based on absorption of light by these structures. However, the image does not offer contrast based on scattering of light by the superficial layers. In contrast, the PLI is designed to reject multiply scattered light and generate an image based only on photons scattered from the superficial tissues, thereby imaging the fabric pattern of the superficial dermis whose disruption by cancer growth becomes discernable. The PLI illuminates the skin from an oblique angle through a glass plate that is optically coupled to the skin by a gel or drop of water, so that surface glare does not enter the camera. Then the difference image, "parallel" - "perpendicular", subtracts the multiply scattered light that constitutes most of the backscattered light and obscures details of the superficial tissues. Hence, the PLI image might be called an image based on the "subsurface glare" of the superficial tissues, excluding the glare from the skin surface, and the images are not at all like dermatoscopy images. Application of PLI to the black mouse of this study differed from our previous work with PLI on human skin because the strong absorption by the superficial melanin of this mouse influenced the images and allowed discrimination of superficial versus deeper melanoma.

The long-term goal of this work is to contribute to on-going efforts to "humanize" the mouse melanoma model so that basic science on melanoma onset and progression can be conducted. Such "humanization" involves developing melanoma models in which melanoma originates in the epidermis rather than in the deeper dermis as in current mouse models. Our rCSLM images can detect the early progression of melanoma in sub-epidermal layer and its violation of the epidermal-dermal junction. Our PLI images can survey the entire back of a mouse and discriminate early lesions that are superficial versus deeper.

8.C:Materials and Methods

8.C.1 Animals

The C57/Black-6 mouse model (C57/B6) was developed at the National Institutes of Health (Jhappan *et al*, 2003). The model develops melanoma in sub-epidermal locations, as illustrated in Figure 1 showing a histological preparation of formalin fixed tissue that was prepared using melanin bleach with a nuclear fast red counter stain. All animal studies were approved by the Oregon Health & Science University Institutional Review Board.

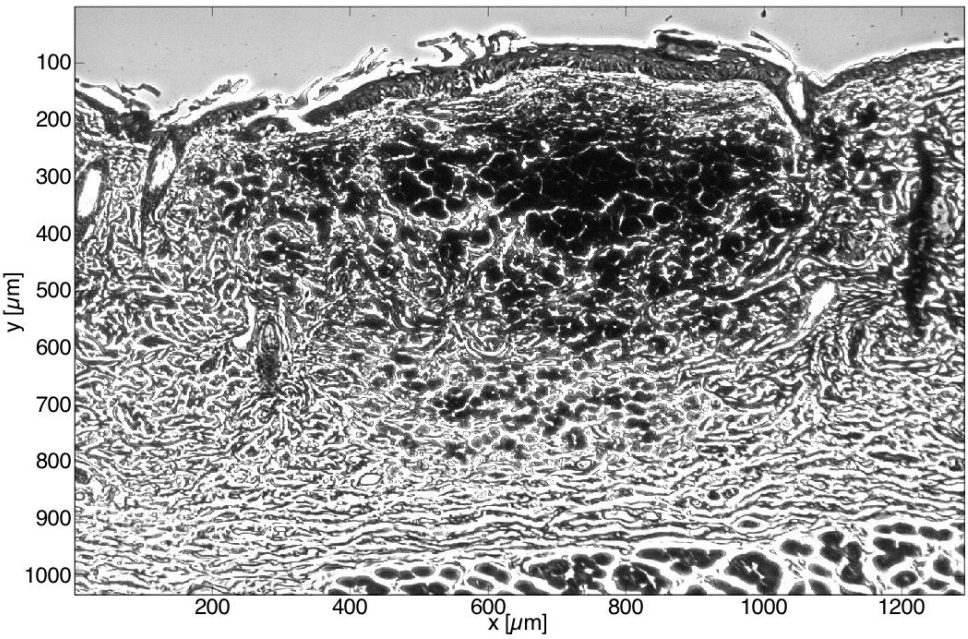

Figure 8.1 Histopathology of melanoma lesions in the C57/B6 mouse. The formalin fixed specimen was prepared using a melanin bleach with a nuclear fast red counter stain. The melanoma lesions originated in the dermis. (Bar = 50 μm).

8.C.2 Reflectance-mode confocal scanning laser microscopy (rCSLM)

Figure 8.2a shows the basic design of the rCSLM system. A collimated argon ion laser operating at 488 nm wavelength, 10 mW power, was sent to the sample via an optical scanning assembly and an objective lens (NA = 0.90, water-dipping lens, 60x magnification, Olympus America, Melville, NY). The beam was directed upward toward the animal by a mirror and focused into the mouse through a droplet of water (normal saline) that coupled the objective lens to the mouse skin through a 4-mm-dia. aperture in the stage that held the animal. The x-y scanning assembly consisted of two galvanometer mirrors and a pair of relay lenses that directed the laser beam into the objective lens at slightly varying angles such that the focus was translated in an x-y plane within the tissue. The laser beam reflected by the tissue from the focus of the lens was recollimated and returned through the optical train until a portion of the beam was re-directed by a beam splitter toward a lens/pinhold/photodetector assembly. Only photons scattered from the focus in the tissue could refocus through the pinhole to reach the photodetector, thereby achieving confocal detection. A normalized pinhole radius of 1.3 (pinhole radius = 1.3 x Airy disk radius) was used trading reduced z-axis resolution for increased light collection. The stage was controlled by a computer-controlled z-axis micrometer that allowed 1-μm steps. For each z-axis step of the stage over a 60 μm range, an x-y horizontal image was acquired by the system. Data was acquired using an A/D converter controlled by Labview^{TM} software (National Instruments Corp., Austin, TX), and image reconstruction was conducted using MATLAB^{TM} software (The Mathworks Inc., Natick, MA).

Figure 8.2b depicts the two types of images that were generated. A horizontal image portrayed an x-y plane at a single depth z. A transverse image portrayed an x-z plane at a single lateral position y. Because the skin is not flat, each horizontal image cuts an x-y plane through the tissue, such that the surface reflectance at the stratum corneum appears as a circle of high reflectivity and the image within the circle is at some depth within the tissue.

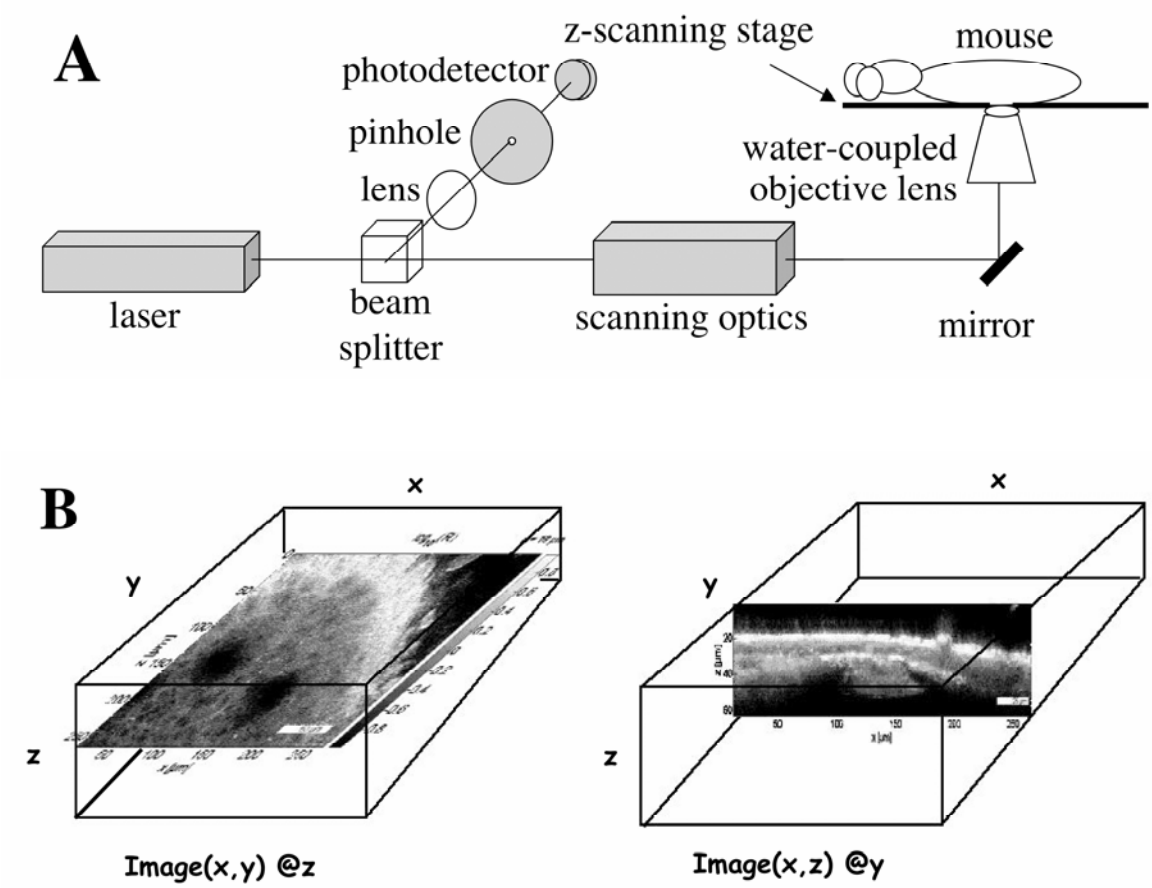

Figure 8.2 Reflectance-mode confocal scanning laser microscopy (rCSLM). (a) The reflectance of a blue laser focused into the tissue by a 60x objective lens is collected by a photodetector as scanning mirrors move the focus over an x-y plane of tissue. A z-axis microscope stage moves the stage holding the animal in 1-μm steps, and x-y images are acquired at a series of tissue depths. (b) The two types of images produced are the horizontal image (x-y at a depth z) and the transverse image (x-z image at position y).

8.C.3 Polarized light imaging (PLI)

Figure 8.3a shows the basic design of the polarized light camera. A white light source was passed through a linear polarizer that was aligned so that the transmitted electric field was parallel to the scattering plane, defined as the source/tissue/camera triangle. The illumination was delivered at an oblique angle (45 degrees) onto a glass

plate contacting the skin of the animal such that glare from the air/glass and glass/skin interfaces was directed away from the camera. Only light that entered the skin could scatter toward the camera and be collected. The animal was coupled to the glass plate by a drop of clear gel (ultrasound coupling gel, ESC Medical Systems Inc., Lumenis Inc. – US Operations, Santa Clara, CA). The light passing to the camera passed through an analyzing polarization assembly consisting of an electronically controlled Faraday rotator (Displaytech Inc., Longmont, CO) that either did or did not rotate the orientation of the polarized light by 90 degrees before the light passed through a second linear polarizer then entered the camera. As the Faraday rotator was switched, the camera received light that was oriented either parallel to or perpendicular to the orientation of the illumination light, yielding two images called “PAR” and “PER”, respectively. A color CCD camera (Micropublisher, QImaging Inc., Canada) acquired the images as 384x512 pixel images for the red, green and blue channels of the camera. For this paper, only the green channel images were used. A DARK image was acquired with the camera aperture closed and this image was subtracted from the PAR and PER images before they were processed.

Figure 8.3b illustrates the different fates of photons propagating in the system. About 5% of the delivered photons were deflected as surface glare from the air/glass and glass/tissue interfaces. About 6% of the photons were scattered by the superficial skin layers involving a single or few number of scattering events such that the photons still retained the polarization of the illumination light, contributing only to the PAR image. About 4% of the photons penetrated more deeply in the skin and were multiply scattered such that their polarization was randomized, yielding equal contributions (2% each) to the PAR and PER images. About 85% of the photons were absorbed by skin largely due to the melanin of the C57/B6 mouse. These % values are only approximate and pertain only to these highly pigmented mouse skin sites. In less pigmented skin sites, the distribution of photons amongst these different pathways is different, with the multiply scattered escaping light approaching 40%, the absorbed fraction dropping to 50%, and the superficial scattering about the same at 5-10%.

The fraction of photons that is superficially scattered and retains its polarization may be denoted as “S”, while the fraction multiply scattered may be denoted “D”, such that

$$\begin{aligned} PER &= D \\ PAR &= S + D \\ PAR - PER &= S \end{aligned} \tag{8.1}$$

and the total reflectance R is

$$R = PAR + PER = S + 2D \tag{8.2}$$

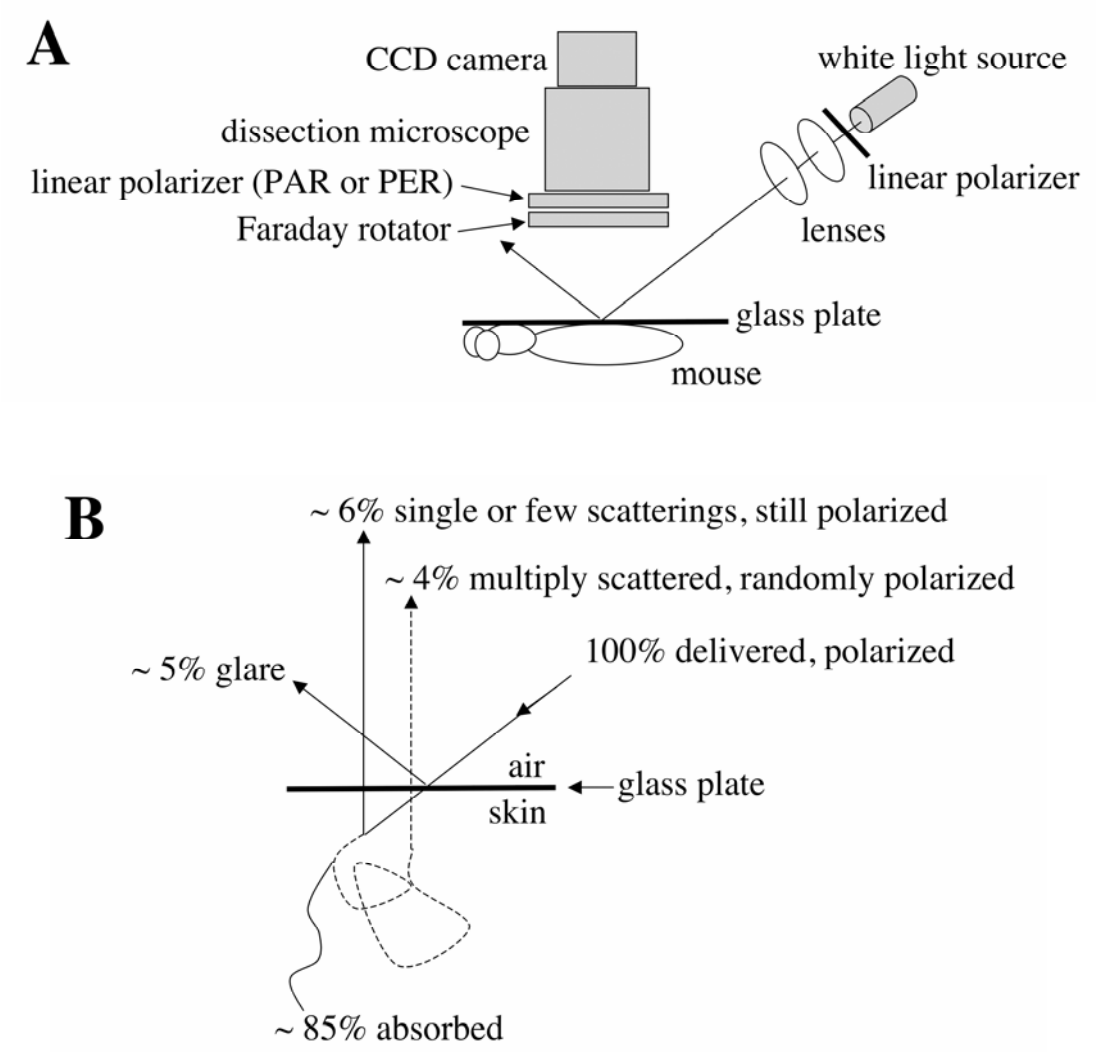

Figure 8.3 Polarized light imaging (PLI). (a) The basic setup is a linearly polarized white-light source that illuminates from an angle of about 45°. The tissue is coupled by a drop of clear gel to a glass plate, such that surface glare from the air/glass and glass/skin surfaces is reflected obliquely away from the camera. Only photons that enter the skin are scattered toward the camera. An analyzing linear polarizer in front of the camera is electronically rotated and aligned either parallel to the illumination or perpendicular to the illumination, yielding two images called PAR and PER, respectively. (b) The photons that scatter from the subsurface but superficial tissue layers retain the polarization of the illumination light (labeled S). The photons that penetrate more deeply and are multiply scattered become randomly polarized (labeled D). Therefore, PER = D, PAR = S + D, and total reflectance R = PAR + PER = S + 2D.

8.D Results

8.D.1 Reflectance-mode confocal scanning laser microscopy (rCLSM)

Figure 8.4 shows examples of rCSLM images. Figure 8.4a shows a horizontal x-y image at a particular depth z. The x-y plane cuts through the irregular surface of the skin such that the surface of the skin presents as a ring of bright reflectance from the stratum corneum, labeled “S” in the figure. The center of the image is at a depth of 19 μm. The keratinocytes of the viable epidermis present as a pattern of dark regions surrounded by brighter material because nuclear chromatin filaments scatter less than cytoplasm and cell membranes (Rajadhyaksha *et al*, 2004[73]). Two melanocytes are labeled as “M1” and “M2”, and appear brighter than the surrounding epidermis due to the strong photon scattering from the melanosomes.

Figure 8.4b shows the same view as Figure 8.4a, however, the depth of the image is 8 μm deeper. Now, the regions underlying the two melanocytes M1 and M2 appear dark. Apparently, the photons are scattered by the melanocyte in their effort to penetrate into and scatter from the region below the melanocyte. Hence, the photon intensity is strongly attenuated and this region presents as a dark region.

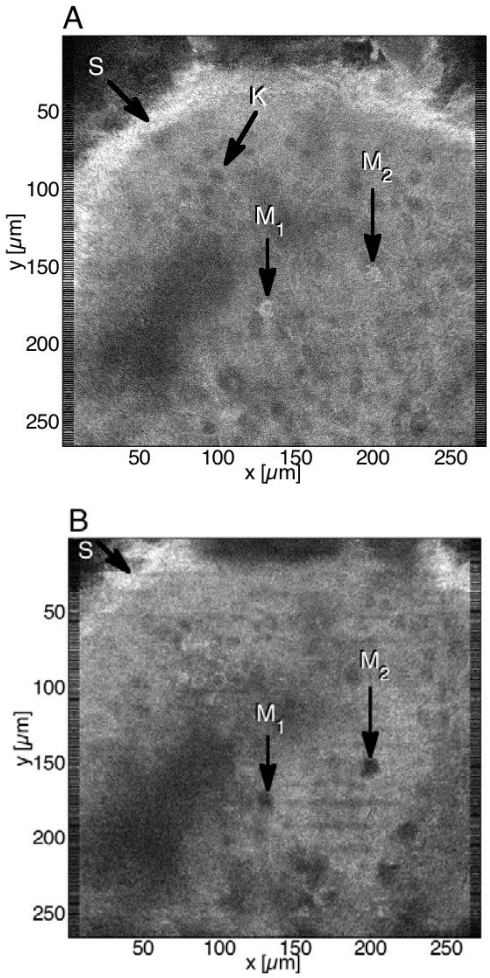

Figure 8.4 Horizontal images using reflectance-mode confocal scanning laser microscopy (rCSLM) for an in vivo mouse dorsal skin site. (a) The stratum corneum (S) is at the skin surface. The depth of the center of image is 19 μm below the skin surface. A keratinocyte (K) shows a typical dark nuclear region surrounded by a brighter cytoplasm and cellular membrane. Two melanocytes (M_1, M_2) are shown, displaying an increased brightness due to scattering by melanosomes. (b) An 8-μm deeper image. The depth of the center of image is 27 μm below skin surface. The two positions below the melanocytes (M_1, M_2) now present dark regions because the overlying melanocytes scatter photons that attempt to penetrate to and reflect from the region below each melanocyte.

Figure 8.5 shows a transverse x-z plane located at one y position. The stratum corneum (S) strongly scatters light and appears bright. The epidermis (epi) is less strongly scattering and appears as a darker layer. The dermal-epidermal junction (dej) and the underlying dermis are more strongly scattering. The dej includes bright melanocytic cells that strongly scatter light. In the center of the image below the dej there is a tumor (T) roughly 20 μm x 50 μm in size. The tumor scatters light rather strongly relative to the surrounding dermis. A patch of bright melanin-containing cells populates the upper portion of the tumor.

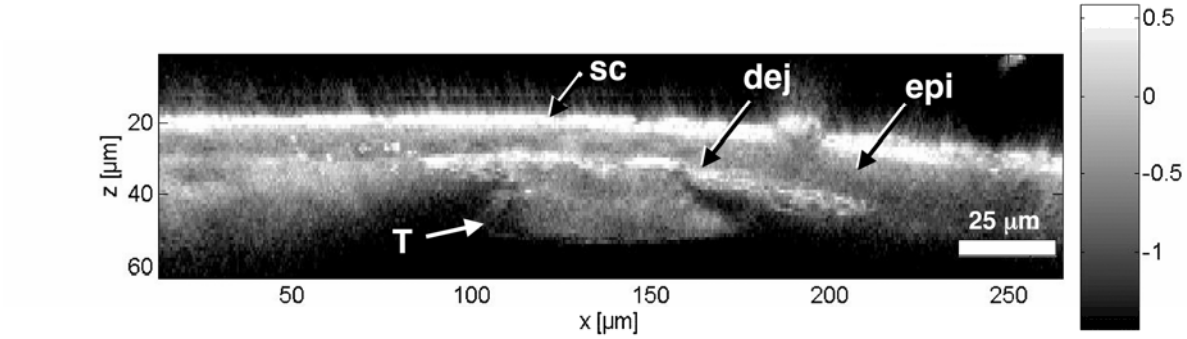

Figure 8.5 Transverse images using reflectance-mode confocal scanning laser microscopy (rCSLM). The water/skin surface at the stratum corneum (sc) appears bright. The epidermis (epi) has lower scattering and presents a darker layer. The dermis is strongly scattering and presents a brighter layer. The melanoma appears bright where light first enters the lesion and melanosomes scatter strongly, and appears dark where melanin absorption prevents efficient penetration and escape of photons. In the center of this image, a 50-μm-wide x 20-μm-thick melanoma lesion is centered at a depth of 15 μm below the epidermis. Bright melanocytes are seen at the dermal-epidermal junction (dej).

Figure 8.6 shows axial scans through a cultured melanoma cell on a glass cover slip and through a melanocyte within the epidermis of the in vivo mouse skin site. The cultured cells were 1984-1 melanoma cells derived from TP-Ras mice treated with DMBA (Broome *et al*, 1999[74]). Figure 8.6a shows an axial scan through one melanoma

cell and the underlying glass slide. This axial scan allows a quantitative assessment of the reflectivity of the melanoma cell ($R_{melanoma} = 0.42x10^{-3}$) using the water/glass interface as a calibration standard ($R_{water\text{-}glass} = 4.4x10^{-3}$). Figure 8.6b shows an axial scan through the melanocyte labeled M1 in Figure 8.4a, illustrating the magnitude of melanocyte reflectance relative to that of the surrounding epidermal cells. The melanocyte reflectance of Figure 8.6b was tentatively equated with that of the melanoma cell in Figure 8.6a to achieve calibration, implying that the background reflectance of the epidermis is about 1.5×10^{-4}.

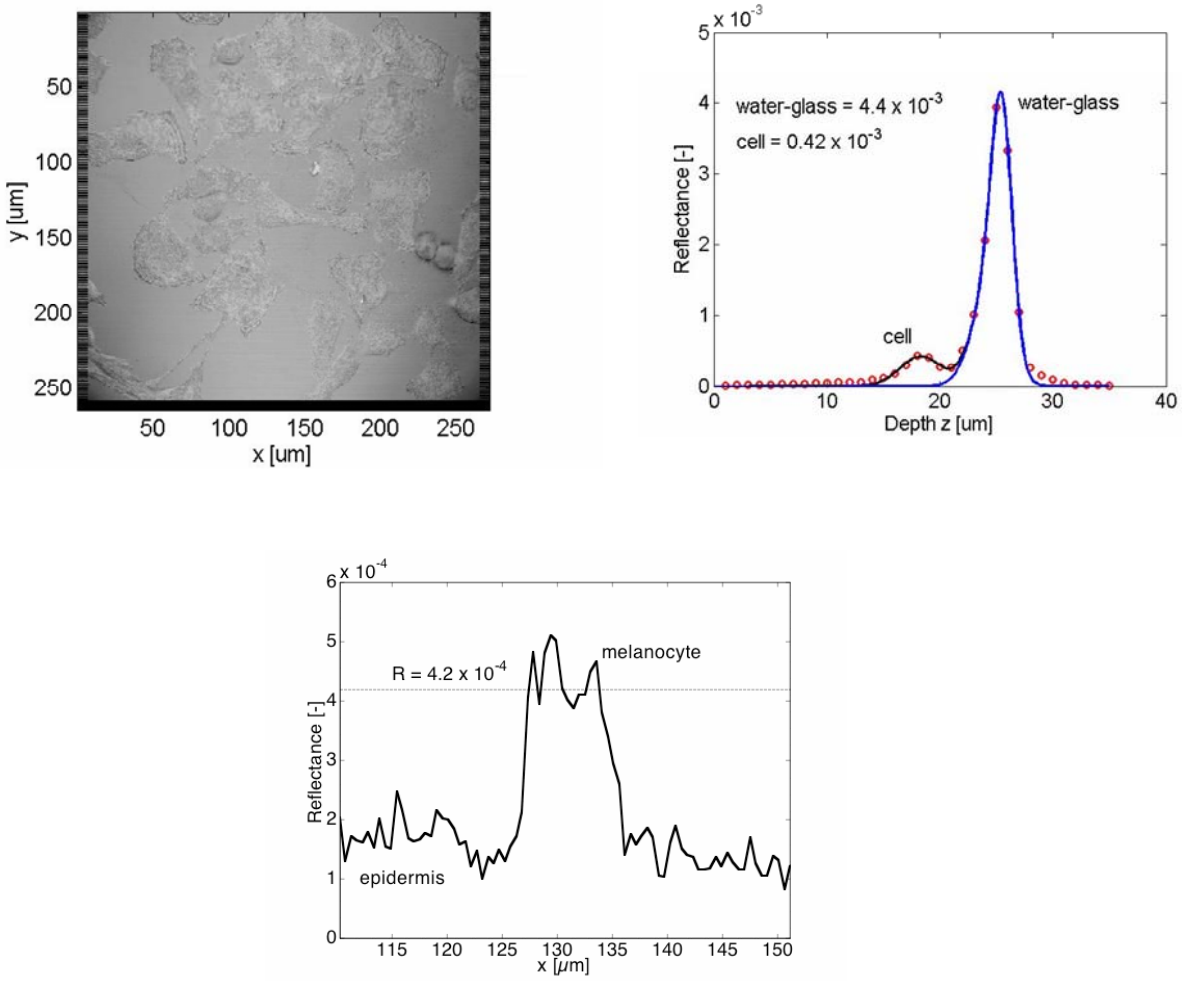

Figure 8.6 Reflectivity of melanoma cells in rCSLM images. (upper left) Axial scan of melanoma cells cultured on a glass cover slip, showing reflectance signal through one melanoma cell and the underlying glass plate. The reflectance of the water/glass interface ($4.4x10^{-3}$) is used as a calibration to allow specification of the reflectance of the melanoma cell ($0.42x10^{-3}$). The scans signals were averaged over the pixels corresponding to one cell. (upper right) Axial scan of reflectance through the melanocyte labeled M1 in Figure 8.6a, tentatively calibrated as being similar to the $0.42x10^{-3}$ cell reflectance of Figure 8.4a, which implies a background reflectance for the epidermis of $0.15x10^{-3}$.

8.D.2 Polarized light imaging (PLI)

Figure 8.7 shows PER and PER-PAR images for the green channel of the color camera. The pixels values were normalized by the total reflectance from a 100% white reflectance standard, so the values are in fractional units of reflectance, 0-1.00. For example, a value of 0.08 implies that the reflectance was 8%. The PER image (Figure 8.7a) consists of D, where D is half of the multiply scattered escaping light. The PAR image (not shown) is brighter because it consists of S + D, where S is the subsurface glare due to single or few scatterings of photons such that the original polarization of the illumination is retained. The difference image, PAR-PER (Figure 8.7b), consists of (S+D) – D = S, which isolates the superficial scattering, S.

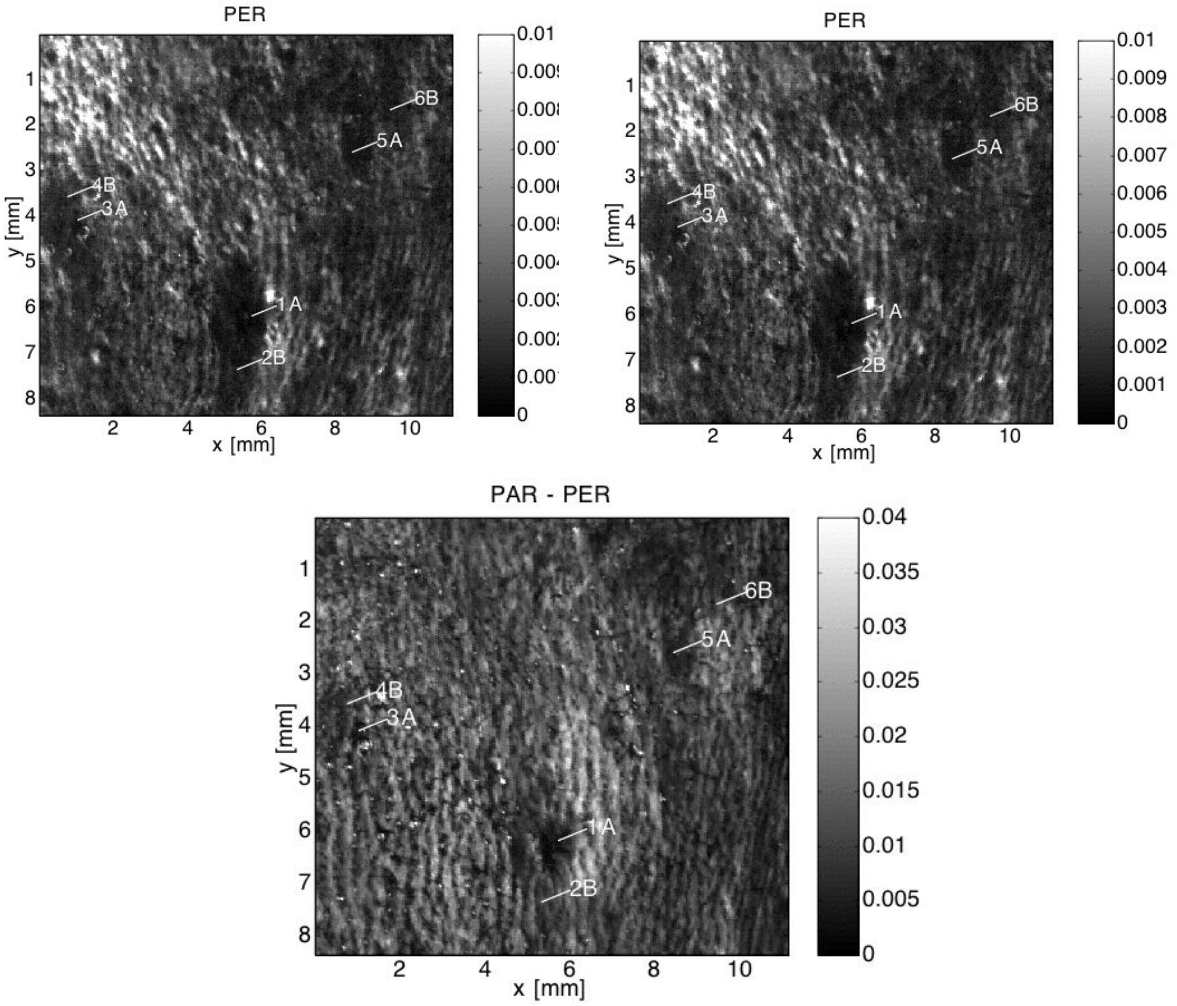

Figure 8.7: Polarized light images (PLI) of C57/B6 mouse with melanoma lesions, using the green channel of the color camera. (upper right) PER image corresponds to deeply multiply scattered light, D, which has randomized the polarization. (lower) PAR-PER image isolates the photons that have undergone a single or few scatterings, S, which retains the polarization of the illumination light. The color bar is in reflectance units where 1.00 indicates the pixel values from a 100% diffuse reflectance standard. Six lesion sites are indicated by labels. A label "A" denotes a superficial melanoma that appears dark in both the PER and PAR-PER images, and a label "B" denotes a deeper melanoma that appears dark in the PER image but lighter in the PAR-PER image due to scattering by the superficial tissues overlying the melanoma.

Two categories of melanoma structure were observed and labeled A and B in Figure 8.7:

(A) Superficial melanoma lesions, characterized by a low value of PER and a low value of PAR-PER. Multiply scattered light penetrates to the lesion where the melanin absorbs photons, so PER is low. Because the lesion is superficial, even superficially scattered photons are attenuated by the melanoma's melanin, so PAR-PER is low too.

(B) Deep melanoma lesions, characterized by a low value of PER but a higher value of PAR-PER. As before, the multiply scattered light penetrates to the lesion and is attenuated, so PER is low. However, the superficially scattered photons scatter off the epidermis and upper dermis and do not reach the deeper melanoma, so PAR-PER is higher.

Values of PAR (i.e., S+D), PER (i.e., D), and PAR-PER (i.e., S) for the lesions indicated in Figure 8.7 are summarized in Table 8.1 as the mean ± standard deviation values for 9 pixels centered at the position indicated in Figure 8.7.

TABLE 8.1: Pixel values of PER, PAR, and PAR-PER for superficial (A) and deeper (B) melanoma lesions.

Lesion	PER (= D)	PAR (= S+D)	PAR-PER (= S)
1A	0.0008 ± 0.0002,	0.0045 ± 0.0003,	0.0037 ± 0.0003
2B	0.0016 ± 0.0002,	0.0146 ± 0.0010,	0.0129 ± 0.0010
3A	0.0012 ± 0.0005,	0.0071 ± 0.0008,	0.0058 ± 0.0008
4B	0.0021 ± 0.0002,	0.0139 ± 0.0008,	0.0117 ± 0.0007
5A	0.0006 ± 0.0003,	0.0059 ± 0.0003,	0.0052 ± 0.0003
6B	0.0010 ± 0.0003,	0.0145 ± 0.0009,	0.0135 ± 0.0009

(mean ± SD, n = 9 pixels, corresponding to the labeled lesions in Figure 8.7.)

Not shown in this report are the color images of PAR, PER and PAR-PER. While the color PAR and PER images look similar to the gray-black image of Figure 8.7A, the color PAR-PER images show an interesting distribution of colors where shifts in color toward red or blue indicate how the skin's architecture (i.e., the depth of the melanoma) and ultrastructure (i.e., the diameter of collagen fiber bundles) is shifting the balance of red versus blue photon reflectance.

8.E Discussion

These preliminary results were shown at the 53rd annual Montagna Symposium on Skin Biology to illustrate the opportunity for novel optical imaging to assist the early detection of skin pathology in murine models. The early detection of the lesions such as skin cancer facilitates acquisition by biopsy of early stages of disease. Non-invasive imaging allows study of the time course of cancer progression. Our current imaging can visualize the onset of melanoma in sub-epidermal locations and its progression as it compromises the epidermis.

The rCSLM studies continue on quantitative assessment of the reflectivity of various cell types as part of an effort to investigate the underlying mechanisms of optical contrast based on photon scattering. The magnitude of photon scattering and the angle- and wavelength-dependence of photon scattering offer a fingerprint that characterizes the architecture and ultrastructure of the skin, a fingerprint that may provide a characterization of the progression of a disease. Our current work is exploring the threshold optical change that allows detection of an early lesion.

The PLI studies continue to explore the mechanisms of contrast available from superficially but subsurface scattered photons. The work of this report is exploring the opportunity for PLI to distinguish superficial versus deep melanoma lesions in the C57/B6 murine model.

In non-melanoma skin pathology, the PAR-PER image presents a complex pattern of reflectivity due to the structure of the superficial papillary dermis, similar to a textured fabric. Pathology disrupts this textured pattern allowing the eye of the doctor to discern the margins of the lesions. Our current clinical work is exploring the use of PLI to guide surgical excision of skin cancers in the dermatology clinic.

Chapter 9: Optical Properties of Murine Skin at 488 nm

9.A Abstract

The scattering coefficient, μ_s (cm^{-1}) and the scattering anisotropy, g were experimentally determined in the murine model. Transmission and anisotropy was measured in 186 skin samples from eight mice. In young animals, the dermal layer is much more translucent than in older animals. The age dependence was found to be: [2days 800 (cm^{-1})] [3days 944 (cm^{-1})] [5days 1,520 (cm^{-1})] [7days 2,086 (cm^{-1})] [10days 2,419 (cm^{-1})] [13days 2,476 (cm^{-1})]. It is believed that fibrosis occurs as collagen fibers become more dominant with age, increasing the scattering. The anisotropy measurements yielded g = 0.98 leading to a reduced scattering coefficient of 16 to 50 (cm^{-1}) for mouse skin between 2 and 13 days of age.

9.B Introduction

Any diagnostic or therapeutic optical work with biological tissue requires knowledge of the relevant tissue optical properties. Transdermal diagnostics and therapeutics rely on light propagation through the skin, which is governed by the tissue optical properties (absorption, scattering, and anisotropy of scatter). This study omits analysis absorption. Despite a lack of an analytical solution to the radiative transport equation and in vivo (blood) tissue-absorption measurements, valuable transport parameters can be obtained by studying scattering, with it's dominating properties in radiative transport through highly scattering biomaterials like skin. Skin is multilayered, however the optical property difference between the epidermis and dermis is mainly due to differences in absorption caused by absorbers such as melanin and blood content. The influence of multylayered structure on estimates of optical properties obtained from

reflectometry has been reported by Farrell et. al [75]. Here, a closer look is taken at thin sections of tissue, which are composed of only one of the layers found in skin.

The scattering properties of skin in the early stages of life was studied by Saidi et. al in the human neonatal model[76]. Scattering was found to increase with gestational age from 10 to 46 (cm^{-1}) in gestational ages of 24 to 60 weeks. The scattering in skin arises from collagen. The goal of this work is to characterize a similar trend in scattering increase in the murine model. We expect collagen fibrosis to progress faster in mice.

9.C Materials and methods

Upon sacrifice of eight (Rosa 26) mice from two litters of different ages, the skin was removed and shaved gently. In subjects under 4 days of age, shaving was not necessary, as hair hadn't developed. The skin was immediately soaked in 0.9% sodium chloride irrigation saline solution and allowed to fully hydrate. The samples were then placed between glass slides and frozen for sectioning. The samples were immersed in Tissue-Tek® (O.C.T. 4583 compound) as an imbedding medium and immediately refrozen in liquid nitrogen to minimize the influence of Tissue-Tek on the skin optical properties. Cryostatic sectioning was then used to produce slices of 2-30 (+/- 1) microns in thickness. The samples were sliced first on the epidermal side of the skin. The slices were immediately immersed in saline solution to standardize the degree of hydration. It should be emphasized that such saline-soaked tissue, which is about 85% water, may not be optically equivalent to *in vivo* skin, which is closer to 70% water. The saline-soaked tissue, nevertheless, offered a standard, reproducible tissue preparation, which avoided the variations due to differences in water content between samples. During experimentation, samples were fully hydrated between a glass microscope slide and a cover slip.

Two types of measurements were made on the skin samples. First, the total attenuation coefficient was measured, and then the anisotropy of scattering was measured.

Scattering was measured by collecting ballistic photons with and without the skin sample in the laser beam path. The light source was a 200 mW, 488 nm argon-ion laser (Melles Griot 35-LAL415-220), and the photodetector was a Melles Griot (13PEM001) power meter. An iris the size of the laser (diameter = 2.5mm) was used to mask the 1-cm^2 detector surface area of the transmitted power detector so that only ballistic photons were collected. The iris was 46 cm from the sample leading to a solid angle of collection equal to $24*10^{-6}$ steradians. This means that "on-axis" photons scattered at angles less than 0.16 degrees were collected as ballistic photons. It is assumed that the total power contained in these photons is negligible. After measuring the raw laser power passing through a blank microscope slide ($P_o \approx 10mW$), the sample was placed in the beam path and transmitted power was measured ($M \approx 1mW$). Knowing the tissue thickness (T) of the tissue sample and the relative power transmitted through the sample composed of ballistic photons, one can easily calculate the total attenuation coefficient (μ_t) using Beer's law:

$$\mu_t = -\log(M/P_o)/T \tag{9.1}$$

Another characteristic optical property of tissue is the anisotropy (g), which describes the directionality of scattering as the average of the cosines of the scattering angles. A device similar to that used by Jacques et. al.[59] was constructed to measure the scattered light as a function of scattering angle with the major differences being that the collection fiber was not immersed in an index matching solution. A goniometric arm rotated about the sample and measured the angular dependence of scattered light intensity.

9.D Analysis

The collection angle (θ_{coll}) in the data sets was corrected for diffraction using Snell's law for refraction to represent the true angle of scatter (θ_{scat}):

$$\theta_{scat} = \sin^{-1}(n_2/\ n_1*\sin(\theta_{coll})) \tag{9.2}$$

The measured phase functions were fit by varying g in a modified Henyey-Grenstein (H-G) phase function to minimize the error between the H-G fit and the data.

H-G phase function[58]:

$$I(\theta) = (1 - g^2)/(1 + g^2 - 2g\cos(\theta))^{3/2} \qquad (9.3)$$

Each sample yielded a different value for g when fit by the H-G phase function. A typical fit to the data is shown.

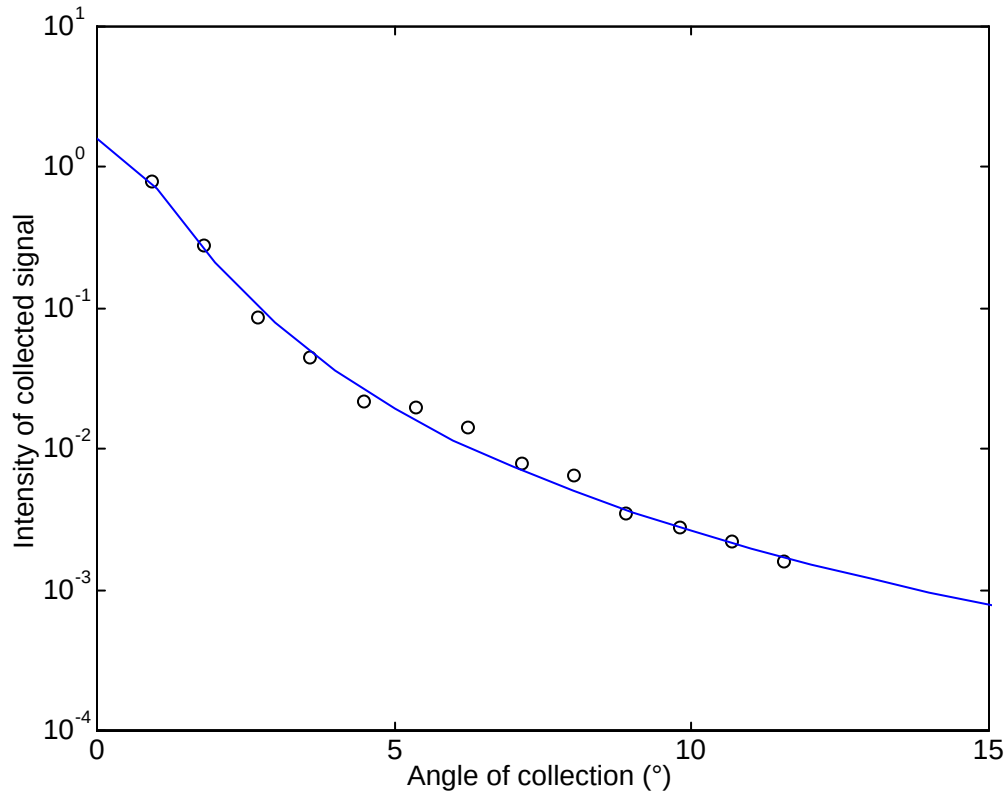

Figure 9.1 Sample fit to the angular dependance of scattered light intensity.

Samples of varying thickness were analyzed. The effective g seemed to be correlated to the optical thickness of the sample. The thicker the sample, the more the apparent g decreased as the effect of multiple scattering spreads the transmitted light.

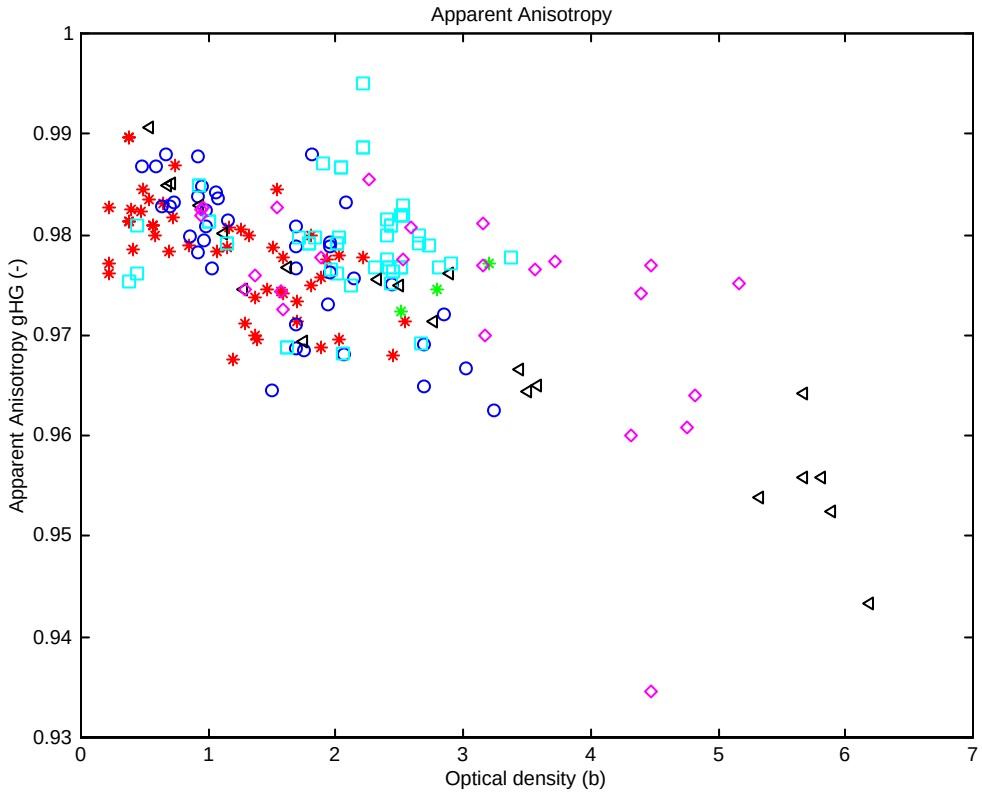

Figure 9.2 Anisotropy results for all samples.

In principal, it should be possible to calculate the absorption coefficient using a numerical integration technique by subtracting the total transmittance through the sample from that of a reference sample. However, errors inherent in the numerical integration technique make it highly unreliable and the approximate value of $\mu_a < 10$ (cm^{-1})[77] should be considered reasonable.

As a check on the ballistic photon method of deducing the scattering coefficient, transmission for each age group was plotted as a function of thickness and fitted with a Beer's law decaying exponential. The 13 day old samples for example:

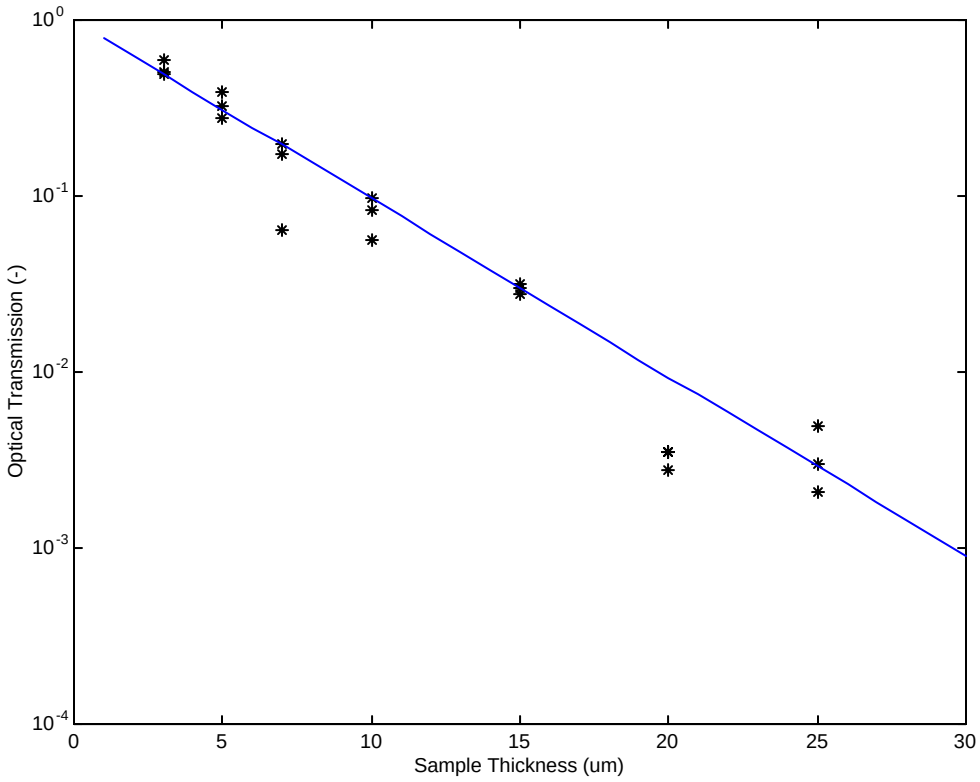

Figure 9.3 Optical transmission through slabs of 13 day-old mouse skin. The total attenuation coefficient (slope of fit) was fit for the data in each age group.

Yet a third algorithm to extrapolate the total attenuation coefficient was implemented via Monte Carlo techniques. MCML by Jacques *et al* was used to simulate the goniometric experiment. Photon packets were launched normally incident into the tissue phantom which consisted of a 1mm glass microscope slide, a certain thickness of tissue with optical properties [mus,g,mua = 1 (1/cm)], and a 100 micron glass cover slide. The emerging phase function was recorded as a function of exit angle I(θ). In this manner, the scattering phase function was determined via simulation. The input variables to the program were the scattering coefficient of the tissue, the anisotropy, and the tissue thickness. The scattering coefficient was varied from 150 to 3000 (1/cm) in steps of 150(1/cm), the anisotropy was varied from 0.965 to 0.995in steps of 0.0025 and the

thickness was varied from 3 to 30 microns in steps of 3 microns. These values were chosen to cover the range of the experimental samples they simulated. A total of 2600 simulations were run with all permutations of input parameters. Once the phase function I(θ) was recorded for a particular sample, it was fit with the same Heyney-Greenstein phase function as the experimental phase function with the apparent anisotropy as the fitting variable.

Each combination of tissue optical properties lead to a different dependence of apparent anisotropy on tissue thickness. The trend was found to be of the form:

$$\text{Apparent Anisotropy} = -(\text{Thickness}.\hat{}A)*B + C \qquad (9.4)$$

Where A, B and C were fitting variables. Each optical property combination lead to a characteristic set of A,B, and C. For each of the optical property combinations, an error was computed between equation 9.4 and the experimental result for each age group. In this manner, the smallest error suggested the combination of optical properties that best matched the experimental result. An example of apparent anisotropy as a function of sample thickness is shown:

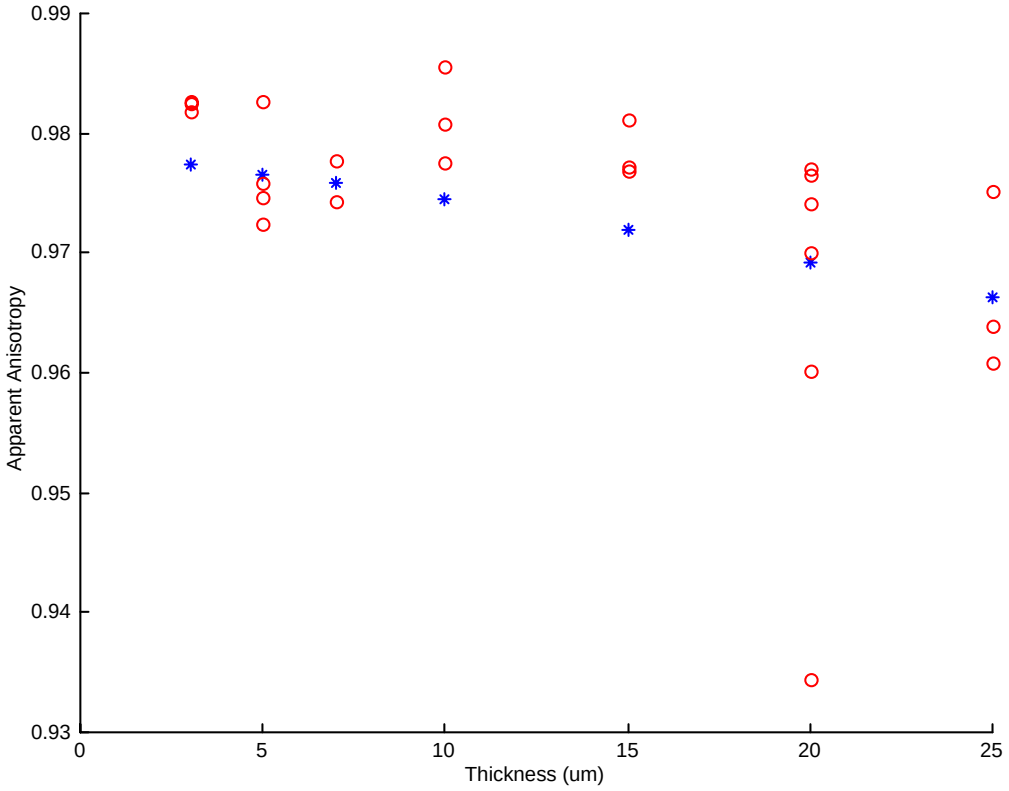

Figure 9.4 Apparent anisotropy was fit as a function of sample thickness. The circles represent experimental results and the asterisks represent the best-fit combination of optical properties from the Monte Carlo simulation.

9.E Results

The scattering coefficient increased from 800 to 2,476 (cm^{-1}) when age increased from 2 to 13 days.

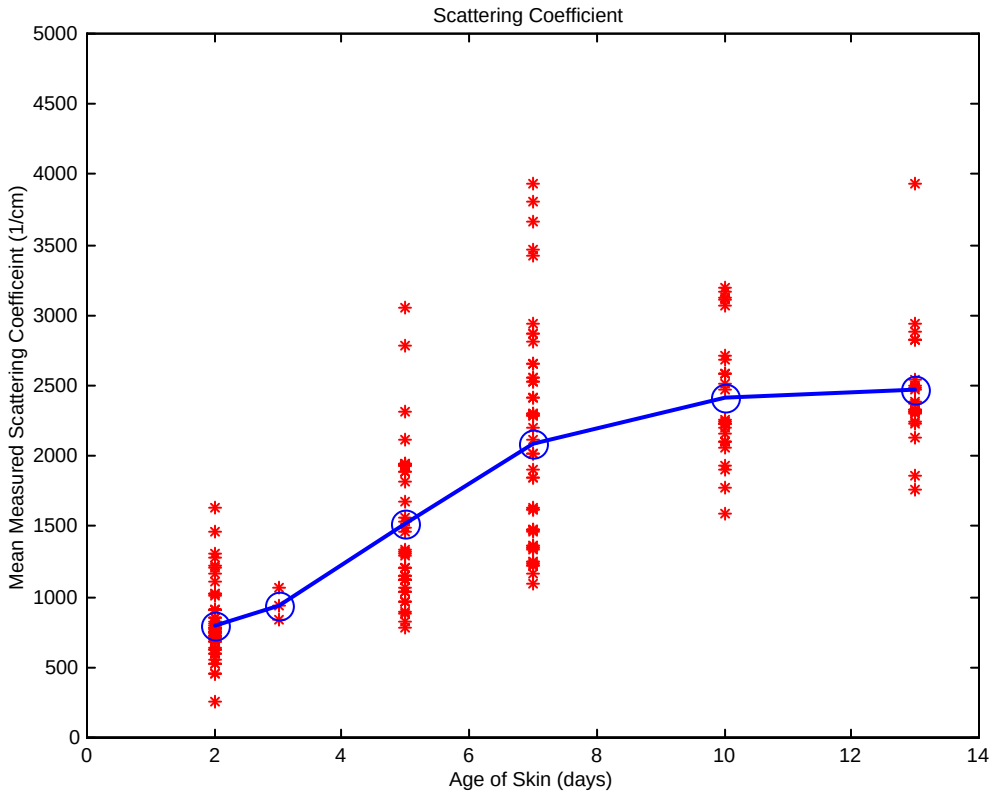

Figure 9.5 Skin scattering coefficient is shown as a function of mouse age.

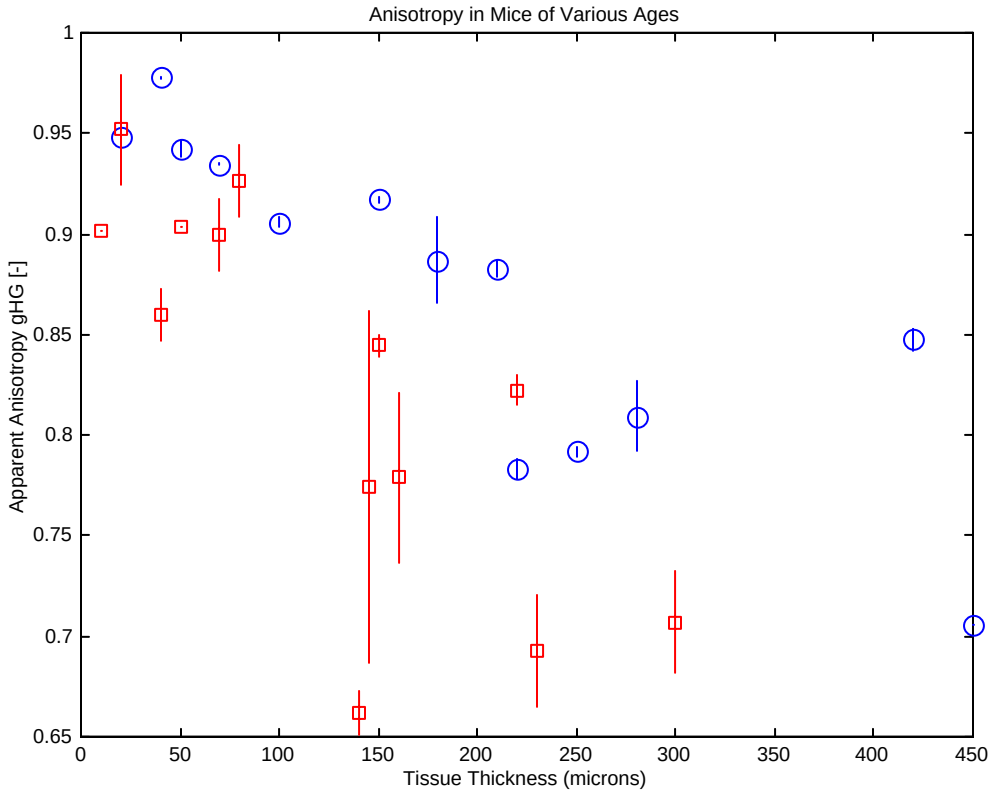

Figure 9.6 Apparent anisotropy for varying sample thickness for two mouse age groups.

Goniometric data showed how older skin had a greater light spreading effect (lower anisotropy). Circles represent three mice of the same litter of ages 2 and 3 days while squares represent 5 mice from 3 litters of ages varying from 16 to 30 days. The thickness of these optically dense samples ranged from 10 to 450 microns. This work first lead the authors to investigate thinner samples because with samples more than a mean free path thick, effects of scattering and scattering anisotropy become indistinguishable because reasonable ballistic photon measurements can not be made. Furthermore, the phase function resulting from he thick samples was obviously a result of multiple scattering, and the trend in apparent anisotropy of scatter supported the multiple scatter theory.

In subsequent work on much thinner samples (2 to 30 microns), the apparent anisotropy for a single scattering event measured on thin samples was found to be about 0.98. Ages of 2,5,7,10 and 13 days are plotted as asterisks, circles, squares, diamonds, and triangles respectively. The anisotropy was seen to fall with increasing thickness as expected, but with such thin samples, the scattering is predominantly single scattering so the anisotropy value of 0.98 is an appropriate estimate for the true anisotropy. To be precise, the mean free path lengths of skin of ages 2, 3, 5, 7,10 and 13 days are 12.5, 10.6, 6.6, 4.8, 4.1, and 4.0 microns respectively, so the inferred true values of anisotropy should be taken from the figure where the data falls at those thickness values. Since the four g values for the four ages falls between 0.975 and 0.980, a blanket statement that the anisotropy of scatter in all ages is 0.980 seems appropriate. This implies that the range of reduced scattering was 16 to 50 (cm^{-1}) in ages 2 to 13 days respectively. This puts the reduced mean free path between 203 and 630 microns which is the depth limit to which confocal imaging is possible[29] due to focal brodening at deeper layers. The results for scattering coefficients deduced from three methods are shown:

Table 9.1 Summary of results. Columns two and three show the experimentally determined scattering coefficient according to a thin sample measurement and the fit to a set of samples of various thickness. The fourth column shows the predicted scattering coefficient of skin according to the Monte Carlo Simulation.

Age (Days)	(1/cm)Ballistic Photon Measurement	(1/cm) Fit of Transmission Versus Thickness for Beer's Law decaying exponential	(1/cm) Monte Carlo Simulation Optical Properties of Best Fit
2	800	768	750
3	944	931	810
5	1520	1615	1050
7	2086	2297	450
10	2419	2846	2100
13	2476	2336	3000

9.F Discussion

Scattering arises from mismatches of refractive index within the skin. Mie theory leads to a good model for the scattering properties of collagen fibers. An analysis by Jacques[78] assumes a collagen fiber refractive index of 1.38 and that of the dermal background substance to be 1.35. For fibers of diameter 400 nm to 5 microns, Mie theory predicts μ_s' to be 20 to 30 (1/cm) and g to be 0.85 to 0.98.

The scattering coefficient we report is much higher than previously published values:

Table 9.2 Summary of literature review for the scattering properties of skin.

Source	Year	Wavelength	Skin Type	$\mu_s' = \mu_s (1-g)$ [cm^{-1}]
Anderson et al	1981	635 nm	Human	80
Jacques, Prahl[79]	1987	488 nm	Mouse	62 = 239(1-0.74)
Jacques et al.[59]	1987	633 nm	Human	34 = 187(1-0.82)
Marchesini et al.[80]	1989	635 nm	Human	44
VanGemert et al.[81]	1989	300 – 550 nm	Human	? = ? (1 – [0.7-0.9])
Marchesini et al. [80]	1992	635 nm	Human	21 to 32
Treweek et al. [82]	1996	633 nm	Human	5 = 420(1-0.988)
Nickell et al. [83]	2000	400 – 800 nm	Human	10 to 20
Saidi et al. [76]	1995	650 nm	Human	10 to 46

Taking the anisotropy of scattering (0.98) into account our value of reduced scattering becomes:

$$\mu_s' = \mu_s (1-g) = 16 \text{ to } 50 \text{ [cm}^{-1}\text{]} \quad \text{ages 2 to 13days} \tag{9.5}$$

This value for reduced scattering is quite consistent with previously published values. The mechanism of light spreading is where the discrepancy lies between our data and that previously published. Jacques and Prahl measured $\mu_s' = 239(1-0.74) = 62$ [cm^{-1}]. Our recent work would suggest that there are many more scattering events per unit sample depth, but that the light-spreading effect per scattering event was less due to high anisotropy of scattering. Similar high anisotropy measurements were found by Treweek et al. [77]. The skin dermis is primarily composed of collagen fibers, which are 3-8 μm in diameter, and collagen fibrils, which are less than 100 nm in diameter. The anisotropy of scatter for a 3 μm-diameter fiber is ≈ 0.97 as predicted by Mie theory, which is in fairly good agreement with our measured anisotropy value.

One possible explanation for our high measurement of anisotropy is the unknown diameter of collagen fibers in the skin. Saidi et al. did histology on neonatal skin and found that the average diameter of collagen fibers was 2 to 5 microns. Weather mouse dermis actually has larger collagen fibers (8-10 microns) or our high g measurement is an error is yet to be seen. The other possible explanation for a higher anisotropy could be that there are less small particles (<1 micron). Scattering from such small particles is better modeled by Rayleigh scattering which typically is much more isotropic. The size distribution of scattering particles determines the effective anisotropy as the absence of small particles may have artificially raised our measured anisotropy.

Chapter 10: Confocal Fluorescence Spectroscopy of Subcutaneous Cartilage Expressing Green Fluorescent Protein versus Cutaneous Collagen Autofluorescence (Published, see [21])

10.A Abstract

Optically monitoring the expression of green fluorescent protein (GFP) in the cartilage underlying the skin of a mouse allows tracking the expression of the chondrocyte phenotype. This paper considers how confocal microscopy with spectral detection can sense GFP fluorescence in the cartilage despite light scattering and collagen autofluorescence from the overlying skin. An *in vivo* experiment tested the abilities of a topical optical fiber measurement and a confocal microscope measurement to detect GFP in cartilage under the skin versus the collagen autofluorescence. An *ex vivo* experiment tested the ability of a confocal microscope without and with its pinhole to detect a fluorescent microsphere underneath an *ex vivo* skin layer versus the collagen autofluorescence. In both systems, spectroscopic detection followed by linear analysis allowed spectral discrimination of collagen autofluorescence (M_C) and the subdermal green fluorescence (M_G) due to either GFP or the microsphere. Contrast was defined as $M_G/(M_G+M_C)$. The in vivo contrast for GFP using optical fiber and confocal measurements was 0.16 and 0.92, respectively. The *ex vivo* contrast for a fluorescent microsphere using a confocal system without and with a pinhole was 0.13 and 0.48, respectively. The study demonstrates that a topical optical fiber measurement is affected by collagen autofluorescence, while a confocal microscope can detect subdermal fluorescence while rejecting collagen autofluorescence.

10.B Introduction

The expression of a biomarker such as green fluorescent protein (GFP) offers a means to monitor the kinetics of cell phenotype expression in animal models. We are assessing two systems for optical monitoring of GFP expression in cartilage to track expression of the chondrocyte phenotype during bone growth plate development. The bone growth plate is a dynamic structure in which a cartilage template is synthesized at the leading edge, degraded and replaced by bone at the trailing edge called the ossification front. The process is orchestrated by chondrocytes that live out a differentiation program in the growth plate. In the system we have been using, the GFP gene sequence is linked to the sequence for type-2 collagen, which is a marker for the chondrocyte phenotype. As fibroblasts convert to chondrocytes, the GFP is expressed along with type-2 collagen and the cells become fluorescent[42]. Such expression is currently assessed by confocal fluorescence microscopy in biologically frozen sections of excised tissue providing an image at a single time. An optical technique that could noninvasively image GFP expression *in vivo* would allow tracking of the dynamics of the chondrocyte population and possibly tracking of individual chondrocyte expression. This paper presents a demonstration of the relative abilities of topical optical fiber detection versus confocal detection of GFP expression in subdermal cartilage.

The confocal technique spatially limits light detection to a confocal volume within the tissue being studied by placing a pinhole in front of the detector. Light emitted or scattered from the confocal volume is focused through the pinhole before reaching the detector. Light emitted or scattered from outside the confocal volume fails to focus through the pinhole and does not reach the detector. Confocal microscopy enables imaging of optically thin sections within optically thick (i.e., turbid) samples[30], and can be implemented both as fluorescence imaging and reflectance imaging. Imaging beneath the surface of the skin is an active research area[8,9,84,85]. Local changes in refractive index, melanin and fluorescence have been used as sources of contrast. Research efforts have focused on reflectance imaging of keratinocytes within the epidermal and dermal layers in humans, but relatively little work has been attempted to image subcutaneous

fluorescence through the full thickness of mouse skin. In this work the young mouse skin was about 260 μm thick when uncompressed as measured with a micrometer, which is about 3 transport mean-free paths (mfp = $1/(\mu_a+\mu_s(1-g))$ where μ_a is the absorption coefficient, μ_s is the scattering coefficient and g is the anisotropy of scattering) according to previous studies documenting the optical properties of mouse skin of various age. Noninvasive imaging of GFP expression in subdermal cells is an attractive goal, but weak target fluorescence, optical attenuation and collagen autofluorescence limit detectability, where detectability has been defined by Gan and Sheppard 1993[86]. Many methods for increasing contrast and clarity in images of GFP fluorophores surrounded by autoflourescent tissue have been investigated[20]. Many biological fluorophores such as collagen (in skin) and lipofuscin[23] (in brain tissue) have emission spectra that overlap that of GFP and can thwart imaging with artifacts and poor contrast. It is possible to use methods such as narrow band filtering[87] and fluorescence lifetime discrimination[23] to separate GFP fluorescence from unwanted autofluorescence. Two green fluorescent targets with similar fluorescent yield were used in this work, a polystyrene microsphere and tissue containing GFP. The green fluorescence in the sphere containing "fluorescein-like" dye is comparable to that of a GFP containing cell in quantum efficiency and the product of extinction coefficient and concentration.

The benefit of using a confocal fluorimeter for measuring subdermal fluorescence is that it minimizes collagen autofluorescence and maximizes subdermal green fluorescence. This spatial filtration is intrinsic to the confocal design. By adding a pinhole gate in the sample's conjugate plane, the focal volume of the sample is confined and detection of the target fluorescence is optimized. While this confocal technique is successful in removing detected fluorescent emission from surrounding regions, some autofluorescence is detected which partially corrupts the subdermal target fluorescence signal. The purpose of this work is to spectrally quantify and compare the green signal and autofluorescent noise.

10.C Materials and Methods

10.C.1 Animal Model

Experiments used transgenic mice (Rosa 26) which harbored a Col2-GFP reporter that marks chondrocytes by enhanced green fluorescent protein (EGFP) expression linked to type-2 collagen expression in the cartilage[42]. Mice were approximately one week in age. In the experiments labeled as *in vivo*, the optical fiber probe measurements were made on the ear of one mouse in vivo. The confocal microscope measurements were made on the abdomen (subdermal cartilage in the xyphoid process) of a second mouse freshly euthanized. The two fluorimeters were not assembled at the same time so the same animal could not be used. Although the measurement sites were anatomically different, they do illustrate the confocal principal and are suitable for spectral analysis. In the experiment labeled as *ex vivo*, abdominal skin samples were excised from a third mouse that was not transgenic and did not express EGFP. EGFP contains mutations[41] from GFP that shift its excitation peak from 475 to 490 nm which is appropriate for excitation using the 488 nm light of the argon laser. The emission peak is roughly at 509 nm depending on the chemical environment. The autofluorescence of collagen in human skin has been studied extensively in the ultraviolet range[88]. Collagen autofluorescence peaks at about 550 nm when excited in the 470-490 nm range. The autofluorescence spectrum for mouse skin is nearly identical to that of human skin[89].

10.C.2 Confocal System

The confocal laser fluorimeter (Fig. 10.1) used an argon ion laser (Melles Griot 35-LAL-415-220R, 488 nm wavelength, adjusted to provide 1 mW to the sample) to excite fluorescence that was measured with a spectrometer (Ocean Optics Inc., set to 100 ms acquisition time). Excitation and emission light were separated using a dichroic beam splitter (Custom Scientific 500 UHP DCLP) and a Raman rejection filter (Omega Optical XR3000, OD 5). The dichroic beam splitter allowed excitation light to be injected into the optical path of the system and fluorescent emission light to pass to the detector. For

detecting GFP beneath collagen, a band-pass filter centered at approximately 510 nm for GFP emission (≈500-530 [nm]) would best discriminate against collagen autofluorescence, which peaks at longer wavelengths[88]. In this work a long-pass filter at 500 [nm] was chosen based on its transmission of the GFP fluorescence and collagen autofluorescence in the 500 to 700 nm range. A Raman rejection filter (Omega Optical XR3000, OD 5) further blocked excitation light from reaching the detector. A 50-mm-diameter collection pinhole and 60-x, 0.85 NA objective lens achieved confocally matched gating. The lateral resolution element, defined as $0.46\lambda/NA$[27], was 0.26 [μm] which mapped to about 50 [μm] in the pinhole plane. The returning fluorescence emission was focused into an optical fiber that carried light to the spectrometer.

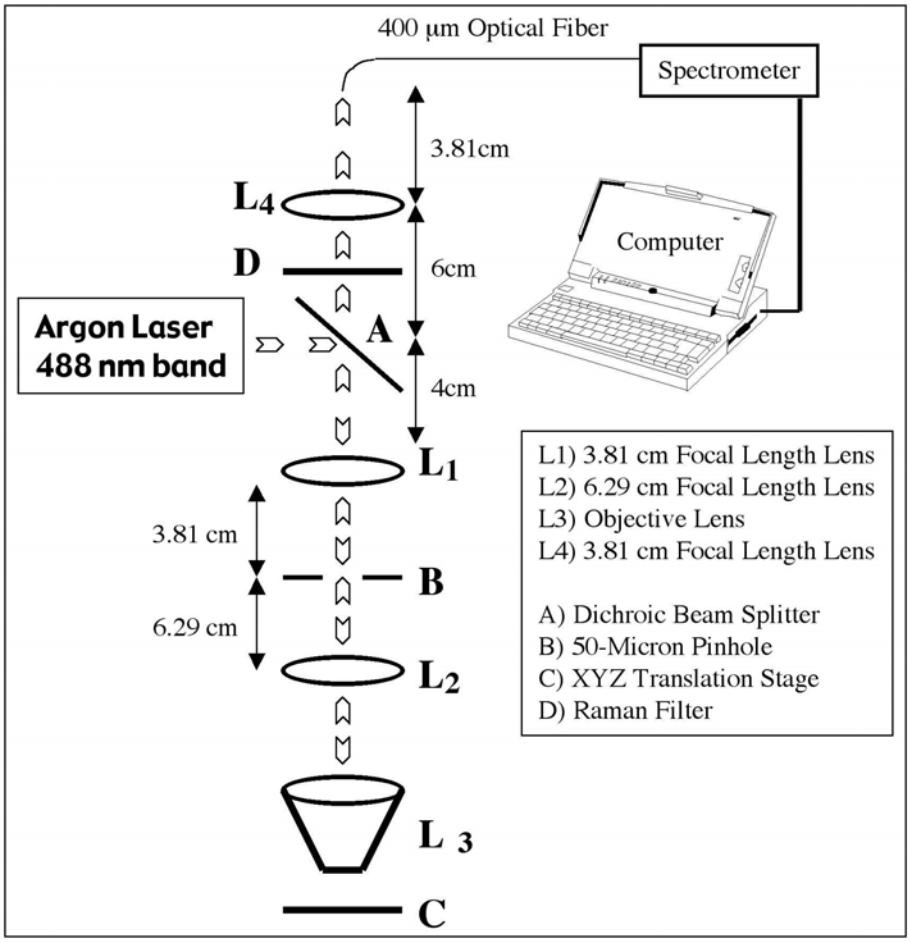

Figure 10.1) Experimental apparatus

10.C.3 Optical Fiber Probe

An optical fiber probe fluorimeter was used to collect multiply scattered fluorescent emission measured from a transgenic mouse. The fiber probe fluorimeter consisted of a single 600-μm-core-diameter optical fiber (0.39 NA) that delivered excitation and collected fluorescent emission while in contact with the skin. The single fiber of the probe was coupled by an SMA connector to an optical fiber bundle probe in which the central fiber (300-μm-core-diameter) injected excitation light into the single fiber probe and the surrounding ring of twelve collection fibers (100-μm-core-diameter) collected returning fluorescent emission from the single fiber probe. The system used a pulsed nitrogen dye laser to excite fluorescence at 460 nm. Twenty pulses of 30 [μJ] were used for each measurement. An optical multi-channel analyzer (OMA) (Princeton Instruments Inc.) detected and accumulated counts for the twenty fluorescence spectra measured. A high-pass absorption filter blocked the 460-nm excitation light from entering the OMA. The probe was held in contact with the skin during measurements.

10.C.4 Whole Animal Experiment

The optical fiber probe fluorimeter was used to collect multiply scattered fluorescent emission from subdermal EGFP-expressing chondrocytes measured on a transgenic mouse. The probe was held in contact with the skin of a mouse pup at the base of the ear. The system was brought into the animal facilities allowing measurements to be conducted on the live mouse. In a second mouse, the confocal fluorimeter was positioned over EGFP-expressing chondrocytes in the subdermal xyphoid process (breast bone) of the intact freshly euthanized animal. The specimen holder was a plastic 1-mm slide with a 2-cm square window. Over the window was glued a 100 μm glass cover slip and against the cover slip rested the mouse chest where the xyphoid process pressed the skin to the glass. The whole animal was then translated toward the objective lens until the focus lay within the cartilage of the xyphoid process. The animal's position was adjusted by micrometer control of the xyz translation stage to maximize the spectral reading of

EGFP. Because the confocal system could not be brought to the animal facilities, the mouse was euthanized less than one hour before measurement.

10.C.5 Excised Tissue Experiment

Skin samples were obtained from a euthanized third mouse that was not transgenic and did not express EGFP. The tissue preparation consisted of a 100-μm glass cover slip, a 100-μm layer of mouse skin and a 1-mm glass microscope slide. The skin layer was prepared by frozen section and included the stratum corneum surface. The tissue was kept hydrated during the preparation process by submersion in phosphate buffered saline. The tissue was therefore different from the *in vivo* skin because it didn't have as much blood content. The absorption was therefore less but the difference was assumed negligible for optical transport because scattering dominates over absorption in skin[59]. A 6mm diameter green fluorescent microsphere (Molecular Probes A-7313), whose fluorescent yield is comparable to a cell expressing GFP, was placed on the glass slide beneath the murine skin layer. The focus of the confocal fluorimeter was aligned with the microsphere by micrometer adjustment of the xyz translation stage holding the preparation. The fluorescence spectrum was recorded. The pinhole was then removed from the system to illustrate a wide-field measurement and the spectrum recorded. Separate measurements of the fluorescence of the microsphere and of the autofluorescence of the skin were also recorded, which served as reference spectra for subsequent analysis.

10.D Analysis

The acquired fluorescence spectra were normalized by the transmission spectra of the dichroic beam splitter and Raman filter. The resulting spectra were then fit using a least squares algorithm that modeled the total fluorescence spectrum $F_T(l)$ as a weighted sum of the reference spectra $F_C(l)$ for collagen and $F_F(l)$ for the target fluorophore, either EGFP or fluorescent microsphere, in units of [counts]:

$$F_T(\lambda) = C_C F_C(\lambda) + C_F F_F(\lambda) \tag{10.1}$$

where C_C and C_F were the fitting parameters and *l* denotes wavelength. For the *in vivo* measurement using the confocal system, the $F_C(l)$ was obtained from direct measurement of the skin of the third non-transgenic mouse. For the *in vivo* measurement using the optical fiber and OMA system, the $F_C(l)$ was approximated by a Gaussian that accounted for both the collagen autofluorescence and the effect of the tissue optics that influences the penetration of excitation, the escape of emission and the collection efficiency of the fiber[90]. The $F_F(l)$ for EGFP was obtained from Clontech Inc., Palo Alto, CA. The $F_F(l)$ for the microsphere was obtained by direct measurement of an isolated microsphere. The total magnitude of fluorescence for each fluorophore was determined by integrating the curves that composed the best fits to the experimental data. The total counts detected for each fluorophore in each experiment was calculated by summing the counts over all wavelengths for the weighted spectra of the particular fluorophore. For instance, the magnitude of the collagen fluorescence (M_C [counts]) was calculated:

$$M_C = \sum_{\lambda=500nm}^{\lambda=700nm} C_C F_C(\lambda) \tag{10.2}$$

The contrast for target detection was calculated by dividing the magnitude of fluorescence of the target fluorophore (M_F) by the sum of the target and collagen magnitudes.

$$Contrast = \frac{M_F}{M_C + M_F} \tag{10.3}$$

10.E Results

The whole animal experiment used the optical fiber probe to measure the ear of a live mouse, and used the confocal system to measure the abdomen of an intact freshly

euthanized mouse. Figure 10.2 shows the results. The curves shown are the fitted curve for collagen (denoted by A), the fitted curve for EGFP (denoted by B), the combination (denoted by C), and the actual data (denoted by D). The confocal system showed only a slight amount of background collagen fluorescence (A) and a strong signal from the EGFP (B). The fiber probe showed a large background of collagen autofluorescence (A) with a small amount of EGFP fluorescence (B).

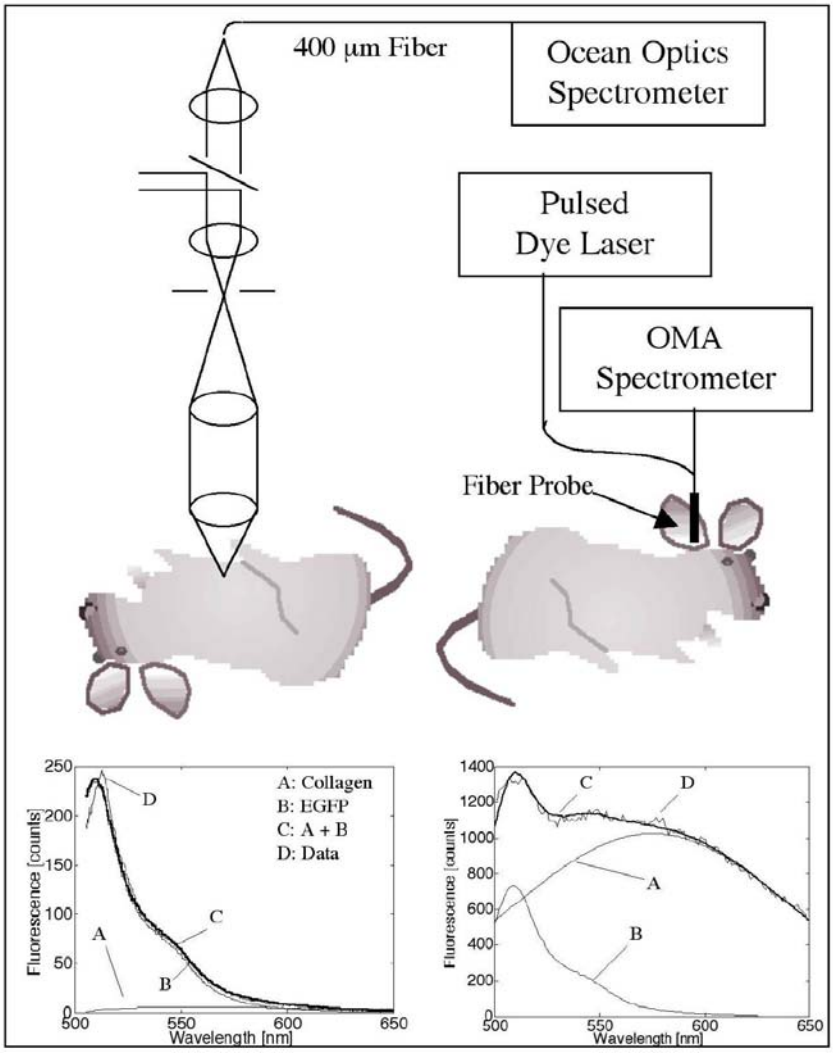

Figure 10.2) Whole animal experiment. Fluorescence spectra from Rosa 26 mice shows collagen fluorescence and EGFP fluorescence. The locations of measurements were the (left) xyphoid process and (right) ear for the confocal and fiber probe, respectively.

The excised tissue experiment used the confocal system to measure a fluorescent microsphere beneath a layer of skin from the nontransgenic mouse. Figure 10.3 shows the results, and the labeling is the same as in Figure 10.2. With the pinhole in place, the system yielded a confocal measurement in which the peak microsphere fluorescence (peak of curve B) was greater than the peak collagen fluorescence (A). With the pinhole removed, the system yielded a wide-field measurement in which the peak microsphere fluorescence (B) was less than the peak collagen fluorescence (A).

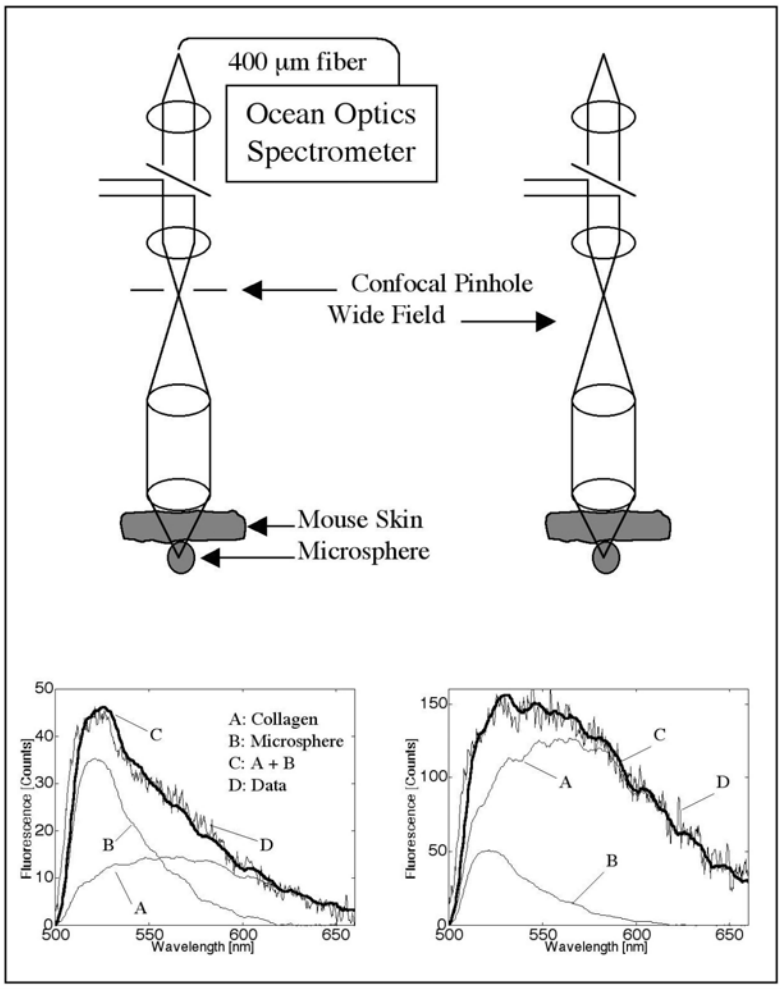

Figure 10.3) Excised tissue experiment. The fluorescence spectrum from a fluorescent microsphere beneath a 100-mm layer of mouse skin is shown for measurements (left) with a pinhole and (right) without a pinhole.

Table 10.1 summarizes the results for all the experiments. In the *in vivo* measurements of EGFP, the contrast for green fluorescence was 0.92 versus 0.16 using the confocal system and the optical fiber probe, respectively. In the *ex vivo* measurements of microsphere fluorescence, the contrast for green fluorescence was 0.48 versus 0.13 using the confocal system (with pinhole) and the wide-field system (no pinhole), respectively.

Table 10.1: Magnitude of the measured collagen autofluorescence (M_C) and the target fluorescence (M_G) as calculated in equation 10.2, and the contrast as calculated in equation 10.3.

	M_C [counts]	M_F [counts]	Contrast
Microsphere (wide field)	43,720	6,732	0.13
Microsphere (confocal)	5,010	4,660	0.48
Mouse(wide field = fiber)	127,040	24,922	0.16
Mouse(confocal)	1,863	20,808	0.92

10.F Discussion

The experiments illustrate the ability of a confocal measurement to optimize the selective measurement of a subdermal fluorophore while rejecting the collagen autofluorescence in the overlying skin. This general method would be useful in a number of different applications such as determining localized microscopic variations in photosensitizing drug content for photodynamic therapy or variations in collagen autofluorescence in skin. Although the fluorescence efficiency of collagen is not very high relative to that of the green fluorophores in these experiments, the skin presents a large volume such that the optical fiber probe collects a large amount of collagen autofluorescence. As illustrated in figure 10.4, the voxel of collection or sampling volume for the fiber probe is the portion of the diffuse glow-ball of fluorescent emission

which escapes within the cone of collection[90] of the fiber. The confocal system limits the collection of fluorescence from the whole skin volume to the subdermal confocal volume which is on the order of a cubic micron[27], and consequently the fluorescence of the subdermal green fluorophores can dominate over the collagen autofluorescence.

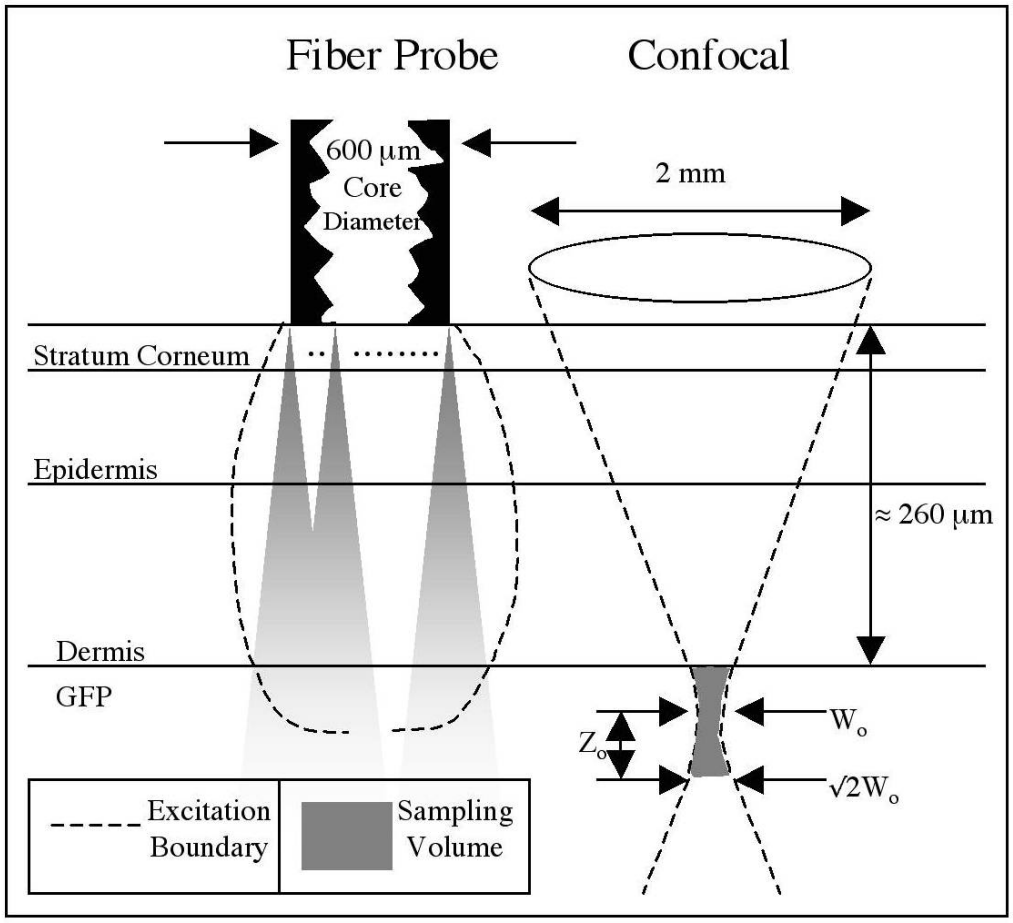

Figure 10.4) Sampling volume. The fiber probe collects fluorescence escaping within the cone of acceptance (shown convolved across the fiber face) defined by the fiber's numerical aperture (0.39). The confocal fluorimeter collects fluorescence from the confocal volume, which is on the order of a cubic micron located at the focus of the objective lens described in the radial direction by the focal waist W_o and in the axial direction by Z_o the distance at which the radial beam has expanded to $\sqrt{2}W_o$. Scattered photons are filtered out by the confocal design but accepted by the fiber probe device. Figure not drawn to scale.

The results also illustrate the advantage of spectral discrimination of collected fluorescence. A confocal microscope with a single filter and detector will acquire a signal comprised of both collagen autofluorescence and any subdermal green fluorescence. The confocal detection optimizes the fluorescence from the confocal volume, but there is still some contribution from the collagen of the overlying skin. Spectral detection can separate these two contributions to the total signal. The experiment of this report would be useful in determining the proper filters for spectral discrimination of the target fluorescence whether it be GFP or any other fluorophore, especially in confocal microscopy where autofluorescence can compromise imaging capability.

The spectra shown in this report are observed fluorescence, corrected for the filters but not for the detection systems nor for the effects of tissue optics. The goal of this report was to emphasize how the measurement system affected the relative strengths of subdermal green fluorescence and overlying collagen autofluorescence. If one wishes to quantify the amount of green fluorophore in units of concentration, one must consider how the tissue optics and the geometry of the measurement system combine to affect the penetration of excitation, the return to the tissue surface of fluorescent emission, and the collection of detectable emission as photons escape the tissue and enter the measurement system. For example with the optical fiber probe, only about 10% of the photons that escape the tissue and enter the fiber are collected within the solid angle of collection that allows the fiber to guide the photons to the detector. About 90% (varies with optical properties of tissue and numerical aperture of fiber) of the photons that enter the fiber immediately escape the fiber and are not detected[90]. Although this paper does not discuss these corrections, we have concluded that the confocal technique was successful at improving the signal to noise ratio when measurement of a subdermal target fluorescence was contaminated with collagen autofluorescence.

Chapter 11: Monte Carlo modeling of focused light in turbid media.

11.A Abstract

The ability to focus within a light-scattering medium is affected by the absorption coefficient (μ_a), scattering coefficient (μ_s), and the anisotropy of scattering (g). The relationship between optical properties and the fluence rate at the focus, F_{focus} [W/cm^2], was specified by Monte Carlo simulations. The summary expression was $F_{focus} = F_{max}\exp(-(\mu_a + a\mu_s)z_{focus}b)$, where F_{max} is the fluence rate at the focus for clear water (no scattering or absorption) and z_{focus} is the position of the focus within the tissue. The factor a is a function of the anisotropy which describes how scattering becomes less important when g approaches unity, $a = 1 - \exp(-(1-g)/0.263)$, and b describes how the effective photon path length increases when the incident beam is broad, $b = ((0.470w_1)^2 + z_{focus}^2)^{1/2}/z_{focus}$ where w_1 is the 1/e radius of the incident Gaussian beam. Monte Carlo simulations provided the data for specifying the functions a and b. The expression holds until $(m_a + m_s)z_{focus}$ exceeds 3.5 and thereafter Monte Carlo simulations are required to accurately predict F_{focus}.

OCIS codes: (170.6280) Spectroscopy, fluorescence and luminescence; (170.6510) Spectroscopy, tissue diagnostics

11.B Introduction

In photo-medicine, noninvasive methods of treatment and diagnosis rely on light propagation in tissue. One such transport scenario is the ability to focus in an optically turbid medium such as biological tissue. The goal of this work is to give the reader who wants to focus light in tissue, a simple way to predict the actual fluence rate at the focus

as a function of media properties and focal geometry. It is assumed that the medium is homogeneous.

11.C Methods

It is only possible to focus in a turbid medium if the depth of focus (z_{focus}) is shallow enough so that many photons can make it to the focus without getting scattered or absorbed. Wang and Gan [29] reported that focusing a beam incident on a turbid media has a strong effect on the fluence distribution when z_{focus} is less than or comparable to the transport mean free path (mfpp) defined as

$$mfpp = 1/(m_a + m_s(1-g)) \quad (11.1)$$

where m_a is the absorption coefficient (cm^{-1}), m_s is the scattering coefficient (cm^{-1}), and g is the scattering anisotropy (dimensionless). The scattering and absorption can be expressed as a total attenuation coefficient, $m_t = m_a + m_s$. The optical depth is defined as $m_t z_{focus}$ (dimensionless). In this work, g = 0.90 except in figure 10.3a, the 1/e radius of the incident beam (w_1) = 200 mm except in figure 10.5, and z_{focus} = 300 mm.

The Monte Carlo simulation used for this study was modified from code by Jacques [54] available on the web [91] which is a simplified version of the program by Wang et al. [92]. The program launched one million photon packets each with an initial weight W set to 1 and this weight was attenuated during propagation until terminated by the roulette method. Energy deposition due to tissue absorption was recorded in cylindrical coordinates of r and z bins due to the cylindrical symmetry of the problem. Fluence rate was calculated by dividing the local density of energy deposition rate in each bin, A (W/cm^3), by the absorption coefficient m_a to yield the local fluence rate F (W/cm^2).

As illustrated in Fig. 11.1, photon packets were launched from positions distributed along the surface as a Gaussian beam with 1/e radius w_1 and oriented toward a

focus at depth z_{focus} which had a lateral Gaussian distribution with 1/e radius w_o. Each photon packet was launched from a radial position ($r = r_1$, $z = 0$) toward a position ($r = r_o$, $z = z_{focus}$). This method only approximates true Gaussian optics based on wavefront analysis. The Monte Carlo method was used to map two random numbers, rnd_o and rnd_1, into the two radial positions, r_1 at the surface and r_o at the $z_{focus,}$ using the expressions:

$$r_1 = w_1(-\ln(rnd_1))^{1/2} \tag{11.2}$$

$$r_o = w_o(-\ln(rnd_o))^{1/2} \tag{11.3}$$

In our study, we chose w_o to be 6 mm as a typical focal waist size expected from a 0.85 NA lens. propagated from the exit pupil of the focusing lens toward the focus. In this paper, the specification of the incident Gaussian beam is assumed to pertain to the light entering the tissue's surface, and correction for refraction due to the index mismatch at the air/tissue surface is left to the reader.

The choice of pixel size affected the value of the fluence rate at the focus, F_{focus}, because the pixel averages the fluence rate over the pixel volume. A pixel size was chosed to be dr = dz = 9.23 mm such that the fluence rate achieved by a simulation that mimiced in a clear aqueous solution matched the value expected based on the analytic expression: $w_o = NA(2l/p)$ where NA is numerical aperture and l is wavelength.

Photons which backscattered and escaped the tissue were terminated. Photons which underwent total internal reflection at the tissue boundary were assumed to have negligible effect on Ffocus and therefore were also terminated. In the simulation, a matched boundry condition at the air/tissue surface achieved immediate termination of all photon packets whose z position became negative.

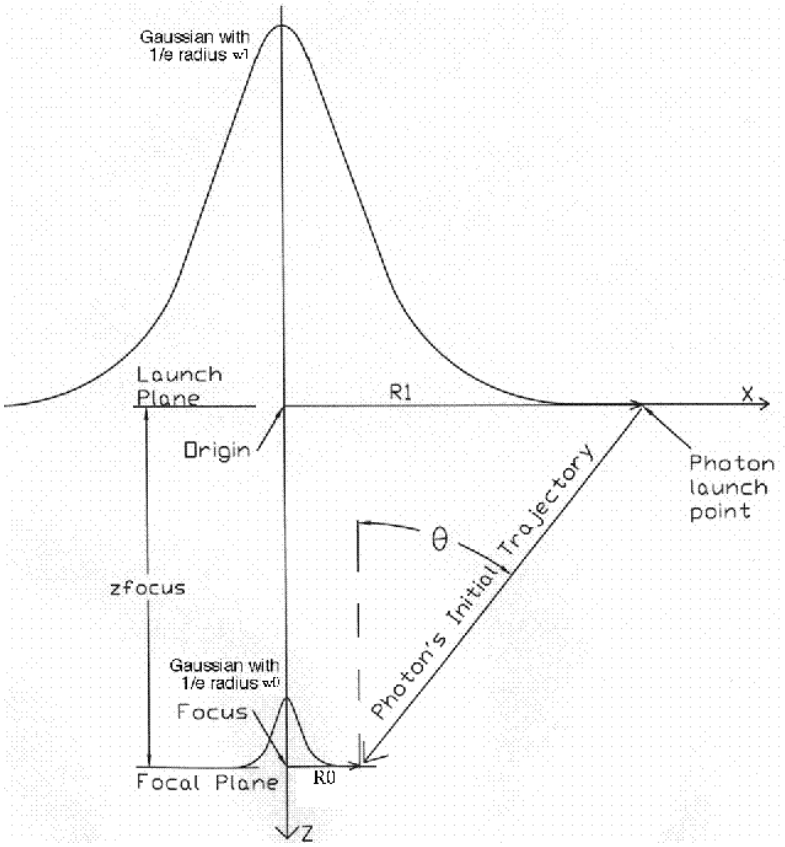

Figure 11.1 Schematic of how photon packets were launched in Monte Carlo simulation.

11.D Results

Figure 11.2 illustrates a typical Monte Carlo simulation. The parameters are w_1 is 200 mm, w_o is 6 mm, z_{focus} is 300 mm, m_a is 1 cm^{-1}, m_s is 100 cm^{-1}, and g is 0.90. The figure shows how scattering partially frustrates the ability to focus at the depth z_{focus} within the tissue.

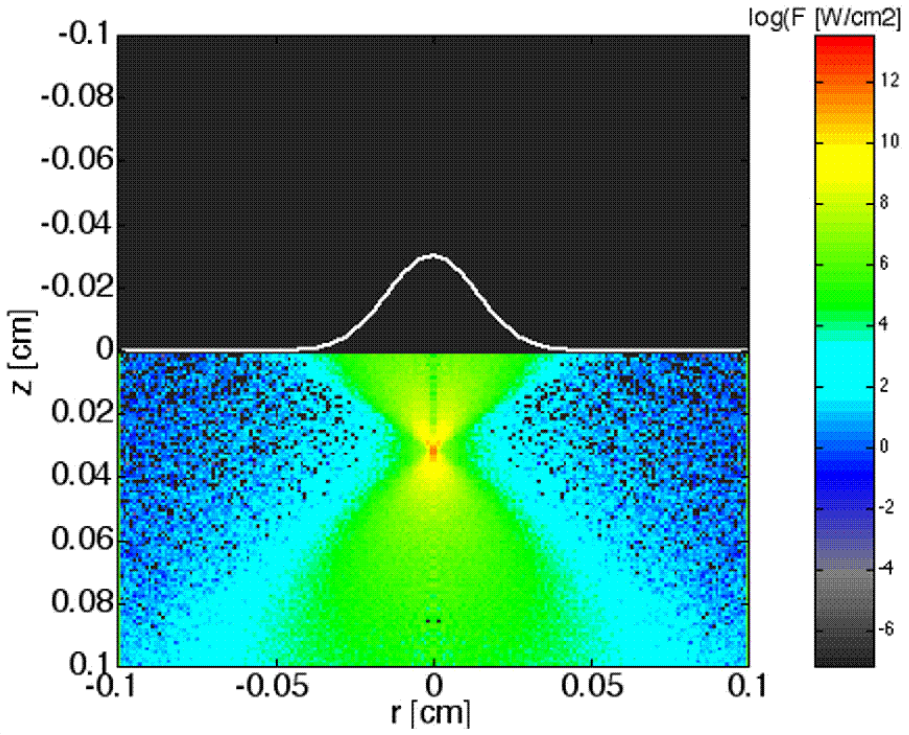

Figure 11.2 Monte Carlo simulation.

Figure 11.3ab shows the dependence of the fluence rate at the focus, F_{focus}, on the optical depth, $m_t z_{focus}$. The relationship is summarized:

$$F_{focus}/F_{max} = \exp((a\, m_s + m_a)\, z_{focus} b) \qquad (11.\ 4)$$

Where

$a = 1 - \exp(-(1-g)/0.263)$

and

$b = ((0.470 w_1)^2 + z_{focus}^2)^{1/2}/z_{focus}$

F_{max} is the fluence rate at the focus for clear aqueous medium (no scattering). F_{focus} is the fluence rate at the focus in the presence of tissue scattering and absorption. a is a function that describes how scattering frustrates the focus less when g approach unity. b is a function that describes how the photon path lengths increase when the incident beam is broadened. The net effective path length of photons to reach the focus is

z_{focus}b. When the incident beam is narrow ($W_1 << z_{focus}$), the value of b is unity and the photons travel a distance z_{focus} to the focus. When W_1 is larger than z_{focus}, b increases above unity.

The data in Fig. 11.3a were generated using various combinations of optical properites with g = 0. The data shows as circles varied m_a while keeping m_s equal to 1 cm^{-1} in order to illustrate a typical Beer's law attenuation, $F_{focus}/F_{max} = \exp(-m_t z_{focus})$. The data shown as crosses varied m_s while keeping m_a equal to 1 cm^{-1} in order to illustrate how isotropic scattering initially followed a Beer's law description but multiply scattered photons caused the curve to transition toward the prediction based on diffusion theory (dashed line).

The data in Fig. 11.3b were generated using various combinations of optical properties with g = 0.9. The data shows as circles is the same as in Fig. 3a for reference, i.e., m_a was varied while keeping m_s equal to 1 cm^{-1}. The data shown as crosses varied m_s while keeping m_a equal to 1 cm^{-1} in order to illustrate how anisotropic scattering allowed more multiply scattered photons to contribute to F_{focus}, and again the curve transitions toward the prediction based on diffusion theory (dashed line). Also shown are three data shown as squares based problem modeled by Wang and Liang [29]. Our Monte Carlo simulation reproduced their problem and agreed with their data at $m_t z_{focus} = 10$ and 20 (reported as z_{focus} = 0.2 cm and 0.1 cm as Fig. 3a in their paper), however our simulation for $m_t z_{focus} = 5$ differed from their result.

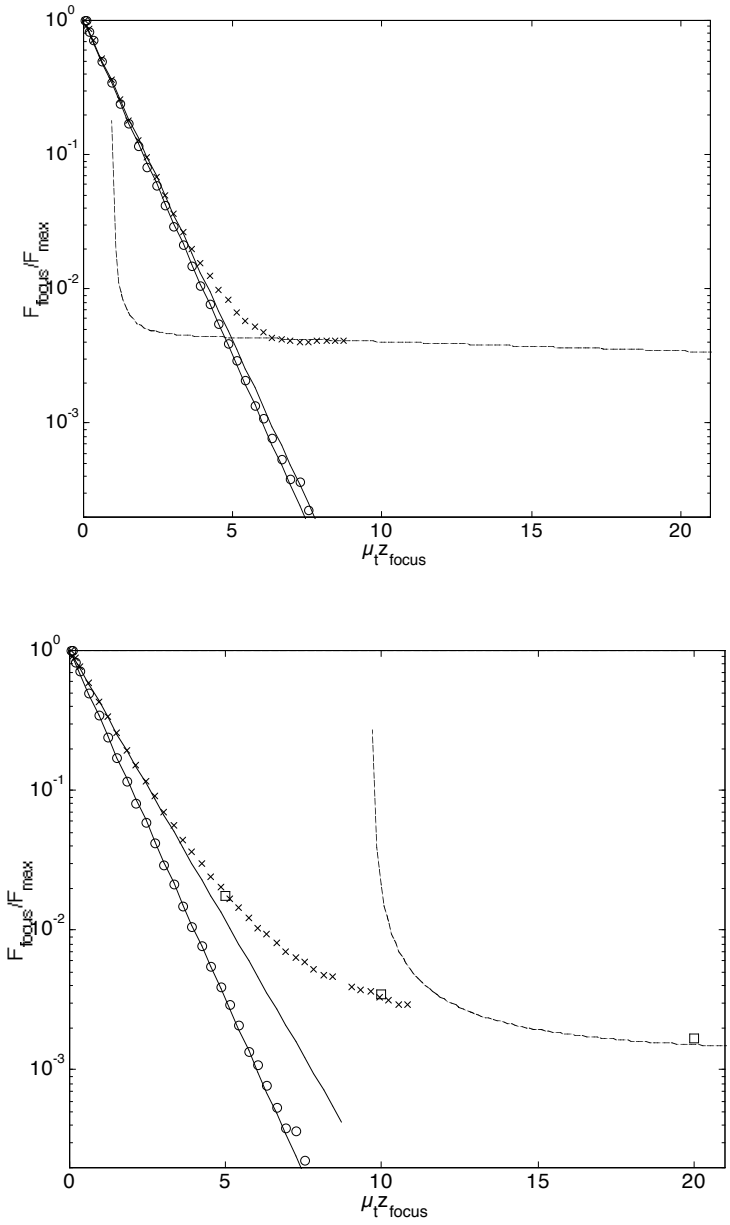

Figure 11.3 The fluence rate at the focus in absorbing, scattering media, F_{focus}, relative to the value in clear aqueous medium, F_{max}, expressed as F_{focus}/F_{max}, versus increasing optical depth, $m_t z_{focus}$. (circles) Changing absorption m_a with constant low scattering, m_s = 1 cm^{-1}. (crosses) Changing scattering m_s with constant low absorption m_a. (solid lines) Simple exponential attenuation. (dashed lines) Predictions of diffusion theory. (a) With anisotropy g = 0. (b) With anisotropy g = 0.90. (squres) Data calculated to repeat the examples reported in Wang and Liang[29].

Figure 11.4 shows the function a versus g for g ranging from 0 to 0.999. The symbols show the mean +/- standard deviation for three Monte Carlo simulation results at each g value. The solid line shows the expression for a(g) in Eq. 4. As g approaches unity, a approaches zero and the effective scattering am_s decreases toward zero because the deflection angle per scattering decreases toward zero. As g approaches zero, a approaches unity and am_s approaches m_s and scattering becomes maximally effective in attenuating F_{focus}. Because the anisotropy of biological tissues often falls within 0.90-0.95 [93], a is small and scattering serves more to broaden the lateral focal waist at z_{focus} than to attenuate F_{focus}.

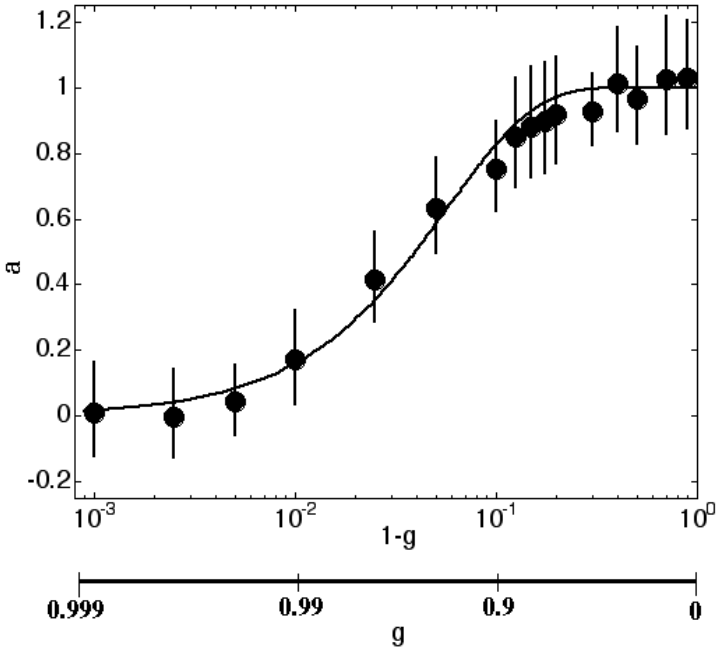

Figure 11.4. The function a versus 1-g and versus g. The solid line is a = 1 – exp(-(1-g)/0.263).

Figure 11.5 shows the function b versus the ratio w_1/z_{focus}. The symbols show the mean +/- standard deviation for three Monte Carlo simulation results at each value of w1 with z_{focus} constant at 300 mm. The solid line shows the behavior of b versus w_1/z_{focus} based on the expression for b in Eq. 11.4. The function b describes the effect of increased net effective photon length on F_{focus}/F_{max}. When $w_1 << z_{focus}$, b equals 1 and the effective

photon path from the surface to the focal point is z_{focus}. When $w_1 > z_{focus}$, b is greater than 1 and the effective photon path exceeds the distance z_{focus}.

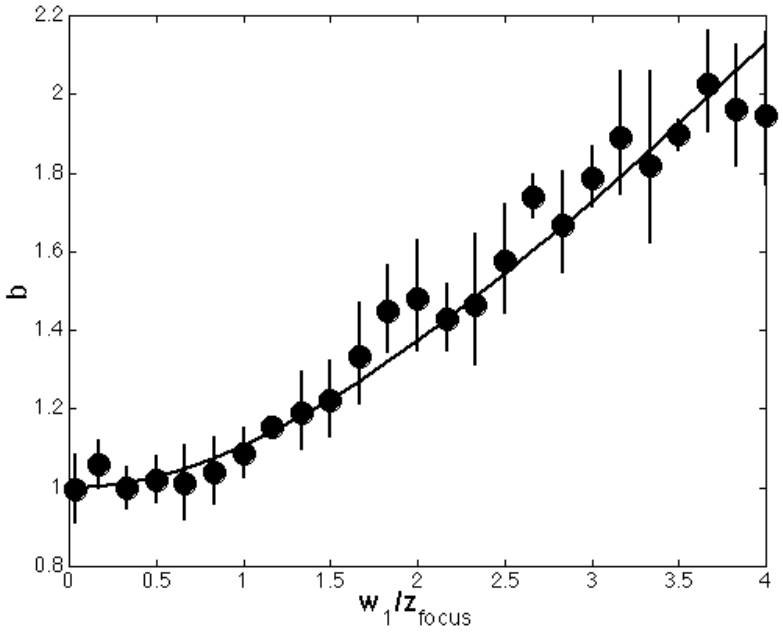

Figure 11.5 The function b versus w_1/z_{focus} describes how broadening the 1/e radius of the incident Gaussian beam, w_1, relative to the depth of focus, z_{focus}, increases the effective pathlength of the photons, bz_{focus}, to reach the focal point. Solid line is $b = ((0.470w_1)^2 + z_{focus}^2)^{1/2}/z_{focus}$

11.E Discussion

In Wang and Liang [1], the fluence rate at the focal depth, z_{focus}, increased when the z_{focus} was moved from focusing deep in the tissue to focusing near the surface. In this paper, we have reproduced this behavior and have added a description of how F_{focus}/F_{max} decreases when z_{focus} is moved from the surface toward deeper depths in a tissue. Wang and Liang reported the data that describes how F_{focus}/F_{max} first increases above the value expected for unfocused collimated light as the zfocus is moved toward the surface. This paper adds the behavior of F_{focus}/F_{max} as the optical depth first begins to increase and the behavior remains exponential in form and can be called a “modified” Beer’s law. As the

optical depth $m_t z_{focus}$ exceeds 3.5, the behavior of F_{focus}/F_{max} deviates from Eq. 11.4 and we rely on the Monte Carlo simulations of Figs. 3ab to describe the behavior. For zfocus equal to 3.5/mt, the value of F_{focus}/F_{max} has dropped to a value well predicted by Eq. 11.4.

The results shown in Figs. 3ab can be applied to problems using different numerical apertures because the Monte Carlo data is normalized by the predictions for a clear aqueous solution with no scattering or absorption. Hence, the results are applicable to problems based on a focusing lens with variable numerical aperture. The limits of this assertion have not yet been checked.

How does the F at z_{focus} using a lens to focus compare to the F at z_{focus} due to an unfocused collimated beam? The latter is specified by the prediction of diffusion theory for $m_t z_{focus}$ set to infinity. Figures 3ab indicate that F_{focus}/F_{max} deviates from the predictions of Eq. 4 when $m_t z_{focus}$ exceeds 3.5 for both g = 0 and g = 0.90. For example, in the near-infrared wavelength range for a typical tissue, g = 0.90, m_a = 0.1 cm^{-1} and m_s = 100 cm^{-1} (m_t = 101 cm^{-1}). The prediction of Eq. 4 for F_{focus}/F_{max} holds until z_{focus} reaches a depth of 3.5/(101 cm^{-1}) = 0.0347 cm or 347 mm. At this choice of z_{focus}, F_{focus}/F_{max} has dropped to 0.050 which is 33-fold higher than the value 0.0015 expected for an unfocused collimated beam. When $m_t z_{focus}$ reaches 10 such that z_{focus} equals 990 mm, F_{focus}/F_{max} equals 0.003 which is still twice the value expected for an unfocused collimated beam.

In summary, Eq. 11.4 provides a simple description of the fluence rate at the focus as a function of the optical properties of the media, the focal depth z_{focus}, and the size of the incident Gaussian beam at the surface characterized by its 1/e radius w_1. Equation 11.4 is applicable up to an optical depth of 3.5, and thereafter Monte Carlo simulations as described here are needed to specify F_{focus}.

Bibliography

[1] Minsky M., Memoir on inventing the confocal scanning microscope, Scanning J. 10:123-128; 1988, US Patent # 3013467, Filed 1957, Awarded 1961

[2] Wilson T., Sheppard C.J.R., Theory and practice of scanning optical microscopy. London: Academic Press, 1984

[3] Pawley J., The 39 Steps: A Cautionary Tale of Quantitative 3-D Fluorescence Microscopy, *BioTechniques*, 28(5):884-997, 2000.

[4] Corcuff P., Gonnord G., Pierard G.E., Leveque J.L., In vivo confocal microscopy of human skin: a new design for cosmetology and dermatology, *Scanning*, 18:351-355, 1996.

[5] Dwyer P.J., DiMarzio C.A., Rajadhyaksha M., Confocal reflectance theta line-scanner for imaging human skin in vivo, *Opt Lett*, 31(7):942-944, 2006.

[6] Gonzalez S., Rubinstein G., Rajadhyaksha M., White W.M., Gonzalez E., Anderson R.R., Non-invasive (real-time) imaging of histologic margin of a proliferative skin lesion in vivo, *Int Invest Dermat*, 0022-202X:538-538, 1998.

[7] Selkin B., Rajadhyaksha M., Gonzalez S., Langley R.G., In vivo confocal microscopy in dermatology, *Dermatologic Clinics*, 19(#2):369-377, 2001.

[8] Rajadhyaksha M., Grossman M., Esterowitz D., Webb R.H., Anderson R.R., Video-rate confocal scanning laser microscopy for human skin: melanin provides strong contrast, *Journal of Investigative Dermatology*, 104:946-952, 1995.

[9] Rajadhyaksha M., Gonzalez S., Zavislan J.M., Anderson R.R., Webb R.H., *In vivo* confocal scanning laser microscopy of human skin II: advances in instrumentation and comparison with histology, *Journal of Investigative Dermatology*, 1999.

[10] Busam K.J., Hester K., Charles C., Sachs D.L., Antonescu C.R., Gonzalez S., Halpern A.c., Detection of clinically amelanotic malignant melanoma and assessment of its margins by in vivo confocal scanning laser microscopy, *Archives of Dermatology*, 137: 923-928, 2001.

[11] Swindle L.D., Thomas S.G., Freeman M., Delaney P.M., View of normal human skin in vivo as observed using fluorescent fiber-optic confocal microscopic imaging, *Journal of Investigative Dermatology*, 121:706-712, 2003.

[12] H.D. Cavanagh, W.M. Petroll, J.V. Jester, The application of confocal microscopy to the study of living systems, *Neuroscience and Behavioral Reviews,* Vol. 17, 483-498, 1993.

[13] Jester JV, Andrews PM, Petroll WM, Lemp MA, Cavanagh HD, In vivo, real-time confocal imaging, *Journal of Electron Microscopy Technique*, 18:50-60, 1991.

[14] Maurice M., A scanning slit optical microscope, *Investigative Opthalmology*, 13(12):1033-1037, 1974.

[15] Maurice D.M., Zhao J., Nagasaki T., A novel microscope system for time-lapse observation of corneal cells in a living mouse, *Exp Eye Res*, 78(3):591-7, 2004 Mar.

[16] Koester C., Scanning mirror microscope with optical sectioning characteristics: applications in ophthalmology, *Applied Optics*, 19(no. 11):1749-1757, June 1980.

[17] MacAulay C., Dlugan A., Use of digital micro mirror devices in quantitative microscopy, *Proceedings of the SPIE*, Vol. 3260, 0277-786X, 1998.

[18] Hanley Q.S., Verveer P.J., Gemkow M.J., Arndt-Jovin D., Jovin T.M., An optical sectioning programmable array microscope implemented with a digital micromirror device, *Journal of Microscopy,* 196:317-331, 1999.

[19] Seibel E.J., Smithwick Q.Y.L., Unique features of optical scanning, single fiber endoscopy, *Lasers in Surgery and Medicine*, 30(3):177-183, 2002.

[20] Billinton A., Knight A.W., Seeing the Wood through the Trees: A Review of Techniques for Distinguishing Green Fluorescent Protein from Endogenous Autofluorescence, *Analytical Biochemistry*, 291: 175-197, 2001.

[21] CHAPTER 11 IN THIS THESIS, reprinted with permission. Gareau D.S., Bargo P.R., Horton W.A., Jacques S.L., Confocal fluorescence spectroscopy of subcutaneous cartilage expressing green fluorescent protein versus cutaneous collagen autofluorescence, *J Biomed Opt*, 9:254-258, 2004.

[22] Doyle K.P., Snider A., Stenzel-Poore M.P., Working with GFP in the Brain, *BioTechniques,* 34:2-4, 2003.

[23] Staughton T.J., Mcgillicuddy C.J., Weinberg P.D., Techniques for reducing the interfering effects of aurofluorescence in microscopy: improved detection of sulphorhodamine B-labeled albumin in arterial tissue, *Journal of Microscopy*, 201(1):70-76, 2000.

[24] Boutet de Monvel J., Le Calvez S., Ufendahl M., Image restoration for confocal microscopy: improving the limits of deconvolution, with application to the visalization of the mammalian hearing organ, *Biophysical Journal*, 80:2455-2470, 2001.

[25] Petran M., Hadravski M., Benes J., Kucera R., The tandem scanning reflected light microscope Part 1 the principal, and its design, *Proceedings of the Royal Microscopical Society*, 20(3):125-129, 1985.

[26] Straub M., Lodemann P., Holroyd P., Jahn R., Hell S.W., Live cell imaging by multifocal multiphoton microscopy, *Eur J Cell Biol*, 79(10):726-34, 2000 Oct.

[27] Rajadhyaksha M., Gonzalez S., Real-time in vivo confocal fluorescence microscopy, Chapter 5 in Handbook of Biomedical Fluorescence, M.A. Mycek and B. Pogue (Eds), 143-180, Marcel-Dekker, New York (2003).

[28] R. H. Web, Theoretical Basis of Confocal Microscopy, *Methods in Enzymology*, 307, 3-26, 1999.

[29] Wang L.V., Liang G., Absorption distribution of an optical beam focused into a turbid medium, *Appl Opt*, 38:4951-4958, 1999.

[30] Schmitt J.M., Knuttel A., Yadlowski M., Confocal microscopy in turbid media, *J Opt Soc Am*, 11(# 8):2226-2235, 1994.

[31] Cheong W.F., Prahl S.A., Welch A.J., A review of the optical properties of biological tissues, IEEE *J. Quantum Electron*, 26:2166-2185, 1990.

[32] Kemp M., Rudolph W., Welsch E., Comparitive study of confocal and heterodyne microscopy for imaging though scattering media, *J Opt Soc Am*, 13(1):46-52, 1996.

[33] Smithpeter C.L., Dunn A.K., Welsh A.J., Richards-Kortum R., Penetration limits of *in vivo* confocal reflectance imaging, *Applied Optics*, 37(13):2749-2754, 1998.

[34] Aguirre A.D., Hisung P., Ko T.H., Harti I., Fujimoto, High-resolution optical coherence microscopy for high-speed, in vivo cellular imaging, *Opt Lett*, 28:2064-2066, 2003.

[35] Pierce M.C., Strasswimmer J., Park B.H., Cense B., de Boer J.F., Advances in optical coherence imaging for dermatology, *J Invest Dermatol*, 123:458-463, 2004.

[36] Yeh A.T., Kao B., Jung W.G., Chen Z., Nelson J.S., Tromberg B.J., Imaging wound healing using optical coherence tomography and multiphoton microscopy in an in vitro skin-equivalent tissue mode, *JBO* **9(2):**248-253, 2004.

[37] Mansotti L., Basic principals and advanced technical aspects of ultrasound imaging. In: Guzzardi R., ed. Physics and Engineering of Medical Imaging, Boston: Martinus Nijhoff; 1897:263-317, 1987.

[38] Markisz J.A., Aquillia M.G., Technical magnetic resonance imaging, Stanford, Stamford, CN: Appleton and Lange, 1996.

[39] Izatt J.A., Hee M.R., Owen G. M., Optical coherence microscopy in scattering media. *Optics Letters,* 19(#8):590-592, 1994.

[40] Pierce M.C., Strasswimmer J., Park B.H., Cense B., de Boer J.F., Advances in optical coherence imaging for dermatology, *J Invest Dermatol,* 123:458-463, 2004.

[41] Hadjantonakis A.K.,Nagy A., The color of mice: in the light of GFP-variant reporters, *Histochem Cell Biol,* 115, 49-58, 2000.

[42] Cho J.Y., Grant T.D., Lunstrum G.P., Horton W.A., Col2-GFP reporter mouse--a new tool to study skeletal development, *Am J Med Genet,* 106(4):251-3, 2001 Winter.

[43] Gan X.S., Schilders S.P., Gu M., Image formation in turbid media under a microscope, *J Opt Soc Am,* 15#8: 2052-2058, 1998.

[44] Stelzer E.H.K., Contrast, resolution, pixelation dynamic range and signal-to-noise ratio: fundamental limits to resolution in fluorescence light microscopy, *Journal of Microscopy,* 189(1):15-24, 1997.

[45] Sandison D.R., Piston D.W., Williams R.M., Webb W.W., Quantative comparison of background rejection, signal-to-noise ratio, and resolution in confocal and full-fiels laser scanning microscopes, *Applied Optics,* 34(19):3576-3588, 1995.

[46] Ding H., Lu J. Q., Wooden W. A., Kragel P. J., Hu X., Refractive indices of human skin tissues at eight wavelengths and estimated dispersion relations between 300 and 1600 nm, *Phys. Med. Biol.,* 51:1479-1489, 2006.

[47] Product description, ATCC The global biorescource center, Available: http://www.atcc.org/common/catalog/numSearch/numResults.cfm?atccNum=CRL-6475 [Viewed 10-15-06].

[48] Unsharp Masking, Coulour Science, Available: http://www.colour-science.com/Research/AUM/AUM, [viewed 10-01-05] images reproduced with permission.

[49] Dwyer P.J., DiMarzio C.A., Zavislan J.M., Fox W.J., Rajadhyaksha M., Confocal reflectance theta line-scanning microscope for imaging human skin *in vivo*, *Optics Letters,* 31(no. 7), April 1, 2006.

[50] Gu M., Sheppard C.J.R., Confocal fluorescent microscopy with a finite-sized circular detector, *JOSA Communications*, 9(no. 1):151-153, 1992.

[51] Sheppard C.J.R., Gu M., Imaging performance of confocal fluorescence microscopes with finite-sized sources, *Journal of Modern Optics*, 41(no. 8):1521-1530, 1994.

[52] Gan X., Schilders S., Gu M., Combination of annular aperture and polarization gating methods for efficient microscopic imaging through a turbid medium: theoretical analysis, *Microsc Microanal*, 3:495-503, 1997.

[53] Monte Carlo, Oregon Medical Laser Center, Available: http://omlc.ogi.edu/software/mc/ [Viewed 10-15-06].

[54] Jacques S.L., Light distributions from point, line and plane sources for photochemical reactions and fluorescence in turbid biological tissues. *Photochem Photobiol*, 67:23-32, 1998.

[55] Gareau D.S., Jacques S.L., Transcutaneous imaging of green fluorescent protein expression in cartilage of mice, Proc SPIE, 4617B, 2001.

[56] Monte Carlo Simulations: Sampling example: A Gaussian Laser Profile, Available: http://omlc.ogi.edu/classroom/ece532/class4/example.html [Viewed 10-15-06].

[57] J.W. Goodman, Introduction to Fourier Optics, © 1968 McGraw-Hill

[58] Henyey L.G., Greenstein J.L., Diffuse radiation in the galaxy, *J. Astrophysics*, 93:70-83, 1941.

[59] Jacues S.L., Alter C.A., Prahl S.A., Angular dependance of He-Ne laser light scattered by huan dermis, *Lasers Life Science*, 1:309-333, 1987.

[60] Noonan F.P., Recio J.A., Takayama H., Duray P., Anver M.R., Rush W.L., De Fabo E.C., Merlino G., Neonatal sunburn and melanoma in mice, *Nature*, 413: 271-272, 2001.

[61] Wang X., Milner T.E., Chang M.C., Nelson J.S. Group refractive index measurement of dry and hydrated type I collagen films using optical low-coherence reflectometry, *Journal of Biomedical Optics*, 1:212-216, 1996.

[62] Vitkin I.A., Woolsey J., Wilson B.C., Anderson R.R., Optical and thermal characterization of natural (sepia officinalis) melanin, *Photochem Photobiol*, 59:455-462, 1994.

[63] Eugene Hecht (2002) Optics, © Pearson Education: New Jersey

[64] Absorption Spectrum for Biological Materials, Oregon Graduate Institute, Available: http://omlc.ogi.edu/classroom/ece532/class3/muaspectra.html [Viewed 10-15-06].

[65] Greger A., Koller S., Kern T., Massone C., Steiger K., Richtig E., et al. Diagnostic applicability of in vivo confocal laser scanning microscopy in melanocytic skin tumors, *J Invest Dermatol,* 124:493-498, 2005.

[66] Brunsting A., Mullaney P, Differential light scattering from spherical mammalian cells, *Biophysical Journal,* 14:439-453, 1974.

[67] CHAPTER 8 IN THIS THESIS, reprinted with permission. Gareau D.S., Lagowski J., Rossi V., Viator J.A., Merlino G., Kulesz-Martin M., Jacques S.L. Imaging melanoma in a murine model using reflectance-mode confocal scanning laser microscopy and polarized light imaging. J Investig Dermatol Symp Proc. Nov;10(2):164-9, 2005.

[68] Jacques S.L., Roman J., Lee K., Imaging superficial tissues with polarized light. *Lasers Surg, Med,* 26:119-129, 2000.

[69] Jacques S.L., Ramella-Roman J.C., Lee K, Imaging skin pathology with polarized light, *J Biomed Opt,* 7:329-340, 2002.

[70] Wilson T, Sheppard CJR, *Theory and practice of scanning optical microscopy*. © 1984, Academic Press: New York.

[71] Chow SK, Hakozaki H, Price DL, Maclean AB, Deerinck TJ, Bouwer JC, et al. Automated microscopy system for mosaic acquisition and processing, *J Microscopy,* 222(2):76-84, 2006.

[72] Jhappan C, Noonan FP, Merlino G. Ultraviolet radiation and cutaneous malignant melanoma, *Oncogene,* 22(20):3099-112, 2003.

[73] Rajadhyaksha M.M., Gonzalez S., Zavislan J.M., Detectability of contrast agents for confocal reflectance imaging of skin and microcirculation, *J Biomed Opt,* 9:323-331, 2004.

[74] Broome P.M., Gause P.R., Hyman P., Gregus J., Lluria-Prevatt M., Nagle R., Bowden G.T., Induction of melanoma in TPras transgenic mice, *Carcinogenesis* 20(9):1747-1753, 1999.

[75] Farrell T.J., Patterson M.S., Essenpreis M., Influence of layered architecture on estimates of tissue optical properties obtained from spatially resolved diffuse reflectometry, *J. Applied Optics,* 37:1958-72, 1998.

[76] Saidi I.S., Jacques S.L., Tittel F.K., Mie and Rayleigh modeling of visable light scattering in neonatal skin, *J. Applied Optics,* 34:7410-18, 1995.

[77] Treweek S.P., Barbenel J.C., Direct measurement of the optical properties of human breast skin, *Med & Biol Eng & Comput,* 34:285-289, 1996.

[78] Jacques S.L., Origins of Tissue Optical Properties in the UVA, Visable, and NIR Regions, OSA TOPS on Advances in Optical Imaging and Photon Migration 2, 1996.

[78] Anderson R.R., Parrish J.A., The optics of human skin, *J Invest Dermatol*, 77:13-19, 1981.

[79] Jacues S.L., Prahl S.A., Modeling optical and thermal distributions in tissue during laser irradiation, *Lasers in Surgery and Medicine*, 6:494-503, 1987.

[80] Marchesini R., Clemente C., Pignoli E., Brambilla M., Optical properties of in vitro epidermis and their possible relationship with optical properties of in vivo skin, *J Photochem Photobiol*, B: Biol, 16:127-140, 1992.

[81] Van Gemert M.J.C., Jacques S.L., Strenborg H.J.C.M., Star W.M., Skin Optics, *IEEE Trans Biomed. Eng*, 36:1146-1154, 1989.

[82] Treweek S.P., Barbenel J.C., Direct measurement of the optical properties of human breast skin, *Med & Biol Eng & Comput*, 34:285-289, 1996.

[83] Nickell S., Hermann M., Essenpreis M., Farrell T.J., Kramer U., Patterson M.S., Anisotropy of light propagation in human skin, *Phys Med Biol*, 45:2873-2886, 2000.

[84] Bertrand C., Corcuff P., *In vivo* spatio-temporal visualization of the human skin by real time confocal microscopy, *Scanning*, 16:150-154, 1994.

[85] Corcuff P., Bertrand C., Leveque J. L., Morphotometry of human epidermis in vivo by real-time confocal microscopy, *Archive of Dermatological Research*, 285:475-481, 1993.

[86] Gan X. S., Sheppard C. J. R., Detectability: a new criterion for evaluation of the confocal microscope, *Scanning*, 15:187-192, 1993.

[87] Coralli C., Cemazar M., Kanthou C., Tozer G.M., Dachs G.U., Limitations of the Reporter Green Fluorescent Protein under Simulated Tumor Conditions, *Cancer Research*, 61:4784-4790, June 2001.

[88] Na R., Stender I. M., Henriksen M., Wulf H. C., Autofluorescence of human skin is age related after correction for skin pigmentatin and redness, *J Invest Dermatol*, 116:536-540, 2001.

[89] Zeng H., MacAulay C., McLean D. I., Palcic B., Spectrascopic and microscopic characteristics of human skin autofluorescence emission, *Photochemestry and Photobiology*, 61:639-645, 1995. (Figure 3g).

[90] Bargo P.R., Jacques S.L., Sleven R., Goodell T., Optical properties effects upon the collection efficiency of multifiber probe configurations, *IEEE J. Selected Topics in Quantum Electronics* **9**:314-321, 2003.

[91] mc321.c, Jacques S. L., Available: http://omlc.ogi.edu/classroom/ece532/class4/ssmc/mc321.c [Viewed: 10-15-06].

[92] Wang L.H., Jacques S. L., Zheng L.Q., MCML - Monte Carlo modeling of photon transport in multi-layered tissues, *Computer Methods and Programs in Biomedicine*, **47**, 131-146, 1995.

[93] Daria V.R., Saloma C., Kawata S., Excitation with a focused, pulsed optical beam in scattering media: diffraction effects, *Applied Optics*, **39**, (28), 1575 – 1579, 2000.

[94] Welch, van Gemert, Optical-Thermal Response of Laser-Irradiated Tissue, Appendix 8A.1, Plenum Press, New York, 1995.

[95] Mie Scattering calculations, Scott Prahl, Available: http://omlc.ogi.edu/calc/mie_calc.html [Viewed: 10-15-06].

Appendix

A1 ConfocalFluor.m, a back-of-the envelope calculation.

This simulation yields the fluorescent optical power that hits the detector during confocal microscopy. Typical values are chosen for the power of the laser (*laser*) and the optical properties (*mus*, *mua*). The optical section thicknes (*Xsec*, *Zsec*) are from Equation 1.1 and items marked with the triple asterisk (***) are from reference [27].

```
% Confocalmath.m DSG 2006
% This is a simple model, back of the envelope
% calculation of confocal detection of GFP in skin
clear

mus  = 100;                 % Scattering coefficient [cm^-1]
NA   = 0.90;                % Numerical aperture [-]
theta  = asin(NA);          % half angle [rad]
deg    = theta*180/pi;      % half angle [deg]
zfocus = 0.0100;            % focal depth [cm]

% light
laser  = 10e-3;             % [W]
lambda = 488e-7;            % [cm]
h      = 6.626e-34;         % [J s] Plancks constant
c      = 2.997e10;          % [cm/s] light speed in vaccum
e      = (h*c)/lambda;      % [J/Photon]
n              = 1.33;      % Refractive index
Xsec = 2*0.46*lambda/NA;    % Diff. Lim. optical section [cm]
Zsec = 2*1.4*lambda/NA^2;   % Diff. Lim. optical section [cm]
area   = pi*(Xsec/2)^2;     % [cm^2] confocal cross-sectional area
```

```
% fluorophore
extcoeff = 3.92e4;                  % [cm^-1 M^-1] ***
C       = 100e-6;                   % [M = mole/liter] concentration ***
Av      = 6.02e23;                  % #/mole
QY      = 0.80;                     % quantum yield [-]

% optofocal penetration calculation
Toptics = 0.6;                      % measured one-way microscope throughput [-]
flens   = 1/2*(1-cos(theta));       % Fractional collection by Obj. lens [-]
mua = log(10)*extcoeff*C;           % absorption coefficient [1/cm]
Ttis   = exp(-(mus + mua)*zfocus);  % [cm^-2]
E = laser*Toptics*Ttis/area;        % irradiance [W/cm2] at confocal volume
Q = E*n/c;                          % optical energy density [J/cm3]
Cph = Q/e*1000/Av;                  % photon concentration [moles/liter]
% Rajadhyaksha et al ***%
% [liter] = [cm^3*1e-6] confocal volume %
V = 1e-6*(pi/12)*(Zsec^3*tan(theta)^2+6*Xsec*Zsec^2*tan(theta)+12*Xsec^2*Zsec);

Nabs = mua*c/n*Cph*V;               % absorbed photons [moles/second]
Nemt = Nabs*QY;                     % emitted photons [moles/second]
Nemt = Nemt*Av;                     % emitted photons [photons/second]
Nemt = Nemt*e;                      % emitted photons [jouls/second]

powerdetected = Nemt*flens*Ttis*Toptics;
disp(sprintf('---> %5.2d fluorescent Watts detected', powerdetected))
```

A2 Multifocal.doc, a back-of-the envelope calculation.

This calculation determines the minimum dwell time for efficient collection of fluorescence in scanning laser microscopy. Although not used for the work in this thesis since the scan is relatively slow, this calculation predicts the limit of fluorescence lifetime on fast scanning.

Conventional 3D fluorescent laser-scanning microscopy is realized with a raster pair of galvanometric mirrors and a sample stage that steps along the optical axis. Greatly enhanced scan speed can be achieved by replacing a mirror (fast axis of raster scan) with a spinning polygon, but there is a limit to the speed of data acquisition. Consider the following example:

Consider acquisition an image cube of $n = 512^3 = 1.34\times10^8$ voxels. The dwell time (t) on any particular group of GFP molecules is the entire scan time divided by the number of voxels scanned. For instance, if the duration of the entire scan (s) is to be one second:

$t = s/n = 1/n = 7.5\times10^{-9}$ seconds

This is a sufficiently long dwell time if the fluorescence was from the Green Fluorescent Protein (GFP) from the jellyfish *Aequorea victoria* whose lifetime (time at which the exponential decay of fluorescent emission has decreased to 1/e) is about $tau = 4\times10^{-9}$ seconds. What if one wishes to scan faster than one frame per second? If the acquisition

period (s) were to decrease (faster acquisition), the dwell time (t) would decrease beneath the fluorescence lifetime, which is a show-stopper because such fast scans would move past fluorescent molecules before fluorescent light could be generated. The limiting factor in fluorescence imaging of large volumes where fast scans are necessary becomes the fluorescence lifetime. In general, the fraction of fluorescent emission collected is related to the dwell time (Tp) and the fluorescence lifetime (tau) is as follows:

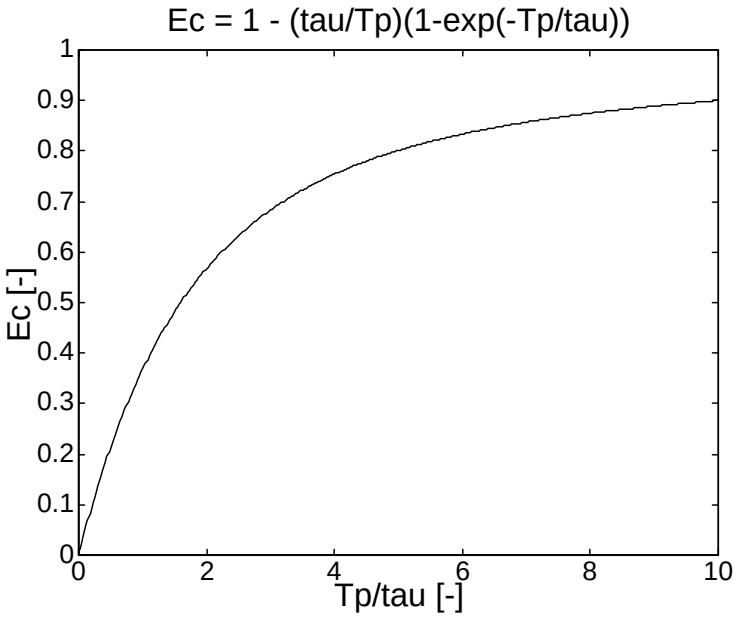

Figure(1) Fraction of fluorescence collected as a function of dwell time. This relationship illustrates that to collect for instance half the fluorescent power, one must dwell twice the fluorescence lifetime.

In ballpark figures, if your fluorescence lifetime is a nanosecond and you require millisecond temporal resolution, you can only scan a million samples per second with single point scanning, the limit of spatiotemporal resolution. The bottom line is it becomes a trade off between scanning fast enough to acquire your data set on a time scale relevant to the experiment (i.e. sufficient spatiotemporal resolution) and dwelling long enough to collect fluorescence (i.e. fluorescence lifetime limit). Multofocal scanning microscopy overcomes this barrier, offering better spatiotemporal resolution while capturing more fluorescent power than point scanning systems.

A3 ThermDam.m, a back-of-the envelope calculation.

This simulation calculates the maximum dwell time for a particular laser power before thermal damage results at the focus. Since thermal denaturation can damage the specimen, it is important to consider the amount of optical power used in the system.

```
% ThermDam.m
% Dan Gareau 1/29/06
% this program assumes constant laser power focused into tissue
% the output is the damage caused at the focus per time exposure
% expressed in dwell time until thermal damage (Ω = 1)
% thermal diffusion not considered, "worst case" estimate

clear all
close all

%----------------------user choices-----------------------------%
P = 0.01;                          % Power [W]
lambda = 488e-7;                   % wavelength [cm]
mua = 3;                           % epi abs coeff [cm^-1]
musp = 50;                         % derm reduced scat coeff [cm^-1]
Zfocus = 0.0100;                   % Focal depth [cm]
ΔS = 30;                           % [J/(mol*K)]  Entropy (Jacques)
ΔH = 1e5;                          % [J/(mol)] Enthalpy (Dog Prostate)
%---------------------------------------------------------------%
```

```
kB = 1.38e-23;                  % Boltzmann's constant [J/K]
kP = 6.626e-34;                 % Plank's constant [J*s]
kR = 8.3;                       % Gas constant [J/(mol*K)]
NA = 0.9;                       % Numerical Aperture [-]
n = 1.33;                       % Sample Refractive Index [-]
theta = asin(NA/n);             % Half angle of focus [Rad]
G = 1.16;                       % Geometrical factor: focused Gaussian

Ttis = exp(-(mua + musp)*Zfocus*G);     % Transmission to focus [-]
Ptis = P*Ttis;                          % Power penetrating to Zfocus [W]

delX = 0.46*lambda/NA;          % resolution element [cm]
delZ = 1.4*n*lambda/NA^2;       % section thickness [cm]

% ------   Confocal Volume  [cm^3] ----------- %
% ------   Rajadhyaksha, Hnbk. 2003 ---------- %
Vf = (pi/12)*(delZ^3*tan(theta)^2 + 6*delX*delZ^2*tan(theta) + 12*delX^2*delZ);
Pabs = Ptis*mua*delZ;           % Power absorbed in confocal volume [W]
Ed = Pabs/Vf;                   % Absorbed energy density [J/cm^3/s]

% initial conditions
Ω = 0;                          % No damage, initial condition...
time = 0;                       % at time T [s] = 0
tempCELCUIS = 32;               % Body Temp. [C]
temp = tempCELCUIS + 273;       % Body Temp. [K]

% Calculate damage as Ω = 1 = -ln(N(t)/N(0))
dt = Ptis/5e5;                  % [s] timestep
de = Ed*dt;                     % [J/cm^3] absorbed energy in conf. vol.
deCal = de/4.18;                % [Cal/cm^3]
```

```
dtemp = deCal;                  % [K] because 1 [Cal] raises [1cm^3] 1 [K]

i = 0;                          % initialize index
while Ω < 1
        i = i + 1;              % incriment index
        time = time + dt;       % Incriment current time [s]
        temp = temp + dtemp;    % Incriment current temp [K]
        k = kB*temp/kP*exp(ΔS/kR)*exp(-ΔH/(kR*temp));
        Ω = Ω + k*dt;
end

DwellMax = i*dt      %%% result in [seconds]
```

A4) GetResol.m, a data processing tool.

This program loads the result of a point-spread function measurement and determines the resolution limit of the system according to the Rayleigh criteria.

```
% get resolution  Dan Gareau 5-18-06
% this code numericaly determines the resolution
% limit from a point-spread function (PSF)
% it loads fitresults.mat file containing the PSF
% which consists of the position (zz) and
% the signal at that position (s)
% the output is the Rayleigh resolution limit
% in the units of the input position (zz)

clear all
close all
load fitresults

z = zz; % Distance [µm]
s = g;   % Signal [AU]
n = length(z);

figure(1)
plot(z, s, 'k-', 'linewidth',2)
dz = z(4) - z(3);

% find the index (ii) of peak signal intensity
for i = 1:n
        if s(i) == max(s);
                ii = i;
        end
end

% sp is s cropped so peak is central
if ii < n/2 % max is greater than center
        sp = zeros(1,2*ii)
        for iii = 1:2*ii;
                sp(iii) = s(iii);
        end
else            % max is less than center
        sp = zeros(1,2*(n-ii));
        for iii = 1:(2*(n-ii));
                sp(iii) = s(n-2*(n-ii)+iii);
        end
end
```

```
np = length(sp);

% Find Resolution
midmiddle = 1;          % initial condition
ind = 0;                % Counter
while midmiddle > (8/pi^2), % Rayleigh
        ind = ind + 1   % increment
        nc = np + ind*2;
        creation = zeros(1,nc);
        for i = 1:np
                creation(i) = sp(i);
        end
        for i = 1:np
                ic = nc-i;
                creation(ic) = creation(ic) + sp(i);
        end
        creation = creation/max(creation);
        midmiddle = creation(round(nc/2));
        figure(2)
        plot([1:nc]*dz, creation)
        drawnow
        clear creation
end
resol = (ind*2 + 1)*dz
```

A5) fcmc.c

```
/*********************************************
 *  mc321.c in ANSI Standard C programing language
 *        This Program models the axial point spread function for
 *  confocal fluorescence microscopy in homogenious turbid media
 *  Adapted from Code by Steven L. Jacques based on prior collaborative work
 *  with Lihong Wang, Scott Prahl, and Marleen Keijzer.
 *  partially funded by the NIH (R29-HL45045, 1991-1997) and
 *  the DOE (DE-FG05-91ER617226, DE-FG03-95ER61971, 1991-1999).
 *  note, this code is not particularly clean or well commented.  If you want
 *  to see more easilly readable code, see rcmc, also in the appendix
 **********/

#include <math.h>
#include <stdio.h>
#include <string.h>
#include "nrutil.h"
#include <time.h>

#define PI         3.1415926
#define LIGHTSPEED  2.997925E10                    /* in vacuo speed of light [cm/s] */
#define ALIVE       1               /* if photon not yet terminated */
#define DEAD        0               /* if photon is to be terminated */
#define THRESHOLD   1e-4                /* used in roulette */
#define CHANCE      0.1             /* used in roulette */
#define COS90D      1.0E-6
    /* If cos(theta) <= COS90D, theta >= PI/2 - 1e-6 rad. */
#define ONE_MINUS_COSZERO 1.0E-12
    /* If 1-cos(theta) <= ONE_MINUS_COSZERO, fabs(theta) <= 1e-6 rad. */
    /* If 1+cos(theta) <= ONE_MINUS_COSZERO, fabs(PI-theta) <= 1e-6 rad. */
#define MYSIGN(x)          ((x)>=0 ? 1:-1)
#define InitRandomGen    (double) RandomGen(0, 1, NULL)
    /* Initializes the seed for the random number generator. */
#define RandomNum        (double) RandomGen(1, 0, NULL)
    /* Calls for a random number from the randum number generator. */
#define THESIZE 130
#defineTHE_NP THESIZE
```

```
/* DECLARE FUNCTION */
double RandomGen(char Type, long Seed, long *Status);
float bessj1(float x);


int main() {

time_t  now;
double startTime, endTime;

/* Propagation parameters */

double  Rtwo, Rone, rr;          /* radius of launched photon [cm] */
double xsurf, ysurf, rsurf;
double  alpha;                           /* angle of Rone */
double Fdepth, FLUthick, FLUdepth1, FLUdepth2, FLUdepth3,lambda, w, wp;
double numericalapperture;
double  REFindex, drad, summ, Tsumm, unity, frac;

double  x, y, z, x2, y2;           /* photon position */
double  xlast, ylast, zlast;    /* keep track of last photon position */
double  ux, uy, uz;                      /* photon trajectory as cosines */
double  uxy, uxx, uyy, uzz;    /* temporary values used during SPIN */
double  s, sxy;                  /* step sizes. s = -log(RND)/mus [cm] */
double  costheta;                        /* cos(theta) */
double  sintheta;                        /* sin(theta) */
double  cospsi;                          /* cos(psi) */
double  sinpsi;                          /* sin(psi) */
double  psi;                             /* azimuthal angle */
long     i_photon;                       /* current photon */
long     j_photon;                       /* current local photon */
double  W, WF, Wtot;           /* photon weight */
double  absorb;     /* weighted deposited in a step due to absorption */
short   photon_status;                   /* flag = ALIVE=1 or DEAD=0 */

/* other variables */
double  **Ccyl;  /* cylindrical photon concentration */
double  **CcylF;  /* cylindrical photon concentration */
double  Fcyl;       /* fluence in cylindrical shell */
double  Fcylout;       /* fluence in cylindrical shell */
double  mua;        /* absorption coefficient [cm^-1] */
double  mus;        /* scattering coefficient [cm^-1] */
double  mut;        /* total attenuation coefficient [cm^-1] */
double  g;         /* anisotropy [-] */
double  albedo;     /* albedo of tissue */
double  muaF, musF;            /* absorption coefficient [cm^-1] */
```

```
double  QY, QYgfp;              /* absorption coefficient [cm^-1] */
double  NphotonsFOR;                    /* number of photons in excitation simulation */
double  NlocalphotonsBAC;   /* number of photons in fluorescent simulation */
double  NphotonsBAC;                    /* number of photons in simulation */
int       NR, NZ, NP;       /* number of radial positions */
double  radial_size;            /* maximum radial size */
double  r;                      /* radial position */
double  dr,dz;                  /* radial bin size */
long    ir, iz, iir, iiz, irL;      /* index to radial position */
int       j, index;                                     // dummy
double  shellvolume;  /* volume of shell at radial position r */
long    seed;
double theta, signal;
long    ppp;
double  Vx, Vy, Vz, Key, Yfoc, Xfoc, Rph, DzStep, Zstart;
/* dummy variables */
double  rnd, Ncoll;             /* assigned random value 0-1 */
double  u, u2, temp;    /* dummy variables */
char    name[20];
double Sout[30];
double  RRad;
int bin2put;
FILE*   target;                 /* point to output file */
FILE*   target2;                /* point to output file */
double* RadialProfile;
double* opt;
double* radius;
double* Airy;
double* PDF;
double* CPDF;
double* Fdraw;
double* checkL;                         // check launch radius at focus
int       ExEmFLAG;

char    ss[255];

double **Fexzz;
double **Femzr;

RadialProfile  = dvector(1,THESIZE); /* rows */
opt     = dvector(1,1000); /* rows */
radius  = dvector(1,1000); /* rows */
Airy    = dvector(1,1000); /* rows */
PDF     = vector(1,1000); /* rows */
CPDF    = dvector(1,1000); /* rows */
Fdraw   = dvector(1,1000); /* rows */
```

```
checkL  = dvector(1,1000); /* rows */

Ccyl    = dmatrix(1,THESIZE,1,THESIZE); /* rows, columns */
CcylF   = dmatrix(1,THESIZE,1,THESIZE); /* rows, columns */

Fexzz   = dmatrix(1,THE_NP,1,THESIZE);  // f = z_focus, z = z_position
Femzr           = dmatrix(1,THE_NP,1,THESIZE);  // z = z_focus, r = r_det

/**** INPUT
  Input the optical properties
  Input the bin and array sizes
  Input the number of photons
*****/

seed                    = 1;
numericalapperture      = 0.90;
lambda = 488e-7; // [cm]
FLUthick        = 0.0001;   /*Thickness of imbedded fluorophore [cm] */
FLUdepth1       = 0.0020;   /*Depth of front edge of imbedded fluorophore [cm] */
FLUdepth2       = 0.0040;   /*Depth of front edge of imbedded fluorophore [cm] */
FLUdepth3       = 0.0060;   /*Depth of front edge of imbedded fluorophore [cm] */


mua         = 2;        /* Absorption coefficient at excitation wavelength [cm^-1] */
mus         = 2500;     /* Scattering coefficient at excitation wavelength [cm^-1] */
g           = 0.98;             /* Anisotropy of scatter */
muaF  = mua;                    /* Absorption coefficient at emission wavelength [cm^-1]
*/
musF  = mus;                    /*  1160; Scattering coefficient at emission wavelength
[cm^-1] */
QYgfp = 0.8;                    /* Quantum yield of fluorescence for imbedded fluorophore
*/
QY    = 0.0;                    /* Quantum yield of fluorescence for background tissue */
Rph   = 0.0005;
DzStep = 0.0001;
Zstart = 0.0001;

/* note, number of photons run determines the duraion of the simulation */
/* 1850000 was the value for the results in Dan Gareau's thesis */
/* this size simulation took about 3 months, decrease Nphotons for more reasonable
duration*/
NphotonsFOR    = 1850000;  /* set number of photons in forward simulation */
NphotonsBAC    = 1850000;    /* *100 set number of photons in fluorescence simulation
from each voxle */
```

```
radial_size = 1e-4*THESIZE;                     /* cm, total range over which bins extend */
NR          = THESIZE;                          /* set number of bins.  */
NZ                  = THESIZE;
NP                  = THE_NP;                                   /* number of zfocus positions
(formerly called Nruns) */
dr          = radial_size/(NR-1);           /* cm */
dz          = dr;                                   /* cm */
mut                 = mua + mus;
albedo      = mus/(mut);

printf("NR = %d\n", NR);
printf("NZ = %d\n", NZ);
printf("NP = %d\n", NP);


/*************************************************************************
************
 * create lookup table for airy focal distrabution
 ****/
/* initalize */
for (j = 1; j <=1000; j++){
          radius[j] = 0;
          Airy[j] = 0;
          opt[j] = 0; // v
          PDF[j] = 0;
          CPDF[j] = 0;
}
drad = 1.0e-7; // [cm]
for (j = 1; j <=1000; j++){
          radius[j] = drad * j;
          opt[j]    = (2.0*PI/lambda)*numericalapperture*drad*j;
          u         = (2.0*bessj1(opt[j])/opt[j]);
          Airy[j]   = u*u;
          PDF[j]    = Airy[j]*2*PI*radius[j];
}
// Normalize PDF[]
summ = 0.0;
for (ir = 1; ir <=1000; ir++){
          summ = summ + PDF[ir];
}
Tsumm = summ * drad;
for (ir = 1; ir <=1000; ir++){
          PDF[ir] = PDF[ir] / Tsumm;
}
for (ir = 1; ir <= 1000; ir++) {
```

```
        summ = 0;
        for (iir = 1; iir <= ir; iir++)
                summ = summ + PDF[iir]*drad;
        CPDF[ir] = summ;
}
irL = 1;
for (j = 1; j <= 1000; j++){
        ir = irL;
        u  = 1; // i flag = 1 enables loop
        while ( u && (CPDF[ir] < 1.0*j/1000) ) {
                ir = ir + 1;
                if ( ir > 1000 ) {
                        ir = ir - 1;
                        u = 0; // disable loop (used only at end, j ≈ 1000)
                }
        }
        irL = ir;
        frac = (1.0*j/1000 - CPDF[ir-1]) / (CPDF[ir] - CPDF[ir-1]);
        rr = radius[ir-1] + frac*(radius[ir] - radius[ir-1]);
        Fdraw[j] = rr; // predicted target radius rf <----------------------------
}
/*************************************************************************
**********/

//*****************************************************
//*************** fluorophore positions ************
//*****************************************************
int k[5];
k[0] = 20;  /* microns */
k[1] = 40;
k[2] = 60;
k[3] = 80;

int jjz;
for (jjz=0; jjz<3; jjz++) {
        iiz = k[jjz];

for (index = 1; index <=THESIZE; index++)
        for(j = 1; j <= THE_NP; j++){
        Femzr[j][index] = 0.0;
        Fexzz[j][index] = 0.0;
}

/************************ ppp ***************/
/************************ ppp ***************/
/************************ ppp ***************/
```

```
// time to completion
startTime = clock();
int jclock = 0;

long Nclock = 40 + 60 + 80 + 100 - 4;
for (ppp=iiz-((jjz+2)*10 - 1); ppp<=iiz+((jjz+2)*10 - 1) ; ppp++){  // try NP different focal depths, zf(ppp) == Fdepth

////// time report
if (jclock < 30) {
        endTime = clock();
        if (jclock>0)
                printf("estimated completion time = %5.2f min\n", (endTime - startTime)/jclock/CLOCKS_PER_SEC/60*Nclock );
}
jclock++;
int i;
for (i=0; i<=80; i++)
        if ( i < (int)(jclock/Nclock*80) )
                printf("*");
        else
                printf("-");
printf("\n");
////// end time report

Fdepth = Zstart + (ppp - 1)*DzStep;
w = tan(0.5*asin(numericalapperture))*Fdepth;

/**** INITIALIZATIONS
*****/
i_photon = 0;
(double) RandomGen(0, seed, NULL);

for (ir=1; ir<=NR; ir++)
        for (iz=1; iz<=NR; iz++) {
                Ccyl[iz][ir] = 0.0;
                CcylF[iz][ir] = 0.0;
                }

Wtot = 0.0;

/***********************************
 * EXCITATION
 ***************************/
 ExEmFLAG = 0;
```

```
/**** RUN
  Launch N photons, initializing each one before progation.
*****/
printf("launch forward photons @ zf(ppp=%d), jjz=%d\n", ppp, jjz);
do {


/**** LAUNCH
  Initialize photon position and traectory.
  Implements an isotropic point source.
*****/

i_photon += 1;  /* increment photon count */

u = (double)i_photon;



if (fmod(u,10000)==0) printf("Excitation ppp/jjz = %d/%d, %d forward photons, \n",
ppp,jjz, i_photon);

/******
 * DAN's LAUNCH
 *****/
// Gaussian at surface --> Rone
while ((rnd = RandomNum) <= 0.0);
 /* yields 0 < rnd <= 1 */
Rone = w*sqrt(-log(rnd));       /*(Dan) Gaussian distribution radius*/

// Airy at focus ---> Rtwo
while ((rnd = RandomNum) <= 0.0);
u = 999.0*rnd;
index = (int)(u - fmod(u,1)) + 1; // floor(u)
Rtwo = Fdraw[index];
while ((rnd = RandomNum) <= 0.0);

x = Rone;
y = 0;
z = 0;

while ((rnd = RandomNum) <= 0.0);
psi = rnd*2.0*PI;
x2  = Rtwo*cos(psi);
y2  = Rtwo*sin(psi);

sxy = sqrt(y2*y2 + (x2 - x)*(x2 - x));
```

```
s   = sqrt(Fdepth*Fdepth + sxy*sxy);

uz  = Fdepth/s;
ux  = (x2-x)/s;
uy  = (y2-y)/s;

W = 1.0;                /* set photon weight to one */
//printf("W = %0.5f\n", W);
Wtot += W;
photon_status = ALIVE;      /* Launch an ALIVE photon */



/* HOP_DROP_SPIN_CHECK
  Propagate one photon until it dies as determined by ROULETTE.
*******/
do {


/**** HOP
  Take step to new position
  s = stepsize
  ux, uy, uz are cosines of current photon traectory
*****/
 while ((rnd = RandomNum) <= 0.0);   /* yields 0 < rnd <= 1 */
 s = -log(rnd)/mut;         /* Step size.  Note: log() is base e */
 x += s * ux;                    /* Update positions. */
 y += s * uy;
 z += s * uz;


/**** DROP
  Drop photon weight (W) into local bin.
*****/
  absorb = W*(1 - albedo);      /* photon weight absorbed at this step */
  W -= absorb;                /* decrement WEIGHT by amount absorbed */

  /* cylindrical */
  r = sqrt(x*x + y*y);          /* current cylindrical radial position */
  ir = (long)(r/dr) + 1;        /* ir = index to spatial bin */
  iz = (long)(fabs(z)/dz) + 1;  /* ir = index to spatial bin */
  if (ir >= NR) ir = NR;        /* last bin is for overflow */
  if (iz >= NR) iz = NR;        /* last bin is for overflow */
  Ccyl[iz][ir] += absorb;       /* DROP absorbed weight into bin */
```

```
/**** SPIN
   Scatter photon into new traectory defined by theta and psi.
   Theta is specified by cos(theta), which is determined
   based on the Henyey-Greenstein scattering function.
   Convert theta and psi into cosines ux, uy, uz.
*****/
  /* Sample for costheta */
  rnd = RandomNum;
     if (g == 0.0)
        costheta = 2.0*rnd - 1.0;
     else if (g == 1.0)
        costheta = 1.0;
     else {
        double temp = (1.0 - g*g)/(1.0 - g + 2*g*rnd);
        costheta = (1.0 + g*g - temp*temp)/(2.0*g);
        }
  sintheta = sqrt(1.0 - costheta*costheta); /* sqrt() is faster than sin(). */

  /* Sample psi. */
  psi = 2.0*PI*RandomNum;
  cospsi = cos(psi);
  if (psi < PI)
    sinpsi = sqrt(1.0 - cospsi*cospsi);     /* sqrt() is faster than sin(). */
  else
    sinpsi = -sqrt(1.0 - cospsi*cospsi);

  /* New traectory. */
  if (1 - fabs(uz) <= ONE_MINUS_COSZERO) {      /* close to perpendicular. */
    uxx = sintheta * cospsi;
    uyy = sintheta * sinpsi;
    uzz = costheta * MYSIGN(uz);   /* MYSIGN() is faster than division. */
    }
  else {                                /* usually use this option */
    temp = sqrt(1.0 - uz * uz);
    uxx = sintheta * (ux * uz * cospsi - uy * sinpsi) / temp + ux * costheta;
    uyy = sintheta * (uy * uz * cospsi + ux * sinpsi) / temp + uy * costheta;
    uzz = -sintheta * cospsi * temp + uz * costheta;
    }

  /* Update traectory */
  ux = uxx;
  uy = uyy;
  uz = uzz;


/**** CHECK ROULETTE
```

```
  If photon weight below THRESHOLD, then terminate photon using Roulette technique.
  Photon has CHANCE probability of having its weight increased by factor of 1/CHANCE,
  and 1-CHANCE probability of terminating.
*****/
if (W < THRESHOLD) {
  if (RandomNum <= CHANCE)
    W /= CHANCE;
  else photon_status = DEAD;
  }


} /* end STEP_CHECK_HOP_SPIN */
while (photon_status == ALIVE);

 // If photon dead, then launch new photon.
} /////////////// end RUN ////////////////////
while (i_photon < NphotonsFOR);


// update Fexzz
ir = 1;
for (iz=1; iz<=NZ; iz++) {
        Fexzz[ppp][iz] = Ccyl[iz][ir]/NphotonsFOR;  // total in each ring_bin, normalized
}



/**********************************
 * EMISSION
 **************************/
 ExEmFLAG = 1;

/*************************************************************************************
**************/
                    /*   RUN THE BACKWARD PROBLEM          */
/*************************************************************************************
**************/

/* Convert optics to emission wavelength */
mua = muaF;
mus = musF;
mut = mua + mus;
albedo  = mus/mut;
Ncoll = 0;
```

```
i_photon = 0;
signal = 0.0;

/**** RUN
  Launch N photons, initializing each one before progation.
*****/
printf("launch backward photons @ zf(%d), jjz = %d\n\n", ppp, jjz);
WF = 1.0;
for (ir=1; ir<=NR; ir++){
        RadialProfile[ir] = 0;}


// initialize Ccyl
for (iz=1; iz<=NZ; iz++)
        for (ir=1; ir<=NR; ir++)
                Ccyl[iz][ir] = 0.0;

for (j_photon=1; j_photon<=NphotonsBAC; j_photon++)  { // LAUNCH N photons isotropically

/**** LAUNCH
  Initialize photon position and trajectory.
  Implements an isotropic point source.
*****/
i_photon += 1;  /* increment photon count */

u = (double)i_photon;

if (fmod(u,10000)==0) printf("Emission ppp/jjz = %d/%d, %d forward photons, \n", ppp,jjz, i_photon);

photon_status = ALIVE;      /* Launch an ALIVE photon */

/* Choose Launch position */
//x = (iir - 0.5)*dr;
x = 0.0;
y = 0.0;
z = (iiz - 0.5)*dz; // isotropic launch for escaping photons

/* Launch Isotropically */
while ((rnd = RandomNum) <= 0.0);   /* yields 0 < rnd <= 1 */
costheta = 2.0*rnd - 1.0;
sintheta = sqrt(1.0 - costheta*costheta);        /* sintheta is always positive */
while ((rnd = RandomNum) <= 0.0);   /* yields 0 < rnd <= 1 */
psi = (2.0*rnd - 1.0)*PI;
```

```
W  = 1.0;

/* calculate cosines */
ux = sintheta*cos(psi);
uy = sintheta*sin(psi);
uz = costheta;

/* HOP_DROP_SPIN_CHECK
  Propagate one photon until it dies as determined by ROULETTE.
*******/
do {

/**** HOP
  Take step to new position
  s = stepsize
  ux, uy, uz are cosines of current photon trajectory
*****/
 while ((rnd = RandomNum) <= 0.0);   /* yields 0 < rnd <= 1 */
 s = -log(rnd)/mut;         /* Step size.  Note: log() is base e */
 xlast = x;       /* save last positions */
 zlast = z;
 ylast = y;
 x += s * ux;                    /* Update positions. */
 y += s * uy;
 z += s * uz;

/**** DROP
  Drop photon weight (W) into local bin.
*****/

if (z < 0.0) {              /* if photon has crossed the UPPER tissue boundry, no BOTTOM
boundary ... semi-infinite tissue */

        Xfoc = x - (z - Fdepth) * ((x-xlast)/(z-zlast));
        Yfoc = y - (z - Fdepth) * ((y-ylast)/(z-zlast));

        RRad = sqrt(Xfoc*Xfoc + Yfoc*Yfoc);
        bin2put = (int)(RRad/dr) + 1; // acts like floor()

        xsurf = x - z*((x-xlast)/(z-zlast));
        ysurf = y - z*((y-ylast)/(z-zlast));
        rsurf = sqrt(xsurf*xsurf + ysurf*ysurf);

   if (rsurf < w)
        if (bin2put < THESIZE) {
```

```
                RadialProfile[bin2put] += WF*W;
                }

        if (sqrt(Xfoc*Xfoc + Yfoc*Yfoc) < Rph) {
                signal += WF*W;
                Ncoll += 1;
                }
        photon_status = DEAD;
        }

else{
  absorb = W*(1.0 - albedo);      /* photon weight absorbed at this step */
  W -= absorb;                    /* decrement WEIGHT by amount absorbed */

  /* cylindrical */
  r = sqrt(x*x + y*y);          /* current cylindrical radial position */
  ir = (long)(r/dr) + 1;        /* ir = index to spatial bin */
  iz = (long)(fabs(z)/dz) + 1;       /* ir = index to spatial bin */
  if (ir >= NR) ir = NR;        /* last bin is for overflow */
  if (iz >= NR) iz = NR;        /* last bin is for overflow */
  CcylF[iz][ir] += WF*absorb;        /* DROP absorbed weight into bin */
  }

/**** SPIN
  Scatter photon into new trajectory defined by theta and psi.
  Theta is specified by cos(theta), which is determined
  based on the Henyey-Greenstein scattering function.
  Convert theta and psi into cosines ux, uy, uz.
*****/
 /* Sample for costheta */
        while ((rnd = RandomNum) <= 0.0);   /* yields 0 < rnd <= 1 */
   if (g == 0.0)
     costheta = 2.0*rnd - 1.0;
   else if (g == 1.0)
     costheta = 1.0;
   else {
     double temp = (1.0 - g*g)/(1.0 - g + 2*g*rnd);
     costheta = (1.0 + g*g - temp*temp)/(2.0*g);
     }
 sintheta = sqrt(1.0 - costheta*costheta); /* sqrt() is faster than sin(). */

 /* Sample psi. */
 while ((rnd = RandomNum) <= 0.0);   /* yields 0 < rnd <= 1 */
 psi = 2.0*PI*rnd;
 cospsi = cos(psi);
 if (psi < PI)
```

```
  sinpsi = sqrt(1.0 - cospsi*cospsi);     /* sqrt() is faster than sin(). */
 else
  sinpsi = -sqrt(1.0 - cospsi*cospsi);

 /* New trajectory. */
 if (1 - fabs(uz) <= ONE_MINUS_COSZERO) {      /* close to perpendicular. */
  uxx = sintheta * cospsi;
  uyy = sintheta * sinpsi;
  uzz = costheta * MYSIGN(uz);   /* MYSIGN() is faster than division. */
  }
 else {                                 /* usually use this option */
  temp = sqrt(1.0 - uz * uz);
  uxx = sintheta * (ux * uz * cospsi - uy * sinpsi) / temp + ux * costheta;
  uyy = sintheta * (uy * uz * cospsi + ux * sinpsi) / temp + uy * costheta;
  uzz = -sintheta * cospsi * temp + uz * costheta;
  }

 /* Update trajectory */
 ux = uxx;
 uy = uyy;
 uz = uzz;


/**** CHECK ROULETTE
  If photon weight below THRESHOLD, then terminate photon using Roulette
technique.
  Photon has CHANCE probability of having its weight increased by factor of
1/CHANCE,
  and 1-CHANCE probability of terminating.
*****/
if (W < THRESHOLD) {
        while ((rnd = RandomNum) <= 0.0);   /* yields 0 < rnd <= 1 */
        if (rnd <= CHANCE)
    W /= CHANCE;
  else photon_status = DEAD;
  }


} /* end STEP_CHECK_HOP_SPIN */
while (photon_status == ALIVE);
/* If photon dead, then launch new photon. */

}  /*************************** end RUN N photons isotropically
*******************/

// SAVE Femzr(zf=ppp, ir)
```

```
for (ir=1; ir<=NR; ir++)
        Femzr[ppp][ir] = RadialProfile[ir]/NphotonsBAC;


/*****************************************************************************
**************/
                /*      Done with reverse problem    */
/*****************************************************************************
**************/



}/************
 * end of ppp launch positions

*****************************************************************************
******
 ***************************          END          OF          PPP
****************************************

*****************************************************************************
******/
printf("done with jjz:ppp launches.\n");


/********
 * OUTPUT TO FILE
 ******/

//*******************************************************
// ******** save Fexfz ********************************
sprintf(name,"Fexzz%d.dat", jjz);
printf("%s\n", name);
target = fopen(name, "w");
for (ppp=1; ppp<=NP; ppp++)
        for (iz=1; iz<=NZ; iz++) {
                fprintf(target, "%6.3e", Fexzz[ppp][iz]);
                if (iz<NZ)
                        fprintf(target, "\t");
                else
                        fprintf(target, "\n");
        }
fclose(target);

sprintf(name,"Femzr%d.dat", jjz);
printf("%s\n", name);
```

```
target = fopen(name, "w");
for (ppp=1; ppp<=NP; ppp++)
        for (iz=1; iz<=NZ; iz++) {
                fprintf(target, "%6.3e", Femzr[ppp][iz]);
                if (iz<NZ)
                        fprintf(target, "\t");
                else
                        fprintf(target, "\n");
        }
fclose(target);



}//*****************************************************
//********** END jjz fluorophore positions ************
//*****************************************************

free_dvector(RadialProfile, 1, THESIZE);
free_dmatrix(Ccyl,1,THESIZE,1,THESIZE);
free_dmatrix(CcylF,1,THESIZE,1,THESIZE);
free_dmatrix(Fexzz,1,THE_NP,1,THESIZE);
free_dmatrix(Femzr,1,THESIZE,1,THESIZE);

//} // end SWITCH
} /* end of main */

/* SUBROUTINES */


/*****
 * bessj1(x)
 * Returns the Bessel function 1(x) for any real x.
 * Be sure to #include <math.h>
 * From Numerical Recipes in C.
 ****/
 float bessj1(float x) {
        float ax,z;
        double xx,y,ans,ans1,ans2; // Accumulate polynomials in double precision.

if ((ax=fabs(x)) < 8.0) { //Direct rational approximation.
        y=x*x;
        ans1=x*(72362614232.0+y*(-7895059235.0+y*(242396853.1                +y*(-
2972611.439+y*(15704.48260+y*(-30.16036606))))));
        ans2=144725228442.0+y*(2300535178.0+y*(18583304.74
+y*(99447.43394+y*(376.9991397+y*1.0))));
        ans=ans1/ans2;
```

```
} else {  //Fitting function (6.5.9).
        z=8.0/ax;
        y=z*z;
        xx=ax-2.356194491;
        ans1=1.0+y*(0.183105e-2+y*(-0.3516396496e-4       +y*(0.2457520174e-5+y*(-
0.240337019e-6))));
        ans2=0.04687499995+y*(-0.2002690873e-3            +y*(0.8449199096e-5+y*(-
0.88228987e-6 +y*0.105787412e-6)));
        ans=sqrt(0.636619772/ax)*(cos(xx)*ans1-z*sin(xx)*ans2);
        if (x < 0.0) ans = -ans;
}
return ans;
}

/**************************************************************************
***
 *      RandomGen
 *      A random number generator that generates uniformly
 *      distributed random numbers between 0 and 1 inclusive.
 *      The algorithm is based on:
 *      W.H. Press, S.A. Teukolsky, W.T. Vetterling, and B.P.
 *      Flannery, "Numerical Recipes in C," Cambridge University
 *      Press, 2nd edition, (1992).
 *      and
 *      D.E. Knuth, "Seminumerical Algorithms," 2nd edition, vol. 2
 *      of "The Art of Computer Programming", Addison-Wesley, (1981).
 *
 *      When Type is 0, sets Seed as the seed. Make sure 0<Seed<32000.
 *      When Type is 1, returns a random number.
 *      When Type is 2, gets the status of the generator.
 *      When Type is 3, restores the status of the generator.
 *
 *      The status of the generator is represented by Status[0..56].
 *
 *      Make sure you initialize the seed before you get random
 *      numbers.
 ****/
#define MBIG 1000000000
#define MSEED 161803398
#define MZ 0
#define FAC 1.0E-9

double RandomGen(char Type, long Seed, long *Status){
  static long i1, i2, ma[56];   /* ma[0] is not used. */
  long       m, mk;
  short      i, ii;
```

```
 if (Type == 0) {              /* set seed. */
   m = MSEED - (Seed < 0 ? -Seed : Seed);
   m %= MBIG;
   ma[55] = m;
   mk = 1;
   for (i = 1; i <= 54; i++) {
     ii = (21 * i) % 55;
     ma[ii] = mk;
     mk = m - mk;
     if (mk < MZ)
       mk += MBIG;
     m = ma[ii];
   }
   for (ii = 1; ii <= 4; ii++)
     for (i = 1; i <= 55; i++) {
       ma[i] -= ma[1 + (i + 30) % 55];
       if (ma[i] < MZ)
         ma[i] += MBIG;
     }
   i1 = 0;
   i2 = 31;
 } else if (Type == 1) {       /* get a number. */
   if (++i1 == 56)
     i1 = 1;
   if (++i2 == 56)
     i2 = 1;
   m = ma[i1] - ma[i2];
   if (m < MZ)
     m += MBIG;
   ma[i1] = m;
   return (m * FAC);
 } else if (Type == 2) {       /* get status. */
   for (i = 0; i < 55; i++)
     Status[i] = ma[i + 1];
   Status[55] = i1;
   Status[56] = i2;
 } else if (Type == 3) {       /* restore status. */
   for (i = 0; i < 55; i++)
     ma[i + 1] = Status[i];
   i1 = Status[55];
   i2 = Status[56];
 } else
   puts("Wrong parameter to RandomGen().");
 return (0);
}
```

```
#undef MBIG
#undef MSEED
#undef MZ
#undef FAC
```

A6) rcmc.c

```
/*** rcmc.c ***/
/*** DSG SLJ September 2005 ***/

#include <math.h>
#include <stdio.h>
#include <string.h>
#include "nrutil.h"

#define PI         3.1415926
#define LIGHTSPEED      2.997925E10 /* in vacuo speed of light [cm/s] */
#define ALIVE       1               /* if photon not yet terminated */
#define DEAD        0               /* if photon is to be terminated */
#define THRESHOLD   1e-4            /* used in roulette */
#define CHANCE      0.1             /* used in roulette */
#define COS90D      1.0E-6
    /* If cos(theta) <= COS90D, theta >= PI/2 - 1e-6 rad. */
#define ONE_MINUS_COSZERO 1.0E-12
    /* If 1-cos(theta) <= ONE_MINUS_COSZERO, fabs(theta) <= 1e-6 rad. */
    /* If 1+cos(theta) <= ONE_MINUS_COSZERO, fabs(PI-theta) <= 1e-6 rad. */
#define MYSIGN(x)          ((x)>=0 ? 1:-1)
#define InitRandomGen    (double) RandomGen(0, 1, NULL)
    /* Initializes the seed for the random number generator. */
#define RandomNum        (double) RandomGen(1, 0, NULL)
    /* Calls for a random number from the randum number generator. */
#define THESIZE 250

/* DECLARE FUNCTION */
double RandomGen(char Type, long Seed, long *Status);
float bessj1(float x);


int main() {


/* Propagation parameters */

double  Rtwo, Rone, rr;       /* (Dan) radius of launched photon [cm] */
double Fdepth, lambda, w;
double numericalapperture;
double  RunNum, drad, summ, Tsumm, unity, frac;
```

```
double RunsTotal, Nrunsmus, Nrunsg;
double  NrunsZ;
int       imus, ig, zzz;

double  x, y, z, x2, y2;    /* photon position */
double  xlast, ylast, zlast;    /* keep track of last photon position in tissue*/
double  xsurf, ysurf, rsurf;    /* keep track of last photon position */
double  ux, uy, uz; /* photon trajectory as cosines */
double  uxy, uxx, uyy, uzz;  /* temporary values used during SPIN */
double  s, sxy;         /* step sizes. s = -log(RND)/mus [cm] */
double  costheta;   /* cos(theta) */
double  sintheta;   /* sin(theta) */
double  cospsi;     /* cos(psi) */
double  sinpsi;     /* sin(psi) */
double  psi;       /* azimuthal angle */
long     i_photon;   /* current photon */
long     j_photon;   /* current local photon */
double  W, WF, Wtot;         /* photon weight */
double  absorb;     /* weighted deposited in a step due to absorption */
short   photon_status;  /* flag = ALIVE=1 or DEAD=0 */

/* other variables */
double  **Ccyl;  /* cylindrical photon concentration */
double  Fcyl;       /* fluence in cylindrical shell */
double  Fcylout;       /* fluence in cylindrical shell */
double  mua;        /* absorption coefficient [cm^-1] */
double  mus;        /* scattering coefficient [cm^-1] */
double  musStart;        /* scattering coefficient [cm^-1] */
double  dmus;        /* scattering coefficient [cm^-1] */
double  gStart;        /* scattering coefficient [cm^-1] */
double  dg;        /* scattering coefficient [cm^-1] */
double  mut;        /* total attenuation coefficient [cm^-1] */
double  g;         /* anisotropy [-] */
double  albedo;     /* albedo of tissue */
double  NphotonsFOR;   /* number of photons in simulation */
double  Nphotons;   /* number of photons in simulation */
long     NR;        /* number of radial positions */
double  radial_size;  /* maximum radial size */
double  r;         /* radial position */
double  dr,dz;         /* radial bin size */
long     Fiz, ir, iz, iir, iiz, irL;         /* index to radial position */
int       j, index;    // dummy
int                izf; /* index of focal depth in fantom
double  shellvolume;  /* volume of shell at radial position r */
long     seed;
double  Vx, Vy, Vz, Yfoc, Xfoc, DzStep, Zstart;
```

```
/* dummy variables */
double  rnd;        /* assigned random value 0-1 */
double  u, u2, temp;    /* dummy variables */
char     name[20];
double Sout[30];
/*double          RadialProfile[THESIZE];*/
double  RRad;
int bin2put;
FILE*   target;     /* point to output file */
double** EXprofile;
double** EMprofile;
double* opt;
double* radius;
double* Airy;
double* PDF;
double* CPDF;
double* Fdraw;
double* checkL; // check launch radius at focus
int       ExEmFLAG;

char     ss[255];


opt     = dvector(1,1000); /* rows */
radius  = dvector(1,1000); /* rows */
Airy    = dvector(1,1000); /* rows */
PDF     = vector(1,1000); /* rows */
CPDF    = dvector(1,1000); /* rows */
Fdraw   = dvector(1,1000); /* rows */
checkL  = dvector(1,1000); /* rows */

Ccyl    = dmatrix(1,THESIZE,1,THESIZE); /* rows, columns */

/**** INPUT
  Input the optical properties
  Input the bin and array sizes
  Input the number of photons
*****/

seed                    = 1;
numericalapperture      = 0.90;
lambda = 488e-7; // [cm]

musStart    = 500;      // Smallest scattering coef. in grid
dmus        = 50;       // incremental step size [cm-1]
gStart      = 0.70;     // Smallest scattering anisotropy in grid
```

```
dg          = 0.05;          // incremental step size [-]

mua = 2;


// in the following choose Nrunsmus = Nrunsg + 1
// the last mus run is for mus = 0; (calibration)

Nrunsg = 6;     /* Neffrunsg = Nrunsg - 1 */
Nrunsmus = 7;

NrunsZ = 8;     /* # Depth runs in the sample */
DzStep = 0.0003;// incremental z-step size [cm]
Zstart = 0.0003;// shallowest depth [cm]

EXprofile  = dmatrix(1,NrunsZ,1,THESIZE); // [z,r] @ Zfocus
EMprofile  = dmatrix(1,NrunsZ,1,THESIZE); // [z,r] @ surface

RunsTotal = ((Nrunsmus - 1) * Nrunsg) + 1;
Nphotons = 1.5e10;  // runs for a long-ass time to overcome noise

radial_size = 0.0060;                   /* cm, total range over which bins extend */
NR          = THESIZE;                          /* set number of bins.  */
dr          = radial_size/(NR-1);       /*9.23e-4; radial_size/(NR-1);*/  /* cm */
dz          = dr;       /* cm */

/* make paramaters.m a file for matlab analysis of data */

sprintf(ss, "parameters.m");
target = fopen(ss, "w");
fprintf(target, "%% input parameters for Monta Carlo \n\n");

fprintf(target, "musStart = %3.0f;\n", musStart);
fprintf(target, "Nrunsmus = %1.0f;\n", Nrunsmus);
fprintf(target, "dmus = %3.0f;\n", dmus);

fprintf(target, "gStart = %f;\n", gStart);
fprintf(target, "Nrunsg = %1.0f;\n", Nrunsg);
fprintf(target, "dg = %0.3f;\n", dg);

fprintf(target, "zStart = %0.6f;\n", Zstart);
fprintf(target, "NrunsZ = %2.0f;\n", NrunsZ);
fprintf(target, "DzStep = %0.6f;\n", DzStep);

fprintf(target, "mua = %1.1f;\n", mua);
```

```
fprintf(target, "NR = %d;\n", NR);
fprintf(target, "dr = %0.8f;\n", dr);
fprintf(target, "Nphotons = %20.0f;\n", Nphotons);

fclose(target);

/*************************************************************************
************

*************************************************************************
***********
 * create lookup table for airy focal distrabution
 ****/
/* initalize */
for (j = 1; j <=1000; j++){
        radius[j] = 0;
        Airy[j] = 0;
        opt[j] = 0; // v
        PDF[j] = 0;
        CPDF[j] = 0;
}
drad = 1.0e-7; // [cm]
for (j = 1; j <=1000; j++){
        radius[j] = drad * j;
        opt[j]    = (2.0*PI/lambda)*numericalapperture*drad*j;
        u         = (2.0*bessj1(opt[j])/opt[j]);
        Airy[j]   = u*u;
        PDF[j]    = Airy[j]*2*PI*radius[j];
}
// Normalize PDF[]
summ = 0.0;
for (ir = 1; ir <=1000; ir++){
        summ = summ + PDF[ir];
}
Tsumm = summ * drad;
for (ir = 1; ir <=1000; ir++){
        PDF[ir] = PDF[ir] / Tsumm;
}
for (ir = 1; ir <= 1000; ir++) {
        summ = 0;
        for (iir = 1; iir <= ir; iir++)
                summ = summ + PDF[iir]*drad;
        CPDF[ir] = summ;
}
irL = 1;
for (j = 1; j <= 1000; j++){
```

```
		ir = irL;
		u  = 1; // i flag = 1 enables loop
		while ( u && (CPDF[ir] < 1.0*j/1000) ) {
			ir = ir + 1;
			if ( ir > 1000 ) {
				ir = ir - 1;
				u = 0; // disable loop (used only at end, j ≈ 1000)
			}
		}
		irL = ir;
		frac = (1.0*j/1000 - CPDF[ir-1]) / (CPDF[ir] - CPDF[ir-1]);
		rr = radius[ir-1] + frac*(radius[ir] - radius[ir-1]);
		Fdraw[j] = rr;		// predicted target radius rf <----------------------------
}
/**************************************************************************************
***********
**************************************************************************************
***********/

RunNum = 0;

//   Choose Mus (scattering coefficient)
for (imus = 1 ; imus<= 3 ; imus++){
		mus = musStart + dmus*(imus - 1);
		if (imus == Nrunsmus) { mus = 0; }
		if (imus < Nrunsmus) { mus = musStart + dmus*(imus - 1); }
		mut		= mua + mus;
		albedo	= mus/(mut);

		printf("\ndmus = %f", dmus);
		printf("\nmusStart = %f", musStart);
		printf("\nimus = %d", imus);
		printf("\nmua = %1.1f\n", mua);
		printf("\nmus = %1.1f\t imus = %d\n", mus, imus);
		printf("\n\nAlbedo = %0.20f\n", albedo);
		NphotonsFOR  = (double)( (long)( Nphotons*(1-albedo) ) );  /* set number of
photons in forward simulation */
		printf("\n\n=========> NphotonsFor = %0.0f\n", NphotonsFOR);
		//NphotonsFOR = 1e2;

//   Choose g (scattering Anisortopy)

		for (ig = 1 ; ig<=Nrunsg ; ig++){

			RunNum += 1;
```

```
                // the following if prevent unnscissary runs at mus = 0
                if (RunNum <= RunsTotal) {

                        g = gStart + dg*(ig - 1);

                        printf("imus = %d \t ig = %d\n", imus, ig);
                        printf("mus = %0.0f \t g = %0.3f\n", mus, g);

//      Scan confocal volume axially into phantom  zzz = index of z step
                        for (iz=1; iz<=NrunsZ; iz++)
                        for (ir=1; ir<=NR; ir++) {
                        EMprofile[iz][ir] = 0;
                        EXprofile[iz][ir] = 0;
                        }


                        for (zzz = 1 ; zzz<=NrunsZ ; zzz++){
                                // printf("zzz = %0.0d \n", zzz);
                                Fdepth = Zstart + (zzz - 1)*DzStep;
                                w = tan(0.5*asin(numericalapperture))*Fdepth;
                                izf = (int)(1.0*Fdepth/DzStep);

/**** INITIALIZATIONS
*****/
                                i_photon = 0;
                                (double) RandomGen(0, seed, NULL);

                                for (ir=1; ir<=NR; ir++)
                                for (iz=1; iz<=NR; iz++)
                                Ccyl[iz][ir] = 0.0;


                                Wtot = 0.0;

/**** RUN
  Launch N photons, initializing each one before progation.
*****/
                                do {

/******
 * DAN's LAUNCH
 * Initialize photon position and traectory.
 * Gaussian at surface and Airy at subsurface focus.
 *****/
```

```
                        i_photon += 1;  /* increment photon count */
                        if (1) {
                                u = (double)i_photon;
                                        if  (fmod(u,10000)==0)  printf("run
number mu/g/z = %d/%d/%d, %d forward photons, \n", imus,ig,zzz, i_photon);

                        }
// Gaussian at surface --> Rone

                        while ((rnd = RandomNum) <= 0.0);
                        /* yields 0 < rnd <= 1 */
                        Rone = w*sqrt(-log(rnd));          /*(Dan) Gaussian
distribution radius*/

// Airy at focus ---> Rtwo
                        while ((rnd = RandomNum) <= 0.0);
                        u = 999.0*rnd;
                        index = (int)(u - fmod(u,1)) + 1; // floor(u)
                        Rtwo = Fdraw[index];
                        while ((rnd = RandomNum) <= 0.0);

                        x = Rone;
                        y = 0;
                        z = 0;

                        while ((rnd = RandomNum) <= 0.0);
                        psi = rnd*2.0*PI;
                        x2  = Rtwo*cos(psi);
                        y2  = Rtwo*sin(psi);

                        sxy = sqrt(y2*y2 + (x2 - x)*(x2 - x));
                        s   = sqrt(Fdepth*Fdepth + sxy*sxy);

                        uz  = Fdepth/s;
                        ux  = (x2-x)/s;
                        uy  = (y2-y)/s;

                        W = 1.0;                /* set photon weight to one */
                        Wtot += W;
                        photon_status = ALIVE;      /* Launch an ALIVE
photon */


/* HOP_DROP_SPIN_CHECK
```

```
  Propagate one photon until it dies as determined by ROULETTE.
*******/

                                        do { // while (photon_status == ALIVE);

/**** HOP
  Take step to new position
  s = stepsize
  ux, uy, uz are cosines of current photon traectory
*****/
                                        while ((rnd = RandomNum) <= 0.0);    /*
yields 0 < rnd <= 1 */
                                        s = -log(rnd)/mut;          /* Step size.  Note:
log() is base e */
                                        xlast = x;        /* save last positions */
                                        zlast = z;
                                        ylast = y;
                                        x += s * ux;                        /* Update
positions. */
                                        y += s * uy;
                                        z += s * uz;

/**** DROP
  Drop photon weight (W) into local bin.
*****/
                                        if (z < 0.0) {            /*  if  photon  has
crossed the tissue boundry */
                                        Xfoc = x - (z - Fdepth) * ((x-xlast)/(z-
zlast));
                                        Yfoc = y - (z - Fdepth) * ((y-ylast)/(z-
zlast));
                                        RRad = sqrt(Xfoc*Xfoc + Yfoc*Yfoc);
                                        bin2put = (int)(RRad/dr) + 1; // acts like
floor()

                                        xsurf = x - z*((x-xlast)/(z-zlast));
                                        ysurf = y - z*((y-ylast)/(z-zlast));
                                        rsurf = sqrt(xsurf*xsurf + ysurf*ysurf);

                                        if (bin2put < THESIZE)
                                                if (rsurf < w){
```

```
                                        //printf("WF = %e\t W =
%f\n", WF, W);
                                        EMprofile[zzz][bin2put] +=
W;
                                        }

                                photon_status = DEAD;
                                }

/* cylindrical */               else{
                                absorb = W*(1 - albedo);        /* photon
weight absorbed at this step */
                                W -= absorb;                    /* decrement
WEIGHT by amount absorbed */
                                r = sqrt(x*x + y*y);            /* current
cylindrical radial position */
                                ir = (long)(r/dr) + 1;          /* ir = index to
spatial bin */
                                iz = (long)(fabs(z)/dz) + 1;    /* ir = index to
spatial bin */
                                if (ir >= NR) ir = NR;          /* last bin is for
overflow */
                                if (iz >= NR) iz = NR;          /* last bin is for
overflow */
                                Ccyl[iz][ir] += absorb;         /* DROP
absorbed weight into bin */
                                }

/**** SPIN
  Scatter photon into new traectory defined by theta and psi.
  Theta is specified by cos(theta), which is determined
  based on the Henyey-Greenstein scattering function.
  Convert theta and psi into cosines ux, uy, uz.
*****/
 /* Sample for costheta */
                                rnd = RandomNum;
                        if (g == 0.0)
                                costheta = 2.0*rnd - 1.0;
                                else if (g == 1.0)
                                costheta = 1.0;
                                else {
                                double temp = (1.0 - g*g)/(1.0 - g +
2*g*rnd);
                                costheta = (1.0 + g*g - temp*temp)/(2.0*g);
                                }
                                sintheta = sqrt(1.0 - costheta*costheta);
```

```
                                        /* sqrt() is faster than sin(). */

 /* Sample psi. */
                                        psi = 2.0*PI*RandomNum;
                                        cospsi = cos(psi);
                                        if (psi < PI)
                                        sinpsi = sqrt(1.0 - cospsi*cospsi);     /* sqrt()
is faster than sin(). */
                                        else
                                        sinpsi = -sqrt(1.0 - cospsi*cospsi);

 /* New traectory. */
                                        if          (1          -          fabs(uz)          <=
ONE_MINUS_COSZERO) {      /* close to perpendicular. */
                                        uxx = sintheta * cospsi;
                                        uyy = sintheta * sinpsi;
                                        uzz  =  costheta  *  MYSIGN(uz);        /*
MYSIGN() is faster than division. */
                                        }
                                        else {          /* usually use this option */
                                        temp = sqrt(1.0 - uz * uz);
                                        uxx = sintheta * (ux * uz * cospsi - uy *
sinpsi) / temp + ux * costheta;
                                        uyy = sintheta * (uy * uz * cospsi + ux *
sinpsi) / temp + uy * costheta;
                                        uzz = -sintheta * cospsi * temp + uz *
costheta;
                                        }

                                         /* Update traectory */
                                        ux = uxx;
                                        uy = uyy;
                                        uz = uzz;


/**** CHECK ROULETTE
  If photon weight below THRESHOLD, then terminate photon using Roulette
technique.
  Photon has CHANCE probability of having its weight increased by factor of
1/CHANCE,
  and 1-CHANCE probability of terminating.
*****/
```

```
                                        if (W < THRESHOLD) {
                                        if (RandomNum <= CHANCE)
                                        W /= CHANCE;
                                        else photon_status = DEAD;
                                        }

                                        //printf("working till here\n");
                                        } /* end STEP_CHECK_HOP_SPIN */
                                        while (photon_status == ALIVE);

 /* If photon dead, then launch new photon. */


                                    } /* end do RUN */
                                    while (i_photon < NphotonsFOR);


                                    for (ir=1; ir<=NR; ir++)
                                    EXprofile[izf][ir] = Ccyl[izf][ir]/NphotonsFOR;




                                } /* end of zzz */



/************************ SAVE Results ***********************************/

                                if (RunNum < RunsTotal) {
                                sprintf(ss, "Mus%dG%d.m", imus, ig);
                                target = fopen(ss, "w");
                                }

                                if (RunNum == RunsTotal) {
                                sprintf(ss, "Mus0.m");
                                target = fopen(ss, "w");
                                }

                                fprintf(target, "em = [\n");
                                for (iz=1; iz<=NrunsZ; iz++)
                                        for (ir=1; ir<=NR; ir++) {
                                        fprintf(target,                                 "%1.8e",
EMprofile[iz][ir]/NphotonsFOR);
                                        if (ir <  NR) fprintf(target,"\t");
                                        if (ir == NR) fprintf(target,"\n");
```

```
                                        }
                                fprintf(target, "];\n\n\n");

                                fprintf(target, "ex = [\n");
                                for (iz=1; iz<=NrunsZ; iz++)
                                        for (ir=1; ir<=NR; ir++) {
                                        fprintf(target,                                 "%1.8e",
EXprofile[iz][ir]/NphotonsFOR);
                                        if (ir <  NR) fprintf(target,"\t");
                                        if (ir == NR) fprintf(target,"\n");
                                        }
                                fprintf(target, "];");
                                fclose(target);


                        } /*if (RunNum < RunsTotal)*/
                } /* end of g */
        } /* end of mus */
free_dmatrix(EXprofile,1,NrunsZ,1,THESIZE);
free_dmatrix(EMprofile,1,NrunsZ,1,THESIZE);
free_dmatrix(Ccyl,1,THESIZE,1,THESIZE);
} /* end of main */

/* SUBROUTINES */

/*****
 * bessj1(x)
 * Returns the Bessel function 1(x) for any real x.
 * Be sure to #include <math.h>
 * From Numerical Recipes in C.
 ****/
 float bessj1(float x) {
        float ax,z;
        double xx,y,ans,ans1,ans2; // Accumulate polynomials in double precision.

if ((ax=fabs(x)) < 8.0) { //Direct rational approximation.
        y=x*x;
        ans1=x*(72362614232.0+y*(-7895059235.0+y*(242396853.1                   +y*(-
2972611.439+y*(15704.48260+y*(-30.16036606))))));
        ans2=144725228442.0+y*(2300535178.0+y*(18583304.74
+y*(99447.43394+y*(376.9991397+y*1.0))));
        ans=ans1/ans2;
} else {  //Fitting function (6.5.9).
        z=8.0/ax;
        y=z*z;
        xx=ax-2.356194491;
```

```
        ans1=1.0+y*(0.183105e-2+y*(-0.3516396496e-4       +y*(0.2457520174e-5+y*(-
0.240337019e-6))));
        ans2=0.04687499995+y*(-0.2002690873e-3            +y*(0.8449199096e-5+y*(-
0.88228987e-6 +y*0.105787412e-6)));
        ans=sqrt(0.636619772/ax)*(cos(xx)*ans1-z*sin(xx)*ans2);
        if (x < 0.0) ans = -ans;
}
return ans;
}

/*************************************************************************
***
 *      RandomGen
 *      A random number generator that generates uniformly
 *      distributed random numbers between 0 and 1 inclusive.
 *      The algorithm is based on:
 *      W.H. Press, S.A. Teukolsky, W.T. Vetterling, and B.P.
 *      Flannery, "Numerical Recipes in C," Cambridge University
 *      Press, 2nd edition, (1992).
 *      and
 *      D.E. Knuth, "Seminumerical Algorithms," 2nd edition, vol. 2
 *      of "The Art of Computer Programming", Addison-Wesley, (1981).
 *
 *      When Type is 0, sets Seed as the seed. Make sure 0<Seed<32000.
 *      When Type is 1, returns a random number.
 *      When Type is 2, gets the status of the generator.
 *      When Type is 3, restores the status of the generator.
 *
 *      The status of the generator is represented by Status[0..56].
 *
 *      Make sure you initialize the seed before you get random
 *      numbers.
 ****/
#define MBIG 1000000000
#define MSEED 161803398
#define MZ 0
#define FAC 1.0E-9

double RandomGen(char Type, long Seed, long *Status){
  static long i1, i2, ma[56];   /* ma[0] is not used. */
  long       m, mk;
  short      i, ii;

  if (Type == 0) {              /* set seed. */
    m = MSEED - (Seed < 0 ? -Seed : Seed);
    m %= MBIG;
```

```
    ma[55] = m;
    mk = 1;
    for (i = 1; i <= 54; i++) {
      ii = (21 * i) % 55;
      ma[ii] = mk;
      mk = m - mk;
      if (mk < MZ)
        mk += MBIG;
      m = ma[ii];
    }
    for (ii = 1; ii <= 4; ii++)
      for (i = 1; i <= 55; i++) {
        ma[i] -= ma[1 + (i + 30) % 55];
        if (ma[i] < MZ)
          ma[i] += MBIG;
      }
    i1 = 0;
    i2 = 31;
  } else if (Type == 1) {       /* get a number. */
    if (++i1 == 56)
      i1 = 1;
    if (++i2 == 56)
      i2 = 1;
    m = ma[i1] - ma[i2];
    if (m < MZ)
      m += MBIG;
    ma[i1] = m;
    return (m * FAC);
  } else if (Type == 2) {       /* get status. */
    for (i = 0; i < 55; i++)
      Status[i] = ma[i + 1];
    Status[55] = i1;
    Status[56] = i2;
  } else if (Type == 3) {       /* restore status. */
    for (i = 0; i < 55; i++)
      ma[i + 1] = Status[i];
    i1 = Status[55];
    i2 = Status[56];
  } else
    puts("Wrong parameter to RandomGen().");
  return (0);
}
#undef MBIG
#undef MSEED
#undef MZ
#undef FAC
```

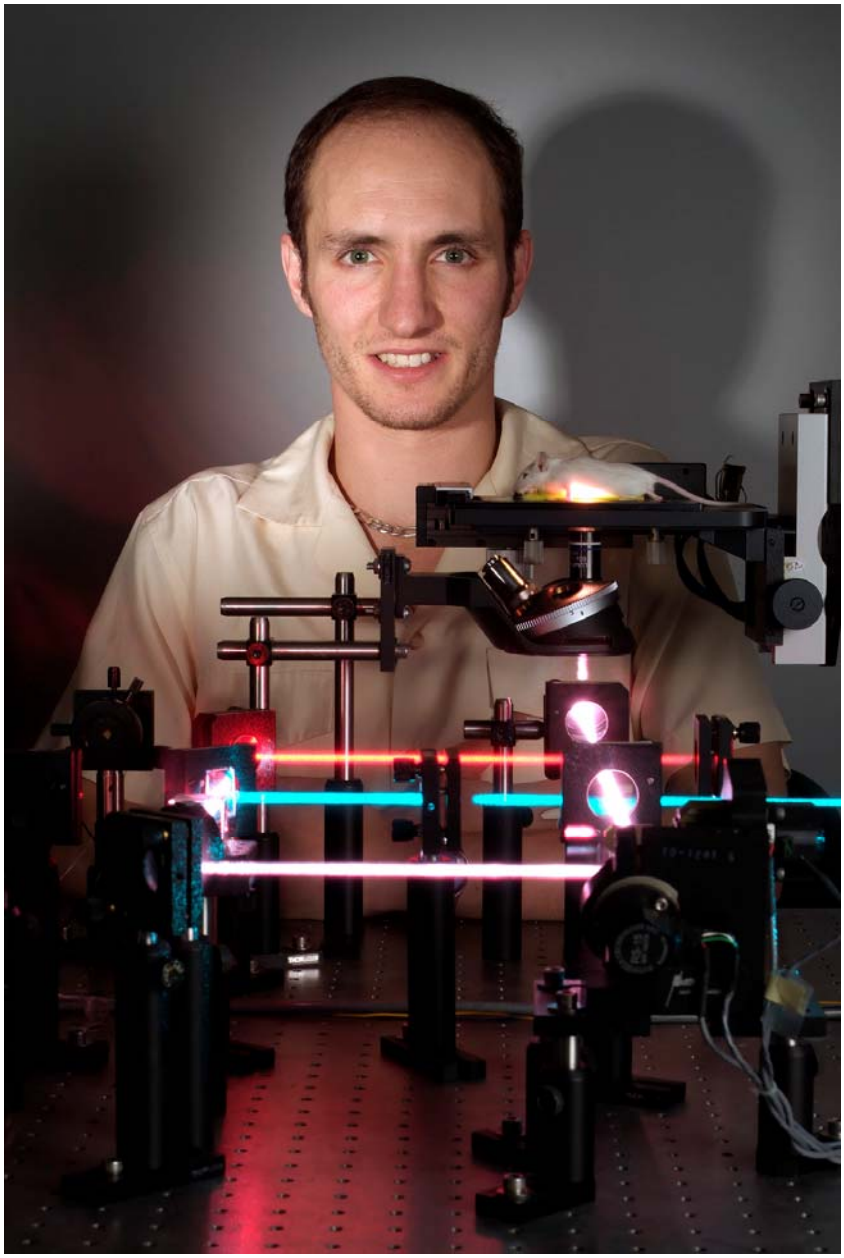

Biographical Sketch

Dan Gareau was born in Buffalo NY on Christmas eve 1976. Dan attended Moses Brown School in Providence, RI, the University of Vermont in Burlington, VT, and the Oregon Graduate Institute of Science and Technology in Beaverton, OR for his high school, bachelors degree in electrical engineering and masters degree in electrical engineering respectively. Dan's interests include dermatology, neuroscience and fishing. Dan served as student body president for the Oregon Health and Science University for two terms, mentored prize-winning young scientists and received both the student achievement and student leadership awards for 2005. Dan has been published in the Journal of Biomedical Optics and the Journal of Investigative Dermatology. (Photo: David Burch)